

**Structure-based drug design on the enoyl-ACP
reductases of *Yersinia pestis* and
*Burkholderia pseudomallei***

**Struktur-basiertes Wirkstoffdesign an Enoyl-ACP
Reductase von *Yersinia pestis* und
*Burkholderia pseudomallei***

Dissertation

for a doctoral degree at the Graduate School of Life Sciences,

Julius-Maximilians-Universität Würzburg,

Section Biomedicine

submitted by

Maria Wenefriede Hirschbeck

from Schwabach

Würzburg, August 2012

Submitted on:

Office stamp

Members of the *Promotionskomitee*:

Chairperson: **Ulrike Holzgrabe**

Primary Supervisor: **Caroline Kisker**

Supervisor (Second): **Christoph Sotriffer**

Supervisor (Third): **Peter Tonge**

Date of Public Defense:

Date of Receipt of Certificates:

Table of content

Summary.....	1
Zusammenfassung.....	2
1. Introduction	3
1.1 Spread of resistance provokes a pressing need for new antibacterials against Gram-negative pathogens.....	3
1.2 Biothreats.....	7
1.2.1 <i>Burkholderia pseudomallei</i> and Melioidosis	8
1.2.2 <i>Yersinia pestis</i> and the Plague.....	10
1.3 Bacterial fatty acid biosynthesis pathway FAS-II as promising drug target.....	12
1.3.1 FAS-II.....	13
1.3.2 Enoyl-ACP reductases.....	15
1.3.2.1 FabI.....	16
1.3.2.2 FabV.....	19
1.4 Research objective	21
2. Materials and Methods.....	22
2.1 Materials	22
2.1.1 Chemicals	22
2.1.2 Inhibitors	22
2.1.3 Plasmids.....	22
2.1.4 Bacterial culture	23
2.1.5 Enzymes and Kits.....	23
2.1.6 Crystallization screens.....	24
2.1.7 Equipment	24
2.1.8 Computer Software	26
2.2 Methods	28
2.2.1 Microbiology techniques.....	28
2.2.1.1 Transformation.....	28
2.2.1.2 Plasmid amplification	29
2.2.1.3 Protein expression.....	29
2.2.2 Protein purification	30
2.2.2.1 Cell lysis	30
2.2.2.2 Ni ²⁺ -affinity chromatography	30
2.2.2.3 Thrombin cleavage	32
2.2.2.4 Size-exclusion chromatography	33
2.2.3 Protein characterization.....	34
2.2.3.1 SDS-PAGE analysis	34

2.2.3.2	Thermofluor analysis.....	35
2.2.4	Protein Crystallization	36
2.2.4.1	Vapor diffusion method	36
2.2.4.2	Protein preparation.....	37
2.2.4.3	Screening	38
2.2.4.4	Optimization.....	38
2.2.5	X-ray crystallography.....	39
2.2.5.1	Data collection and processing	39
2.2.5.2	Phase determination	41
2.2.5.3	Molecular replacement - MR	42
2.2.5.4	Single isomorphous replacement with anomalous scattering – SIRAS.....	43
2.2.5.5	Model building, refinement and validation	45
3.	Results	48
3.1	FabV.....	48
3.1.1	Expression of FabV from different Pathogens	48
3.1.2	Buffer optimization using Thermofluor analysis	50
3.1.3	Purification	51
3.1.3.1	Removal of the hexahistidine tag.....	53
3.2	Crystal structures of FabV from <i>Y. pestis</i> –T276S variant and wild type.....	55
3.2.1	Binary cofactor complex of YpFabV	55
3.2.1.1	Crystallization	55
3.2.1.2	Data collection and structure solution (SIRAS)	56
3.2.1.3	Validation	60
3.2.2	Binary and ternary complexes of cleaved YpFabV	63
3.2.2.1	Crystallization	63
3.2.2.2	Data collection and structure solution.....	64
3.2.2.3	Validation	68
3.3	Enoyl-ACP reductase FabV from <i>B. pseudomallei</i> (BpFabV)	69
3.3.1	Crystallization	69
3.3.2	Data collection and Structure solution	70
3.3.3	Validations of the two BpFabV apo structures	73
3.4	Enoyl-ACP reductase FabI from <i>B. pseudomallei</i> (BpFabI).....	75
3.4.1	Expression	75
3.4.2	Buffer optimization using the Thermofluor analysis.....	76
3.4.3	Purification	77
3.4.4	Crystallization	78
3.4.5	Data collection and Structure solution	80
3.4.5.1	MR of BpFabIapo.....	80

3.4.5.2 MR of ternary inhibitor complexes of BpFabI	82
3.4.6 Validation of the BpFabI structures	84
3.4.6.1 BpFabIapo.....	84
3.4.6.2 Ternary complexes of BpFabI with Inhibitors	84
4. Discussion.....	86
4.1 Structural characterization of FabV as potential drug target	86
4.1.1 Overall structure (apo –binary – ternary)	86
4.1.2 The active site.....	89
4.1.3 Stabilization of the substrate- binding loop.....	92
4.1.4 NADH binding	94
4.1.1.1 Influence of the T276S variant on NADH binding	97
4.1.5 Inhibitor binding.....	99
4.1.6 Potential ACP interaction site	103
4.1.7 Potential FAD binding site.....	106
4.2 Functional considerations on FabV.....	107
4.3 Structural characterization of BpFabI as potential drug target	109
4.3.1 Overall structure	109
4.3.2 Active site and NADH binding	112
4.3.3 Inhibitor binding and substrate-binding loop dynamics	116
4.4 Future perspective: Inhibitors targeting FabI and FabV	123
5. References.....	126
6. Appendix	134
6.1 Supplemental Figures.....	134
6.2 Abbreviations	137
6.3 List of Figures, Tables and Equations	139
6.4 DNA and amino acid sequences of protein constructs	142
6.5 Thermofluor Screen	146
6.6 Crystallization screens.....	146
Acknowledgements	151
Affidavit	152
List of publications.....	153

Summary

Spreading drug resistances among Gram-negative pathogens and the paucity of new agents on the antibacterial drug market against these tenacious bacteria create a pressing need for the development of new antibiotics. The bacterial fatty acid biosynthesis pathway FAS-II, especially the enoyl-ACP reductase catalyzing the last step of the elongation cycle, is an established drug target against tuberculosis but has not been extensively exploited for drug design against other bacterial pathogens. In this thesis the enoyl-ACP reductases of the Gram-negative biothreat organisms *Burkholderia pseudomallei* and *Yersinia pestis* were targeted in a structure-based drug design approach. The structure of the most recently identified enoyl-ACP isoenzyme FabV was characterized by X-ray crystallography and could be determined in three different states. FabV from *B. pseudomallei* was obtained in the apo-form of the enzyme, whereas FabV from *Y. pestis* was characterized in a binary complex with the cofactor NADH as well as in a ternary complex with NADH and the triclosan-based 2-pyridone inhibitors PT172 and PT173. Analysis of the FabV structure revealed the typical fold of the short chain dehydrogenase/reductase superfamily with the NADH-binding Rossmann fold and a substrate-binding pocket with a conserved active site geometry compared to the related isoenzyme FabI. Additional structural elements of FabV are located around the active site. The monomeric form of the enzyme is thereby stabilized and the substrate-binding loop is kept in a closed, helical conformation. The ternary complexes of FabV exhibited a similar inhibitor-binding mode as observed for triclosan inhibition in FabI and point to a potential substrate-binding mechanism.

B. pseudomallei possesses FabI as an additional enoyl-ACP reductase isoenzyme, which was structurally characterized in the apo form and in ternary complexes with NAD⁺ and the diphenyl ether inhibitors triclosan, PT02, PT12 or PT404 as well as the 4-pyridone inhibitor PT155. The structural data of the ternary enoyl-ACP reductases complexes of *B. pseudomallei* and *Y. pestis* hold the promise for the possibility to develop antibacterials targeting FabV or even both isoenzymes, FabI and FabV, based on the triclosan scaffold.

Zusammenfassung

Die Ausbreitung von Antibiotikaresistenzen in Gram-negativen Pathogenen sowie der Mangel neuer Medikamente auf dem Arzneimittelmarkt gegen diese hartnäckigen Bakterien weist einen dringenden Bedarf an neuen Antibiotika auf. Die bakterielle Fettsäurebiosynthese (FAS-II), speziell die Enoyl-ACP-Reduktase, welche den finalen Schritt des Elongationszyklus katalysiert, ist ein etablierter Angriffspunkt in der Tuberkulosetherapie. Sie wurde jedoch bisher noch nicht für die gezielte Wirkstoffentwicklung gegen andere bakterielle Krankheitserreger genutzt. In dieser Dissertation waren die Enoyl-ACP Reduktasen aus *Burkholderia pseudomallei* und *Yersinia pestis* Gegenstand des strukturbasierten Wirkstoffdesigns. Die Struktur des zuletzt gefundenen Isoenzym der Enoyl-ACP-Reduktase, FabV, wurde röntgenstrukturanalytisch charakterisiert und konnte in drei verschiedenen Zuständen bestimmt werden. Die Struktur des FabV Proteins aus *B. pseudomallei* wurde in der Apo-Form gelöst, während FabV aus *Y. pestis* in binären und ternären Komplexen mit NADH bzw. NADH und einem Triclosan-basierten 2-Pyridon-Inhibitor, PT172 bzw. PT173 charakterisiert wurde. FabV weist die typische Struktur eines Mitglieds der Short-Chain-Dehydrogenase/Reduktase Superfamilie mit einer NADH-bindenden Rossmann-Faltung und einer Substratbindetasche auf mit einer, im Vergleich zu dem verwandten Isoenzym FabI, konservierte Geometrie des aktiven Zentrums. Zusätzliche strukturelle Elemente sind um das aktive Zentrum gefaltet und stabilisieren damit das Enzym in seiner monomeren Form. Darüber hinaus halten sie den Substratbindeloop in einer geschlossenen helikalen Gestalt. Die ternären FabV Komplexe zeigen Übereinstimmungen mit dem bekannten Bindungsmechanismus des Inhibitors Triclosan in FabI und deuten auf einen möglichen Substratbindungsmechanismus hin.

B. pseudomallei besitzt FabI als zusätzliches Isoenzym der Enoyl-ACP-Reduktasen. Dieses Isoenzym wurde in der Apo-Form und in ternären Komplexen mit NAD^+ und den Diphenylether-Inhibitoren Triclosan, PT02, PT12 und PT404 sowie dem 4-Pyridon-Inhibitor PT155 strukturell charakterisiert. Die strukturellen Daten der ternären Enoyl-ACP-Reduktase Komplexe von *B. pseudomallei* und *Y. pestis* stellen die Möglichkeit in Aussicht Antibiotika zu entwickeln, welche FabV oder auch beide Isoenzyme, FabI und FabV, inhibieren.

1. Introduction

1.1 Spread of resistance provokes a pressing need for new antibacterials against Gram-negative pathogens

For some decades during the last century a bacterial infection had lost its horror. Antibiotics seemed to be a reliable tool to combat most of the diseases caused by bacteria. However, due to the spread of antibiotic resistance among bacterial pathogens the fear of infections returned to the patient's bedside (Bassetti et al., 2011). The emergence of multi drug resistant (MDR) strains, non-susceptible to three or more antimicrobial classes, and moreover extensively drug resistant (XDR) strains, that are non-susceptible to all known antimicrobial classes, in the clinics have a severe impact on public health, illustrated by increased mortality rates, higher costs and length of hospital stay (Giske et al., 2008). At the same time the number of new antibacterials on the market decreased over the last decades, which further worsens the situation (Figure 1).

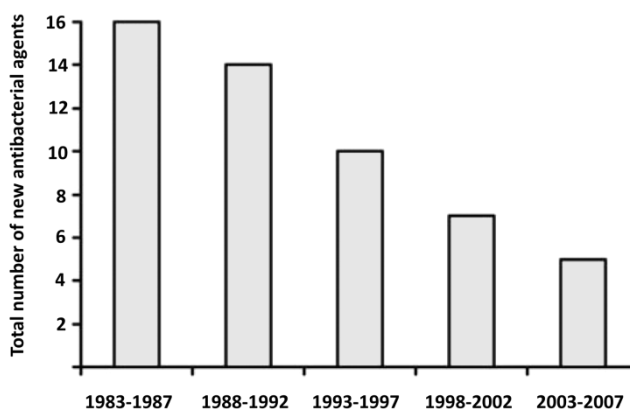


Figure 1: Systemic antibacterials approved by the US Food and Drug Administration, modified from (Spellberg et al., 2008)

All the recently approved antibacterials are improved members of already known antibiotic classes. They exhibit a broader antibacterial spectrum, improved safety, simpler application or insusceptibility to certain resistance mechanisms. Since 1987 no new class of antibiotics had been discovered, which is called the “discovery void” (Silver, 2011). Even the classes that reach the clinic in the last decade (linezolid (2000), daptomycin (2003) and retapamilin (2007)) root in more than 25 year-old discoveries (oxazolidinones (Fugitt and Luckenbaugh, December 1978, 5-Halomethyl-3-phenyl-2-oxazolidinones. U.S.

patent 4,128,654.), acid lipopeptides (Debono et al., 1987) and pleuromutilins in 1952 (Novak and Shlaes, 2010)).

There are diverse mechanisms of resistance, which can be disseminated among pathogens (and non-pathogenic bacteria) via horizontal gene transfer. Resistance genes can be encoded on transferable elements as plasmids or transposons. They are often associated in clusters and can be transferred together (Bassetti et al., 2011). Antibacterial action can be impaired by drug inactivation due to cleavage, as in the case of the abundant β -lactamases, or to modifying enzymes, changing the scaffold of the drug. Another way to prevent antibacterial action is to keep the drug out of the cell with elevated export by efflux pumps or impaired import due to an elaborated cell wall as in mycobacteria or mutated porins (Blair and Piddock, 2009; Meyer, 2005). On the target side the inhibited enzyme can be mutated to change the binding site, the expression of the target can be up-regulated (Tsay et al., 1992) or an isoenzyme takes over the function of the target. By biofilm formation the bacteria build an exopolysaccharide matrix and thereby create an additional impermeable physical barrier blocking antibiotic treatment as well as host immune defense. Cells are recruited to the biofilm via a quorum sensing system utilizing diffusion of small molecules, acyl-homoserine lactones. As a reaction they slow down growth and enhance transcription of resistance genes (Hentzer et al., 2003; Lewis, 2005). Closely related are the so-called persister cells, which are tolerant to antibiotic treatment due to a decreased growth rate, cellular biosynthesis and increased stress response (Balaban et al., 2004). They can persist during antibacterial treatment and switch back into an active phenotype as soon as the pressure is released. An additional way to adapt to the presence of antibiotics are mutator cells. They display defects in their methyl-directed mismatch repair system and therefore have 1000-fold higher mutation rates and an additionally higher frequency in horizontal gene transfer (Boe et al., 2000; Chopra et al., 2003). The impairment of the mutator phenotype is compensated by the ability of the cells to adapt to new environments and antibiotic stress.

The clinically most important MDR pathogens are summarized under the catchphrase "ESCAPE" (Boucher et al., 2009; Peterson, 2009). They contain the three Gram-positive pathogens *Enterococcus faecium*, *Staphylococcus aureus* and *Clostridium difficile* and the Gram-negatives *Acinetobacter baumannii*, *Pseudomonas aeruginosa* and

Enterobacteriaceae (*Escherichia coli*, *Klebsiella pneumoniae*). These pathogens became the focus of drug development endeavors in industry and academia. Especially for methicillin-resistant *Staphylococcus aureus* (MRSA) a variety of new compounds is in the pipelines of the big pharmaceutical. However, for the Gram-negative pathogens most of the few promising drug candidates fail in the clinical phases (Bassetti et al., 2011; Silver, 2011). This might be partially due to the huge focus on MRSA. The greater challenge is to overcome the Gram-negative cell wall in order to get the compound to its target. It is not the lack of potential drug targets but the cell entry across this effective barrier that makes drug discovery against Gram-negative pathogens a difficult endeavor. In contrast to the Gram-positive cell wall, which is composed of the cytoplasmic membrane and a thick, overlying peptidoglycan network traversed by lipoteichoic acid chains, in Gram-negative cells the peptidoglycan layer is thinner and is located in the periplasmic space between the inner and the outer membrane, which is additionally decorated with lipopolysaccharids (LPS) (Figure 2).

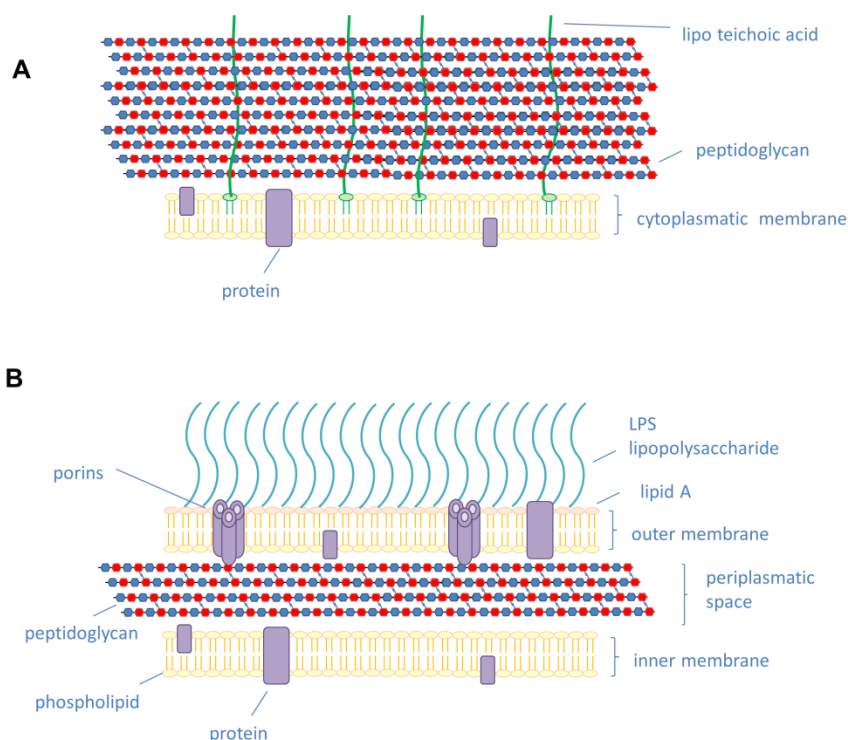


Figure 2: Cell wall of Gram-positive (A) and Gram-negative (B) bacteria

To cross the outer membrane the compound has to pass the porins, water-filled channels that are used by the bacterium for nutrient transport into the cell. They transport hydrophilic, charged compounds not larger than 600 Da (in *E. coli*). Having passed the

porins the compound is in the periplasmic space, but if the actual target is in the cytoplasm it has to traverse the cytoplasmic membrane which requires a hydrophobic portion in the compound (Silver, 2011). To meet these conditions for entry without losing the affinity to the target is quite a challenge for medicinal chemists in drug discovery. Furthermore the relative nonselective resistance-nodulation-cell division (NDR) efflux pumps in Gram-negatives, in particular in *Pseudomonas aeruginosa*, add a synergetic effect to this enhanced biophysical barrier, reducing the intracellular drug concentration even more (Blair and Piddock, 2009). This effect is mirrored by the spectra and target locations of antibacterials displayed in Figure 3.

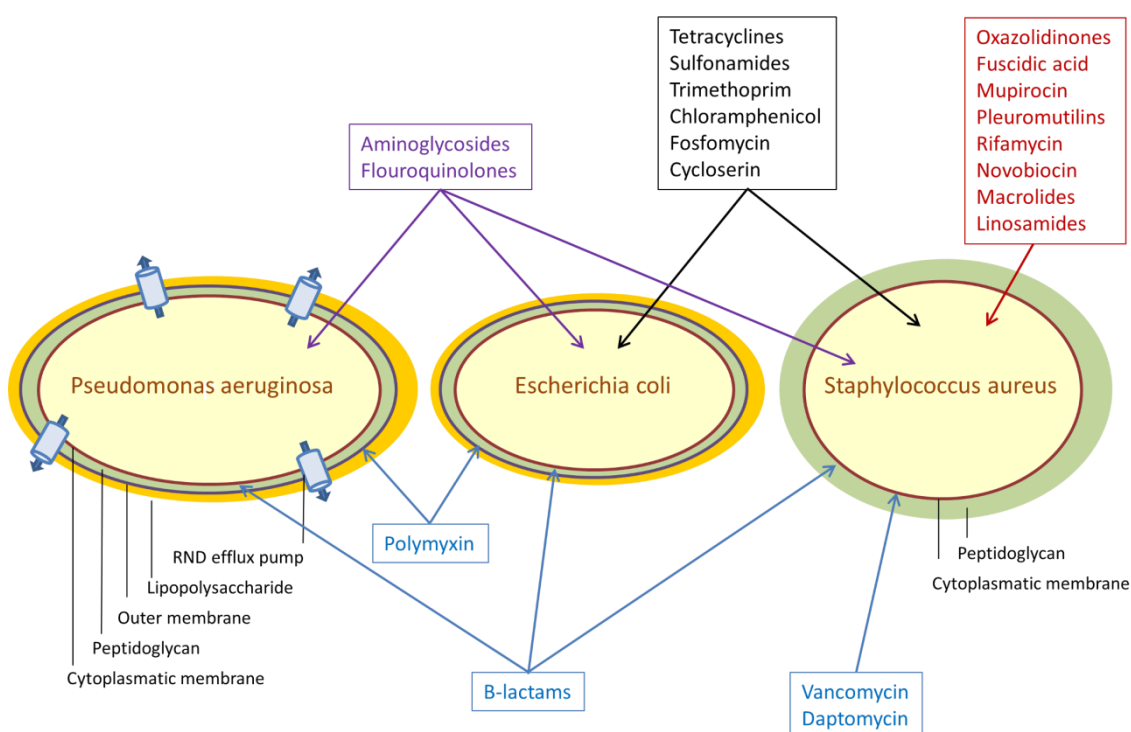


Figure 3: Spectra and target locations of antibacterials, modified after (Silver, 2011)

In the red box antibacterials with cytoplasmatic targets, active against Gram-positives (exemplary *S. aureus*) only are shown, in the black box cytoplasmatic antibacterials active against Gram-positives and some Gram negatives (exemplary *E. coli*) and in the purple box cytoplasmatic antibacterials active also against the Gram-negative *P. aeruginosa* are shown. Antibacterials active at the cell wall are illustrated in blue boxes.

More than half of the cytoplasmatic antibacterials are exclusively active in Gram-positives (Figure 3, shown in red). Among the active cytoplasmatic classes against the Gram-negative *E. coli* only aminoglycosides and fluoroquinolones (Fig. 3, shown in purple) are also active against *P. aeruginosa*. The residual two classes active against *P. aeruginosa* (shown in blue in Figure 3) are targeting the cell wall. The spread of resistant Gram-negative pathogens, the lack of compounds in developmental pipelines and the particular difficulty

to ensure cell entry of the compound underline the importance of new drug developments against Gram-negative pathogens.

1.2 Biothreats

Biothreats are bacteria, viruses or toxins that are feared to be used as bioweapons. Bacterial examples of bioweapons are *Bacillus anthracis*, *Yersinia pestis*, *Vibrio cholerae*, *Burkholderia pseudomallei* or *Francisella tularensis* (Table 1) (Leitenberg, 2001).

Table 1: Bioweapons: pathogens and diseases

Bacteria		Viruses		Toxins	
<i>Bacillus anthracis</i>	Anthrax	<i>Variola virus</i>	Smallpox	Botulinal toxins	Botulism
<i>Yersinia pestis</i>	Plague	<i>VEE virus</i>	Venezuelan equine encephalitis	Ricin	Ricin poisoning
<i>Francisella tularensis</i>	Tularemia	<i>Marburg virus, Ebola virus</i>	Hemorrhagic fever	Staphylococcal enterotoxin B (SEB)	SEB poisoning
<i>Brucella spp.</i>	Brucellosis				
<i>Burkholderia pseudomallei</i>	Melioidosis				
<i>Coxiella burnetii</i>	Q fever				
<i>Vibrio cholerae</i>	Cholera				

Compared to conventional weapons only small amounts of biothreat organisms might cause an unpredictable disastrous outcome (Szinicz, 2005). Unlike chemical weapons, biological agents can amplify inside the victim and disseminate from host to host. The spreading of antibacterial resistance genes even increases the danger arising from these pathogens. Bioweapons have been classified as weapons of mass destruction, along with nuclear and chemical weapons. In the Biological and Toxin Weapon Convention the development, production, stock-piling, acquisition or retention of bioweapons and furthermore the research on bioweapons for offensive purpose was banned. This treaty was initially signed in 1972 by the USA, USSR and UK. Meanwhile only 19 countries in the world have not taken part in the agreement (Szinicz, 2005). Although in public there is a great approval of the condemnation of bioweapons, it is known from several countries, also from signatories of the convention, that the treaty was violated. Apart from secret

bioweapon programs in several countries, in particular the fear that bioweapons might be used in irrational terroristic attacks emphasizes the need for new therapeutic agents against biothreat pathogens. This thesis focuses on new antibacterials against the biothreat organisms *B. pseudomallei* and *Y. pestis*.

1.2.1 *Burkholderia pseudomallei* and Melioidosis

Melioidosis was first described by the pathologist Alfred Whitmore and his assistant C.S. Krishnaswami among morphine addicts in Burma in 1911 (Cheng and Currie, 2005). The infectious agent of this serious infection is the Gram-negative, motile bacillus *Burkholderia pseudomallei*, an environmental bacterium, which can be found in soil and surface-water (Peacock, 2006). *Burkholderia pseudomallei* is capable to survive in hostile environments and can tolerate nutrient deficiency, antiseptic and detergent solutions, acidic environments, wide temperature ranges and dehydration.

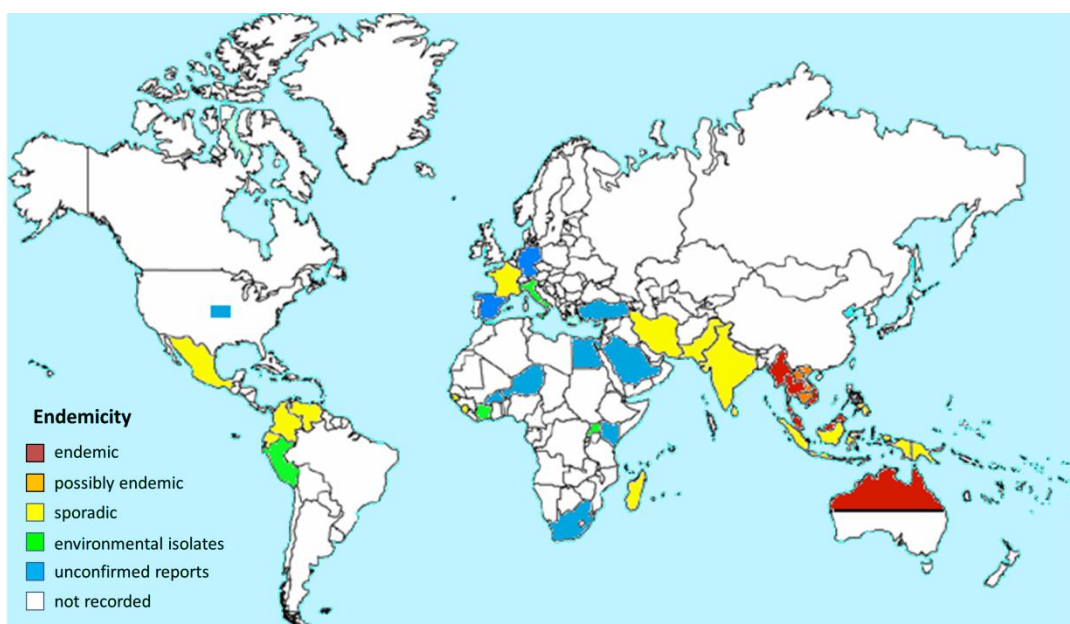


Figure 4: Endemic distribution of Melioidosis, modified after (Cheng and Currie, 2005)

Melioidosis is endemic in tropical latitudes (Figure 4), predominantly in Southeast Asia and Northern Australia, and is highly associated with rainfall during the monsoonal season (Currie and Jacups, 2003). In Australia an outbreak of melioidosis was reported which originated by contamination of drinking water supplies (Cheng and Currie, 2005). Another source of exposure was the tsunami in 2004, where not only victims of the catastrophe but also uninjured bystanders were infected (Athán et al., 2005). The roots of

infections with *B. pseudomallei* are direct inoculation or inhalation of soil or aerosols. The infection can affect virtually any organ in the body, leading to a variety of clinical signs and symptoms. Therefore melioidosis is often called the “great mimicker”. Its most fatal clinical manifestation is septic shock with concomitant pneumonia and bacterial dissemination to distant sites (Wiersinga et al., 2006). 20% of all community-acquired bacteremias in Thailand are caused by melioidosis (Cheng and Currie, 2005). Crucial risk factors for melioidosis are underlying diseases such as diabetes, renal failure, alcohol abuse or immunosuppression. A common feature of these conditions is a deficiency of neutrophils weakening the clearance of the pathogen by the immune response (Cheng, 2010). Diagnostic tests, essential for the rapid treatment of melioidosis, are either time-consuming for example a bacterial culture of a clinical sampling or not reliable as shown for PCR assays or serological methods (Cheng, 2010; Gal et al., 2005). The antimicrobial therapy of melioidosis has to be commenced as soon as a melioidosis infection is suspected. The pathogen is intrinsically resistant to diverse groups of antibiotics such as cephalosporins, penicillins, rifamycins and aminoglycosides and shows reduced susceptibility to quinolones and macrolides (Cheng and Currie, 2005). The biphasic treatment starts with an initial parenteral therapy with admission of ceftazidime or a carbapenem for 10-14 days, followed by 12-20 weeks of an oral eradication phase with trimethoprim-sulfamethoxazole (TMP-SMX) and in parts additional doxycycline (Limmathurotsakul and Peacock, 2011). In cases involving septic shock an adjuvant treatment with granulocyte colony-stimulation factor (G-CSF) during the acute phase was reported to be associated with decreased mortality rates (Cheng et al., 2004). However, even with this extensive antibiotic treatment the mortality rates remain high with approx. 50% in Thailand and 19 % in Australia (Peacock, 2006). Important for the outcome is the availability of intensive care facilities for all patients with severe sepsis. Another problem is recurrent melioidosis. In Thailand 6% of the patients are re-infected with melioidosis in the first year and 10% in the first 10 years, among them 75% were relapses of the original infection and 25% re-infected with different strains (Maharjan et al., 2005).

B. pseudomallei is listed as a potential bioweapon. In USSR, USA and possibly in Egypt researchers pursued the weaponization of melioidosis. As a disease with high mortality rates and intrinsic antibiotic resistances in combination with its tolerance against hostile

environments, it would be an attractive agent for bioweapon development. One effective route of infection is inhalation of dust or aerosols; therefore aerosols would be a forceful way of distributing the disease. Yet the disease does not spread from human to human and it remains to be clarified whether it infects people with an intact immune system. Furthermore it is not known if the research ever yielded weaponized *B. pseudomallei* pathogens. Hence it should rather be called a biothreat than a bioweapon, since up to now there is only the fear that this deadly but rare disease could be turned into an effective bioweapon. In contrast, the closely related pathogen *Burkholderia mallei*, causing the animal disease glanders, had already been used by German troops during World War I as a biological warfare agent against the transport horses of the Russian army.

1.2.2 *Yersinia pestis* and the Plague



Figure 5: Black death, 16th century woodcut (Holbein, Hans. "The Dance of Death." Woodcut, before 1538)

The plague is famous for several waves of disastrous epidemics throughout history. The first reports of bubonic plague were recorded during the plague of Justinian (541-542). It was estimated that about 100 million people died of the pandemic (Achtman et al., 1999). The second pandemic caused by the plague devastated the world's population in the 13th century. Starting in China, where it eliminated half of the population, the so called Black Death (Figure 5) disseminated following the Silk Road to the known world. Following the last great pandemic, which started in 1855 and hit predominantly Asia,

Alexandre Yersin described *Y. pestis* for the first time as the infectious agent causing the plague during an outbreak of the disease in Hong Kong in 1894 (Alexandre Yersin, 2010). However, there were always doubts if the Black Death had its origin in *Y. pestis*. It was hypothesized that the disease was caused by viral hemorrhagic fever (Duncan and Scott,

2005). Only recently the genome of *Y. pestis* could be verified in plague victims from the 13th century outbreak in London (Bos et al., 2011). The disease is enzootic mainly in rodents and other mammals. Humans are infected accidentally by fleabites, especially when the susceptible rodents are dying off due to seasonal changes. Since humans play hardly any role in the maintenance of the disease, it cannot be eradicated by vaccination (Williamson, 2009). Another source of infection is direct inoculation through skin lacerations by handling tissues of infected mammals or inhaling aerosolized bacteria in close contact to an infected patient. This route of infection requires close contact to coughing patients in the terminal phase of the disease. (Butler, 2009; Lowell et al., 2005). Human plague syndromes appear predominantly in bubonic, septicaemic and pneumonic forms, however, most cases show primarily the bubonic form (Butler, 2009). The first patient typically starts with the bubonic or septicaemic disease and develops a secondary pneumonia. Subsequently, the coughing patient disseminates the infection to his family or care attendants (Kool, 2005). During the 20th century the plague caused extensive deaths in India and Vietnam and even in the new millennium plague remains a killer disease in Africa, Asia and the Americas (Perry and Fetherston, 1997; Titball and Leary, 1998). There were 28,956 reported cases during the decade 1992-2001 with 2064 deaths, about 84% of them in Africa (WHO, 2004). Upon expeditious diagnosis, treatment with conventional antimicrobial agents like gentamycin, streptomycin or doxycycline is usually successful (Butler, 2009). However in 1995 two highly drug-resistant *Y. pestis* strains were reported in Madagascar. One strain was observed to be resistant to streptomycin, chloramphenicol, tetracycline, sulfonamide, ampicillin, kanamycin and spectinomycin, the second strain only to streptomycin. Both resistance genes could be located in highly transferable plasmids (Galimand et al., 2006; Guiyoule et al., 2001; Guiyoule et al., 1997). The continuous reports of cases in the endemic areas as well as in areas, where the plague did not occur for decades, together with the threat of resistant strains led to the classification of the plague as a re-emerging disease by the World Health Organization (WHO) (Galimand et al., 2006; WHO, 2004). Although the organism itself is not able to survive outside a host for a longer period of time, it was used as biological weapon throughout history (Richard and Grimes, 2008). In preindustrial times the plague was disseminated among enemies through infected corpses or clothes. The Mongols catapulted plague infected corpses into the besieged town of Kaffa, forcing the Genoese

to flee from the contaminated city. This event might have contributed to the spread of the plague during the second pandemic (Smart, 1997). In the 20th century technical and scientific advances had an impact on the dissemination of *Y. pestis* as a bioweapon. During World War II the Japanese used vector fleas against the Chinese troops and population and the USSR developed an aircraft-mounted dispenser, which sprayed a *Y. pestis* emulsion onto the enemy (Smart, 1997). Risks like the upcoming drug-resistant strains in Madagascar (1995) and the use as a biological weapon underline the threat arising from this unattended organism and show the demand for new targets in the struggle against this disease.

1.3 Bacterial fatty acid biosynthesis pathway FAS-II as promising drug target

A promising but up to now relatively unexploited drug target for antibacterial development is the bacterial fatty acid biosynthesis pathway FAS-II. A good drug target should be (I) essential for the survival of the bacteria, it should be (II) conserved among several bacterial pathogens and it has to be (III) absent, different or non-essential in humans (O'Shea and Moser, 2008). Fatty acid biosynthesis is essential for the survival of bacteria since it is required for membrane phospholipid synthesis (Heath and Rock, 2004). The steps of fatty acid biosynthesis in all organisms are the same. In the FAS-II pathway each step is catalyzed by a discrete enzyme. Every step in the pathway is essential for the completion of fatty acid biosynthesis (Egan and Russell, 1973; Zhang and Cronan, 1998). However, for some of the steps several isoenzymes were identified in different species, which can catalyze the same reaction. This is a drawback for antibacterial drug development, since it reduces the antibacterial spectrum of drug candidates to bacteria possessing the targeted isoenzyme as the sole enzyme for this step. The FAS-II pathway is used for fatty acid biosynthesis in bacteria, protozoa and plants (Payne et al., 2001). Humans as well as other mammals, birds and yeast synthesize their required fatty acids within the FAS-I system (Rozwarski et al., 1999). FAS-I catalyzes the same steps as FAS-II, but instead of a series of distinct enzymes it is a huge, dimeric multi-enzyme complex, catalyzing all steps of the pathway in different domains of the complex (Jenni et al., 2007; Smith, 1994). Since there are only minor homologies in structure and sequence of FAS-I and FAS-II, the enzymes of FAS-II represent specific drug targets. With the restriction, that

due to the presence of isoenzymes some of the steps cannot be used to develop broad spectrum antibiotics, the conditions for a good antibacterial target are fulfilled for the FAS-II pathway.

1.3.1 FAS-II

The mechanism of the bacterial fatty acid biosynthesis pathway was first described in *E. coli* (Egan and Russell, 1973). It starts with acetyl-CoA which is carboxylated by the heterotetrameric acetyl-CoA Carboxylase AccABCD to malonyl-CoA. In the following reaction the malonyl-CoA-ACP transacetylase FabD exchanges the carrier molecule Coenzyme A with the acyl-carrier protein ACP to malonyl-ACP. ACP is a small, mostly α -helical, acidic protein, which shuffles the acyl-intermediates from enzyme to enzyme. The intermediate is attached by a thioester to phosphopantetheine, the prosthetic group of ACP, which is linked to a conserved serine of ACP (Chan and Vogel, 2010).

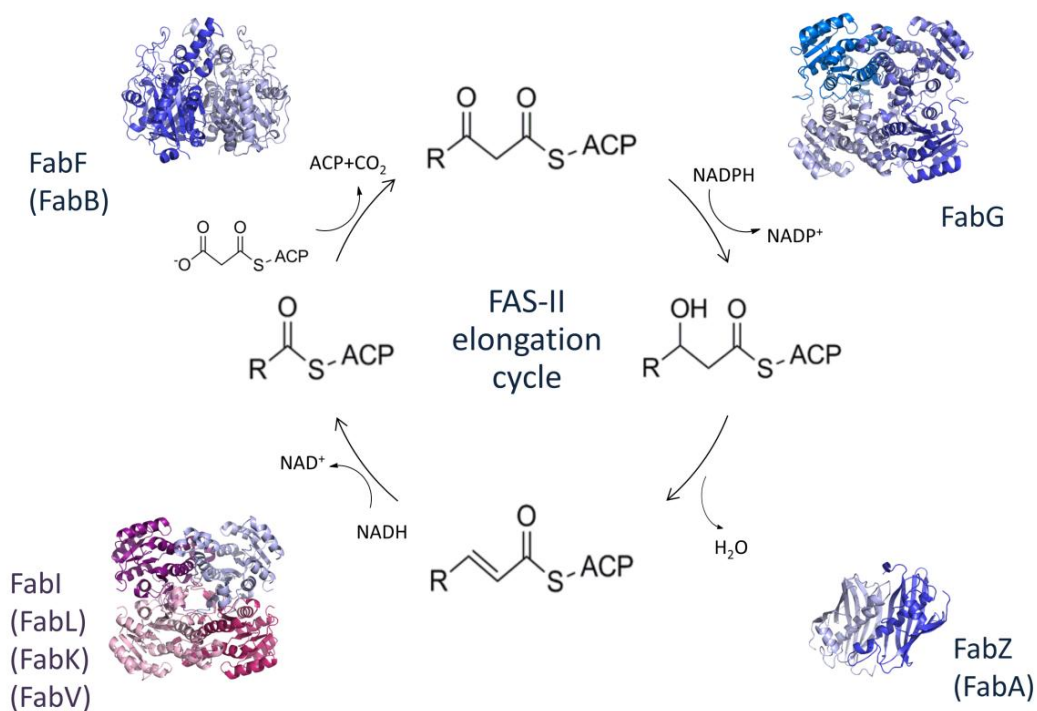


Figure 6: Scheme of the FAS-II elongation cycle

In the elongation cycle a two-carbon unit is added to an acyl-ACP intermediate in a condensation with malonyl-ACP, catalyzed by FabF (PDB ID 2gfw, shown as ribbon diagram, top left). The β -ketoacyl-ACP is reduced by FabG (PDB ID, 1q7c, shown as ribbon diagram, top right) to β -hydroxyacyl-ACP, which is dehydrated to enoyl-ACP by FabZ (PDB ID 1mkb, shown as ribbon diagram at the bottom right). FabI (PDB ID 1dfi, shown in purple as ribbon diagram at the bottom left) reduces enoyl-ACP to acyl-ACP, which can re-enter the cycle. Potential isoenzymes are shown in parentheses. A detailed description is given in the following text.

The β -ketoacyl-ACP synthase FabH initiates the elongation cycle of FAS-II by the condensation of acetyl-CoA and malonyl-ACP with the elimination of CO₂ and CoA. In the first step of the elongation cycle (Figure 6) β -ketobutyryl-ACP (β -ketoacyl-ACP in general) is reduced by the β -ketoacyl-ACP reductase FabG in an NADPH dependent step to β -hydroxyacyl-ACP. The β -hydroxyacyl-ACP dehydratase FabZ or the β -hydroxydecanoyl-ACP dehydratase/isomerase FabA (C₁₀, unsaturated fatty acid synthesis, described below) dehydrates β -hydroxyacyl-ACP to *trans*-2-enoyl-ACP, which is subsequently reduced in an NADH dependent reaction by an enoyl-ACP reductase (FabI, FabK, FabL or FabV) to the product of the cycle, acyl-ACP. To re-enter the elongation cycle and prolong the acyl chain by another 2 carbon atoms, the condensing enzyme FabF or FabB (for unsaturated fatty acids) combines the acyl-ACP with another malonyl-ACP to obtain β -ketoacyl-ACP and CO₂ (Marrakchi et al., 2002b; Wright and Reynolds, 2007).

The FAS-II pathway exhibits some diversity among different species. One source of diversity is the subset of four isoenzymes of enoyl-ACP reductases (1.3.2). Another aspect is the generation of unsaturated fatty acids. Not all bacteria are able to produce unsaturated fatty acids, e.g. Gram-positives as *S. aureus*, and the organisms, which can produce them pursue different mechanisms (Marrakchi et al., 2002b). The most abundant mechanism (e.g. *E. coli* or *P. aeruginosa*) introduces the double bond by the β -hydroxydecanoyl-ACP dehydratase/isomerase FabA. β -Hydroxydecanoyl-ACP is dehydrated to *trans*-2-enoyl-ACP and subsequently changed into *cis*-3-enoyl-ACP by the isomerase activity of FabA. The enoyl-reductase step is omitted at this point and *cis*-3-enoyl-ACP is re-entering the elongation cycle through a condensation with malonyl-ACP catalyzed by FabB instead of FabF (Clark et al., 1983). *Streptococcus pneumoniae* uses another enzyme for the production of unsaturated fatty acids. Here FabZ catalyzes the dehydration and the *trans*-2-*cis*-3-enoyl-ACP isomerase FabM is responsible for the formation of the double bond into the intermediate. In this organism, FabF can conduct the condensation of the unsaturated intermediate (Marrakchi et al., 2002a).

The FAS-II pathway is not an untapped target. The two natural products cerulenin and thiolactomycin are inhibitors of the β -ketoacyl-ACP synthase and especially thiolactomycin has been extensively analyzed to be exploited for drug design (Heath and Rock, 2002; Luckner et al., 2009; Machutta et al., 2010). For the enoyl-ACP reductase FabI

several inhibitors are known e.g. isoniazid (Banerjee et al., 1994; Marrakchi et al., 2000; Quemard et al., 1995), diazaborines (Baldock et al., 1998a) and triclosan (Stewart et al., 1999; Ward et al., 1999). Since the enoyl-ACP reductase is an established and potent drug target, we focused in this study on the inhibition of this step in the Gram-negative biothreat pathogens *B. pseudomallei* and *Y. pestis*.

1.3.2 Enoyl-ACP reductases

Currently, there are four different isoenzymes of the enoyl-ACP reductase known in bacteria. FabI was initially identified and constitutes the most abundant isoform (Heath and Rock, 1995). It was first described in *E. coli*. After it has been discovered, that FabI is the target of triclosan and especially isoniazid, an important drug against tuberculosis; it came in the focus of antibacterial drug development. In 2000 however, two isoenzymes of FabI were uncovered. FabK was described in *S. pneumonia* as a flavoprotein with no significant homology to FabI (Heath and Rock, 2000) and the third isoenzyme FabL was found along with FabI in *Bacillus subtilis* (Heath et al., 2000). The latter is related to FabI with a sequence identity of 24% but confers resistance to triclosan just like the unrelated protein FabK. The most recently discovered isoenzyme FabV was described in *V. cholerae* and is related to FabI and FabL. This isoenzyme also provides resistance to triclosan (Massengo-Tiasse and Cronan, 2008).

Table 2: Known enoyl-ACP reductases of important pathogens

<i>Enterococcus faecium</i>	FabI
<i>Staphylococcus aureus</i>	FabI
<i>Clostridium difficile</i>	FabK
<i>Acinetobacter baumannii</i>	FabI
<i>Pseudomonas aeruginosa</i>	FabI + FabV
<i>Escherichia coli</i>	FabI
<i>Klebsiella pneumoniae</i>	FabI + FabK
<i>Streptococcus pneumoniae</i>	FabK
<i>Vibrio cholerae</i>	FabV
<i>Burkholderia pseudomallei</i>	FabI + FabV
<i>Yersinia pestis</i>	FabV

Due to the emerging diversity of the enoyl-ACP reductases, the pharmaceutical industry lost interest in this target, since it was not suitable for the development of broad spectrum antibiotics. However, especially the isoenzymes FabK and FabL display only a

limited species distribution (Heath and Rock, 2004) and the isoenzymes FabI, FabL and FabV are related, there is thus the potential to develop compounds that might inhibit all or at least two of them efficiently. Another aspect is the increasing need for new antibacterials and the spread of antibiotic resistance. Specific inhibitors against resistant pathogens might become more valuable when resistance against broad spectrum antibiotics disseminates between the pathogens. The Gram-negative pathogens, which will be addressed in this study, exhibit different sets of the enoyl-ACP reductases. In *Y. pestis* FabV is the sole enoyl-ACP reductase; *B. pseudomallei* possesses both FabI and FabV (cf. Table 2).

1.3.2.1 *FabI*

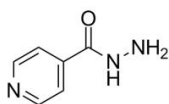
FabI is the most intensively studied target of the FAS-II pathway. One major reason is that it is the target of isoniazid, one of the front-line drugs against the persevering pathogen *Mycobacterium tuberculosis*. But FabI is not only a validated drug target; it also catalyzes the rate-limiting step of the fatty acid pathway and is therefore tightly regulated. Fatty acid biosynthesis is regulated along with phospholipid synthesis. In a feedback inhibition pathway long chain acyl-ACPs inhibit the initiation enzymes acetyl-CoA carboxylase AccABCD and the condensing enzyme FabH as well as FabI, which is finalizing the elongation cycle (Marrakchi et al., 2002b). FabI catalyzes the NAD(P)H-dependent reduction of *trans*-2-enoyl-ACP to the product of the cycle, acyl-ACP. Since it detracts *trans*-2-enoyl-ACP from the equilibrium with β -hydroxyacyl-ACP, with the equilibrium being strongly on the β -hydroxyacyl-ACP side, it drives the pathway forward and is determining the synthesis rate of fatty acids and subsequently membrane lipids (Marrakchi et al., 2002b).

FabI is a member of the short-chain dehydrogenase/reductase superfamily (SDR superfamily) and belongs to the subfamily of “diverse” SDR proteins (Kavanagh et al., 2008; Oppermann et al., 2003). This subfamily has an active site motive of Y-(X₆)-K, which is characterized by a longer linker compared to the usual Y-(X₃)-K motif in the other subfamilies. The catalytic residue Y156 (in *E. coli*) is thought to be involved in the reduction of the enoyl substrate. A hydride ion from the nicotinamide ring of the NADH cofactor attacks the double bond of the enoyl at C3, generating an enolate anion at the

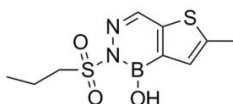
C1 carboxyl oxygen. The enolate is likely protonated by the hydroxyl group of Y156, which is re-protonated by a proton wire comprising K163, the cofactor and solvent water molecules. K163 is mainly involved in cofactor binding (Rafferty et al., 1995). FabI proteins from different organisms conduct catalysis via an ordered sequential bi-bi mechanism with the cofactor binding first in its reduced form and leaving last in the oxidized NAD^+ form (Liu et al., 2011; Xu et al., 2008). The FabI protein is a typical member of the SDR-family with a size of about 260 amino acids and a homo-tetrameric assembly. Crystal structures of FabI showed an NADH-binding Rossmann-fold and an adjacent substrate binding pocket containing the catalytic residues in a hydrophobic environment (Baldock et al., 1996). A remarkable feature is the so-called substrate-binding loop, which is proposed to be flexible, but adopting a helical structure and closing the active site pocket upon ligand binding. The resulting helix is thought to interact hydrophobically with the enoyl-substrate (Qiu et al., 1999).

FabI is the target of a number of established and also newly developed inhibitors (cf. Figure 7).

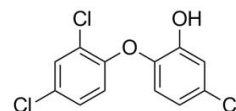
A Established FabI inhibitors:



Isoniazid

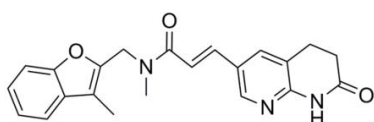


Thiodiazaborine

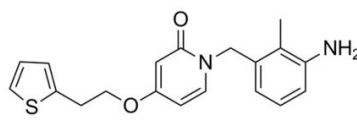


Triclosan

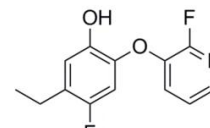
B FabI Inhibitors in clinical trials:



AFN-1252



CG400549



MUT37307

Figure 7: FabI Inhibitors

Isoniazid, the most prominent drug targeting InhA, the FabI homolog of *M. tuberculosis*, has to be activated by the catalase/peroxidase KatG and is covalently attached to the 4-

carbon of the nicotinamide ring of NADH. An additional π -stacking interaction with F149 (*M. tuberculosis*) stabilizes the interaction. The binding site is distinct from triclosan and diazaborines (Banerjee et al., 1994; Marrakchi et al., 2000). Diazaborines are also covalently attached to the cofactor, but to the 2' hydroxyl group of the nicotinamide ribose of NAD⁺. The diazaborine ring interacts via π -stacking with the nicotinamide ring and forms hydrogen bonds to the catalytic residues. Furthermore it exhibits van der Waals interactions to the hydrophobic pocket, including the hydrophobic substrate binding loop, which becomes ordered in its helical closed conformation (Baldock et al., 1996). However, due to the toxic boron in the scaffold, the inhibitors are not suitable for drug design. Triclosan is a widely used antibacterial agent, which can be found in many consumer products such as soaps, cosmetics or toothpaste but also in hospital disinfection agents. It is non-covalently bound in the active site of FabI in a stable ternary triclosan-NAD⁺-FabI complex (Heath et al., 1998). Binding is achieved through hydrogen bonds of its hydroxyl group at the A-ring to Y156 (*E. coli*) and the cofactor as well as by a π -stacking interaction with the nicotinamide ring of the oxidized NAD⁺ cofactor. Triclosan also interacts with the hydrophobic pocket of FabI and recruits the hydrophobic substrate-binding loop for interactions. The helical ordering of the loop upon triclosan binding is thought to cause the slow-binding behavior of triclosan, which is highly favorable for drug design (Lu and Tonge, 2008; Ward et al., 1999). With respect to the *M. tuberculosis* FabI homolog InhA, triclosan acts as a rapid reversible inhibitor in vitro. Here, the substrate binding loop remains flexible (Kuo et al., 2003; Parikh et al., 2000). The closely related enoyl-ACP reductase FabL from *B. subtilis* is reversibly inhibited by triclosan but does not form a stable ternary complex and therefore confers resistance against this antibacterial agent (Heath et al., 2000; Kim et al., 2011). Apart from the known inhibitors of FabI, a number of new compounds have been developed against FabI, mainly to target the increasingly resistant *S. aureus*, which contains FabI as the sole enoyl-ACP reductase (cf. Figure 7B). For this clinically important pathogen pharmaceutical companies accept the narrow spectrum of FabI inhibitors (Silver, 2011). GlaxoSmithKline investigated a series of aminopyridines. The best inhibitor in this series showed an inhibitory effect not only on FabI of *S. aureus* but also on FabK of *S. pneumonia* (Payne et al., 2002). The project was outsourced to Affinium, where the clinical candidate AFN-1252 was developed. This aminopyridine inhibitor is specific for staphylococci and retained no

inhibition on *S. pneumonia* (Karlowsky et al., 2009). AFN-1252 has already been used in phase I trials. Park and collaborators reported on the inhibitor CG400549 which is related to the triclosan scaffold. They identified a hotspot in resistance against this compound in mutations of FabI at F204 to leucine (Park et al., 2007). Interestingly, a mutation of the same residue F204 to cysteine led to a loss of the slow binding behavior of triclosan for *S. aureus* FabI (Fan et al., 2002). The company Mutabilis is also working on a triclosan-based compound, MUT37307. This compound is active against *S. aureus* and other organisms with FabI as the sole enoyl-ACP reductase (Escaich, 2008; Silver, 2011).

Although FabI does not carry the promise for a broad spectrum antibiotic anymore, several FabI inhibitors have been developed. All of them target the Gram-positive pathogen *S. aureus*. In this work we focus on Gram-negative pathogens, especially *B. pseudomallei* and *Y. pestis*, of which only *B. pseudomallei* possesses the FabI isoform. Since triclosan is an effective antibacterial agent against Gram-negative pathogens such as *E. coli*, it has to overcome the protective cell wall and is therefore a suitable lead structure for further compound developments against Gram-negatives.

1.3.2.2 *FabV*

The enoyl-ACP reductase isoform FabV occurs in several relevant Gram-negative pathogens such as *V. cholerae*, *P. aeruginosa*, *B. pseudomallei* or *Y. pestis*. It is the most recently described FabI isoenzyme and was discovered in *V. cholerae*, since this pathogen comprises none of the known enoyl-ACP reductase isoforms (Massengo-Tiasse and Cronan, 2008). It is related to the SDR proteins FabI and FabL but shows some distinct features. FabV is only about 15% identical in sequence to FabI or FabL and is with its ~400 amino acids 60% larger than a typical SDR protein. It was shown to be monomeric in solution, which is also an exception in this superfamily. SDR proteins usually form dimers and tetramers in solution. A known exception to this “rule” is the monomeric porcine carbonyl reductase, which stabilizes itself by an additional α -helix in a 41 residue insertion (Ghosh et al., 2001). The active site motif of FabV is with Y(X₈)K even longer than the extended Y(X₆)K motif of the divergent subfamily, including FabI. It was shown, that FabV prefers NADH over NADPH as a cofactor (Massengo-Tiasse and Cronan, 2008). The FabV isoform of *B. mallei* catalyzes the reduction of the enoyl substrate in an ordered,

sequential bi-bi mechanism as demonstrated for FabI (Lu and Tonge, 2010). The enzyme is inhibited by triclosan, but not efficiently enough to seriously harm the bacterium. In *B. mallei* triclosan acts as a rapid reversible inhibitor with a K_i value of 0.4 μM (Lu and Tonge, 2010). In *P. aeruginosa*, which contains both FabI and FabV, triclosan resistance is caused by FabV (Zhu et al., 2010). Previously it was thought that *P. aeruginosa* was resistant to triclosan due to depletion of the compound via its efflux pumps (Schweizer, 1998). However, the $\Delta fabV$ mutant of *P. aeruginosa* was susceptible to triclosan whereas the $\Delta fabI$ mutant and the wild-type were resistant to triclosan (Figure 8).

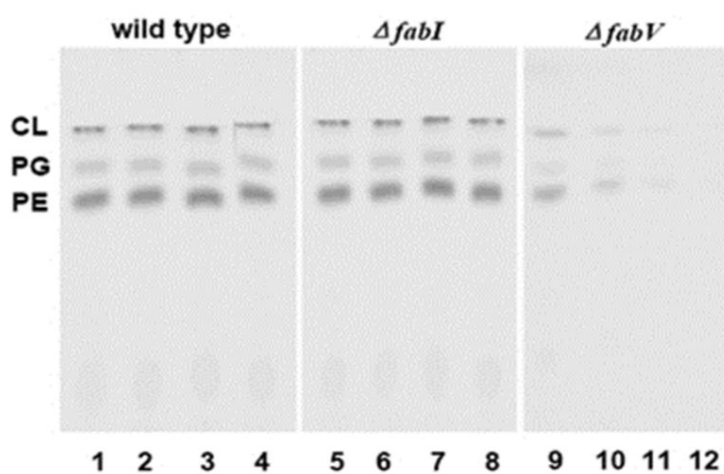


Figure 8: Inhibition of phospholipid synthesis of *P. aeruginosa* PAO1 wild type and mutants by triclosan (Zhu et al., 2010)

Phospholipids extracted before (lane 1, 5, 9), at (lane 2, 6, 10), 30 minutes (lane 3, 7, 11) and 1h (lane 4, 8, 12) after addition of 10 $\mu\text{l/ml}$ triclosan. The phospholipids are labeled with [$1\text{-}^{14}\text{C}$]acetate, PE: phosphatidylethanolamine; PG: phosphatidylglycerol 1 and CL: cardiolipin.

The binding mode of triclosan to FabV, even if it is not of high affinity, can be used as a starting point for drug design. In some cases, as in *Y. pestis* or *V. cholerae*, FabV is the sole known enoyl-ACP reductase of the organism. For these pathogens an effective inhibitor targeting FabV would be sufficient to combat the bacterium. Other organisms such as *B. pseudomallei* or *P. aeruginosa*, also contain FabI, therefore both isoforms have to be inhibited to attack these organisms. Since FabV and FabI are related proteins and both bind triclosan, though with differing affinity, a triclosan derivative may be in reach that effectively inhibits both enzymes.

1.4 Research objective

In a structure-based drug design approach targeting the enoyl-ACP reductases of the Gram-negative pathogens *B. pseudomallei* and *Y. pestis* the structures of FabI (*B. pseudomallei*) and FabV (*B. pseudomallei* and *Y. pestis*) were characterized by X-ray crystallography including binary and ternary complexes with the cofactor NADH and newly developed, triclosan-based inhibitors. Of particular interest were the distinct features of the FabV isoenzyme, which was structurally characterized in this work for the first time, such as the stabilization of the monomeric assembly, the additional structural motifs of FabV or how the differing active site motif affects the 3 dimensional structure. For co-crystallization attempts with potential inhibitors, a selection of triclosan-based inhibitors, including diphenyl ethers and pyridone compounds, were provided by Peter Tonge's laboratory, our collaborators from Stony Brook University, NY, USA. The interactions of different inhibitors with the active site pockets of FabI and FabV were characterized, with a focus on the behavior of the substrate-binding loop, and compared to examine the possibility to design an inhibitor targeting both isoenzymes with sufficient efficiency.

2. Materials and Methods

2.1 Materials

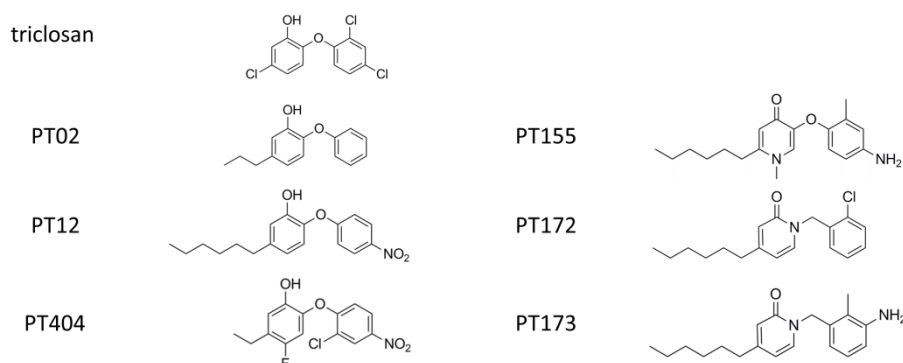
2.1.1 Chemicals

All required chemicals were supplied by Applichem (Darmstadt), Carl Roth (Karlsruhe), Fluka (Neu-Ulm), Hampton Research (Laguna, USA) and Sigma-Aldrich (Seelze). They were used in at least analytical purity grade. For the purpose of crystallography only the highest available purity grade was accepted.

2.1.2 Inhibitors

The following inhibitors, apart from triclosan, were synthesized and kindly provided by Professor Peter Tonge's working group (Table 3).

Table 3: Inhibitors



2.1.3 Plasmids

The plasmids pET15b and pET23b from Novagen were used as expression vectors. The FabI constructs from *B. pseudomallei* and the FabV constructs from *Y. pestis*, *B. pseudomallei*, *B. mallei* and *P. aeruginosa* were kindly provided by our collaboration partners Hao Lu (Lu and Tonge, 2010), Nina Liu (Liu et al., 2011) and Carla Neckles (Hirschbeck et al., 2012) from Professor Peter Tonge's laboratory (StonyBrook University, NY, USA) (Table 4). The expression vectors contain the gene of interest with an N-terminal (pET15b) or C-terminal (pET23b) hexahistidine tag regulated by the T7 RNA polymerase promoter. Expression is negatively controlled by the Lac operator. The LacI repressor, also

included in the vector, inhibits expression of the T7 RNA polymerase until it is inactivated by lactose or the lactose-analog IPTG (Isopropyl β -D-1-thiogalactopyranoside). As a result the repressor releases the DNA, the T7 RNA polymerase is transcribed and translated and can start with the transcription of the recombinant gene of interest.

Table 4: Expression Vectors

Vector	Insert	Source organism	Restriction sites
pET15b	YpFabV	<i>Y. pestis</i> strain A1122	XhoI, EcoRI
pET15b	YpFabV T276S	<i>Y. pestis</i> strain CO92	XhoI, EcoRI
pET15b	BpFabV	<i>B. pseudomallei</i> strain Bp82	NdeI, BamHI
pET15b	BmFabV	<i>B. mallei</i> strain ATCC 23344	NdeI, BamHI
pET15b	PaFabV	<i>P. aeruginosa</i> strain PAO1	NdeI, BamHI
pET23b	BmFabI (=BpFabI)	<i>B. mallei</i> strain ATCC 23344	NdeI, HindIII

2.1.4 Bacterial culture

Bacteria of different plasmid amplification and expression strains (Table 5) were grown in LB-medium (Carl Roth) or on LB-agar plates.

Table 5: Escherichia coli strains

Plasmid amplification			
DH5 α	<i>E. coli</i> F- ϕ 80dlacZ Δ M15 Δ (lacZYA-argF)U169 <i>deoR recA1 endA1 hsdR17</i> (rk-, mk+) <i>phoA supE44</i> λ - <i>thi-1 gyrA96 relA1</i>	Clontech Laboratories	
Expression			
BL21 (DE3)	<i>E. coli</i> F ⁻ <i>ompT hsdSB</i> (rB ⁻ , mB ⁻) <i>gal dcm</i> (DE3)	Novagen	
BL21 (DE3) pLysS	<i>E. coli</i> F ⁻ <i>ompT hsdSB</i> (rB ⁻ mB ⁻) <i>gal dcm</i> (DE3) pLysS (CamR)	Novagen	
Arctic express (DE3)RIL	<i>E. coli</i> B F ⁻ <i>ompT hsdS</i> (rB ⁻ mB ⁻) <i>dcm+</i> Tetr <i>gal</i> λ (DE3) <i>endA Hte</i> [<i>cpn10 cpn60 Gentr</i>] [<i>argU ileY leuW Strr</i>]	Stratagene	

2.1.5 Enzymes and Kits

Table 6: Enzymes, Kits and Miscellaneous Reagents

Enzymes	
DNase	Invitrogen
Thrombin	GE Healthcare

Kits

NucleoSpin Plasmid Kit	Machery-Nagel
NucleoBond Xtra Midi	Machery-Nagel

Miscellaneous reagents

Sypro Orange	Invitrogen
PageRuler prestained protein ladder	Fermentas

2.1.6 Crystallization screens

All crystallization screens used in this study were produced according to the manufacturer's specifications utilizing the Lizzy 2002 pipetting robot (Zinsser Analytic) with the exception of Salt screen I and a PEG pH 6.5 screen, which were self-designed.

Table 7: Crystallization screens

Additive Screen	Hampton Research
Crystal Screen 1	Hampton Research
Crystal Screen 2	Hampton Research
Index	Hampton Research
Nextal PEGs suite	Qiagen
Topaz OptiMix-3	Fluidigm
Topaz OptiMix-PEG	Fluidigm
Wizard Screen I	Emerald BioSystems
Wizard Screen II	Emerald BioSystems
Salt screen I	Self-designed (cf. appendix Table 28)
PEG pH 6.5 screen	Self-designed (cf. appendix Table 29)

2.1.7 Equipment

Table 8: Technical equipment

Autoclave Systec V-150	Systec
Bacterial shaker ISF-1-W	Kühner
Bacterial shaker ISF-1-X	
Balances	
XS 105 Dual Range	Mettler Toledo
XS 6002S Dual Range	
Bio-Photometer	Eppendorf

Materials and Methods

Camera AxioCam MRC	Zeiss
<u>Cell disruptor</u>	
TS-Series	Constant Systems
M-110P	Microfluidics
<u>Centrifuges</u>	
Centrifuge 5415 D	Eppendorf
Centrifuge 5810 R	Eppendorf
Avanti J-26 XP	Beckmann Coulter
<u>Columns for affinity chromatography in batch</u>	
Econo-Column 1,5 x 15 cm	Biorad
Econo-Column 2,5 x 20 cm	
<u>Column / medium for affinity chromatography</u>	
Ni-TED	Protino
HisTrap FF crude, 1 ml and 5 ml	GE Healthcare
HiTrap Benzamidine FF, 1ml	GE Healthcare
Cryo loop	Hampton Research
Crystallization robot HoneyBee 963	Zinsser Analytic
DynaPro Dynamic Light Scattering	Wyatt Technology Corporation
<u>Fast protein liquid chromatography systems</u>	
ÄKTApurifier	
ÄKTAexpress	GE Healthcare
ÄKTA avant	
Gelelectrophoresis Mini-Protean 3-cell	Biorad
<u>Gelfiltration</u>	
HiLoad 26/60 Superdex 200 prep grade	GE Healthcare
HiLoad 16/60 Superdex 200 prep grade	
Incubator B15	Heraeus
Light source KL 2500 LCD	Zeiss
Liquid handling robot Lissy2002	Zinsser Analytic
Magnetic stirrer MR 3002	Heidolph
Microscope Stemi 2000-C	Zeiss
Sealing robot RoboSeal	HJ-Bioanalytik
Spectrophotometer Nanodrop ND 1000	Peqlab
pH-Electrode	Schott
pH-Meter	Schott
Pipettes	Rainin
Pipetboy easypet	Eppendorf
Pipetting robot Lizzy 2002	Zinsser Analytic
Power supply	Biorad
Real time PCR cycler (MX3005P)	Stratagene
<u>Rotors</u>	
JLA 25.50	Beckmann Coulter
JA 8.1000	
Spectrophotometer Nanodrop ND 1000	Peqlab
Thermoblock Rotilabo-Block Heater 250	Carl Roth
Thermomix comfort	Eppendorf
<u>X-ray detectors</u>	
R-Axis IV++	Rigaku
R-Axis HTC	

Materials and Methods

X-ray generators

Ultra X18	Rigaku
MicroMax-007 HF	

Table 9: Consumable supplies

24-well crystallization plate	Crystalgen
96-well crystallization plate	Greiner
Baysilone silicone paste	GE Bayer
<u>Concentrator MWCO 10,000</u>	
Vivaspin 6	Sartorius Stedim Biotech
Vivaspin 20	
Cover slides	Jenabioscience
cuvettes	Carl Roth
Filter 0,22 µm	Carl Roth
Gloves (nitril)	Carl Roth
Greiner tube 15 ml, 50 ml	Greiner
Pipette tips 10 µl, 200 µl, 1000 µl, 5000 µl	Rainin
Reaction tube 1.5 ml	Eppendorf

2.1.8 Computer Software

Table 10: Software

Software	Author/Reference
Arp/Warp	(Morris et al., 2003)
AutoSharp	(Vonrhein et al., 2007)
CCP4 program suite	(CCP4, 1994)
ChemBioDraw Ultra 12.0	CambridgeSoft
ClustalW	(Thompson et al., 1994)
Coot	(Emsley and Cowtan, 2004)
DaliLite server	(Holm and Park, 2000)
Dssp	(Kabsch and Sander, 1983)
Dssp2pdb	(James Stroud, 2002)
ESPrpt	(Gouet et al., 2003)
ExpASY Proteomics Server	http://www.expasy.ch/
iMosflm 1.0.3	(Battye et al., 2011)
LIGPLOT	(Wallace et al., 1995)
<u>Microsoft Office Professional Plus 2010</u>	Microsoft Corporation
Microsoft Word	
Microsoft Excel	
Microsoft Powerpoint	
OriginPro 8.5	Origin Lab Corporation
PDBe Protein Data Bank	(Velankar et al., 2012)
Phaser	(McCoy et al., 2007)
Phenix 1.6.2-432	(Adams et al., 2010)

Materials and Methods

Phenix 1.7.3-938

PRODRG server	(Schuttelkopf and van Aalten, 2004)
---------------	-------------------------------------

Pymol	(Schrodinger, 2010)
-------	---------------------

Refmac5	(Murshudov et al., 1997)
---------	--------------------------

Scala	(Evans, 2006)
-------	---------------

TLSMD server	(Painter and Merritt, 2006)
--------------	-----------------------------

XDS package	(Kabsch, 2010)
-------------	----------------

2.2 Methods

2.2.1 Microbiology techniques

2.2.1.1 Transformation

For plasmid amplification and recombinant protein expression exogenous DNA had to be taken up by the host bacteria, which can subsequently use the genetic information to produce the desired product. The artificial uptake of exogenous DNA, mostly vectors as plasmids, by bacteria is called transformation. With a heat shock or by electroporation the membrane permeability of the cells is increased, which facilitates the entry of nucleic acids into the bacterial cell. In this study different *E. coli* strains (cf. Table 5) were transformed with expression plasmids (cf. Table 4) by heat shock transformation. Since *E. coli* cells are not intrinsically competent for DNA uptake during the heat shock application, the cells have to be treated with ice-cold CaCl₂ solutions in their exponential growth phase to become chemically competent. Although the bacteria are especially prepared for transformation, the uptake of DNA is still a very rare event (~0.1%) (Chen and Dubnau, 2004). Therefore recombinant DNA vectors usually carry an antibiotic resistance gene, in our plasmids a gene providing resistance against ampicillin. In growth medium or on agar plates with the respective antibiotic only the bacteria carrying the vector can grow.

In practice an aliquot of chemo-competent *E. coli* cells (50 µl) was thawed on ice. The cells were incubated on ice with 1 µl of the expression vector (10-100 ng/µl) for 10 minutes. The temperature of the cells was rapidly increased from 0 °C to 42 °C in a thermo block and heat shocked at 42 °C for 60 seconds allowing DNA uptake. Afterwards the cells were chilled again on ice for 2 minutes. To recover from this harsh thermal treatment, the bacteria were mixed with 500 µl of LB-medium (Bertani, 1951) and shaken with 600 rpm at 37°C in a thermo block for at least 20 minutes. To select for the transformed cells 25-100 µl of the culture was plated on a LB-agar plate containing 100 µg/ml ampicillin. Some *E. coli* expression strains as *E. coli* strain BL21 (DE3) pLysS contain additional resistance genes themselves; in this case the additional antibiotic also had to be added to the growth media or LB-agar plates. The LB-agar plates were incubated at 37 °C over night to

allow colony growth. Afterwards the plate was stored at 4 °C and the colonies could be picked for further experiments for about a week.

2.2.1.2 Plasmid amplification

Lyophilized samples of the expression vectors (Table 4) had been kindly provided by the working group of Professor Peter Tonge. For plasmid amplification, 1µl of the dissolved DNA was transformed (cf. 2.2.1.1) into DH5α *E. coli* cells. The DH5α strain is suitable for plasmid amplification since it carries an endA1 mutation that reduces endonuclease digestion of plasmids leading to higher plasmid yield. A single clone was picked from the transformation plate and used to inoculate a 5 ml or 200 ml LB culture including 100 µg/ml ampicillin, depending on the kit which was used for plasmid isolation. The cultures were grown over night at 200 rpm at 37 °C and harvested by centrifugation. The amplified plasmid DNA of the 5 ml or 200 ml cultures was extracted using the NucleoSpin Plasmid Kit or the NucleoBond Xtra Midi kit (Machery-Nagel), respectively, following the manufacturer's manual. The major steps of the kits are cell lysis, pelletization of the cell debris, loading of the DNA onto the silica membrane, washing the membrane with a buffer containing ethanol, drying of the membrane and finally eluting the DNA from the membrane with water. The final DNA concentration was assessed spectrophotometrically at a wavelength of 260 nm using the Nanodrop ND 1000.

2.2.1.3 Protein expression

For recombinant protein expression the expression plasmid (2.1.3) was transformed (2.2.1.1) into an *E. coli* expression strain (Table 5). All LB-media or LB-agar plates used for expression contained 100 µg/ml ampicillin to prevent contamination with bacteria other than the transformed clone. A colony of the transformation was used to inoculate 2 ml LB which was subsequently shaken at 200 rpm for approx. 8 hours at 37 °C. This small culture was used to inoculate the actual 200 ml pre-culture, which grew over night in a bacterial shaker at 200 rpm at 37 °C. Large scale expression was performed in 2 L LB cultures in 5 L Erlenmeyer flasks. The cultures were inoculated to an OD₆₀₀ of 0.05 (25-50 ml pre-culture) and grown in the bacterial shaker at 37 °C until it reached the exponential growth phase at an OD₆₀₀ of 0.6. At this point the expression of the recombinant protein

was induced by the addition of 1 mM IPTG to inhibit the LacI repressor and permit the expression of the T7 RNA polymerase and subsequently the expression of the gene of interest. The expression was conducted for 5 h at 25 °C or for 20 h at 15 °C. Subsequently, bacteria were harvested by centrifugation (at 4 °C, 5000g, 20 min; rotor JLA 8.1000, Beckmann Coulter Avanti Centrifuge J-26 XP) and stored in aliquots of 5-10 g at -80 °C. For expression tests the protein expression was conducted likewise in 5 ml or 200 ml scale.

2.2.2 Protein purification

High purity and homogeneity of the protein sample is an important factor facilitating crystallization. The purification of all recombinant proteins in this work was performed in two predominant chromatographic steps, first a nickel affinity chromatography was performed to isolate the hexahistidine tagged protein from the cell lysate and in a second step the protein sample was separated from remaining contaminants and aggregated protein by size-exclusion chromatography. In the case of YpFabV the hexahistidine tag was removed by thrombin for the later crystallization trials. All steps were performed at 4 °C if not stated otherwise.

2.2.2.1 Cell lysis

Due to the enormous overexpression 5-10 g bacterial pellet was sufficient for a large-scale purification. The cell pellet was thawed and resuspended in Lysis Buffer (= Binding Buffer in Table 12) on ice. 1 g of pellet was resuspended in 10 ml of Lysis Buffer with 0.2 µl DNase (Invitrogen). The cells were lysed in 2 passages through a cell disruptor at a pressure of 1.5 kbar. In order to remove the cell debris, the cell lysate was cleared by centrifugation (4 °C, 25000 g, 30 min; rotor JA 25.50, Beckmann Coulter Avanti Centrifuge J-26 XP). The cleared sample could then be used for Ni²⁺-affinity chromatography.

2.2.2.2 Ni²⁺-affinity chromatography

Affinity chromatography exploits reversible high affinity interactions between the protein of interest and certain interaction partners, which are attached to a chromatography matrix. The use of recombinant fusion proteins, which are connected to high affinity tags, makes this a universally applicable purification technique. In our case, the proteins are

decorated with hexahistidine tags, which bind to divalent metal ions in the immobilized metal ion affinity chromatography (IMAC). The Nickel ions are coordinated by a chelating resin which is attached to the column matrix. The protein is released from the nickel by competition with an excess of imidazole. There were two different IMAC column materials in use. In the pre-packed Histrap FF crude columns the chelating group is coupled to a sepharose matrix and in the Ni-TED material the chelating tris (carboxymethyl) ethylenediamine (TED) group is attached to silica beads. The Ni-TED beads exhibit only one free binding site at the complexed nickel ion instead of two in the Histrap material. Therefore the affinity to histidine tagged proteins is weaker with respect to the Ni-TED beads but much more specific. Hence, the buffers for the Ni-TED purification contain less imidazole (Table 12). The loose Ni-TED beads had to be used in a batch method in contrast to the Histrap columns, the latter are designated for the automatic ÄKTA chromatography systems (cf. Table 8). Apart from the automated performance of the purification, the ÄKTA systems have the advantage that they can monitor pH, temperature, pressure, conductivity and the absorption at up to three different wavelengths which can be used to follow the steps of the purification in real time.

The general procedure for both nickel materials is summarized in Table 11. The cleared cell lysate was loaded onto the column and unbound sample washed out with at least 20 column volumes (CV) of Binding Buffer. Afterwards nonspecifically bound proteins were washed out with 10 CV of a separate Washing Buffer with slightly elevated imidazole concentrations compared to the binding buffer and 1 M NaCl (possible for both methods) or by a gradient over 10 CV reaching 8% Elution Buffer, which is restricted to automated chromatography. The protein was eluted from the Histrap column by a step elution up to 50% Elution Buffer over 10 CV or with a 20 CV gradient reaching 100% Elution buffer. In general, the imidazole concentration should be kept low as imidazole can cause protein precipitation at high concentrations. Elution from the Ni-TED column was achieved with 10 CV of Elution buffer. Here fractionation (5 ml) of the sample was performed manually. To increase the protein concentration in the elution fractions, the Elution Buffer was added in 1 CV portions and incubated with the Ni-beads for 1-5 minutes. The elution fractions of both methods were analyzed by SDS-PAGE and the pure peak fractions pooled for the next purification step.

Table 11: Different Ni-affinity chromatography procedures

	Ni-TED (batch procedure)	HisTrap FF crude (automated procedure)
Column volume	20ml	5-10ml
Equilibration	5CV Binding Buffer	
Sample application	Loading the sample	
Wash out unbound sample	at least 20 column volumes of Binding Buffer (5mM imidazole)	20 column volumes of Binding Buffer (20mM imidazole)
Wash step	10 CV of Washing Buffer (10mM imidazole, 1M NaCl)	10 CV of Washing Buffer (60mM imidazole, 1M NaCl), or gradient over 10 CV to 8% Elution Buffer (500mM imidazole)
Elution	10 CV of Elution Buffer (150mM imidazole), in 1CV steps with short incubation	10 CV step elution to 50% Elution Buffer, or 20 CV gradient to 100% Elution Buffer

Table 12: Buffers for the affinity chromatography

	Binding Buffer = Lysis Buffer	Washing buffer	Elution buffer
Ni-TED	50 mM Tris pH 7.4 500 mM NaCl 5 mM imidazole	20 mM Tris pH 7.4 1 M NaCl 10 mM imidazole	20 mM Tris pH 7.4 500 mM NaCl 150 mM imidazole
HisTrap FF crude 5ml	50 mM Tris pH 7.4 500 mM NaCl 20 mM imidazole	20 mM Tris pH 7.4 1 M NaCl 60 mM imidazole	20 mM Tris pH 7.4 500 mM NaCl 500 mM imidazole

2.2.2.3 Thrombin cleavage

The vector pET15b is designed as such that the hexahistidine tag of the recombinant gene product can be cleaved off with thrombin. Thrombin was purchased from GE Healthcare, dissolved in PBS buffer (137 mM NaCl, 2.7 mM KCl, 10 mM Na₂HPO₄ and 2 mM KH₂PO₄, pH 7.4) and stored at -80 °C. The combined peak fractions containing the protein of the Ni-affinity chromatography were concentrated to 50 mg/ml (in case of the very stable YpFabV) and incubated with 1 U thrombin per mg of protein at room temperature (18-22 °C, depending on the season) for up to 20 hours. The success of the cleavage was analyzed via SDS-PAGE. Thrombin was removed with a HiTrap Benzamidine FF Affinity

Column from GE Healthcare following the manufacturer's manual. Benzamidine is a reversible inhibitor of thrombin, which is attached to the matrix of this affinity column. By loading the sample onto the column the thrombin is removed from the solution while the protein of interest should not bind. The flowthrough from the column, which was completely washed out of the column with 10 ml PBS buffer, was fractionized. The protein content of the fractions was determined spectrophotometrically at a wavelength of 280 nm using the Nanodrop ND 1000. The fractions with relevant protein concentrations were pooled and used for the final size-exclusion chromatography step. After size-exclusion chromatography, the pure peak fractions were incubated with small amounts of Ni-TED resin to remove residual uncleaved protein, which could prevent crystallization of the cleaved protein.

2.2.2.4 Size-exclusion chromatography

Size-exclusion chromatography separates components of the applied sample according to their size and shape. The gel filtration column contains a matrix of porous beads composed of agarose and dextran. The pores in the beads are of different sizes. The smaller the size of a protein, the deeper it can penetrate the branched channels through the beads (cf. Figure 9). Therefore smaller proteins have to cover a longer distance than bigger proteins and elute later from the column. Bigger protein aggregates cannot enter the beads and have to run past them. They elute with the void volume of the column. In this work size exclusion chromatographies with the columns HiLoad 26/60 Superdex 200 and HiLoad 16/60 Superdex 200 with column volumes of 330 ml and 124 ml, respectively, have been performed at different ÄKTA chromatography systems (cf. Table 8) and at a flow rate of 1.5 ml/min. The loaded protein sample was not allowed to exceed 5 ml or 10 ml for the 16/60 or 26/60 column. The column was equilibrated in 1 CV Gel Filtration

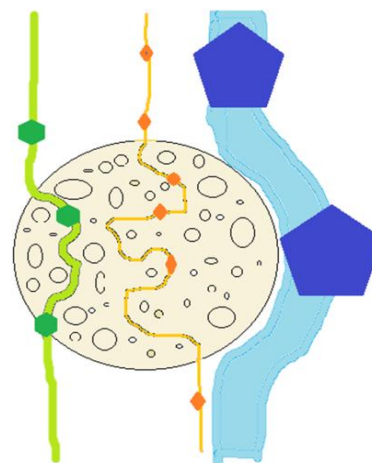


Figure 9: Size-exclusion chromatography

Particles of different sizes on their way through a gel filtration bead

Buffer (Table 13). The sample was applied and eluted with at least 1 CV. Fractionation of the elution started after 0.3 CV. Elution was monitored by the absorption at 260 nm and 280 nm wavelength and samples of the peak fractions were analyzed by SDS-PAGE. Fractions containing pure protein were pooled, concentrated, flash-frozen in liquid nitrogen and stored at -80 °C.

Table 13: Gel Filtration Buffers

FabI	FabV
20 mM Bistris pH 6.5	20 mM PIPES pH 7.5
500 mM NaCl	300 mM KCl
1 mM EDTA	1 mM EDTA

2.2.3 Protein characterization

2.2.3.1 SDS-PAGE analysis

Sodium dodecyl sulfate polyacrylamide gel electrophoresis (SDS-PAGE) (Laemmli, 1970) is a method to analyze the protein content of a sample to evaluate protein purity during purification or the degree of overexpression in an expression test. The protein sample is denatured by incubation at high temperatures. Potential disulfide bridges are disrupted by the addition of the reducing agent DTT (dithiothreitol). The anionic detergent sodium dodecyl sulfate (SDS) interacts via its dodecyl chain with the peptide backbone of the protein covering the whole amino acid chain with its negatively charged sulfate moiety. The overall charge is thereby proportional to the size of the protein. The protein sample can be separated in polyacrylamide gel electrophoresis due to its differential migration velocity through the gel in an electric field. Since all proteins are negatively charged by SDS they migrate towards the anode. The density of the polyacrylamide gel also contributes to the separation of proteins of different sizes.

In this work polyacrylamide gels with a 15% acrylamid/bisacrylamide (AA/BAA) resolving gel and a 5% AA/BAA stacking gel were used (cf. Table 14). In the looser stacking gel the proteins run faster and accumulate when they reach the resolving gel with higher density, thereby they all move together into the resolving gel. 10 µl of protein sample were mixed with 2.5 µl loading buffer (containing SDS and DTT), denatured for 5 minutes at 95 °C and

loaded onto the gel. To be able to estimate the size of the protein bands a protein ladder (PageRuler prestained protein ladder (Fermentas)) with marker proteins of 10-170 kDa was used. Electrophoresis was conducted at 200 V for 1 h in SDS running buffer. To stain the protein bands the gel was incubated with Coomassie solution (5-15 min) and afterwards washed in destaining solution until only the protein bands were still visible in blue.

Table 14: SDS PAGE - gel recipe and solutions

<u>15 % Resolving Gel</u>	<u>5 % Stacking Gel</u>	<u>Loading buffer (5x)</u>
15% AA/BAA (30% mix)	15% AA/ BAA (30% mix)	50 mM Tris pH 6.8
375 mM Tris pH 8.8	125 mM Tris pH 6.8	100 mM DTT
0.1% SDS	0.1% SDS	2% SDS
0.25% APS	0.25% APS	0.1% Bromphenol blue
0.05% TEMED	0.15% TEMED	
<u>SDS Running buffer (1x)</u>	<u>Coomassie Staining solution</u>	<u>Destaining solution</u>
192 mM Glycine	0.5% Coomassie brilliant blue	10% Ethanol
0.1% SDS	50% Methanol	5% Acetic acid
25 mM Tris	10% Acetic acid	

2.2.3.2 Thermofluor analysis

Thermofluor (Pantoliano et al., 2001) is a method to evaluate protein stability in certain surroundings. The influence of buffer components, pH, additives or binding partners such as cofactors or inhibitors on protein stability can be assessed. This method was used to analyze different buffer conditions for the subsequent crystallization of the protein.

The Thermofluor assay is based on the measurement of melting curves of the protein. Unfolding of the protein is detected with the help of the fluorescence dye Sypro Orange (Invitrogen). Sypro Orange exhibits fluorescence at a wavelength of 590nm (orange), which is quenched in aqueous surroundings. In a hydrophobic environment the fluorescence of Sypro Orange is increased. During the unfolding process of a protein that is natively surrounded by aqueous environment, hydrophobic parts, which are usually protected from the solvent in the core of the protein, are exposed and can interact with the fluorescence dye, thereby increasing the fluorescence. The experiment is conducted

in a real time PCR cycler (MX3005P) since the temperature can be tightly regulated and real-time fluorescence detection can be achieved. The inflection point of the measured fluorescence curve is interpreted as melting point of the protein in the respective condition.

In practice, the protein was mixed with Sypro Orange and buffers at concentrations of 100 mM from a buffer screen covering the pH range 4.5-9.8 (Supplemental Table 27: Thermofluor screen) or with a reference buffer as control (cf. Table 15). The mixtures (in a 96-well PCR plate) were heated from 25 °C to 95 °C with an increase of 1 °C per minute.

Table 15: Thermofluor

	Protein (0.5 mg/ml)	Buffer	Sypro Orange (0.5% v/v)
Buffer screen	5 µl	15 µl buffer screen (100mM)	5 µl
Buffer reference	5 µl	15 µl reference buffer	5 µl
Negative control	-	20 µl reference buffer	5 µl

2.2.4 Protein Crystallization

2.2.4.1 Vapor diffusion method

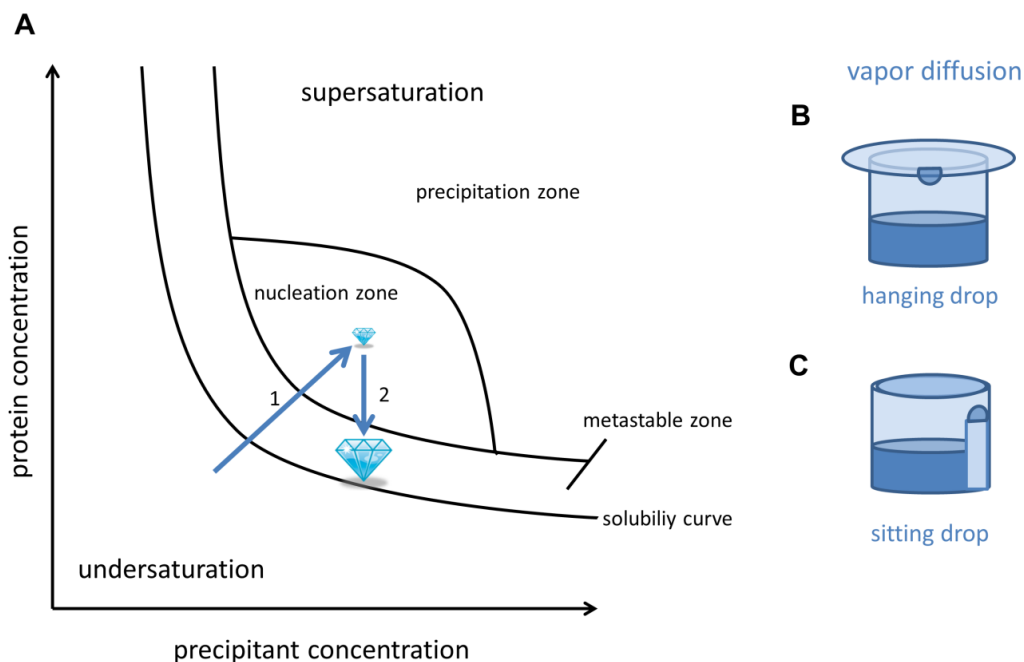


Figure 10: Crystallization by vapor diffusion

A) Phase diagram for crystallization by vapor diffusion, after (Chayen, 2004), B) sketch of a hanging drop setup, C) sketch of a sitting drop setup.

In general crystallization is achieved by bringing a very pure protein sample into the supersaturated state. This forces the protein to go out of solution, which can happen by unordered precipitation or by ordered crystallization, the latter being the desired result. The most common method for crystallization is vapor diffusion. A schematic phase diagram with this method is shown in Figure 10A. The protein solution is mixed in the crystallization drop with the precipitant from the reservoir solution. Thereby the protein concentration as well as the precipitant concentration is halved (under the condition that they are mixed 1:1). The drop is in a closed system together with a larger amount of reservoir solution (approx. 500:1). The precipitant concentrations in both solutions start to equilibrate by vapor diffusion of H₂O and other volatiles out of the drop into the reservoir. Due to the loss of water, the volume of the droplet decreases and the protein as well as the precipitant concentration increase (arrow 1). At some point the protein is supersaturated and has reached the nucleation zone of the phase diagram. Now nucleation may take place and the crystal starts to grow. Upon crystal growth the protein is taken out of the solution and the protein concentration decreases again (arrow 2). Two different experimental setups for vapor diffusion are established. In the hanging drop experiment (Figure 10B) the crystallization drop is hanging from a cover slide, which closes the reservoir, whereas in the sitting drop experiment (Figure 10C) the crystallization drop is placed on a shelf above the reservoir.

2.2.4.2 Protein preparation

A protein sample has to be highly concentrated so that it can reach the supersaturated state during the crystallization trial. The proteins in this work exhibited remarkably high protein solubility and have been concentrated at the end of the purification procedure to 30 mg/ml (BpFabI) or 100 mg/ml (FabVs). Furthermore, the protein solution has to be as homogenous as possible. This was achieved through the optimization of buffer conditions (cf. 2.2.3.2) and extensive centrifugation (at least 30 minutes at 16,100 g) of the sample to remove aggregates, which would lead to precipitation prior to crystallization. For co-crystallization trials the protein was pre-incubated for 1 hour with the ligands to facilitate binding. The cofactor NAD⁺/NADH was dissolved in ddH₂O and added to the protein solution in 10-fold excess. The inhibitors exhibit low water solubility. They were either

added pure to the protein solution (end concentration ~5 mg/ml) or dissolved in the organic solvent DMSO at concentrations of 100 mg/ml and added to the protein solution to reach a final concentration of 5 mg/ml (approx. 100-fold molar excess). However, since the DMSO concentration was decreased to 5%, the inhibitors precipitated again so the actual inhibitor concentration is lower. Higher DMSO concentrations impaired crystal formation. The insoluble fraction of the inhibitor was removed during the centrifugation step.

2.2.4.3 Screening

Crystallization screening was performed in sitting drop setups in 96-well crystallization plates (Greiner). The standard screen was pipetted with the help of the HoneyBee crystallization robot (Zinsser Analytic) with 40 μ l of reservoir solution and crystallization drops consisting of 0.3 μ l reservoir and 0.3 μ l protein solution. The screens were closed with an adhesive sealing foil by the sealing robot RoboSeal (HJ-Bioanalytik). Initial screening was performed at protein concentrations of 10 mg/ml. Depending on the proportion of precipitated conditions to clear drops in the first screens, the protein concentration was reduced or increased. If the proportion of precipitated drops to clear drops was around 1:1, the protein concentration was suitable for the screen. The screens were incubated at 20 °C and evaluated after several time points at the Stemi 2000-C (Zeiss) Microscope.

2.2.4.4 Optimization

Successful crystallization trials were reproduced in hanging drop setups at a larger scale in 24 well crystallization plates (Crystalgen) with a reservoir solution of 1 ml and 1+1 μ l crystallization drops. The drops were mixed on a cover slide and carefully transferred upside down on the reservoir. The gap between the edging of the reservoir well and the cover slide was sealed with silicone paste. In order to optimize crystal growth, factors such as the precipitant concentration, the pH or the salt concentration in the crystallization condition were varied on the 24-well plate. An alternative method to vary crystallization was to change the proportion of protein sample to reservoir solution and use for example 2 μ l of protein and 1 μ l of reservoir solution. Applying this procedure, the

protein advances towards the supersaturated state more slowly but reaches a higher end concentration. The plates were incubated at 20 °C and evaluated after several time points at the Microscope Stemi 2000-C (Zeiss).

2.2.5 X-ray crystallography

Most of the information in this chapter was derived from (Rupp, 2010).

2.2.5.1 Data collection and processing

To analyze protein structures at atomic resolution X-rays, i.e. electromagnetic radiation with a wavelength (λ) of the same order of magnitude compared to the size of atoms, are used. In X-ray crystallography the parallelism of the crystal lattice is exploited in the diffraction experiment. When an x-ray beam encounters a crystal lattice of atoms or molecules, it induces oscillation of the electrons in the lattice at the x-ray frequency. The electrons, returning to the unexcited state, emit radiation at the original energy and wavelength in a random direction. The scattered waves can be described as reflections at the lattice planes of the crystal. In most cases the scattered waves contribute to destructive interference and add up to zero. However, if the x-ray beam hits the lattice plane under the glancing angle θ and Bragg's law (Equation 1) is satisfied, constructive interference takes place and reflections can be recorded on the detector. In the diffraction experiment the intensity and the position of the reflections are recorded. The Miller indices h, k, l can be deduced from the position of the reflections after the orientation of the crystal latticed with respect to a reference coordinate system has been determined (Blow, 2003).

$$n \cdot \lambda = 2 \cdot d \cdot \sin \theta$$

Equation 1: Bragg's law

(d = distance between crystal lattices, ϑ = incidence angle of x-ray, n = integer, λ = wavelength)

In practice the crystals were fished with a nylon loop, transferred into a cryo-solution and subsequently frozen in liquid nitrogen. The cryo-solution contains an increased precipitate concentration compared to the mother liquor and additional cryo-protectants like glycerol or PEG 400 (10-30%). The cryo-protectants prevent the frozen drop in the

loop from the formation of ice crystals and result in a vitrification of the crystal. Ice crystals contribute to the total diffraction and disturb the protein diffraction pattern.

To collect x-ray diffraction images the crystal is mounted on a goniometer and positioned in an x-ray beam. It is cooled to $-180\text{ }^{\circ}\text{C}$ by a nitrogen cryo-stream. A lead beam-stop in the center of the x-ray beam keeps the high energy beam from directly hitting the detector. The detector is very sensitive since it is designed to register weak reflections. The beam-stop therefore saves it from overloads. There are several types of detectors, in this study the diffraction images were recorded by either imaging plate detectors or CCD (charge-coupled device) detectors. As X-ray sources, in-house x-ray generators (Ultra X18 and MicroMax-007 HF, Rigaku) with a rotating Cu-Anode emitting radiation at a fixed wavelength of 1.54 \AA and imaging plate detectors (R-Axis IV++ and R-Axis HTC, Rigaku) were available as well as beam time at different synchrotron facilities (European Synchrotron radiation Facility ESRF, Grenoble; Bessy II, Berlin). The circulating electrons in the synchrotron emit high energy radiation, which is utilized in the surrounding beamlines. A monochromator can filter certain wavelengths out of the polychromatic primary beam. This is essential for multi-wavelength experiments such as MAD (multi-wavelength anomalous diffraction). The mounted crystals were rotated during the exposure around the phi axis. The degree of rotation per frame depended on the quality of diffraction, the crystal mosaicity and the unit cell dimension and was usually 0.1° - 1° to obtain well-separated diffraction spots. The minimal angle range for the collection of complete datasets was determined by iMosflm (Battye et al., 2011).

The diffraction images were indexed and integrated with the help of the programs iMosflm (Battye et al., 2011) and XDS (Kabsch, 2010). If the space group assignment was questionable, the program Pointless (CCP4, 1994) was used to identify the space group with the highest probability. The scaling of the datasets was performed with Scala (Evans, 2006). Scala also provides a number of markers helping to assess data quality such as completeness, redundancy, $\langle I/\sigma I \rangle$ and R_{merge} . The R_{merge} (Equation 2) is a commonly used quality indicator of N merged reflections h within a certain resolution range. Weak reflections in the higher resolution shells lead to higher R_{merge} values indicating an increased measurement error. R_{merge} is often used to determine the high-resolution cutoff of the dataset. A rough guideline states that it should not exceed 60% in the highest

resolution shell. The overall R_{merge} should be better than 15%. Since the R_{merge} displays the cumulative error of the dataset, it gets worse with higher redundancy. The precision-indicating merging R-value R_{pim} (Equation 3) takes into account that the intensities become more accurate with an increasing number of observations in redundant datasets. So although the R_{merge} was the first indicator to judge the high-resolution cutoff, in cases of high redundancy also R_{pim} was considered.

$$R_{\text{merge}} = \frac{\sum_h \sum_{i=1}^N |I_{(h)i} - \overline{I_{(h)}}|}{\sum_h \sum_{i=1}^N I_{(h)i}}$$

Equation 2: Linear merging R-value

(N =number of reflections h)

$$R_{\text{pim}} = \frac{\sum_h \left(\frac{1}{N-1}\right)^{1/2} \sum_{i=1}^N |I_{(h)i} - \overline{I_{(h)}}|}{\sum_h \sum_{i=1}^N I_{(h)i}}$$

Equation 3: Precision-indicating merging R-value

(N =number of reflections h)

2.2.5.2 Phase determination

The objective of the experimental structure solution approach in x-ray crystallography is an electron density map of the protein, which can be used for model building to generate a 3-D model of the protein of interest. The Fourier transformation can be used to calculate the electron density distribution $\rho(x, y, z)$ from the structure factor $F(hkl)$ and vice versa (Equation 4)

$$\rho(x, y, z) = \frac{1}{V} \sum_h \sum_k \sum_l F(hkl) e^{-2\pi i(hx + ky + lz)}$$

Equation 4: Inverse Fourier transform

(ρ = electron density, V = volume of unit cell, F = structure factor, $h/k/l$ = Miller-Indices, $x/y/z$ = coordinates)

The square of the amplitude of the structure factor $|F(hkl)|$ is proportional to the measured intensity ($I(hkl)$) of a reflection (Equation 5).

$$I(hkl) \sim |F(hkl)|^2$$

Equation 5: Relation of structure factor and amplitudes

$$F(hkl) = |F(hkl)|e^{i\varphi(hkl)}$$

Equation 6: Calculation of structure factors

(I=intensity, F = structure factor, h/k/l = Miller-Indices, φ = phase angle)

The information which can be extracted from the diffraction images only contains the amplitudes (=intensities) but not the phase information of the scattered X-rays. However, also the phase φ of the wave is needed for the calculation of the structure factor $F(hkl)$ and therefore for the generation of an electron density map (Equation 6). The fact that the phases cannot be measured directly is termed the phase problem in crystallography. There are different methods available to solve the phase problem (Taylor, 2010). They have in common that they involve additional information to deduce initial phases for the electron density calculation. In this study molecular replacement and single isomorphous replacement combined with anomalous scattering (SIRAS) were conducted to overcome the phase problem.

2.2.5.3 Molecular replacement - MR

The molecular replacement (MR) method exploits phase information derived from a known homologous structure. The proteins have to share at least 25-30% sequence identity. MR is favored over the experimental techniques since it requires only one native dataset. The probability to find a suitable model structure increases with the number of published crystal structures. To apply the phases of the model structure to the electron density calculation the structures have to superpose in the unit cell.

$$P_{uvw} = \frac{1}{V} \sum_{hkl} |F_{hkl}|^2 \cdot \cos|2\pi (hu + kv + lw)|$$

Equation 7: Patterson function P_{uvw}

(F = structure factor, h/k/l = Miller-Indices, u/v/w = Patterson-coordinates)

The correct orientation is obtained with the help of the phase-independent Patterson function (Patterson, 1934; Patterson, 1935) (Equation 7) representing the structures by the sum of their interatomic vectors. The maximal correlation of the Patterson maps is determined in a 6-dimensional search, including 3 axes of rotation and 3 axes of translation. To decrease computational complexity, the search is separated in a rotation and translation step to pursue a 3-dimensional search twice. Important is also the number of molecules (n) present in the asymmetric unit which can be deduced from the Matthews's coefficient V_M (Matthews, 1968) (Equation 8), taking the volume of the unit cell, the space group symmetry and the molecular weight of the protein into account.

$$V_M = \frac{V_{unit\ cell}}{M \cdot z \cdot n}$$

Equation 8: Matthew's coefficient

($V_{unit\ cell}$ = volume of the unit cell, M = molecular weight of the protein, z = number of symmetry operators of the space group)

In protein crystals the Matthews's coefficient is usually between 1.7 and 4.0 Å³/Da corresponding to a solvent content of 30-70%. This is of course a probability-driven rule of thumb. In the case of ypFabV in the crystal form including the hexahistidine tag, the Matthew's coefficient suggested a higher probability for 2 molecules in the asymmetric unit, but it turned out that it was actually only one molecule with the very high solvent content of 70%.

In practice the molecular replacement search was performed with the help of the program Phaser (McCoy et al., 2007) included in the CCP4 suite (CCP4, 1994).

2.2.5.4 Single isomorphous replacement with anomalous scattering – SIRAS

When no homologous protein structure is available, the phase problem has to be solved experimentally. The additional information to determine the phases is hereby deduced from changes in the measured intensities. The SIRAS approach takes advantage of two different phasing methods, isomorphous replacement and anomalous scattering (Taylor, 2010).

For isomorphous replacement the crystal is soaked with heavy atom compounds (Perutz, 1956). When these atoms bind to the protein in the crystal, the electron-rich heavy atoms (H) provoke measurable changes in the structure factor amplitudes of the diffraction dataset $|F_{PH}|$ compared to a native dataset $|F_p|$. Both datasets have to be isomorphous with no major changes in the unit cell parameters.

$$|F_H| = |F_{PH}| - |F_p|$$

Equation 9: Isomorphous difference

This isomorphous difference (Equation 9) is utilized to determine the heavy atom structure factor amplitude $|F_H|$. The phase of F_H is determined with the Patterson method or direct methods. With this information the phase angle of the native structure factor $|F_p|$ can be narrowed down with the help of a Harker construction (cf. Figure 11) to two possible solutions.

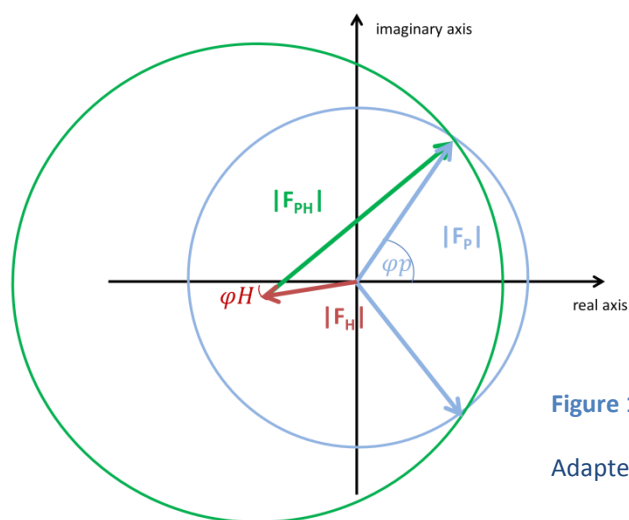


Figure 11: Harker construction for the SIR approach

Adapted from (Taylor, 2010)

To break this so-called phase ambiguity of single isomorphous replacement (SIR) the second method in SIRAS is used – anomalous scattering. Anomalous scattering occurs if the x-ray energy is sufficiently high (at the absorption edge of a heavy atom) to excite an electron and promote it from the inner to a higher shell. When it returns to the lower energy level it emits electromagnetic radiation which, also contributes to the measured intensities. The anomalous contribution f'' of the heavy atom is retarded by 90° in phase and therefore orthogonal to its native structure factors. This anomalous difference disrupts the symmetry of the Friedel pair ($|F_{PH}^+| \neq |F_{PH}^-|$). In the Harker construction

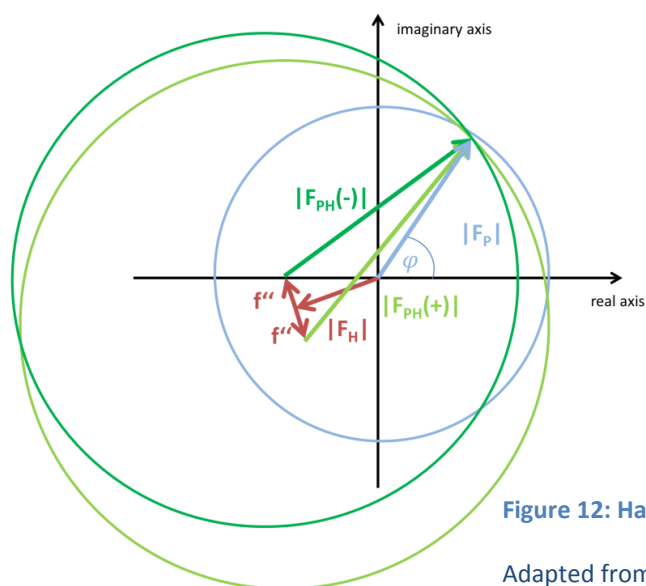


Figure 12: Harker construction for the SIRAS approach

Adapted from (Taylor, 2010)

(cf. Figure 12) the anomalous phase information is used to resolve the phase ambiguity and define an initial phase, which can be utilized to generate the first electron density map of the protein. In this study a crystal of YpFabV was soaked with 200 mM NaI and the anomalous scattering of the bound iodine atoms was exploited. The dataset was measured at a wavelength of 1.25 Å at beamline ID29 (ESRF) to a resolution of 3.1 Å. 15 bound iodine atoms contributed to the isomorphous and anomalous signal of the dataset. An isomorphous native dataset was collected at beamline MX14.1 at Bessy II at a wavelength 0.918 Å to a resolution of 2.1 Å. The SIRAS phasing was performed with the help of the program autoSHARP (Vonrhein et al., 2007) (cf. Table 10).

2.2.5.5 Model building, refinement and validation

The initial error-prone electron density map was used to build a first model. In case of molecular replacement the search model was utilized, the amino acid sequence was corrected and the model adapted to the electron density map. In case of the SIRAS result an *ab initio* model was generated with the help of the automated model building software ARP/wARP (Langer et al., 2008) which created a partial model which was extended and improved manually. Model building and improvement was performed in the program Coot (Emsley and Cowtan, 2004) using the $2F_o - F_c$ map. The $F_o - F_c$ difference

map supported the model building process by emphasizing missing or wrong parts of the model. The preliminary model could then be used in intermediary refinement cycles to improve the phases and thereby the electron density map. Repeated cycles of model building and refinement further improved both model and phases until convergence was achieved. The refinement was performed with the programs Refmac5 (Pannu et al., 1998) or phenix.refine (Adams et al., 2010). Both programs utilize maximum likelihood refinement which aims to maximize the congruence of the observed ($|F_o|$) and the calculated ($|F_c|$) structure factor amplitudes and restrain protein geometry features, like bond lengths and angles, near their optimal values. Non-crystallographic symmetry (NCS) restraints contributed to the improvement of the model. NCS restraints are only applicable if the asymmetric unit contains more than one molecule. It is based on the assumption that all symmetric chains share the same conformation and geometry. In addition, a considerable improvement during refinement was achieved by TLS refinement (translation, libration, screw motion). TLS refinement considers the uniform anisotropy of groups of atoms, in their concerted rigid body motions. The number and size of the groups can be optimized. They can be defined using prior knowledge about the protein (domains, hinge regions, secondary structure elements, etc.) or by the analysis of the isotropic B-factor, which was conducted in this study with the help of the TLSMD server (Painter and Merritt, 2006). For every TLS group 20 additional parameters are introduced to the refinement. TLS does not only support the refinement process, the movement of groups and domains described in TLS can also provide information about the dynamics of the protein.

A common measure for the convergence of the refinement is the R-factor R_{cryst} (Equation 10). It expresses the difference between the calculated and observed structure factor amplitudes. The R-factor should be as small as possible indicating good agreement of model and experiment. At a resolution of 2.5 Å the R_{cryst} is usually about 20% for a successfully refined structure.

$$R = \frac{\sum_{hkl} ||F_o| - |F_c||}{\sum_{hkl} |F_o|}$$

Equation 10: R-value

(F_o = observed structure factor, F_c = calculated structure factor)

The R_{cryst} , however, is prone to model bias, since it is based on data, which is used during refinement. To prevent overfitting of the model a second quality marker, the R_{free} , was established. The R_{free} is derived from data which was excluded from refinement (5% of the data, randomly chosen) and is therefore not affected by the refinement. The R_{free} is usually approx. 3-6% higher than R_{cryst} (cf. PDBe statistics).

Once the refinement of the protein structure has reached convergence, the model has to be validated. Validation of the structures was carried out using the MolProbity server (Chen et al., 2010), independently of the experimental data only relying on protein geometry and potential clashes of atoms in the structure. In terms of geometry the server analyzes the deviation of the bond angles and lengths from their ideal values, the C_{β} deviation and the Ramachandran plot, describing the accordance of the dihedral angles ϕ and ψ of the peptide backbone to the ideal. The plot is separated in the most favored region, the allowed region and the disallowed region containing outliers. Also unusual rotamers of amino acid side chains are analyzed. All these quality markers are based on statistics on protein libraries and outliers are not automatically wrong. If an outlier was detected, the corresponding residue was evaluated in its electron density map and if the map supported this more unlikely conformation of the residue, it was accepted. Furthermore, the server searches for potential atomic clashes of the protonated model. It provides a clash score which is defined as the number of serious steric overlaps ($> 0.4 \text{ \AA}$) per 1000 atoms. Prior to analysis the MolProbity server suggests side chain flips of histidines, glutamines and asparagines, if the hydrogen bond network of the surrounding structures is improved by the flip. After evaluation, the secondary structure elements were assigned with the program dssp (Kabsch and Sander, 1983). Structural features were analyzed with the help of several PDBe tools (Velankar et al., 2012) (cf. 2.1.8). Ligand interactions were examined utilizing Ligplot (Wallace et al., 1995) and Pymol (Schrodinger, 2010). Pymol was further used to create most of the illustrations describing the structures.

3. Results

The enoyl-ACP reductases of *Y. pestis* and *B. pseudomallei*, YpFabV, BpFabI and BpFabV were expressed, purified and crystallized. For the first structural characterization of FabV the x-ray structure had to be solved by experimental phasing (SIRAS). Further FabV structures as well as the FabI structures were solved by molecular replacement. Subsequently, to follow the structure based drug design approach, the drugability of both proteins with diphenyl ether and pyridone inhibitors was probed using co-crystallization trials with FabI and FabV.

3.1 FabV

In the course of the project on FabV, several FabV constructs from various species were utilized for our structure based drug design approach (cf. Table 4). In first experiments the expression and purification of FabV was established with BmFabV (FabV from *B. mallei*). Since crystallization trials with BmFabV were not successful, the source organism was switched to *Y. pestis*. However, the initially utilized YpFabV construct, with which the structure was solved by experimental phasing, contained a T276S mutation. This mutation was revealed when binary and ternary complexes with this variant had been solved. To exclude the possibility, that the missing methyl group of S276 in the variant has an impact on the structure of the protein, the binary complex structures were reproduced with wild type YpFabV. The structural description in the following chapter therefore focuses first on the T276S variant and follows with the description of the wild-type protein.

3.1.1 Expression of FabV from different Pathogens

For the expression of FabV from different pathogens (*B. mallei*, *B. pseudomallei*, *P. aeruginosa* and *Y. pestis*) the vectors were kindly provided by Professor Peter Tonge (Stony Brook University, New York, USA). The different *fabV* genes were cloned into the pET15b expression vector with an N-terminal hexahistidine tag in a T7-promotor controlled region with an ampicillin resistance gene for selection. A first expression test was performed with BmFabV. The vector was transformed into different chemo-competent *E. coli* strains (BL21 (DE3), BL21 (DE3) pLsyS and BL21 (DE3) arctic express). Overnight cultures were inoculated with a single colony of each strain. This pre-culture was used to inoculate small-scale test expression vials. Expression was induced at an

OD₆₀₀ of 0.6 with 1 mM IPTG and the expression temperature (i.e the temperature after induction) set to 15 °C or 25 °C. The expression was analyzed in a time course. The best result could be observed for BL21 (DE3) cells at 15 °C as shown in Figure 13A for FabV from *B. mallei* (BmFabV).

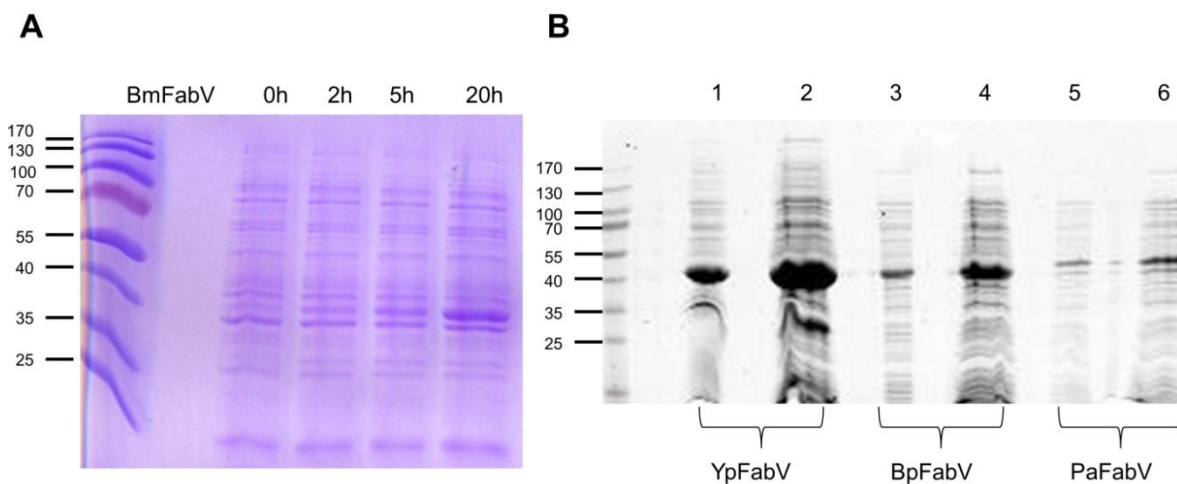


Figure 13: FabV Expression

A) SDS-PAGE of test expression of BmFabV in BL21 (DE3) cells at 15 °C. B) SDS-PAGE of high scale expressions of YpFabV (1+2), BpFabV (3+4) and PaFabV (5+6) in BL21 (DE3) cells (20 h at 15 °C), samples 1/3/5 were diluted 1:5.

In the SDS-PAGE a prominent band next to the 40 kDa marker band appears already 2 hour after induction of the expression with 1 mM IPTG and increases over time. Including the recombinant part of the gene product, the FabV proteins have a molecular weight of 45 kDa indicating that the appearing band most likely represents BmFabV. The highest expression was achieved in an overnight expression, which was used for the following high scale expressions. This protocol was also successful for the remaining FabV constructs BpFabV, PaFabV and YpFabV. The expression levels of the proteins are shown in the respective SDS-PAGE (Figure 13B) with clearly overexpressed proteins visible as a thick band slightly above the 40 kDa marker band. The expression of the FabV T276S variant worked equally well. In general, the overexpression of the protein was increased in high scale expression compared to low scale expression tests.

3.1.2 Buffer optimization using Thermofluor analysis

Pure BmFabV obtained from a first small scale purification (final purification described in detail in 2.2.2 and 3.1.3) precipitated in the preliminary gel filtration buffer (30 mM PIPES pH 6.8, 150 mM NaCl and 1 mM EDTA). To improve the solubility of the protein a Thermofluor analysis (2.2.3.2) was performed testing the thermal stability of BmFabV in different buffer solutions and at different pH values (buffer list see appendix Table 27). The Thermofluor analysis is based on the fluorescence dye Sypro Orange, which gives rise to an elevated fluorescence signal upon binding to the unfolded protein.

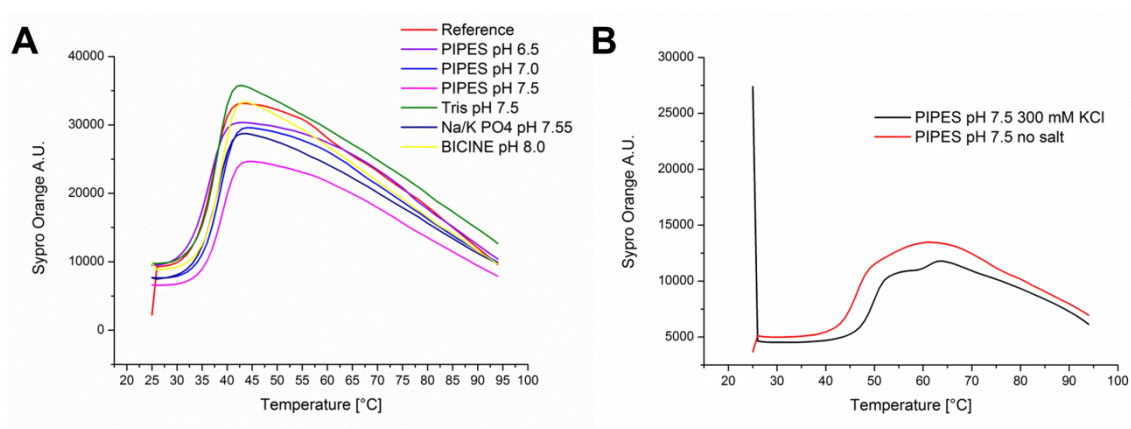


Figure 14: Thermofluor analysis of BmFabV

A) Buffer screen B) Thermofluor with PIPES pH 7.5 and with (black) and without (red) 300mM KCl.

In general, the resulting melting temperatures of BmFabV were very low and varied between 35 °C and 39 °C. The gel filtration buffer was used as a reference. Buffers with pH values between 7.5 and 8.0 led to the highest melting temperatures with the best buffer being PIPES pH 7.5, elevating the melting point from 36 °C to 39 °C (Figure 14A). This didn't seem to be a dramatic effect, but the second batch of protein, purified in PIPES pH 7.5 buffer, was in general more stable with a melting temperature of 46 °C, which could be further improved by the addition of 300 mM KCl to 49 °C (Figure 14B). The resulting buffer (20 mM PIPES pH 7.5, 300 mM KCl and 1 mM EDTA) was used for size-exclusion chromatography and as final protein buffer.

3.1.3 Purification

For protein crystallography the purity and homogeneity of the protein is of particular importance. The purification of the different FabV proteins was achieved with the same protocol. Herein, the purification of T276S variant of YpFabV (Figure 15) and of its wild type (Figure 16) is presented. Furthermore, the BpFabV purification is displayed in the Supplemental Figure 57 of the appendix. The overexpressed protein was isolated from the cell lysate by affinity chromatography utilizing its N-terminal hexahistidine tag and afterwards separated from remaining impurities and aggregated protein, which might prevent crystallization, by size-exclusion chromatography.

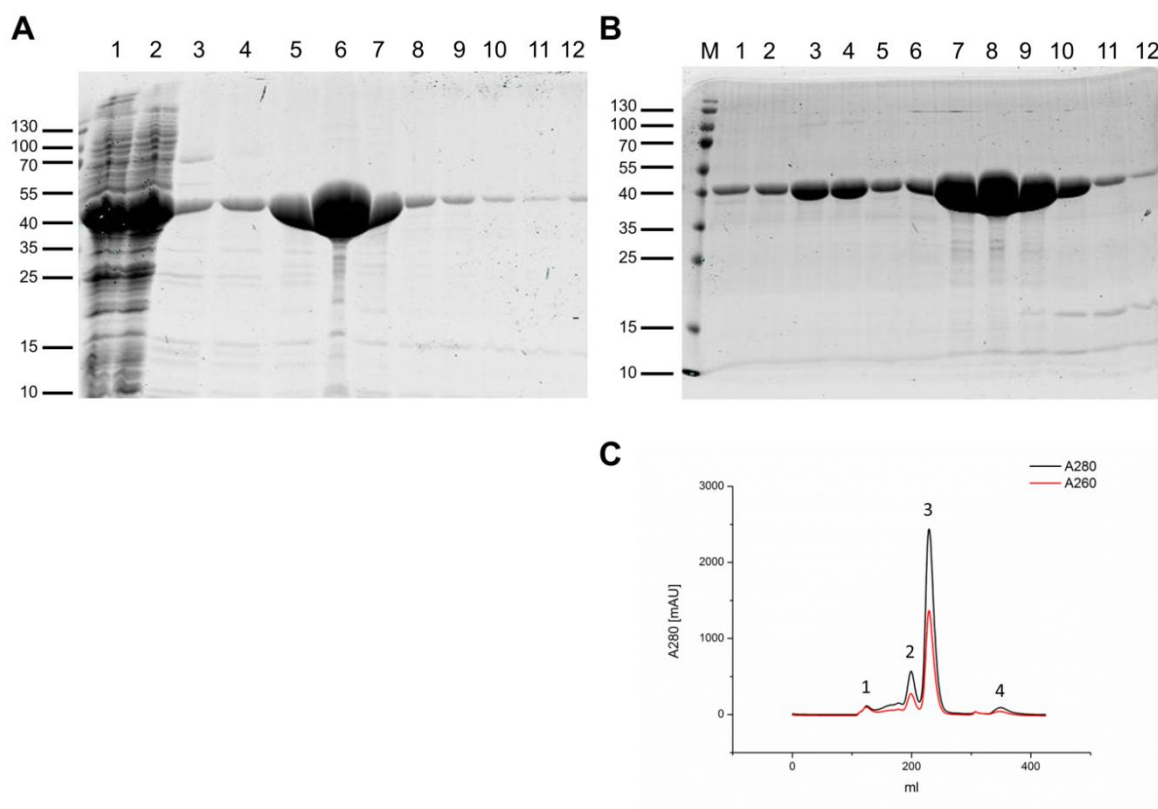


Figure 15: Purification of YpFabV T276S

A) SDS-PAGE of a Ni-TED purification: (1) Load, (2) Flowthrough, (3) Wash out of the unbound sample, (4) Additional wash step, (5-12) Elution. B) SDS PAGE after size exclusion chromatography: (1) Peak 1, (2-5) Peak 2, (6-12) peak 3. C) Chromatogram of the size exclusion chromatography; the absorption at 280 nm is shown in black and at 260 nm in red.

For the nickel affinity chromatography two equivalent approaches were used, a batch method using Ni-TED (Protino) material (Figure 15A) or pre-packed HisTrap FF crude columns (5-10 ml bed volume, GE healthcare) using the ÄKTA chromatography systems (Figure 16A+B). In both methods cleared cell lysate was loaded onto the equilibrated

Results

column, the unbound sample was washed out and unspecific binding contaminants were removed in an additional washing step using small concentrations of imidazole. FabV was eluted from the column with a step to 150 mM or 250mM imidazole (for details see 2.2.2.1). The elution of the protein was followed at the chromatography system using its absorption at wavelengths of 280 nm and 260 nm. Samples from every step and the peak fractions were analyzed via SDS-PAGE. Due to the stringent cleaning procedure all elution fractions reached high purity and were used for the second step of purification (see Figure 15A, Figure 16B).

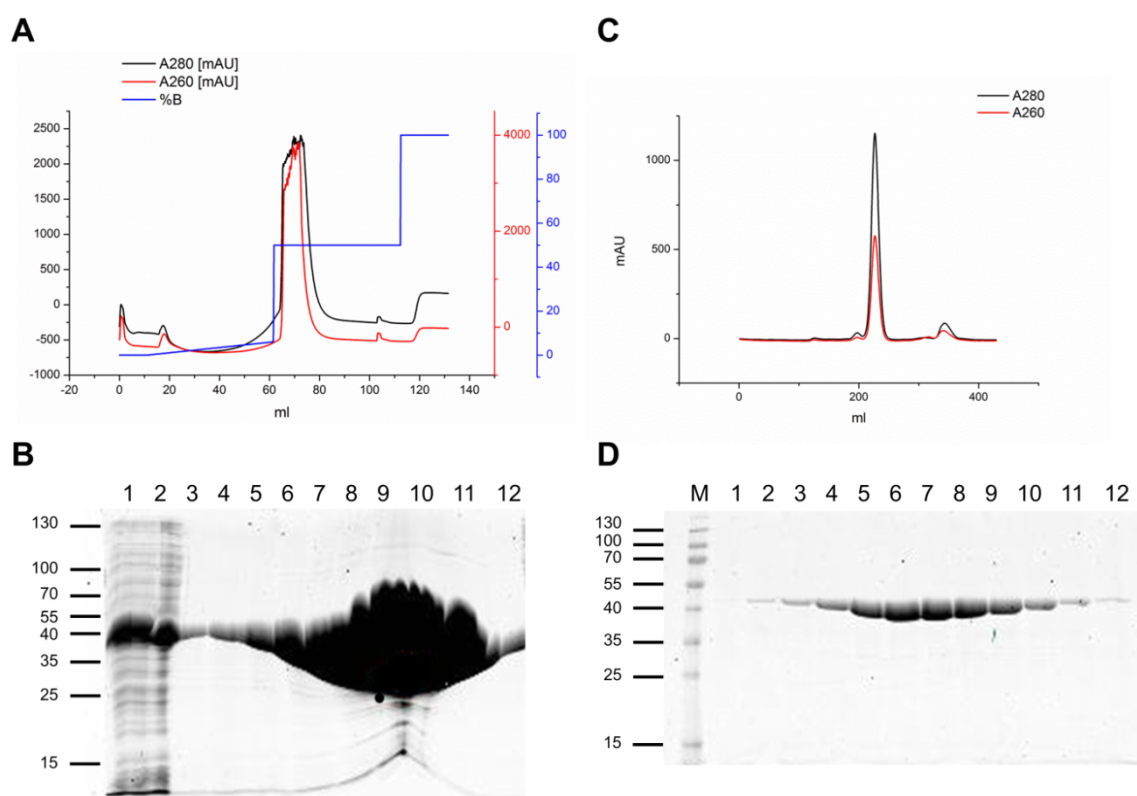


Figure 16: Purification of wild-type YpFabV

A) Chromatogram of a Histrap purification with a step gradient, absorption at 280 nm (black) and 260 nm (red), % Elution buffer (blue). B) SDS-PAGE of Histrap purification: (1) Load, (2) Flowthrough, (3) wash out of the unbound sample, (4) extra wash, (5-12) elution. C) Chromatogram of size exclusion chromatography, absorption at 280 nm (black) and 260 nm (red). B) SDS PAGE of size exclusion chromatography: (1-12) main peak.

Although both Ni-chromatography methods led to similar results, the Histrap purification prevailed in practice due to the higher binding capacity of the column material (50 mg protein /ml bed volume instead of 5 mg protein /ml Ni-TED resin) and the automated

performance at the chromatography system leading to a highly concentrated peak in the elution (see Figure 16A+B). The following size-exclusion chromatography was conducted using a HiLoad Superdex 200 26/60 gel filtration column with a maximal sample volume of 10 ml. The elution fractions of the Ni-TED purification had to be concentrated with a Vivaspin 20 concentrator (10 kDa cutoff) to meet this condition. The elution fractions of the Histrap column commonly could be used directly. After the FabV sample was applied to the equilibrated column, it was eluted with one column volume of the gel filtration buffer. The elution profile was composed of four characteristic peaks (see Figure 15C). Samples from each peak were analyzed in SDS-PAGE. The first peak, shortly after the void volume of the column, represents aggregated protein, mainly FabV (Figure 15B, lane 1). At an elution volume of 200 ml a small FabV dimer peak appeared (lanes 2-5), which was interpreted as a purification artifact due to the extremely high concentrations of FabV. The following peak contained the vast majority of the protein sample and corresponds to the FabV monomer (lanes 6-12) as it was previously described (Massengo-Tiasse and Cronan, 2008). The last small peak corresponds to imidazole, which was used during the affinity chromatography step. The percentage of FabV aggregate and dimer peak varied between the purifications. In a batch with good, soluble protein, which was processed very fast during purification, these peaks hardly appear (Figure 16C). The fractions of the monomer peak displayed very high purity (99%). They were pooled, concentrated to 50-100 mg/ml, flash-frozen in liquid nitrogen and stored at -80 °C. To modify the crystallization behavior of the enzyme, the buffer was partly exchanged by ddH₂O during protein concentration.

3.1.3.1 Removal of the hexahistidine tag

An additional approach to change the YpFabV crystallization behavior was the removal of the recombinant hexahistidine tag using thrombin. A thrombin cleavage site is inserted in the pET15b vector between the hexahistidine tag and the actual start of the *fabV* gene. 17 of the 23 recombinant residues at the N-terminus of the YpFabV construct are removed by the thrombin cleavage, generating a size difference of about 2 kDa. The efficiency of the cleavage was tested at different protein concentrations (1 mg/ml and 50 mg/ml), at different temperatures (4 °C and 22 °C), with different thrombin

concentrations (0.01-1 U/mg YpFabV T276S), after different incubation times and with the addition of 500 mM imidazole (Figure 17A+B).

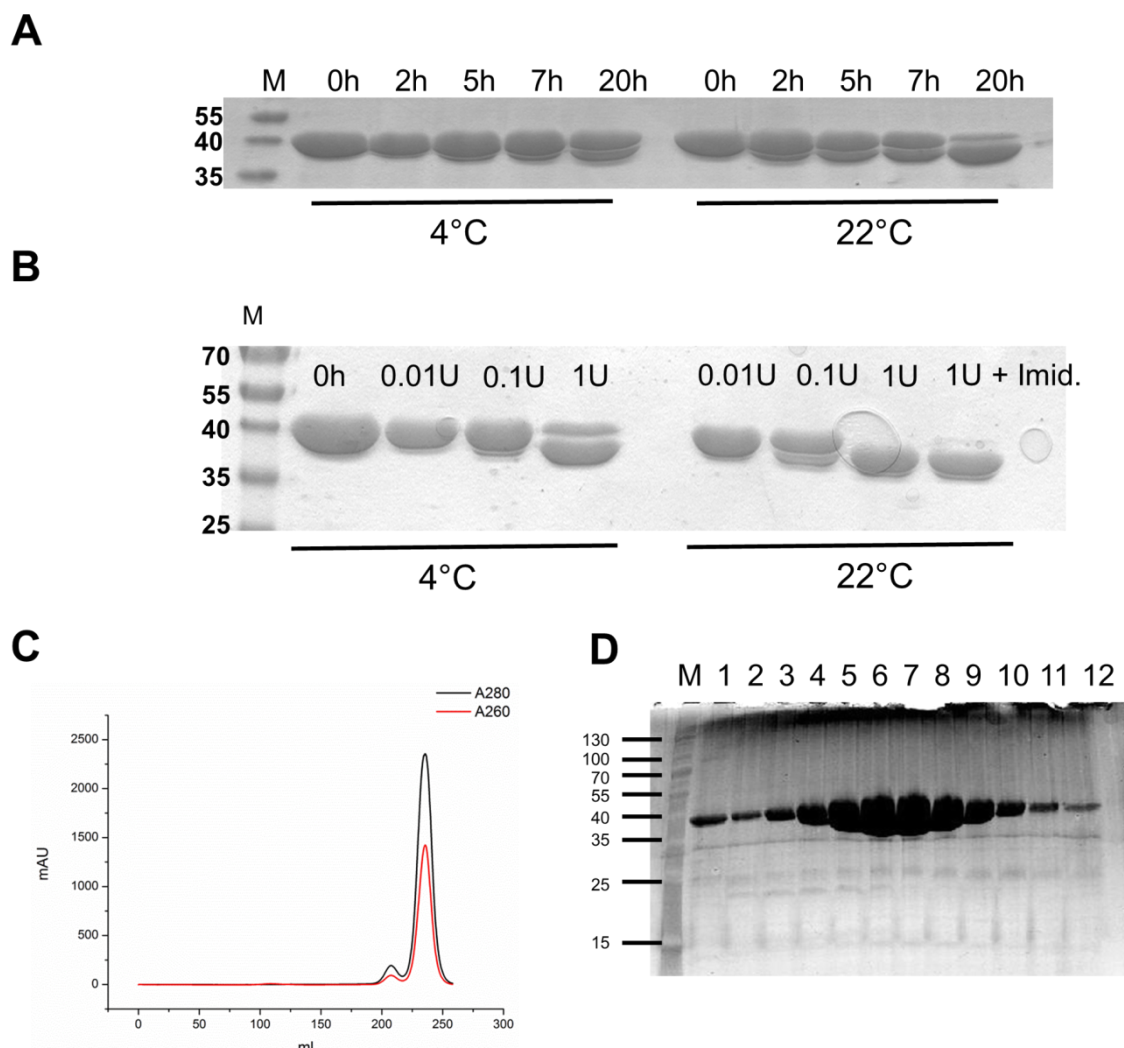


Figure 17: Thrombin cleavage

A) SDS-PAGE of thrombin (1 U/mg protein) test-cleavage of YpFabV T276S (1 mg/ml). B) SDS-PAGE of thrombin (different concentrations) test-cleavage of YpFabV T276S (50 mg/ml), last lane contains 500 mM imidazole C) Chromatogram of size exclusion chromatography, absorption at 280 nm (black) and 260 nm (red). D) SDS PAGE of size exclusion chromatography: fractions of main peak.

In the time course test at low protein concentrations with 1 U thrombin per mg of YpFabV a second band appears below the YpFabV band at both temperatures but delayed at 4 °C (Figure 17A). At 20 °C the majority of the protein is cut after 20 hours. With respect to the thrombin-concentration test at a higher FabV concentration (50 mg/ml) the protein seems to be cleaved with 1 U of thrombin after 20 hours at 22 °C irrespective of the presence of 500 mM imidazole (Figure 17B). These experiments show that the protein can be directly cleaved after nickel affinity chromatography without a prior need for the

removal of imidazole. The eluate of the affinity column was concentrated up to 50 mg/ml, mixed with thrombin and incubated overnight at room temperature. The success of the cleavage was analyzed by SDS-PAGE. Thrombin was removed from the sample using a benzamidine column (GE healthcare), which binds thrombin but not FabV. The flowthrough, containing the FabV sample, was subsequently applied to the size-exclusion column as described for the uncleaved protein (Figure 17C+D). Prior to concentrating the sample after size exclusion chromatography, the peak fractions were incubated shortly with Ni-TED resin to remove residual uncleaved FabV from the sample, since it could interfere with the crystallization of the cleaved protein. The Ni-TED resin was separated by centrifugation and the protein sample concentrated to 50-100 mg/ml, flash-frozen in liquid nitrogen and stored at -80 °C.

3.2 Crystal structures of FabV from *Y. pestis* -T276S variant and wild type

3.2.1 Binary cofactor complex of YpFabV

3.2.1.1 Crystallization

To obtain the first crystal structure of FabV, the recombinant protein from *Y.pestis* in complex with its cofactor NADH was used in crystallization trials. Due to the very high solubility of YpFabV T276S the screens were performed with protein concentrations of 30-100 mg/ml with the addition of a 10-fold molar excess of NADH. The screens were performed as small-scale sitting-drop vapor diffusion experiments with the commercially available crystallization screens Hampton Crystal Screens I+II, Hampton Index Screen, Emerald Wizard Screens I+II, Nextal PEG suite and OptiMix Screens 3+4 (TOPAZ) as well as with the self-designed Salt Screen I, which was developed on the basis of well-diffracting crystals grown in salt-containing conditions (Table 7).

YpFabV T276S crystallized in various conditions, predominantly in the Nextal PEG screen and in the OptiMix Screen 3, in either PEG-containing conditions or crystallization conditions at high salt concentrations (see Figure 18). The crystals grown in PEG conditions (Figure 18 A+E) did not diffract to a resolution better than 8 Å and could not be improved with the help of small molecule additives (Additive Screen HT, Hampton

Research). The crystals grown in salt conditions in the initial screens diffracted already to a resolution of 3 Å (Figure 18 B, C, D, F, G + H)) and could be optimized in hanging drop setups to a resolution of ~2 Å using 1.2-1.5 M sodium malonate as a precipitant. The sodium malonate condition was successful in various buffers and pH ranges with the best diffracting crystals in 100 mM imidazole pH 8.25 or 100mM sodium citrate pH 5.6. The screens and the optimization were accomplished with the T276S variant of YpFabV and could also be utilized for wild-type YpFabV without changes in protocol.

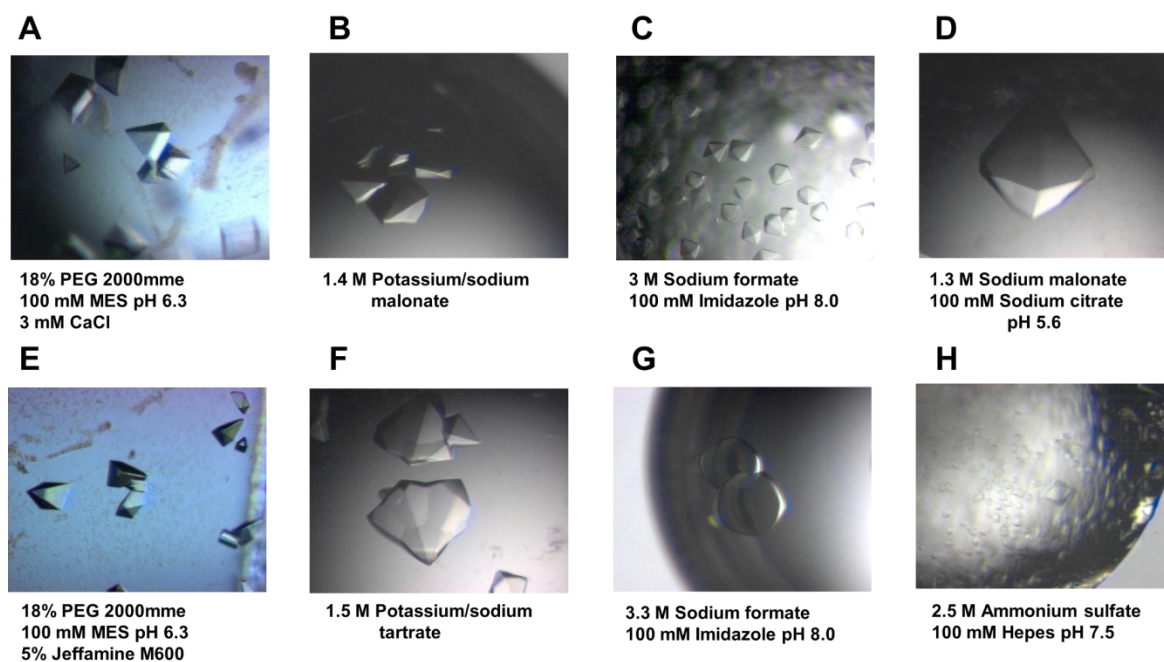


Figure 18: T276S YpFabV crystals from different crystallization screens

3.2.1.2 Data collection and structure solution (SIRAS)

For the initial solution of the FabV structure experimental phasing with the SIRAS phasing method was conducted. Well-diffracting YpFabV T276S crystals were soaked in cryo-protectant solution containing 30% glycerol and 300 mM sodium iodine. For native diffraction datasets crystals of the T276S variant and the wild-type YpFabV were treated likewise but without sodium iodine as additive. A diffraction dataset of the iodine-soaked crystal was collected at beamline ID29 at the European Synchrotron Radiation Facility

(ESRF) at a wavelength of 1.25 Å to a maximal resolution of 3.1 Å (Table 16). An example of a YpFabV crystal and its diffraction pattern is shown in Figure 19.

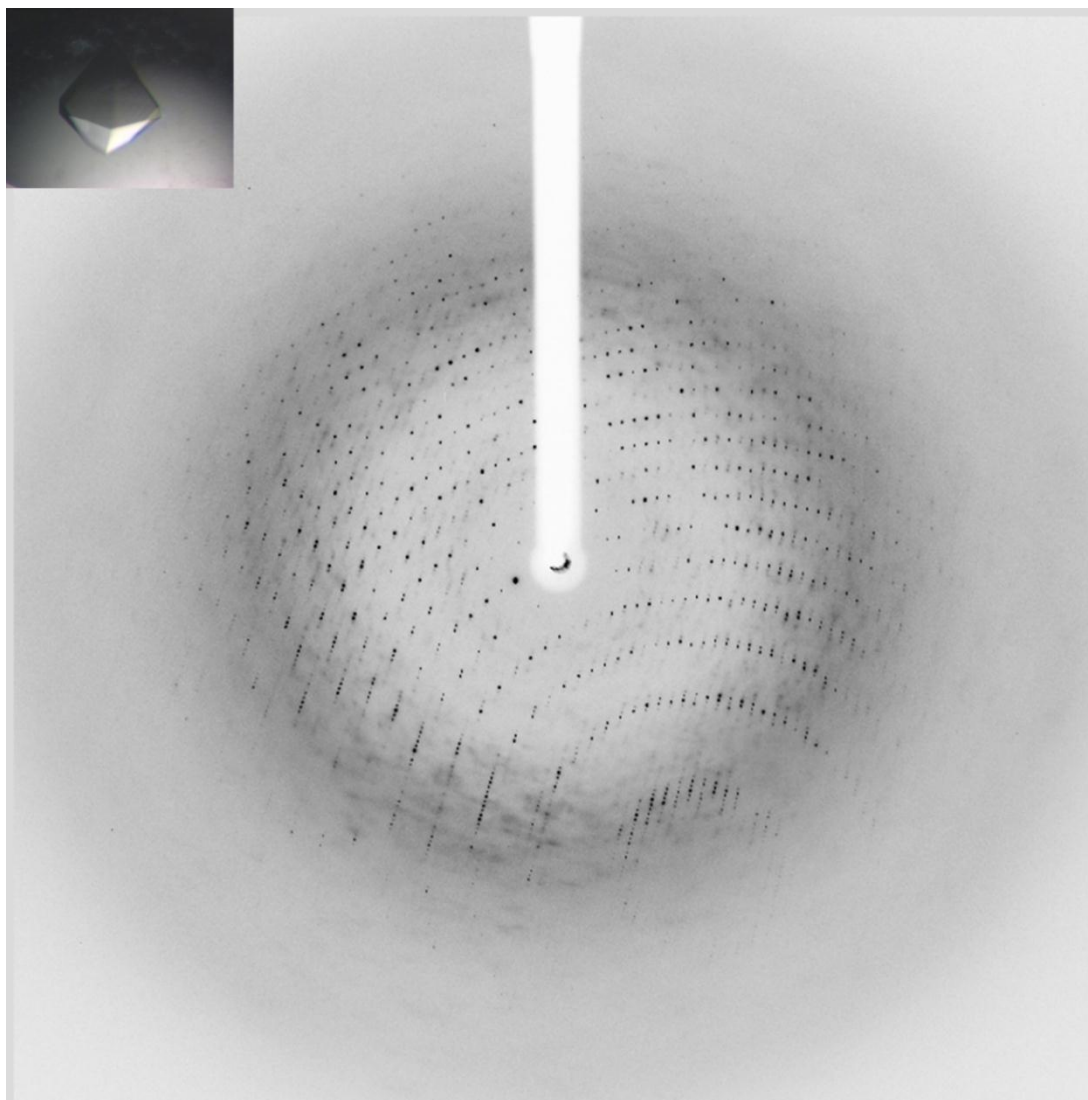


Figure 19: Diffraction pattern and crystal (corner) of YpFabV

The dataset was integrated and scaled using iMosflm (Battye et al., 2011) and Scala (CCP4, 1994; Evans, 2006), respectively. The data quality was examined in the Scala report files. The crystals belong to space group $P6_522$ with the unit cell dimensions of $a=b= 103.8 \text{ \AA}$, $c = 220.2 \text{ \AA}$, $\alpha=\beta = 90^\circ$ and $\gamma = 120^\circ$. The dataset was 100% complete and 33.8-fold redundant with an anomalous completeness and redundancy of 100% and 18.8, respectively at 3.1 Å resolution. A native dataset at a wavelength of 0.918 Å with a better resolution to 2.1 Å could be obtained at beamline MX14.1 at the synchrotron facility BESSY II in Berlin and was merged with the anomalous dataset (Table 16). The anomalous signal was analyzed in SHELX (Sheldrick, 2008) and the processed data was utilized by the

program AutoSHARP (Vonrhein et al., 2007) for heavy atom refinement and phasing. 15 iodine atoms were found and contributed to the anomalous signal of the soaked YpFabV T276S crystal (Figure 20).

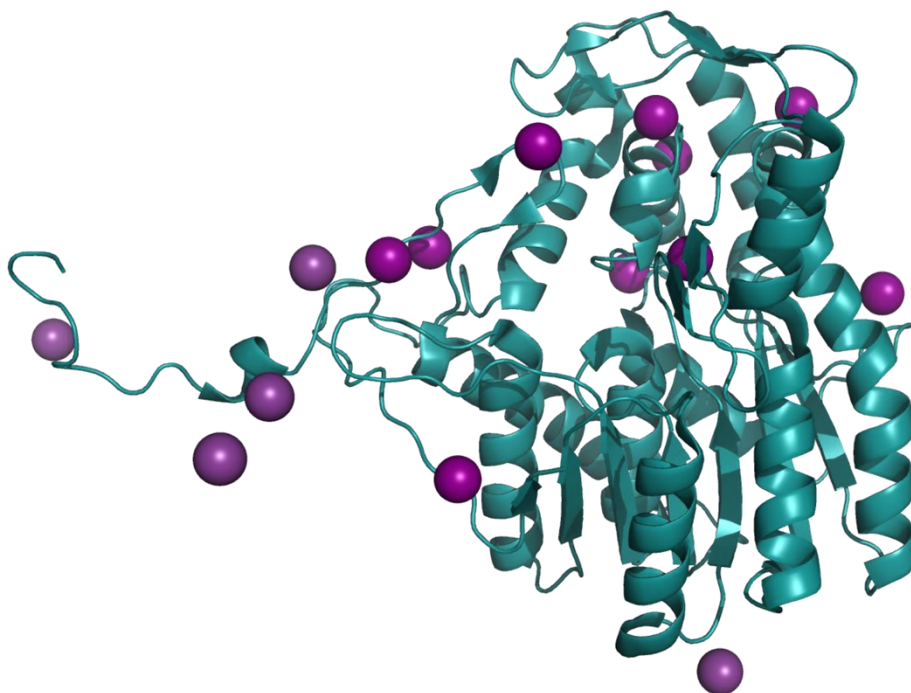


Figure 20: YpFabV structure (teal) as ribbon diagram with bound iodines (purple).

The centric, acentric and anomalous phasing power was 0.95, 1.0 and 0.69, respectively at a resolution of 3.1 Å. The electron density map after density modification was used by the automated model building program ARP/wARP (Langer et al., 2008) to build an initial model containing 9 chains with 384 of 422 residues. 3 of the nine chains (338 residues) were assigned with the amino acid sequence. The model was extended and improved manually with the model building software Coot (Emsley and Cowtan, 2004) with intermediary maximum likelihood refinement cycles including TLS refinement in Refmac5 (CCP4, 1994; Pannu et al., 1998) and phenix.refine (Adams et al., 2010). Additional density could be assigned to the co-crystallized NADH cofactor. The fitting of ligands into the electron density was facilitated by ligand library files generated by the Prodrgr server (Schuttelkopf and van Aalten, 2004). The library files contain geometrical restraints which were used for real space refinement by Coot. The final model contained 415 amino acids.

Results

Table 16: Data collection and refinement statistics of YpFabV structures (incl. hexahistidine tag)

	ypFabV (T276S)	ypFabV (T276S)	ypFabV wt
	Iodine	Native	Incl. tag
Phasing	SIRAS	SIRAS	MR
Data collection			
Wavelength (Å)	1.25	0.918	0.918
Space group	P6 ₅ 22	P6 ₅ 22	P6 ₅ 22
Unit cell parameters			
a/b/c (Å)	103.8/103.8/220.2	104.2/104.2/219.1	102.6/102.6/214.9
α/β/γ	90°/90°/120°	90°/90°/120°	90°/90°/120°
Resolution (Å)	89.9 - 3.1	39.4 - 2.1	45.98-2.3
Total reflections	455,984	344,333	320,803
Unique reflections	13,483	48,035	30,614
Completeness (%)*	100 (100)	99.8 (100)	100 (100)
Redundancy*	33.8 (35.3)	7.2 (7.3)	10.5 (11.3)
Anomalous completeness	100		
Anomalous redundancy	18,8		
Rmerge (%)*	11 (93)	6 (62)	6.0 (82.4)
<I/σ(I)*>	26.9 (5.4)	15.8 (3)	20.1 (2.6)
Phasing			
Iodide per ASU	15		
Phasing power (centric/acentric/anomalous)	0.95/1.00/0.69		
Figure of merit (after phasing) (centric/acentric)	0.127/ 0.092		
Figure of merit (after density modification)	0.598		
Refinement			
Total number of atoms	3,399		3,256
R _{cryst} (%)	19.9		19.4
R _{free} (%)	22.8		23.0
RMSD from ideal			
Bond length (Å)	0.007		0.007
Bond angles (°)	1.140		1.122
Average B-values (Å ² and # of atoms)			
All atoms	(3,399) 72.8		(3,256) 70.8
Protein	(3,195) 74.7		(3,179) 71.2
NAD(H)	(44) 54.2		(44) 50.63
Water	(160) 60.7		(33) 52.8
Na ⁺	(1) 58.3		
Ramachandran plot most favored / allowed/ disallowed (%)	96.2/3.6/0.2		97.3/2.7/0.0
PDB code	3zu2		

All 399 residues of the original YpFabV protein (with the exception of the T276S exchange) could be built into the electron density map and additionally 15 recombinant amino acids including three histidine residues of the hexahistidine tag. Furthermore, the model comprised the NADH cofactor, 160 water molecules and one sodium ion, which was distinguished from water due to its hydrogen bonding pattern. The last refinement step reached R_{cryst} and R_{free} factors of 19.9% and 22.8%, respectively. The wild-type YpFabV dataset was collected at beamline MX14.1 at BESSY II with a wavelength of 0.918 Å and reached a resolution of 2.3 Å (Table 16). The dataset was indexed and integrated in iMosflm (Battye et al., 2011) and scaled using Scala (Evans, 2006). The data was 100% complete and had 10.5-fold redundancy with an R_{merge} of 6.0% and 82.4% in the highest resolution shell (see Table 16).

This time experimental phasing was obsolete since the SIRAS model of the T276S YpFabV variant was available as search model for molecular replacement. Phasing was performed with the help of the program Phaser (McCoy et al., 2007). The initial model was improved in iterative cycles of manual model building in Coot (Emsley and Cowtan, 2004) and maximum likelihood refinement in Refmac5 (Pannu et al., 1998) until convergence at R_{cryst} and R_{free} factors of 19.4% and 23.0%, respectively, was achieved.

3.2.1.3 Validation

The YpFabV structures were validated with the help of the Molprobit server (Chen et al., 2010). The analysis mainly regards the chemical geometry of the protein and clashes between the atoms of the model. For the first model of YpFabV T276S gained by SIRAS phasing, the RMSD from ideal bond lengths (0.007 Å) and angles (1.14°) are in an acceptable range. No C_{β} deviations are present, 1.5% of the residues have unusual rotamers and only one outlier (0.2%) is present in the Ramachandran plot, namely Thr376, which was reviewed in the electron density map. The Ramachandran plot describes the dihedral angles ϕ and ψ of the amino acid backbone (Ramachandran et al., 1963). 3.6% of the residues reside in the allowed region of the plot and 96.2% in the most favored areas (Figure 21).

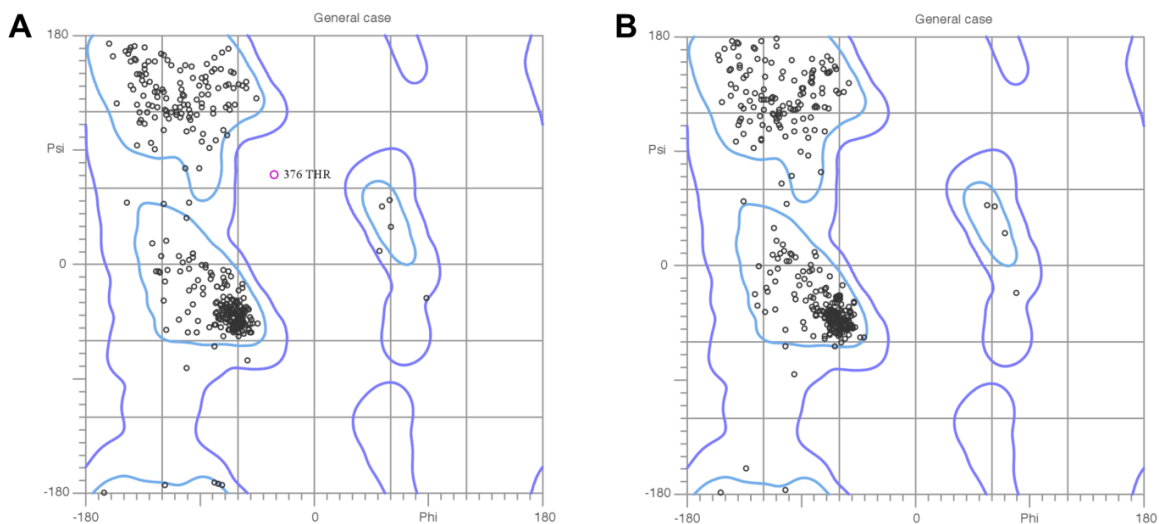


Figure 21: Ramachandran plots for the YpFabV T276S variant (A) and wild-type (B) structures

The most favored region is framed in cyan and the accepted region in blue.

The subsequent wild-type structure of YpFabV showed RMSD from ideal bond lengths and angles of 0.007\AA and 1.12° , respectively. There were no residues with C_β deviation and only 0.9% of the residues appeared in unusual rotamer conformations. There was no Ramachandran outlier and 97.3% of the residues reside within the most favored areas. In addition, the molprobity clash score improved from 19.5 to 14.1 from the first to the second structure. The clashscore represents the number of serious steric overlaps ($> 0.4\text{\AA}$) per 1000 atoms. In general, the quality markers have improved in the YpFabV wild type structure. However, the overall structure of both models is very similar. A structural comparison of YpFabV in the binary and tertiary complexes with the cleaved hexahistidine tag on the basis of secondary structure matching using the PDBeFold server (Krissinel and Henrick, 2004) resulted in an RMSD value of 0.44\AA .

In Figure 22A the structure of YpFabV T276S with the hexahistidine tag is shown as a ribbon diagram. The N-terminus which includes 15 amino acids beyond the N-terminus of the native YpFabV points away from the otherwise very compact protein fold of YpFabV. The N-terminal residues interact with the neighboring FabV molecule in the crystal and thereby build an artificial FabV dimer with an interface area of 1369\AA^2 (PDBePISA server) (Krissinel and Henrick, 2007) (Figure 22B). As the majority of interactions is mediated by the recombinant part of the protein this is most likely a crystallization artifact. However this artificial feature of the YpFabV structure might have an influence on the overall

structure of the protein. Since the interaction site was located in close proximity to the active site pocket the decision was made to solve an additional FabV structure with most of the recombinant amino acids removed prior to crystallization to assure the validity of the structure.

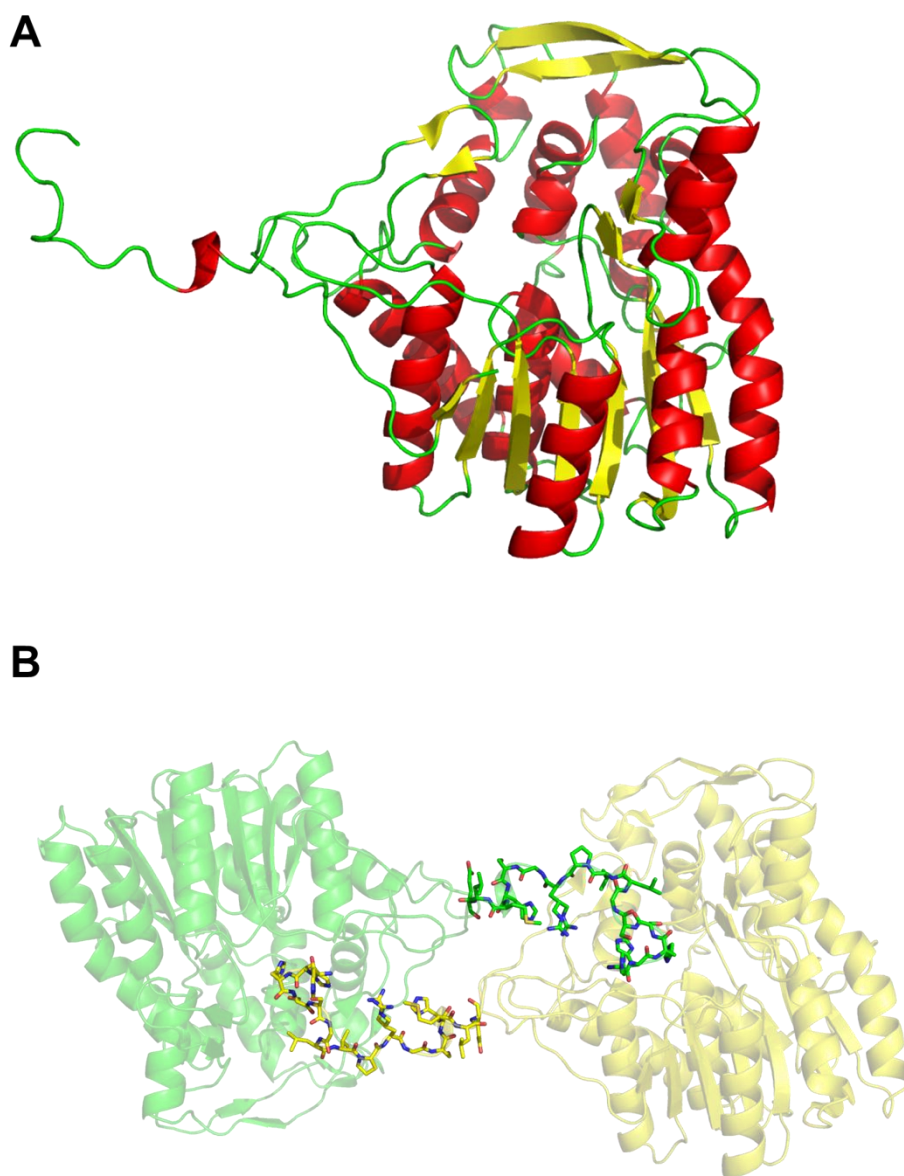


Figure 22: Artificial dimer interface in YpFabV T276S structure

A) Overview of YpFabV T276S structure, colored according to secondary structure elements with helices in red, β -sheets in yellow and loop regions in green. B) Crystallographic interface between two YpFabV molecules in the crystal with the recombinant vector part of the protein in all-bonds representation.

3.2.2 Binary and ternary complexes of cleaved YpFabV

3.2.2.1 Crystallization

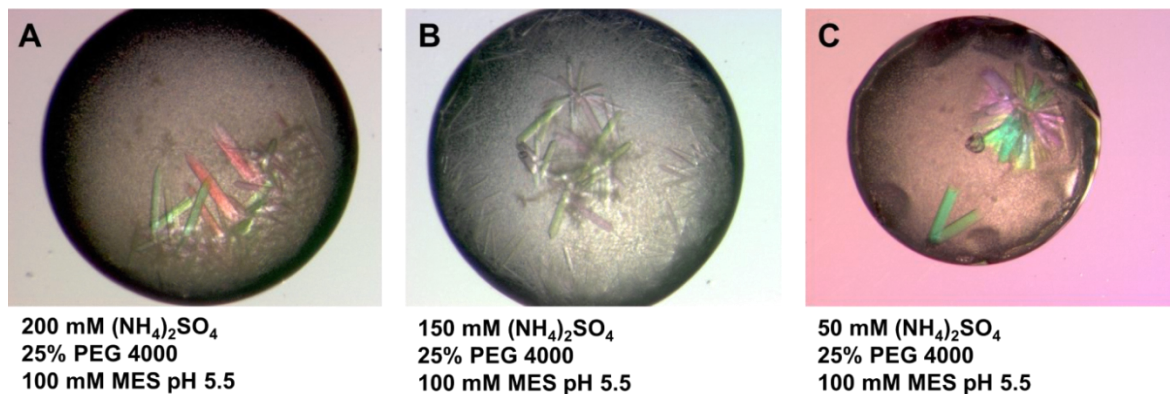


Figure 23: Crystallization conditions of binary cofactor complexes of cleaved YpFabV

To exclude an influence of the recombinant part at the N-terminus of YpFabV on the overall structure, the hexahistidine tag was removed by thrombin (see 3.1.3.1). Crystallization screens were performed with cleaved YpFabV T276S at a concentration of 58 mg/ml and 10 mM NADH (molar ratio \approx 1:10) utilizing Hampton Crystal Screens I+II, Hampton Index Screen, Emerald Wizard Screens I+II, Nextal PEG suite, Protein complex and OptiMix Screens 3+4 (TOPAZ) in sitting drop vapor diffusion setups. Needle-like crystals diffracting up to 2.5 Å at the x-ray home source (MicroMax-007 HF, Rigaku) grew in condition C10 of the Protein complex screen, containing 150 mM $(\text{NH}_4)_2\text{SO}_4$, 25% PEG 4000 and 100 mM MES pH 5.5. In reproduction and optimization trials of the crystallization condition in hanging drop setups the PEG 4000 concentration was successfully varied between 25-39% and yielded rod-like crystals of the variant and YpFabV wild-type diffracting to 2 Å or better (Figure 23). High protein concentrations (\geq 40mg/ml) were pivotal for crystallization, causing immediate precipitation of the protein upon mixing with the reservoir solution with subsequent crystal growth. At lower protein concentrations the protein only precipitated without crystal growth.

Apart from the binary complex of YpFabV with the cofactor NADH, co-crystallization with the 2-pyridone inhibitors PT172 and PT173 was successful utilizing the same crystallization condition (Figure 24). Prior to crystallization, YpFabV T276S was incubated for at least one hour with the cofactor (1:10) and the inhibitor (5 mg/ml; approx. 1:100)

to facilitate binding. The ternary inhibitor complexes crystallized at higher PEG concentrations compared to the binary complex (30-39% PEG 4000). The inhibitor complex crystals diffracted to 2 Å resolution at the x-ray home source (MicroMax-007 HF, Rigaku).

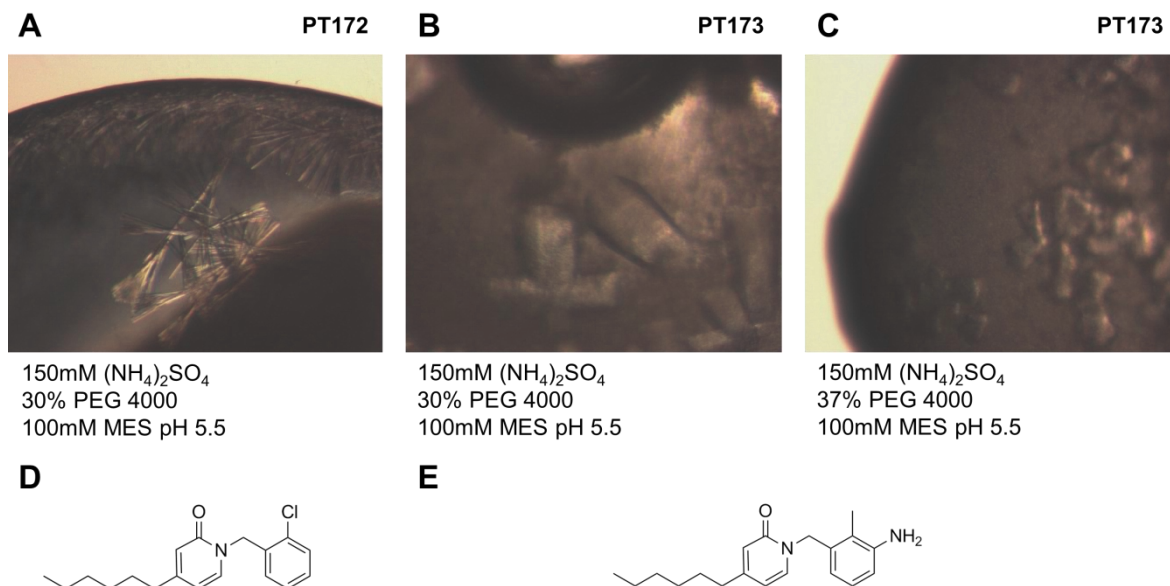


Figure 24: Co-crystallization (A-C) with 2-pyridone inhibitors PT172 (D) and PT173 (E)

3.2.2.2 Data collection and structure solution

For data collection the crystals were frozen in cryo protectant solution containing high PEG 4000 concentrations (37-39%) and 12-15% glycerol and/or up to 10% DMSO. The diffraction datasets of YpFabV wild-type and the T276S variant were collected at beamline MX 14.1 (Bessy II, Berlin) at a wavelength of 0.918 Å reaching a maximal resolution of 1.8 Å (data collection and refinement statistics see Table 17). The dataset of the inhibitor containing crystals were collected at the in-house X-ray source (MicroMax-007 HF, Rigaku) at the typical wavelength of 1.54 Å emitted by the copper rotating anode of this x-ray generator. The cleaved protein crystallized in space group P3₁21. The diffraction images were indexed and integrated with iMosflm (Battye et al., 2011) and

Results

scaled using Scala (Evans, 2006). All datasets showed a completeness of 100% with high redundancies (4.4-7.4-fold).

Table 17: Data collection and refinement statistics for the cleaved YpFabV structures

	ypFabV wt	ypFabV (T276S)	ypFabV (T276S)	ypFabV (T276S)
	cleaved His-tag	cleaved His-tag	PT172	PT173
Data collection				
Wavelength (Å)	0.918	0.918	1.54	1.54
Space group	P3 ₁ 21	P3 ₁ 21	P3 ₁ 21	P3 ₁ 21
Unit cell parameters				
a/b/c (Å)	102.6/102.6/85.0	102.2/102.2/86.8	101.7/101.7/84.6	101.7/101.7/84.6
α/β/γ	90°/90°/120°	90°/90°/120°	90°/90°/120°	90°/90°/120°
Resolution (Å)	33.58-1.8	33.4-1.80	44.1-2.0	42.2-2.0
Total reflections	357,386	352,957	151,845	202,752
Unique reflections	48,371	47,522	34,293	34,559
Completeness (%)*	100 (100)	100 (100)	100 (100)	100 (100)
Redundancy*	7.4 (7.3)	7.4 (7.4)	4.4 (4.3)	5.9 (5.7)
Rmerge (%)*	7.7 (38)	10.6 (63)	6.6 (46)	7.6 (54)
<I/σ(I)*>	17.6 (4.9)	13.2 (3.3)	14.2 (3.0)	13.1 (2.5)
Refinement				
Total number of atoms	3,849	3,777	3,605	3,569
Rcryst (%)	18.1	16.8	17.6	18.8
Rfree (%)	21.6	21.2	22.1	22.8
RMSD from ideal				
Bond length (Å)	0.007	0.007	0.014	0.015
Bond angles (°)	1.08	1.07	1.48	1.51
Average B-values (Å ² and # of atoms)				
All atoms	(3,849) 24.4	(3,777) 26.0	(3,605) 26.7	(3,570) 31.8
Protein	(3,281) 22.8	(3,284) 24.4	(3,303) 25.9	(3,288) 31.0
NAD(H)	(44) 11.8	(44) 16.5	(44) 31.2	(44) 36.2
Water	(507) 35.5	(425) 38.0	(237) 34.0	(215) 39.4
Glycerin	(12) 53.1	(24) 50.8		
Inhibitor			(21) 48.2	(22) 55.5
Na	(1) 21.1	(1) 22.8	(1) 40.1	(1) 50.0
DMSO	(4) 41.5			
Ramachandran plot				
most favored / allowed/ disallowed (%)	97.3/2.7/0.0	97.8/2.2/0.0	97.3/2.7/0.0	97.3/2.7/0.0
PDB code		3zu3	3zu4	3zu5

The good data quality was reflected in the overall R_{merge} values of 7.7% and 10.6% for the wild-type and the variant protein in the binary complexes, respectively. The inhibitor complex crystals generated data with R_{merge} values of 6.6% and 7.6% for PT172 and PT173, respectively. The first structure (binary YpFabV T276S) was solved by molecular replacement in Phaser (McCoy et al., 2007) using the previously solved uncleaved T276S YpFabV structure as a search model. At a later stage, the refined structure of the cleaved YpFabV model served as search model. The models were improved in alternating cycles of manual model building in Coot (Emsley and Cowtan, 2004) and maximum likelihood refinement in phaser.refine (predominantly) (Adams et al., 2010) and Refmac5 (Pannu et al., 1998). The library files for the cofactor and inhibitors were generated with the help of the ProdrG server but had to be manually revised to ensure the correct ligand geometry. During model building two neighboring turns at the edge of the protein (A215-Q219 and K250-R267) showed two alternative conformations in the electron density map. Both orientations could be built into the electron density. This distortion of the protein fold most likely is caused by a crystal contact in proximity of a twofold axis of symmetry. Consequently, these symmetry related regions of the two protein monomers interact with each other (Figure 25).

Within this interface, the two acidic side chains E256 avoid each other due to repulsive Coulomb forces. Since there is only one molecule in the asymmetric unit of this crystal form, both conformations are represented in the electron density. The final models of the binary complexes containing all 399 residues of YpFabV and 5 remaining recombinant amino acids, which were not removed by the thrombin cleavage, plus NADH and solvent molecules, reached $R_{\text{cryst}}/R_{\text{free}}$ factors of 18.1/21.6% and 16.8/21.2% for the wild-type and T276S variant of YpFabV, respectively. The ternary complex crystal structures with PT172 and PT173 are characterized by $R_{\text{cryst}}/R_{\text{free}}$ factors of 17.6/22.1% and 18.8/22.8%, respectively.

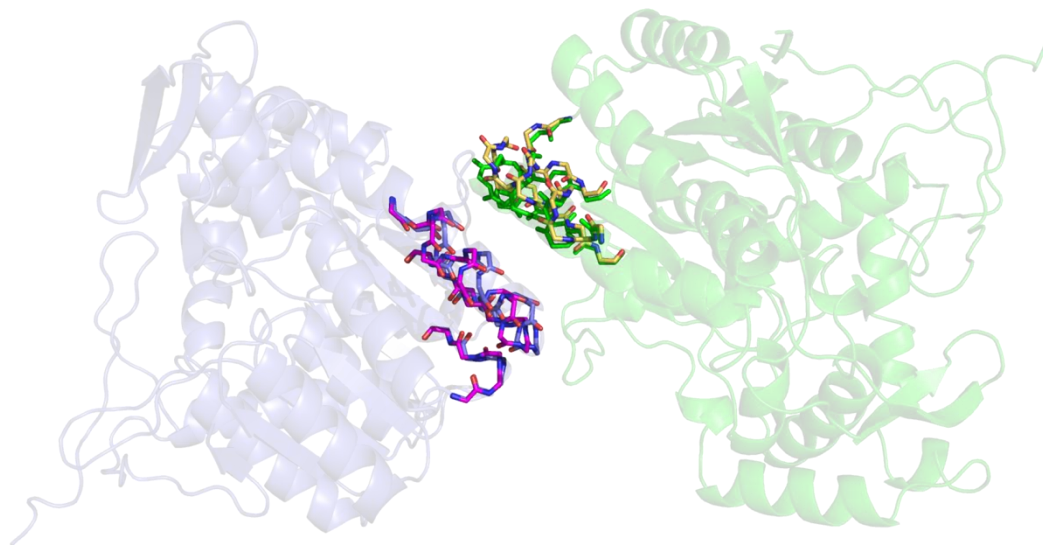
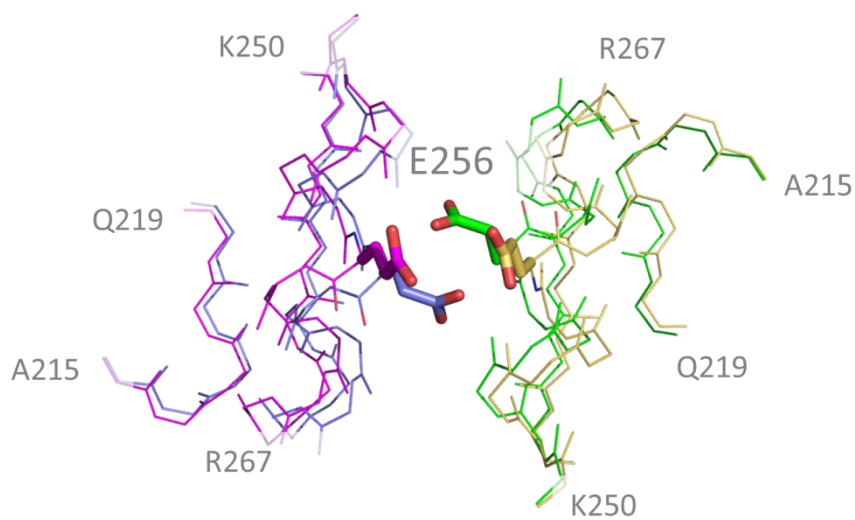
A**B**

Figure 25: Alternate conformations in the cleaved YpFabV structures

A) Two YpFabV molecules sharing a crystal contact with alternate conformations within regions A215 to Q219 and K250 to R267 (residues shown as sticks, only backbone) B) Detailed view of the alternate conformations (backbone only, shown as lines) with repulsive E256 side chain interactions (shown as sticks).

3.2.2.3 Validation

The models of the cleaved YpFabV structures were validated using the Molprobiy server (Chen et al., 2010). None of the structures had any outliers in bond lengths and angles. The RMSD values of the bond lengths were 0.007 Å, 0.007 Å, 0.014 Å and 0.015 Å and of the bond angles 1.08°, 1.07°, 1.48° and 1.51° for the binary structures of YpFabV wild-type and the T267S variant and the ternary complexes with PT172 and PT173, respectively. Only the ternary PT172 complex contains one C_β outlier and none of the structures showed an outlier in the Ramachandran plot (Ramachandran et al., 1963). The percentage of residues in the most favored area of the plot was 97.8% for the binary complex of the wild-type protein and 97.3% for the three remaining structures (Table 17).

To evaluate the accuracy of ligand fitting, the pose of the 2-pyridone inhibitors was examined in their refined 2F_o-F_c and OMIT 2F_o-F_c electron density maps at a σ -level of 1.0 (Figure 26). The OMIT maps were generated in phenix.refine by refinement including simulated annealing using the fully refined model without the bound inhibitor. The OMIT map clearly revealed the presence of ring substituents like the amide carbonyl group at the A-ring or the chlorine at the B-ring and even the hexyl group at the meta position of the A-ring was visible in its entire length, suggesting that the inhibitors had been placed adequately.

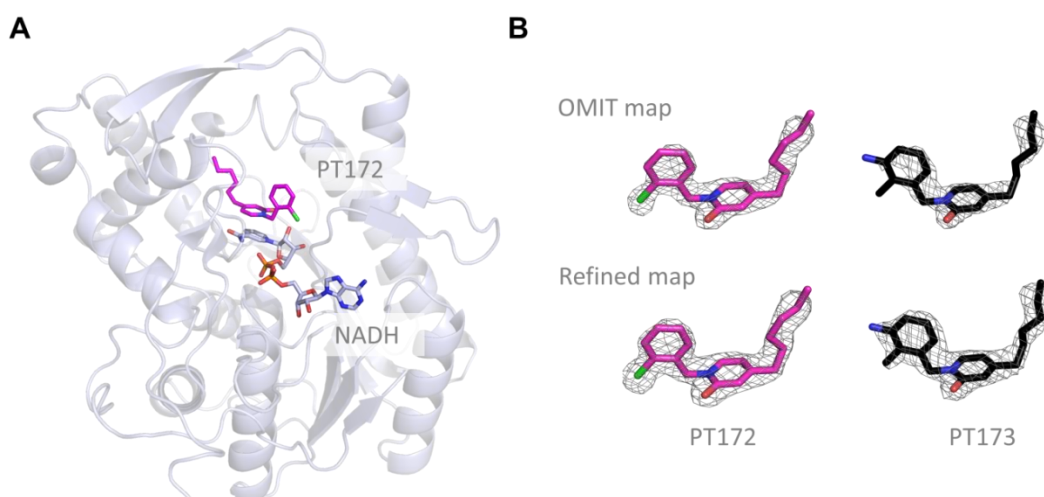


Figure 26: Evaluation of inhibitor fitting

A) Inhibitor PT172 modeled into the YpFabV T276S structure, B) Inhibitors PT172 and PT173 in their 2F_o-F_c map at a σ -level of 1.0, shown as OMIT map and in the refined state

3.3 Enoyl-ACP reductase FabV from *B. pseudomallei* (BpFabV)

3.3.1 Crystallization

The recombinant FabV from *B. pseudomallei* was expressed and purified analogously to YpFabV (cf. 3.1 and Supplemental Figure 57). Crystallization trials were carried out with the commercially available screens Hampton Crystal Screens I+II (Hampton Research), Hampton Index Screen (Hampton Research), Emerald Wizard Screens I+II (Emerald Biostructures), Nextal PEG Screen (Qiagen), Protein complex Screen (Qiagen), OptiMix Screens 3+4 (TOPAZ) and the self-generated Salt screen I and PEG pH 6.5 screen. The screening trials in sitting drop vapor diffusion setups were performed with BpFabV at various concentrations (5-50 mg/ml) and buffers (FabV protein buffer, ddH₂O, with different amounts of NaCl). The screens were performed for apo BpFabV but also with the addition of NADH or NAD⁺ and with the promising inhibitors PT404 and PT113. In contrast to YpFabV, BpFabV only crystallized very rarely in the screens and most of the crystals were not reproducible. Only three salt-based crystallization conditions yielded plate-like crystals - 3 M sodium formate with 100 mM imidazole pH 8.0, 2 M ammonium sulfate with 100 mM MES pH 6.0 and 1.7 M potassium/sodium tartrate (Figure 27).

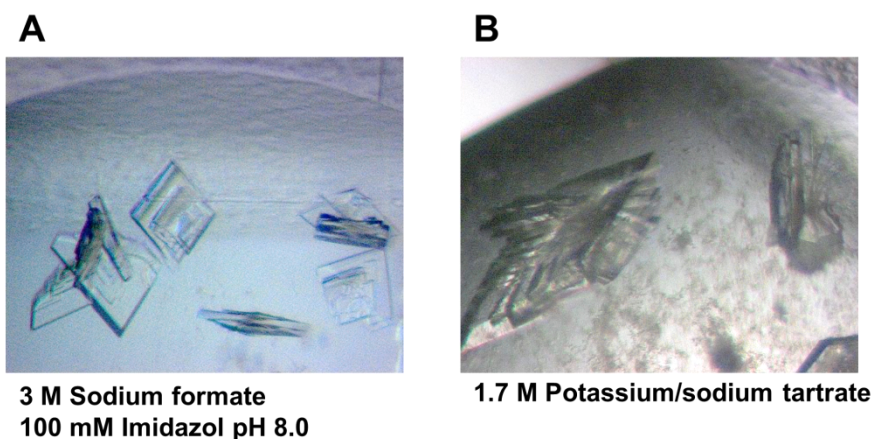


Figure 27: Crystallization conditions of apo BpFabV

Only the sodium formate condition was reproducible in hanging drop setups. The crystallization with sodium formate was successful for a broad range of pH values and buffers. Only at very acidic pH values (100 mM sodium acetate pH 4.6) salt instead of protein crystals were obtained. The crystals from this condition as well as the crystals

from the ammonium sulfate screen condition diffracted to a resolution of at least 2 Å. Although both crystal forms were grown in co-crystallization trials, the solved structures revealed that the protein crystallized only in its apo-form.

3.3.2 Data collection and Structure solution

For the x-ray diffraction experiments, the crystals were cryo-cooled in their mother liquor supplemented with up to 20% glycerol. The diffraction dataset of the crystal from the sodium tartrate condition could be collected at the in-house x-ray generator (MicroMax-007 HF, Rigaku) at a wavelength of 1.54 Å to a resolution of 1.85 Å (the dataset will be referred to as BpFabV1). The diffraction dataset of the crystal grown in the ammonium sulfate condition was collected at beamline MX14.1 at Bessy II at a wavelength of 0.918 Å and reached a resolution of 1.9 Å (the dataset will be referred to as dataset/crystal/structure BpFabV2). Both datasets were indexed and integrated in iMosflm (Battye et al., 2011) and scaled in Scala (Evans, 2006) (Table 18). Although both crystallization conditions included high salt concentrations, the two crystal forms are characterized by a different space group. The crystal BpFabV1 crystallized in space group $P12_11$ with unit cell dimensions of $a= 55.1$ Å, $b= 55.3$ Å and $c= 73.8$ Å and angles $\alpha=\gamma= 90^\circ$ and $\beta= 108.3^\circ$. Data quality was assessed using the Scala report files. At a resolution of 1.85 Å the dataset reached a completeness of 98.1 % with 7.4-fold redundancy and R_{merge} values of 5.3% and 15.9% for the entire resolution range and the highest resolution shell, respectively. In addition, the $I/\sigma I$ values of 26.2 and 10.6 for the overall dataset and the highest resolution shell were very good. The second crystal form BpFabV2 crystallized in space group $P2_12_12_1$ with unit cell parameters $a= 48.6$ Å, $b= 93.3$ Å and $c= 100.9$ Å and $\alpha=\beta=\gamma= 90^\circ$. The dataset was 100% complete and displayed a 3.7-fold redundancy. The R_{merge} was 4.8% and 18.7% and the $I/\sigma I$ 16.8 and 5.9 for the overall dataset and the highest resolution shell, respectively. Both structures could be solved by molecular replacement with using the program Phaser (McCoy et al., 2007). In the case of BpFabV1 the structure of the cleaved YpFabV structure served as a search model. The overall structure of YpFabV fit very well into the BpFabV1 density. The differing residues were changed manually in Coot (Emsley and Cowtan, 2004) to meet the BpFabV sequence and the entire model improved step by step with intermediary cycles of maximum likelihood refinement, which was performed predominantly in phenix.refine (Adams et al., 2010).

Results

Table 18: Data collection and refinement statistics of the BpFabV structures

	bpmFabV apo 1	bpmFabV apo 2 (MES)
Data collection		
Wavelength (Å)	1.54	0.918
Space group	P12 ₁ 1	P2 ₁ 2 ₁ 2 ₁
Unit cell parameters		
a/b/c (Å)	55.1/55.3/73.8	48.6/93.3/100.9
α/β/γ	90°/108.32°/90°	90°/90°/90°
Resolution (Å)	36.73-1.85	35.01-1.90
Total reflections	238,235	135,326
Unique reflections	32,297	36,997
Completeness (%)*	98.1 (96.2)	100 (100)
Redundancy*	7.4 (7.2)	3.7 (3.6)
Rmerge (%)*	5.3 (15.9)	4.8 (18.7)
<I/σ(I)*>	26.2 (10.6)	16.8 (5.9)
Refinement		
Total number of atoms	3,637	3,544
Rcryst (%)	14.8	17.5
Rfree (%)	17.3	21.0
RMSD from ideal		
Bond length (Å)	0.006	0.006
Bond angles (°)	1.049	1.042
Average B-values (Å ² and # of atoms)		
All atoms	(3,637) 15.7	(3,544) 27.4
Protein	(3,024) 13.5	(3,084) 25.9
Water	(589) 26.5	(398) 34.7
Glycerin	(6) 47.2	(18) 44.9
MES		(24) 42.7
SO ₄		(20) 82.6
Ramachandran plot		
Most favored/allowed/disallowed (%)	97.3/2.5/0.2	97.3/2.5/0.2

The final model included the complete BpFabV sequence and three recombinant residues. Apart from solvent molecules no ligand was bound to the protein. The refinement converged at R_{cryst} and R_{free} factors of 14.8% and 17.3%, respectively. The structure of the second dataset BpFabV2 could subsequently be solved using the refined structure of BpFabV1 as search model for the molecular replacement approach. The model was manually improved and refined as described before. The crystal of BpFabV2 was obtained in a co-crystallization trial with PT404 and NAD^+ . During model building an electron density in the active site was initially interpreted as PT404, which would have been unusual because diphenyl ether inhibitors are known to bind to the protein in a ternary complex together with the cofactor. However, the inhibitor could not be fit into the additional electron density, which could finally be explained by the presence of a MES buffer molecule at this position. In Figure 28 the MES molecule is depicted in its $2F_o-F_c$ OMIT map at a contour level of 1.0σ . The binding of a MES molecule in the active site might interfere with successful co-crystallization of ligands in the binding pocket for this crystallization condition. The final model contained the complete BpFabV sequence including seven recombinant residues and solvent molecules and R_{cryst} and R_{free} factors of 17.5% and 21.0%, respectively.

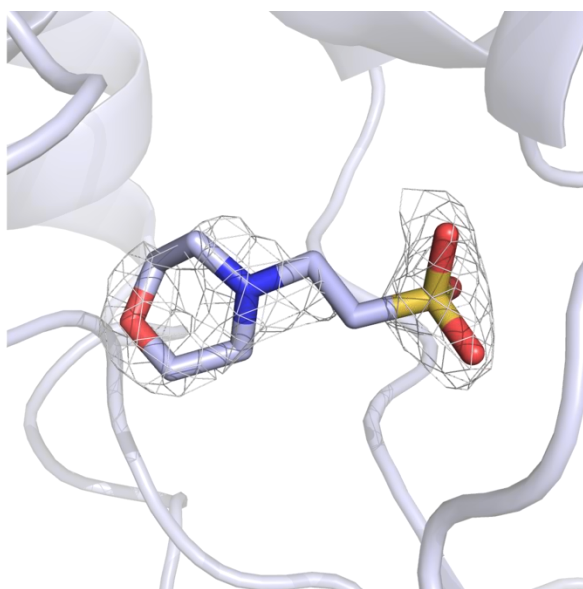


Figure 28: MES molecule in the active site of BpFabV2

The electron density is shown as a $2F_o-F_c$ - OMIT map with a contour level of 1σ .

3.3.3 Validations of the two BpFabV apo structures

The quality of the two different BpFabV apo structures was evaluated with the help of the Molprobiy server (Chen et al., 2010). The RMSD values of the bond lengths and angles were 0.006 Å/0.006 Å and 1.049°/1.042° for the structures BpFabV1 and BpFabV2, respectively. These values are quite low, which is due to the tight restraints used by the phenix.refine program. The clash score of both structures with around 7 is very low. The structures show no C_{β} outliers.

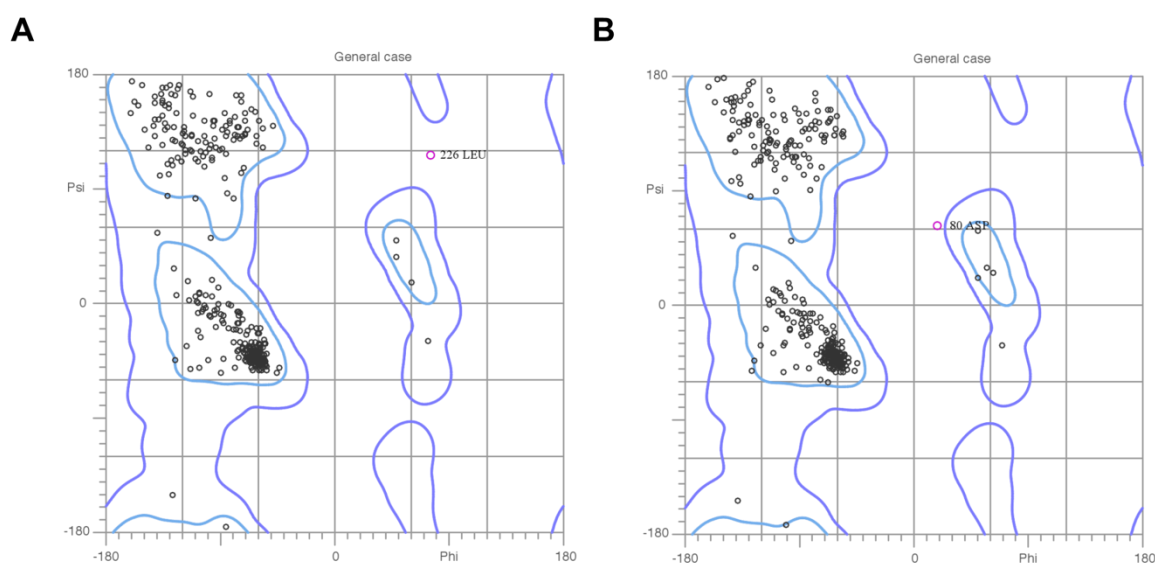


Figure 29: Ramachandran plot for (A) BpFabV1 and (B) BpFabV2

The most favored region is framed in cyan and the accepted region in blue.

There was one outlier in the Ramachandran statistics in each structure. In BpFabV1 the outlier was L226 and in BpFabV2 it was Asp80, the latter lies near the border to the accepted area in the Ramachandran plot (Figure 29). In both cases 97.3% of the residues are within the most favored region of the plot. There are three unusual rotamers in BpFabV1 and one in BpFabV2. Two out of three rotamer outliers in BpFabV1, Y225 and Q229, lie next to the Ramachandran outlier L226. This accumulation of geometrical outliers indicates a problem in the structure at this region. First it was evaluated if the model is actually supported by the electron density, which was the case. In the comparison with the second BpFabV structure differences in the orientation of this loop (Y225-T321) could be detected (Figure R19A). The distortion of the loop could be explained by a crystal contact at the turn. Residue Q320 of the neighboring molecule in

the crystal would clash with Q229 and therefore pushes this residue back, which leads to the distortion of the whole loop (Figure 30 B+C). Since the loop is part of the binding pocket of FabV and contains the active site residue Y225, one of the rotamer outliers, the structure BpFabV1 was not used for structural analysis and comparisons with further FabV structures were performed with BpFabV2 instead.

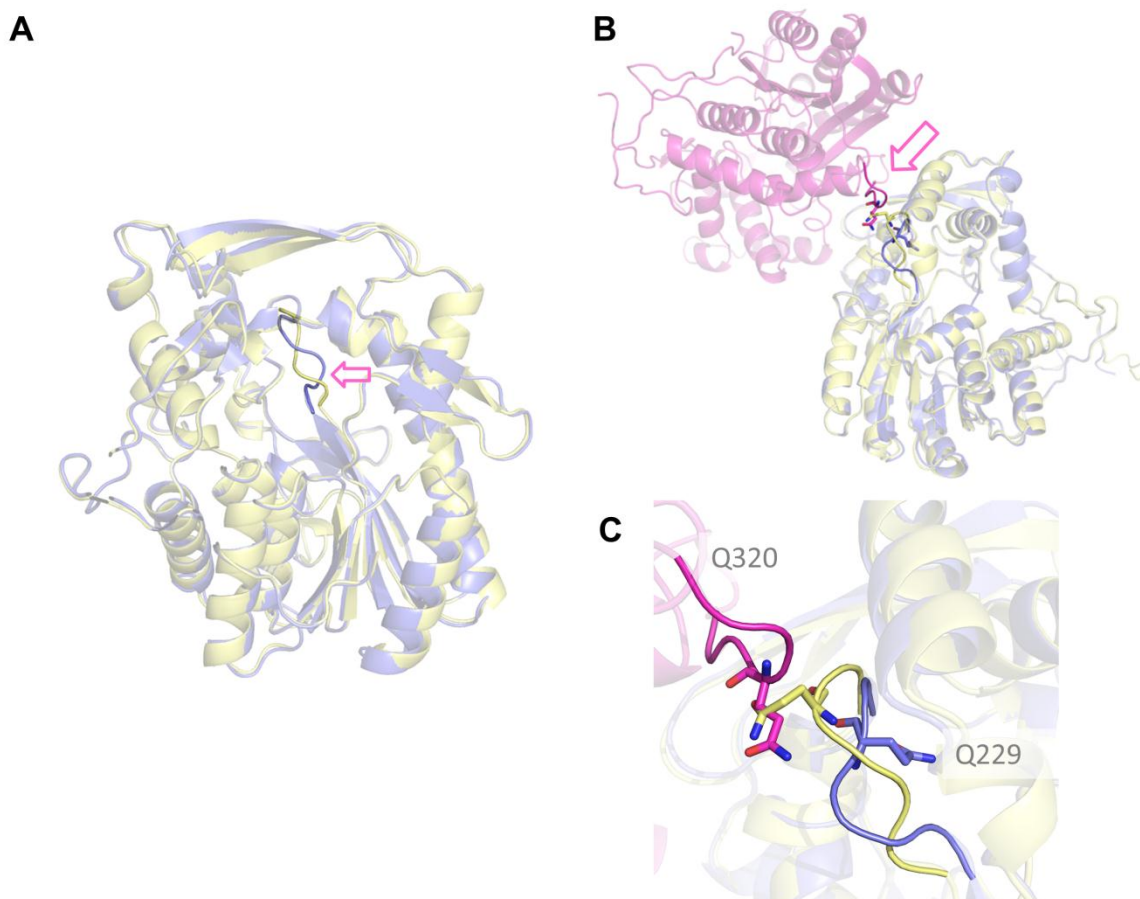


Figure 30: Loop distortion in BpFabV1 by crystal contact

A) Overall structures of BpFabV1 (blue) and BpFabV2 (yellow), the distortion is marked by an arrow. B) Crystal contact between BpFabV1 (blue) and a neighboring molecule in the crystal (magenta), with BpFabV2 superimposed onto BpFabV1. C) Zoom into the clashing region.

3.4 Enoyl-ACP reductase FabI from *B. pseudomallei* (BpFabI)

To develop a new antibacterial against *B. pseudomallei* targeting the enoyl-ACP reduction step of FAS-II both enoyl-ACP reductases, i.e. FabV and FabI, of this organism have to be inhibited. Therefore also BpFabI was expressed and purified for co-crystallization attempts with new inhibitors.

3.4.1 Expression

The gene for BpFabI was cloned and ligated into the expression vector (pET23b) by Nina Liu (Liu et al., 2011). For gene amplification during cloning she used the *B. mallei* strain ATCC 23344. This was possible since the sequences of FabI from *B. mallei* and *B. pseudomallei* are 100% identical. The vector contains the *bpfabI* gene with a C-terminal hexahistidine tag under the control of a T7 promoter and an additional ampicillin resistance gene. To test the expression of BpFabI, the pET23b construct was transformed into BL21 (DE3) and BL21 (DE3) pLysS *E. coli* cells. The test expression at small scale was performed at 25 °C with an induction of expression at an OD₆₀₀ of 0.6 with 1mM IPTG. Samples after 2, 5 and 20 hours were analyzed via SDS-PAGE (Figure 31).

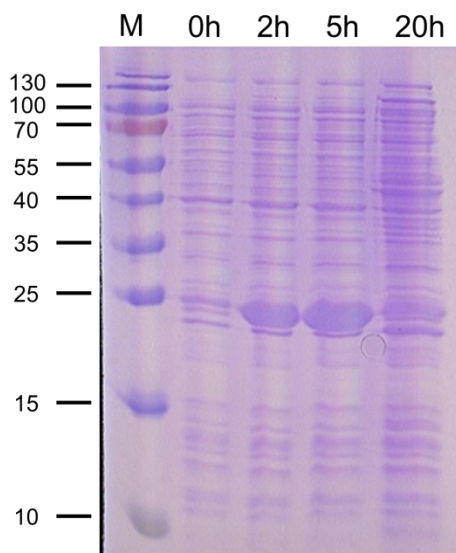


Figure 31: SDS-PAGE of cell lysate from the expression test of BpFabI in pLysS *E. coli* cells at 25 °C

The recombinant BpFabI protein has a size of 29 kDa. At the height of the 25 kDa marker band a very prominent band appeared 2 hours after induction which is interpreted as the FabI construct. The highest expression was already observed after 5h, which decreased in the 20 hours sample. There was no obvious difference between BL21 (DE3) and BL21 (DE3) pLysS. Therefore the high scale expression was performed in BL21 (DE3) at 25 °C for 5 hours. Later on also high scale expression at 15 °C for 20 hours was successful.

3.4.2 Buffer optimization using the Thermofluor analysis

The first small scale purification (cf. 2.2.2 and 3.4.3) was completed in a preliminary gel filtration buffer (30 mM PIPES pH 6.8, 150 mM NaCl and 1 mM EDTA), which was used previously by our collaborators for BpFabI. The protein was soluble in this buffer. However, since the protein should be very stable and homogenous for crystallization in its buffer, a Thermofluor analysis (2.2.3.2) was conducted with the Thermofluor buffer screen. In the buffer screen no buffer led to a higher melting temperature than the reference buffer (preliminary gel filtration buffer) with a melting temperature of 52 °C.

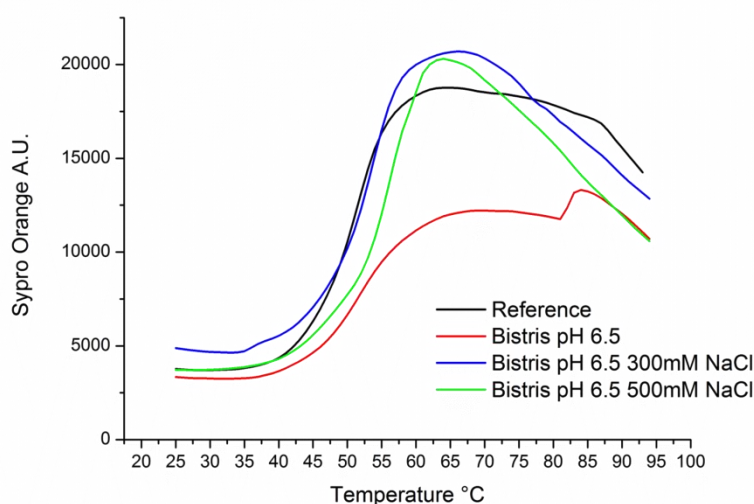


Figure 32: Thermofluor analysis on BpFabI

To exclude the possibility that the thermal stability of BpFabI in the reference buffer was caused by the higher salt content (150 mM NaCl), further screens were performed with the addition of 300 mM and 500 mM salt. The melting temperatures increased with higher salt concentrations. The highest melting temperature (56 °C) was observed in 100

mM Bistris pH 6.5 and 500 mM NaCl. The effect of the increased salt concentration is nicely illustrated in the melting curves of BpFabI in Bistris pH 6.5 (Figure 32). The buffer alone with a melting temperature of 51 °C shows no improvement compared to the reference buffer. Upon addition of 300 mM and 500 mM NaCl, the melting temperature rises to 53 °C and 56 °C, respectively. Applying these results, the gel filtration buffer was changed to 20 mM Bistris pH 6.5, 500 mM NaCl and 1 mM EDTA.

3.4.3 Purification

As previously described for FabV also BpFabI was purified with a two-step protocol using chromatography techniques. The C-terminally hexahistidine-tagged protein was extracted from the cell lysate in a nickel affinity chromatography step followed by a polishing size-exclusion chromatography step.

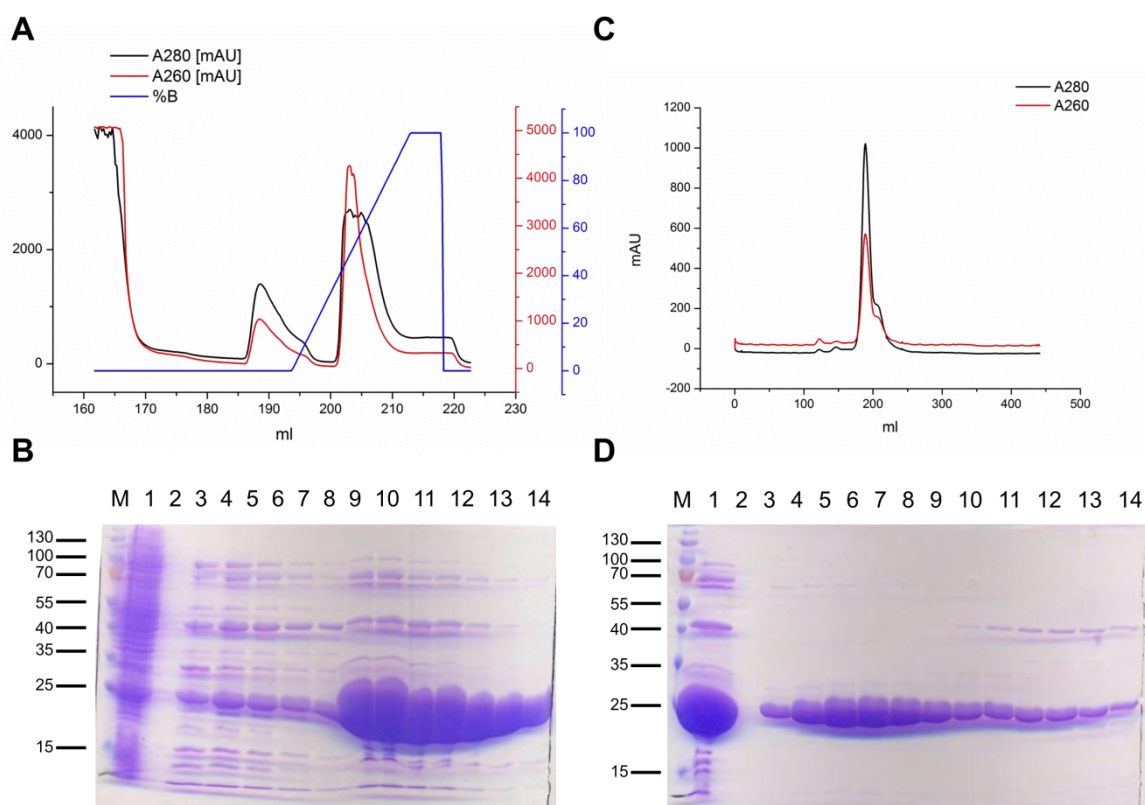


Figure 33: Purification of BpFabI

A) Chromatogram of a Histrap purification with gradient elution, absorption at 280nm (black) and 260nm (red), % Elution buffer (blue). B) SDS-PAGE of a Histrap purification: (1) Load, (2) Flowthrough, (3-7) Extra wash, (8-14) Elution peak. C) Chromatogram of a size exclusion chromatography, absorption at 280nm (black) and 260nm (red). D) SDS PAGE of a size exclusion chromatography: (1) Load-(3-9) main peak, (10-14) shoulder of main peak.

The affinity chromatography was prevalently carried out with HisTrap FF crude columns (GE healthcare) at different ÄKTA chromatography systems (Figure 33A). The cleared cell lysate was loaded on the equilibrated column and unbound sample washed out by 20 column volumes of binding buffer. A second washing step with slightly elevated imidazole concentrations was utilized to remove unspecifically binding contaminants, either with a separate washing buffer with 60 mM imidazole and 1 M NaCl (example in Figure 33) or a gradient up to 6% elution buffer. The elution of the bound protein was accomplished either in a gradient elution to 100% elution buffer (500 mM imidazole) (example in Figure 33) or a step elution with 50% elution buffer. The step elution had the advantage that the peak was concentrated in a smaller volume so that further concentration of the sample for the following size-exclusion chromatography was not necessary. The SDS-PAGE of samples from each step of the purification showed that BpFabI was highly concentrated in the elution peak with only few contaminants in the fractions (Figure 33B). The following size-exclusion chromatography was carried out using a HiLoad Superdex 200 26/60 gel filtration column with a maximal sample volume of 10 ml (2.2.2.4). The elution profile exhibited one major peak with a shoulder at higher elution volumes (Figure 33C+D). Analysis of the peak fractions in SDS-PAGE revealed that the main peak consisted of BpFabI of high purity (99%) represented by a thick band at the height of the 25 kDa marker band. However, the shoulder contained an impurity with an estimated molecular mass of about 40 kDa. Hence, the fractions of the shoulder were excluded from the pure protein sample. The pure fractions were concentrated to up to 30 mg/ml, flash-frozen in liquid nitrogen and stored at -80 °C.

3.4.4 Crystallization

In the PDB database an apo structure of BpFabI had already been deposited (PDB code 3EK2), which was crystallized in 10% PEG 6000 and 100 mM HEPES pH 7.0. In a first crystallization attempt it was tried to reproduce this crystallization condition. However, this approach was not successful. Therefore small-scale sitting drop vapor diffusion screens were performed using BpFabI at a concentration of 12 mg/ml with the addition of 2 mM NAD⁺ with the Hampton Crystal Screens I+II (Hampton Research) and Wizard screens I+II (Emerald Biostructures). Due to various hits in PEG-based crystallization conditions also the Screens Hampton Index Screen (Hampton Research), Nextal PEGs

(Qiagen) and OptiMix Screen 4 (TOPAZ) as well as the self designed PEG pH 6.5 Screen were conducted and yielded further crystal hits in PEG conditions. During the optimization attempts in hanging drop vapor diffusion setups mainly two different PEG conditions generated reproducibly single, rod-shaped crystals of suitable size. The first condition contained PEG 1000 and PEG 8000, each at concentrations of 6-12%. The second one includes a PEG with small molecular weight (PEG 300, PEG 400 or PEG 550 MME) at concentrations of 20-30% with a buffer at pH 6.5 (MES or Bistris). Crystals of both crystal forms diffracted better than 2 Å in x-ray diffraction experiments. The reproducibility of the two crystal forms was dependent on the protein batch. Initial electron density maps derived from the first datasets of BpFabI revealed the presence of weak traces of NAD⁺. Hence, crystallization was repeated with apo BpFabI to obtain a clean apo BpFabI dataset.

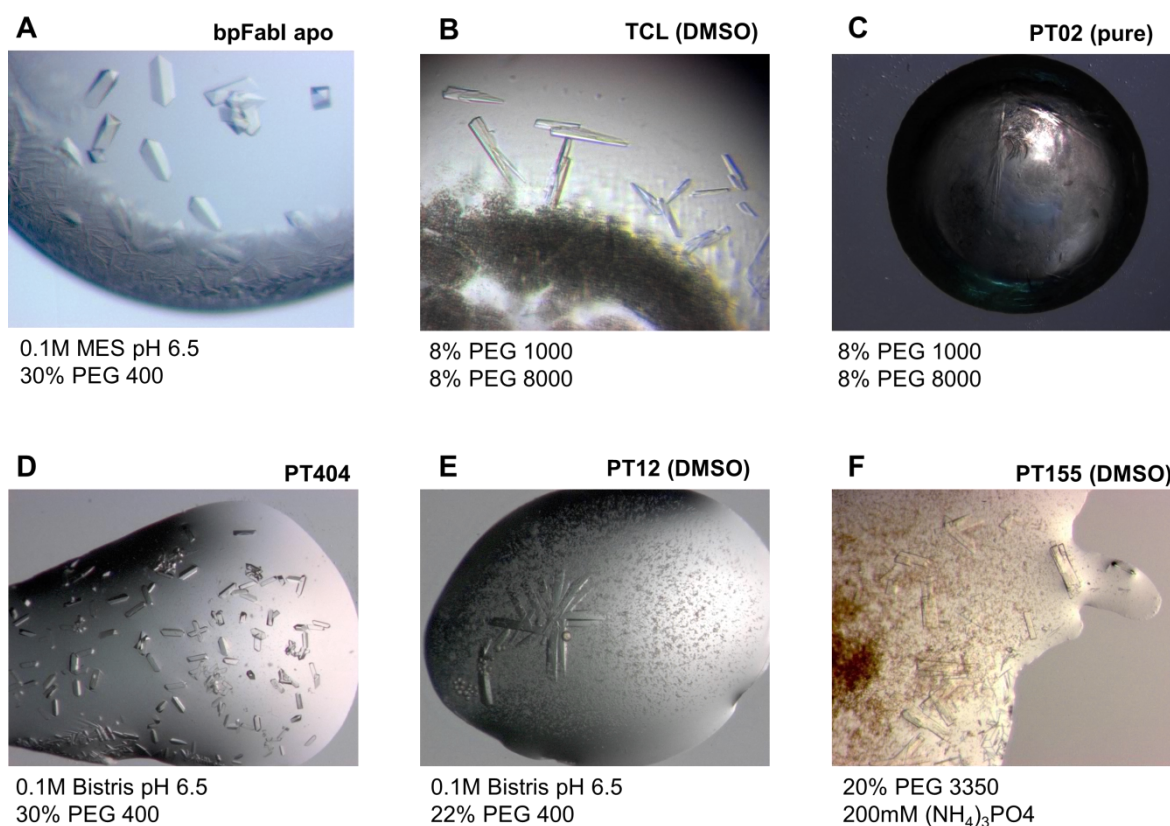


Figure 34: Crystallization condition of BpFabI in its apo form (A) and in the ternary complexes with the cofactor NAD⁺ and the inhibitor triclosan (TCL) (B), PT02 (C), PT404 (D), PT12 (E) or PT155 (F).

The occupancy for NAD⁺ or NADH in structures resulting from crystallization trials of the binary complexes remained low and did not allow successful model building.

Since a set of potential crystallization conditions was established, the actual goal, the co-crystallization with inhibitors (triclosan, PT02, PT12, PT155 and PT404) was approached. For co-crystallization attempts BpFabI (10-30 mg/ml) was incubated for one hour with a tenfold molar excess of NAD⁺ and either pure inhibitor (5 mg/ml, for triclosan and PT02) or inhibitor dissolved in DMSO (100 mg/ml) in a tenfold molar excess (for PT12, PT155 and PT404). Crystallization was achieved with the established crystallization conditions, with the exception of the co-crystallization with PT155. Here crystals were obtained in a small-scale crystallization screen with the Nextal PEG screen (Qiagen) and provided the crystals for the diffraction experiment (20% PEG 3350 and 200 mM (NH₄)₂HPO₄) (Figure 34).

3.4.5 Data collection and Structure solution

Prior to data collection, the crystals were soaked in cryo solutions containing elevated PEG concentrations and 10-25% of the cryo-protectant glycerol and subsequently cryo-cooled in liquid nitrogen.

3.4.5.1 MR of BpFabI_{apo}

The diffraction dataset of apo BpFabI was collected at Beamline ID29 of the ESRF at a wavelength of 0.918 Å and reached a resolution of 1.65 Å (Table 19). The diffraction images were indexed and integrated in XDS (Kabsch, 2010) and scaled in Scala (Evans, 2006). The analysis revealed that BpFabI crystallized in space group I222 with unit cell parameters $a = 74.7$ Å, $b = 75.2$ Å, $c = 85.7$ Å and $\alpha = \beta = \gamma = 90^\circ$ including one FabI chain in the asymmetric unit. The dataset reached a completeness of 96.6% with a 4.4-fold redundancy. The R_{merge} was 6.1% and 70.2% and the $I/\sigma I$ 13.1 and 2.2 for the overall dataset and the highest resolution shell, respectively. Phasing was achieved by molecular replacement in Phaser (CCP4, 1994; McCoy et al., 2007) with the published BpFabI structure (PDB code 3EK2) as the search model. The search model contained residues M1-M258 of the BpFabI sequence (the complete sequence would contain 263 residues) with a gap of nine residues between residue L193 and F203, representing the flexible substrate

Results

binding loop. By manual model building in Coot (Emsley and Cowtan, 2004) with intermediary cycles of maximum likelihood refinement in phenix.refine (Adams et al., 2010) the model was improved and adapted to the electron density map.

Table 19: Data collection and refinement statistics of the BpFabI apo structure and ternary inhibitor complexes

	BpFabI apo	BpFabI+TCL	BpFabI+PT02	BpFabI+PT404	BpFabI+PT12	BpFabI+PT155
Data collection						
Wavelength (Å)	0.918	0.918	0.918	0.918	1.54	1.54
Space group	I222	P1	I222	I222	I222	I222
Unit cell parameters						
a/b/c (Å)	74.7/75.2/85.7	70.4/99.9/139.9	69.6/112.0/262.8	74.6/75.1/86.4	74.6/75.9/89.6	74.3/76.0/89.4
$\alpha/\beta/\gamma$	90°/90°/90°	82.87°/89.20°/78.13°	90°/90°/90°	90°/90°/90°	90°/90°/90°	90°/90°/90°
Resolution (Å)	37.62 - 1.65	69.38 - 2.6	43.98 - 2.6	43.19 - 1.8	29.0 - 1.6	38.0 - 1.8
Total reflections	125,427	417,582	197,779	160,232	150,403	108,611
Unique reflections	28,203	112,071	32,230	22,817	32,015	22,291
Completeness (%)*	96.6 (98.3)	98.5 (97.9)	100 (100)	99.9 (99.9)	98.9 (99.8)	100 (100)
Redundancy*	4.4 (4.3)	3.7 (3.8)	6.1 (6.2)	7.0 (6.7)	4.7 (4.3)	4.9 (4.5)
Rmerge (%)*	6.1 (70.2)	10.6 (52.5)	21 (117)	7,2 (63.7)	3.7 (14.7)	6.9 (26.1)
Rpim	3.0 (35.6)	6.4 (31.3)	9.6 (52)	3,0 (26,5)	1.9 (7.9)	3.5 (13.7)
$\langle I/\sigma(I) \rangle$	13.1 (2.2)	8.9 (3.2)	9.0 (2.5)	15.4 (3.1)	21.8 (7.5)	14.6 (5.0)
Refinement						
Total number of atoms	2,163	31,921	6,046	2,139	2,302	2,354
R _{cryst} (%)	15.9	19.4	22.1	17.5	13.2	13.7
R _{free} (%)	18.6	25.3	28.0	20.9	17.3	16.2
RMSD from ideal						
Bond length (Å)	0.006	0.008	0.008	0.006	0.021	0.007
Bond angles (°)	1.042	1.070	1.135	1.147	1.890	1.130
Average B-values (Å² and # of atoms)						
All atoms	(2,163) 26.4	(31,945) 66.3	(6,046) 84.1	(2,139) 36.2	(2,302) 19.9	(2,367) 13.8
Protein	(1,936) 25.1	(30,400) 67.6	(5,745) 85.8	(1,915) 35.7	(1,917) 17.7	(1,957) 11.8
NAD(H)		(704) 53.4	(132) 60.3	(44) 38.0	(44) 13.9	(44) 11.0
Water	(227) 37.3	(561) 36.9	(118) 41.5	(153) 39.5	(318) 34.1	(343) 25.6
Glycerin				(6) 56.8		
Inhibitor		(272) 558.0	(51) 63.9	(21) 42.3	(23) 20.3	(23) 11.2
Ramachandran plot						
Most favored /allowed/disallowed (%)	98.1/1.9/0.0	97.3/2.7/0.0	95.8/4.2/0.0	97.3/2.7/0.0	97.6/2.4/0.0	97.3/2.7/0.0

During model building the gap of the search model could be closed since there was convincing electron density for the substrate binding loop present. The reason for the stabilization of this, in other apo FabI structures usually flexible, loop, is most likely due to

a crystal contact. (Figure 35) The final model of the apo structure includes 255 residues and 227 water molecules. The first and the seven last amino acids of the BpFabI sequence were not represented in the electron density map. The model reached R_{cryst} and R_{free} factors of 15.9% and 18.6%, respectively.

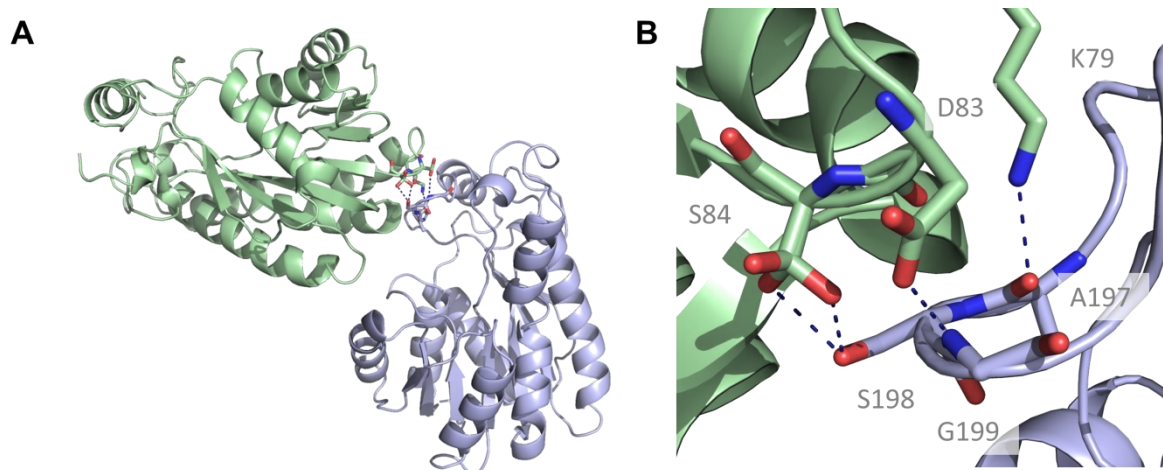


Figure 35: Stabilization of the substrate-binding loop by crystal contacts

A) Overview of the crystal contacts stabilizing the substrate-binding loop. B) Detailed view of the hydrogen bond interactions (dashed line) at the crystal contact

3.4.5.2 MR of ternary inhibitor complexes of BpFabI

The first two ternary inhibitor complexes containing BpFabI with triclosan or PT02 and NAD^+ had been co-crystallized with the PEG 1000/PEG 8000 condition. The diffraction datasets were collected at the beamlines ID21 and ID23 at the ESRF at a wavelength of 0.918 Å and to a resolution of 2.6 Å (Table 19). The datasets were indexed, integrated and scaled using XDS (Kabsch, 2010) or iMosflm (Battye et al., 2011) and Scala (Evans, 2006). Analysis of the data showed that the original space group of the apo FabI seemed to be disrupted due to the interaction with the inhibitor. The triclosan complex could only be indexed in space group P1 with unit cell dimensions of $a = 70.4 \text{ \AA}$, $b = 99.9 \text{ \AA}$, $c = 139.9 \text{ \AA}$ and $\alpha = 82.9^\circ$, $\beta = 89.2^\circ$ and $\gamma = 78.1^\circ$ and a Matthews coefficient of $2.21 \text{ \AA}^3/\text{Da}$ data is characterized by a completeness of 98.5% with a 3.7-fold redundancy and showed an R_{merge} of 10.6% and 52.5% as well as $I/\sigma I$ values of 8.9 and 3.2 for the entire dataset and the highest resolution shell, respectively. The PT02 complex crystallized in space group I222 as observed for the apo BpFabI structure but had differing unit cell constants with $a = 69.4 \text{ \AA}$, $b = 112.0 \text{ \AA}$ and $c = 262.8 \text{ \AA}$ and three BpFabI chains in the asymmetric unit. The

dataset was 100% complete with 6.1-fold redundancy and an R_{merge} of 21% and 117%. These R_{merge} values are extraordinarily high. Since the R_{merge} value increases with higher redundancy, the R_{pim} value was used in this case to determine the high resolution edge, since this measure for data quality is independent of the multiplicity of the data. The R_{pim} of the dataset was 9.6% and 52% for the overall dataset and the highest resolution shell, respectively. Another indication for the data quality at a certain resolution is the I/σ , which was still 2.5 in the highest resolution shell.

The inhibitor complexes containing PT12 or PT404 had been crystallized with the second established crystallization condition using PEG 400 as a precipitant and the 4-pyridone inhibitor PT155 was co-crystallized with a new PEG condition (20% PEG 3350 and 200 mM $(\text{NH}_4)_2\text{HPO}_4$). All three crystals diffracted much better than the co-crystals obtained with triclosan and PT02. The datasets were collected at beamline MX14.1 at Bessy II (PT404) at a wavelength of 0.918 Å to a resolution of 1.8 Å and at the in-house x-ray generator (MicroMax-007 HF, Rigaku) at a wavelength of 1.54 Å to a maximal resolution of 1.6 Å (PT12) and 1.8 Å (PT155). Indexing and integration was conducted in iMosflm (Battye et al., 2011) and Scaling in Scala (Evans, 2006). These ternary inhibitor complexes crystallized in the same space group, I222, as apo FabI and also the unit cell parameter were in the same range (cf. data statistics Table 19). The datasets exhibited completeness of 98.9-100% with an at least 4.7-fold redundancy. The R_{merge} for the complete dataset and the highest resolution shell was 7.2%/63.7%, 3.7%/14.7% and 6.9%/26.1% for the PT404, PT12 and PT155 dataset, respectively. The average I/σ value in the outer shell was greater than 3 in all three datasets.

The structures were solved by molecular replacement in Phaser (McCoy et al., 2007) using either the refined apo BpFabI structure or an already solved and refined ternary complex structure as a search model. The structures were improved in alternating cycles of manual model building in Coot (Emsley and Cowtan, 2004) and maximum likelihood refinement in phaser.refine (predominantly) (Adams et al., 2010) and Refmac5 (Pannu et al., 1998). NCS restraints during refinement proved to be very beneficial for the structures with several protein chains in the asymmetric unit such as the PT02 complex and especially for the triclosan structure with 16 BpFabI chains. The ligands were fitted into the electron density

and refined with the help of library files which were created by the PRODRG server (Schuttelkopf and van Aalten, 2004).

The final complex structures contained 255-257 residues of the BpFabi sequence (cf. apo BpFabi) the cofactor NAD⁺, the respective inhibitor and solvent molecules such as water or glycerol. The refinement of the complex structures including triclosan, PT02, PT404, PT12 and PT155 reached $R_{\text{cryst}}/R_{\text{free}}$ values of 19.4%/25.3%, 22.1%/28.0%, 17.5%/20.9%, 13.2%/17.3 and 13.7%/16.3%, respectively.

3.4.6 Validation of the BpFabi structures

The quality of the refined structures was evaluated utilizing the Molprobit server, which analyses the protein geometry and potential clashes in the structure.

3.4.6.1 BpFabiapo

The high resolution of the BpFabi apo structure is also reflected in very good quality markers. The RMSD values of bond lengths and angles are 0.006 Å and 1.042°, respectively. There is no outlier in the rotamers, the C_β deviation or the Ramachandran plot. 98.0% of the residues are in the most favored region of the Ramachandran plot. The Molprobit clash score, describing the number of serious steric overlaps (> 0.4 Å) per 1000 atoms, is only 4.2.

3.4.6.2 Ternary complexes of BpFabi with Inhibitors

Similarly, the quality of the ternary inhibitor complexes is highly dependent on the respective resolution of the structure. The RMSD values for bond lengths and angles are all in an acceptable range and vary from 0.006 Å to 0.021 Å and from 1.070° to 1.890°, respectively. There is only one residue with a C_β deviation greater than 0.25 Å and no Ramachandran outlier. The fraction of residues in the most favored part of the Ramachandran plot for the ternary complex with triclosan, PT02, PT404, PT12 and PT155 were 97.3%, 95.8%, 97.3%, 97.6% and 97.3%, respectively. The clash score varied from 3.4 (PT12) to 16.7 (PT02). For these geometric quality markers the structures containing triclosan and PT02 which were obtained at a lower resolution of only 2.6 Å benefited

from the NCS refinement in phenix.refine. The complex structure with PT02 showed three rotamer outliers whereas the triclosan structure contained two unusual rotamers.

The quality of ligand fitting of the cofactor and the inhibitors was evaluated with the help of OMIT maps (Figure 36). The OMIT maps were generated in a refinement cycle of the fully refined structure in phenix.refine, which included a simulated annealing step. In the coordinates for this refinement, the ligand was deleted. In Figure 36 the ligands are depicted in their $2F_o - F_c$ OMIT map at a σ -level of 1.0. All ligands were adequately represented in the OMIT maps.

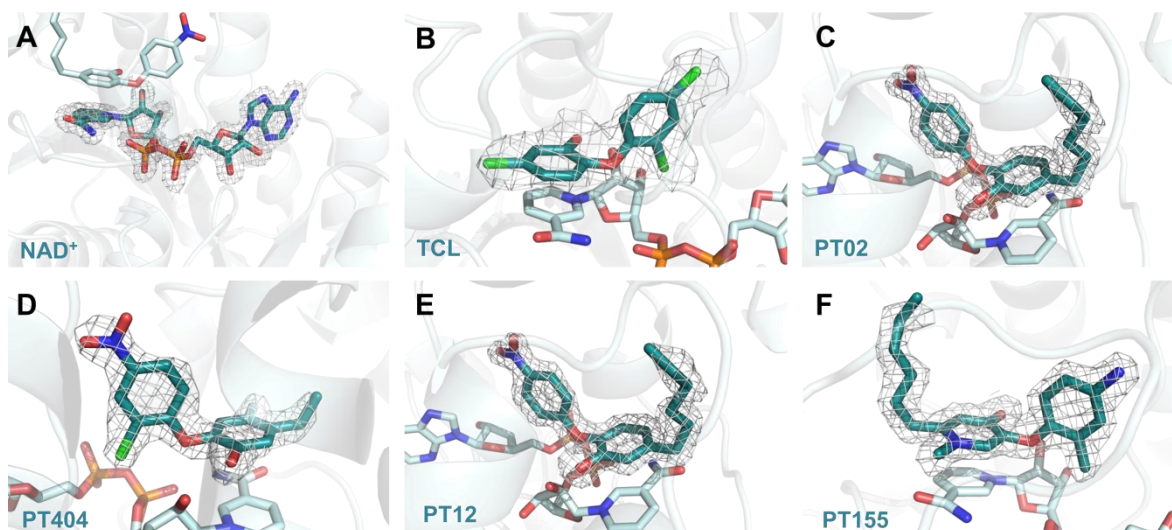


Figure 36: Validation of ligand fitting.

The ligands NAD^+ (from the PT12 complex structure) (A), triclosan (TCL) (B), PT02 (C), PT404 (D), PT12 and PT155 (F) are shown in their electron density map ($2F_o - F_c$ OMIT map) at a contour level of 1σ .

4. Discussion

4.1 Structural characterization of FabV as potential drug target

The enoyl-ACP reductase FabV might be a promising target for drug design approaches against Gram-negative pathogens such as *Y. pestis* or *B. pseudomallei* carrying this isoenzyme. In this study crystal structures of the recently discovered FabV could be solved in various states. The structure of FabV from *B. pseudomallei* (BpFabV) was determined in its apo form, whereas structures of the T276S variant and the wild type of FabV from *Y. pestis* (YpFabV) contained the cofactor NADH in a binary complex. Furthermore the structure of the T276S variant of YpFabV could also be obtained with its cofactor and a 2-pyridone inhibitor (PT172 and PT173) bound in a ternary complex. The structural information could be used to characterize the idiosyncratic features of FabV in the context of the SDR superfamily and explore its potential as drug target.

4.1.1 Overall structure (apo -binary - ternary)

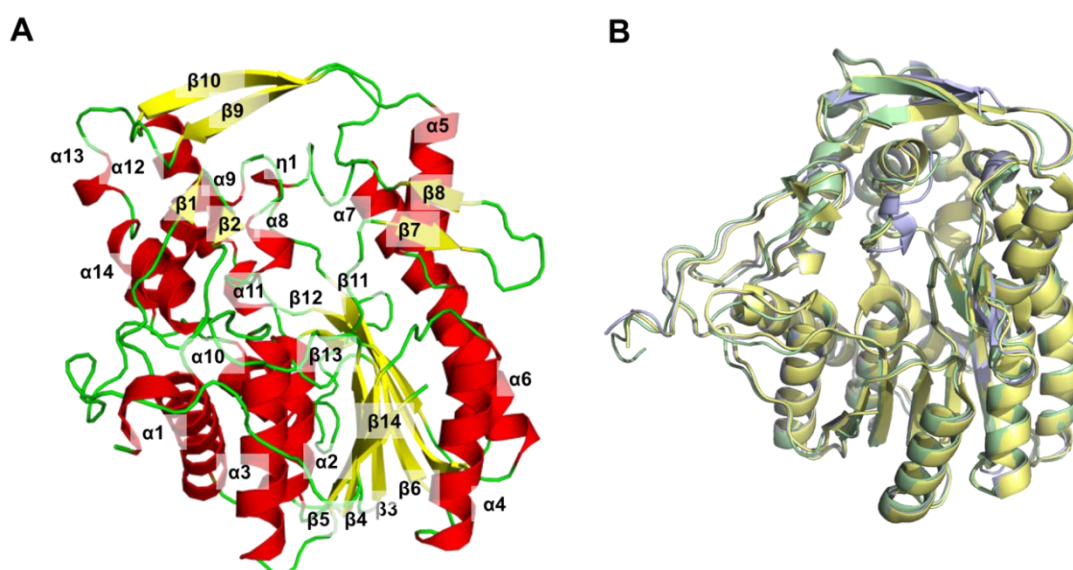


Figure 37: Structure of YpFabV

A) The YpFabV binary complex is depicted as ribbon diagram with helices in red ($\eta = 3_{10}$ helix), β -strands in yellow and loop regions in green. B) Superposition of apo BpFabV (green) and YpFabV in the binary (light blue) and ternary (yellow) complex.

The structure of apo BpFabV and YpFabV binary and ternary complexes show a common overall structure in the superposition (Figure 37). The structural similarity was analyzed with secondary structure matching (SSM) (PDBeFOLD server, (Krissinel and Henrick, 2004)). Although BpFabV and YpFabV share only 75% sequence identity, 95% of the secondary structure elements overlap in the SSM analysis. The apo BpFabV structure (green) could be aligned to the binary (blue) and ternary (yellow) YpFabV structures with RMSD values of 0.98 Å and 0.94 Å, respectively, based on the C_α alignment. The comparison of both YpFabV complexes among each other exhibited an RMSD of 0.48 Å. Neither the origin in different species nor the different ligand bound states of the structures cause major changes in the overall structure.

The overall structure of FabV displays typical features of the SDR superfamily. Predominantly the N-terminal part of the polypeptide chain is folded in a Rossmann fold with eight parallel β-strands in a β-sheet flanked by three and four α-helices on each side. The Rossmann fold generates the NADH binding site (Buehner et al., 1973). The C-terminal part contains the catalytic residues and builds up the substrate-binding pocket thereby providing substrate specificity. This part in the SDR proteins is usually smaller compared to FabV.

A structural comparison against the Protein Data Bank (PDB) with SSM revealed the highest similarity of the binary YpFabV complex with structures of *E. coli* FabI in complex with NAD⁺ and triclosan (EcFabI_{tdl}) (PDB ID: 1C14, 1QG6 and 1QSG; (Qiu et al., 1999; Stewart et al., 1999; Ward et al., 1999)). With a sequence identity to EcFabI_{tdl} of only 17% (sequence alignment shown in Supplemental Figure 58), YpFabV shares 50% of its secondary structure with FabI (Figure 38A). The most similar part is the Rossmann fold, although the Rossmann fold in EcFabI_{tdl} contains one β-strand and one α-helix less than YpFabV (Figure 38B+C). The active site pocket shows more differences. The core of the active site pocket is retained but several additional structural elements of FabV (yellow in Figure 38 B+C), which is about 140 residues longer than FabI, are folded around the active site pocket. Three β-hairpin structures (β1/β2, β7/β8 and β9/β10) are located around the entry of the pocket. The extended β-hairpin β9/β10 is covering the helix α9, which corresponds to the proposed ACP interaction site of FabI (Chan and Vogel, 2010). The substrate-binding loop (violet in Figure 38 B+C) is located N-terminal relative to the ACP

interaction site and builds up helix $\alpha 8$ in FabV. In FabI this loop is proposed to be flexible until a ligand such as triclosan binds and interacts hydrophobically with the protein leading to the ordering of the loop into a helix.

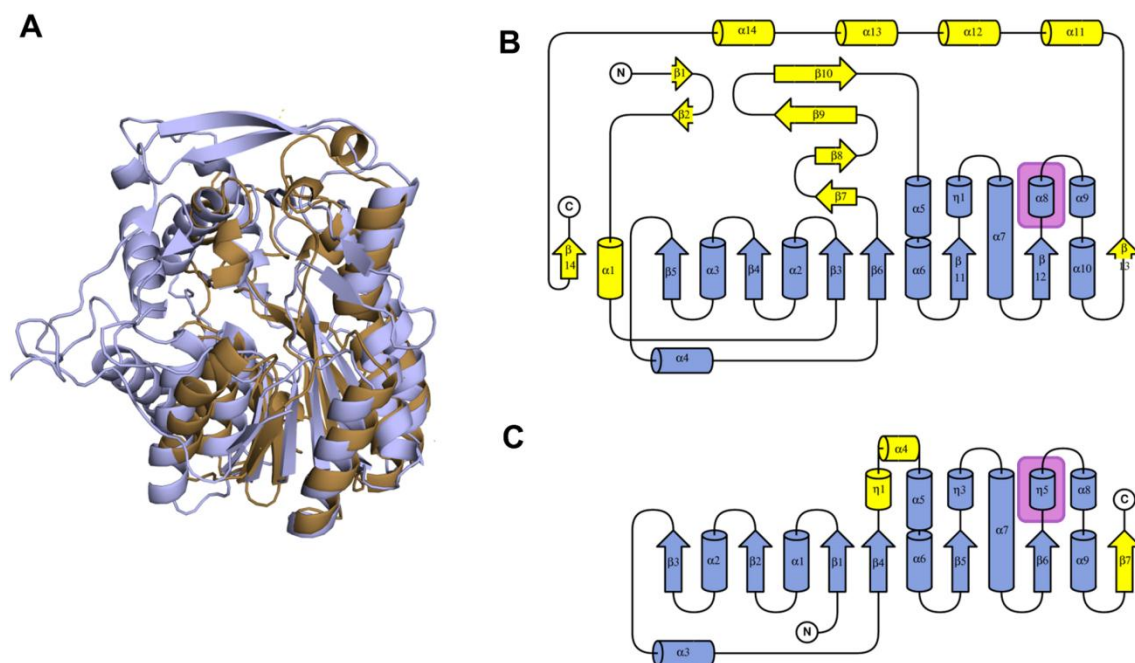


Figure 38: Structural comparison of YpFabV (binary complex containing NADH) with EcFabI (ternary complex containing NAD⁺ and triclosan)

A) Superposition of the binary YpFabV structure (light blue) and the ternary EcFabI_{tcI} (brown) complex (PDB ID 1C14) shown as ribbon diagram. B)/C) Topology diagram of YpFabV (binary) (B) and EcFabI_{tcI} (C) with similar secondary structure elements illustrated in blue and the differing structural elements in yellow, the substrate-binding loop is highlighted in violet.

In contrast to the observations made for FabI, this helix is already in its closed helical conformation when the cofactor is bound in FabV. Furthermore, behind the structural elements carrying the catalytic residue Y235 (around $\eta 1$) four additional helices ($\alpha 11$, $\alpha 12$, $\alpha 13$ and $\alpha 14$) are covering the active site. These extended additional elements are probably the reason why FabV does not need further stabilization of the active site by oligomerization interfaces as it is known from other members of the SDR family such as FabI or FabL. SDR proteins usually form dimers or tetramers. There is one notable exception, the monomeric structure of the SDR family member porcine testicular carbonyl reductase (PTCR) was shown to be a monomer in solution but is stabilized differently compared to FabV by a 41-residue insertion interacting with the two long helices, which usually form the four-helix bundle interface (Q-interface) conserved in the SDR superfamily (Ghosh et al., 2001).

4.1.2 The active site

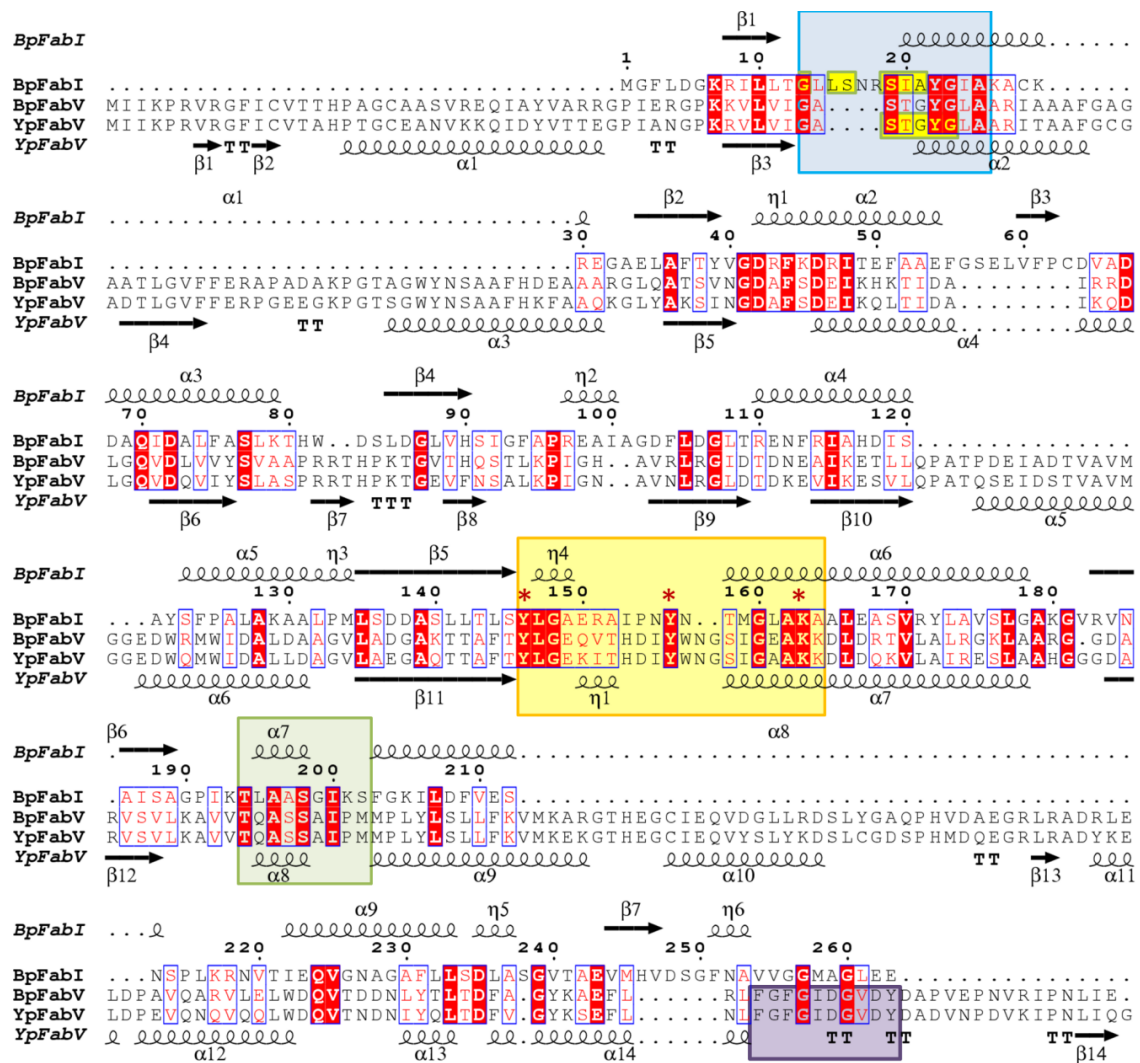


Figure 39: Sequence alignment of BpFabI, BpFabV and YpFabV

Sequence alignment (ClustalW, (Thompson et al., 1994)) of BpFabI, BpFabV and YpFabV. The cofactor binding motif is shown in a blue box with described interaction partners of the cofactor highlighted in yellow. The active site region is highlighted in a yellow box with the catalytic residues marked by red asterisks. The substrate-binding loop is marked in a green box and the potential FAD binding site of FabV in a violet box. Secondary structure elements are indicated by arrows and spirals for β -strands and α -helices, respectively and shown above (*BpFabI ternary*) and below (*YpFabV binary*) the sequence. 3_{10} helices are labeled with η and β -turns with TT. The conserved residues are highlighted in the blue boxes with the most conserved residues colored in white with a red background.

The SDR superfamily is a very diverse superfamily, with low sequence identities among the members. The subfamilies are classified by certain cofactor binding- and active site motifs (Kallberg et al., 2002). The divergent subfamily, composed of enoyl-thioester reductases as FabI or FabL, exhibits an active site motif of YxxMxxxK. Although FabV is

closely related to FabI, it does not share this motif of the divergent subfamily but exhibits two additional residues in between the catalytic Y235 and K244 with no methionine in an $Y(x)_8K$ motif (cf. yellow box in sequence alignment in Figure 39 and Supplemental Figure 58 and Figure 59). The remaining subfamilies have even shorter active site motives with $YxxxK$ and $YxxxN$ (Kavanagh et al., 2008).

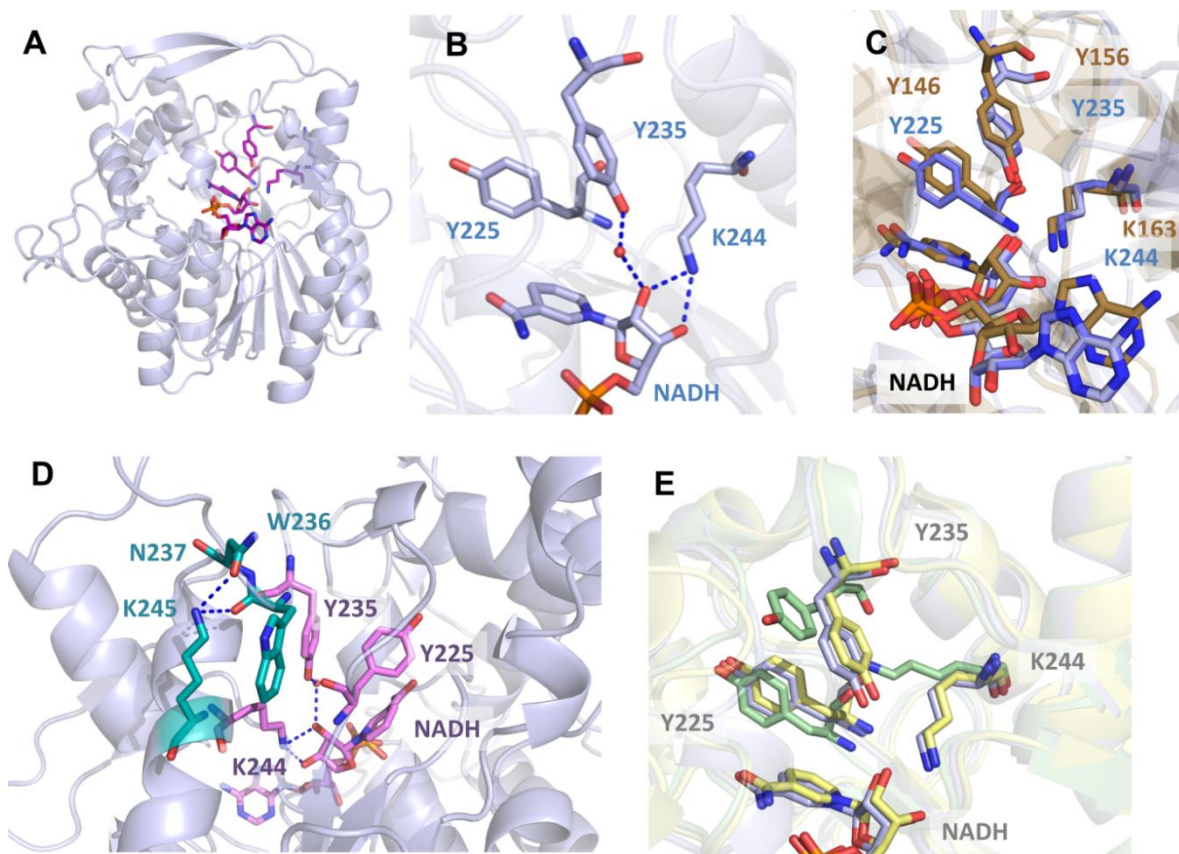


Figure 40: Active site of FabV

A) Ribbon diagram of YpFabV (binary) (light blue) with active site residues and cofactor in all-bond representation (violet). B) Active site residues of YpFabV (binary) and cofactor shown in all-bond representation with hydrogen bonds as dashed lines. C) Superposition of the active site residues and cofactor of YpFabV (binary) (blue) and EcFabI_{tdl} (brown). D) The conserved residue K245 interacts with N237 and W236 (teal) and thereby stabilizes the position of the active site residues Y235 and K244 (violet) relative to each other. E) Superposition of the active site residues and cofactor of apo BpFabV (green), YpFabV binary (light blue) and ternary (yellow) complexes.

In FabV the catalytic residues are part of the C-terminal region of the protein, which is building the binding pocket in vicinity to the nicotinamide ring of the NADH cofactor (depicted in binary YpFabV structure in Figure 40). The hydroxyl group of Y235 interacts via a water molecule with the 2' ribose hydroxyl group of the nicotinamide ribose. The

water molecule probably binds in place of the substrate. K244 interacts with both hydroxyl groups of the ribose and keeps the cofactor in place for catalysis. Moreover it is thought to be involved in re-protonation of Y235 after reduction of the enoyl substrate. A third residue, Y225, is proposed to play a major role in substrate accommodation in the active site. In the superposition with EcFabI_{tcl} (Figure 40C) the FabV active site residues Y225, Y235 and K244 display the same 3D conformation as the EcFabI_{tcl} counterparts Y146, Y156 and K163. The additional two residues between Y235 and K244 have no impact on the active site geometry. Although the active site motif is not retained in FabV, the structural geometry of the catalytic site is conserved.

Residue K245 was found to be conserved in FabV from various species but not in other enoyl-ACP reductases. A mutation of this residue in *B. mallei* FabV to methionine resulted in a 10-fold decreased substrate affinity but unchanged cofactor binding (Lu and Tonge, 2010). It was therefore proposed that K245 is interacting with the substrate in the binding pocket. The crystal structures of FabV, however, revealed, that K245 does not point into the binding pocket but is located on the surface of the protein (Figure 40D). It interacts with the side chain of N237 and the backbone carbonyl of W236 (teal in Figure 4D) and thereby holds the loop carrying Y235 next to K244 (violet in Figure 40D) in place, stabilizing the position of the catalytic residues to each other. It seems to have an indirect effect on substrate binding by maintaining the active site geometry. This additional stabilization might be necessary in FabV because of the larger distance between Y235 and K244 in the sequence and is therefore not conserved in FabI.

A comparison of the active site residues in the apo-structure with the binary and ternary complexes of FabV, reveals that Y225 assumes the same conformation in all three structures whereas Y235 and K244 of apo BpFabV (green) are shifted in their orientation compared to the YpFabV structures (binary: blue, ternary: yellow) (Figure 40E). A probable reason for this shift might be the missing interaction to the cofactor in the apo structure. A closer look into the active site of the apo BpFabV structure shows that the shifted position of Y235 is stabilized by a hydrogen bond to the backbone nitrogen of P282 at the C-terminal end of the substrate-binding loop on the opposite side of the substrate-binding pocket (Figure 41A). K244 interacts with the sulfate moiety of a bound MES buffer molecule, which in turn interacts with V273, therefore this residue also

interacts across the binding pocket. The interaction to MES is an artificial feature of the crystal structure. The comparison to a newly published apo FabV structure from *Xanthomonas oryzae* (XoFabV, PDB ID 3s8m (Li et al., 2011))(in light orange in Figure 41B) showed that the Y225 and Y235 conformation is the same but K244 point towards the NADH position as in the complex structures of YpFabV.

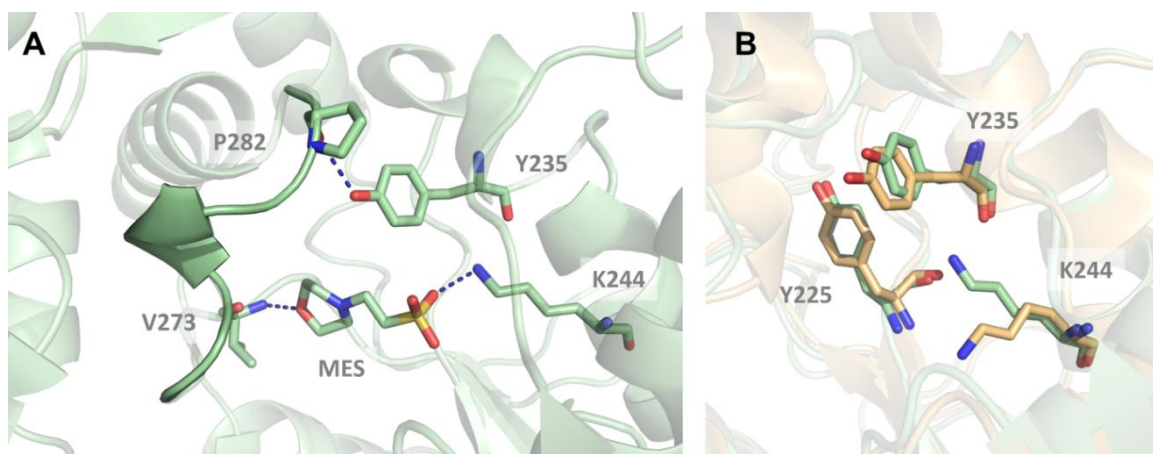


Figure 41: Active site residues in FabV apo structures

A) Interactions of the catalytic residues of apo BpFabV. B) Superposition of the active site residues of apo BpFabV and apo XoFabV (PDB ID 3s8m).

4.1.3 Stabilization of the substrate- binding loop

An interesting feature of the active site of FabV, especially concerning drug development based on triclosan, is the closed, helical substrate-binding loop (helix $\alpha 8$) of FabV. The substrate-binding loop (T276-M284, highlighted in a green box in the sequence alignment in Figure 39 and Supplemental Figure 58 and Figure 59) is closed in all three forms, the apo, the binary and ternary complexes; however, in the binary complex of YpFabV the substrate-binding loop is shifted about 3 Å deeper into the substrate binding pocket compared to the other structures (Figure 42A). In EcFabI_{tcl} the helical conformation is stabilized by additional hydrophobic contacts to the bound triclosan molecule at the center of the helix. This interaction is missing in apo BpFabV and the binary YpFabV structure. In FabV the additional structural elements (depicted in yellow in Figure 42B) are folded around the active site pocket especially the substrate-binding loop (depicted in violet in Figure 42B). The N-terminal part of the substrate binding loop is stabilized by a hydrogen bond network involving water molecules, residues from the edge of the

Rossmann fold including T51, E75, S86, G87, and N90, NADH, residues from the additional structural elements such as the hairpin $\beta 1/\beta 2$ (F10, C12) and helix $\alpha 14$ (L373) (violet in Figure 42C).

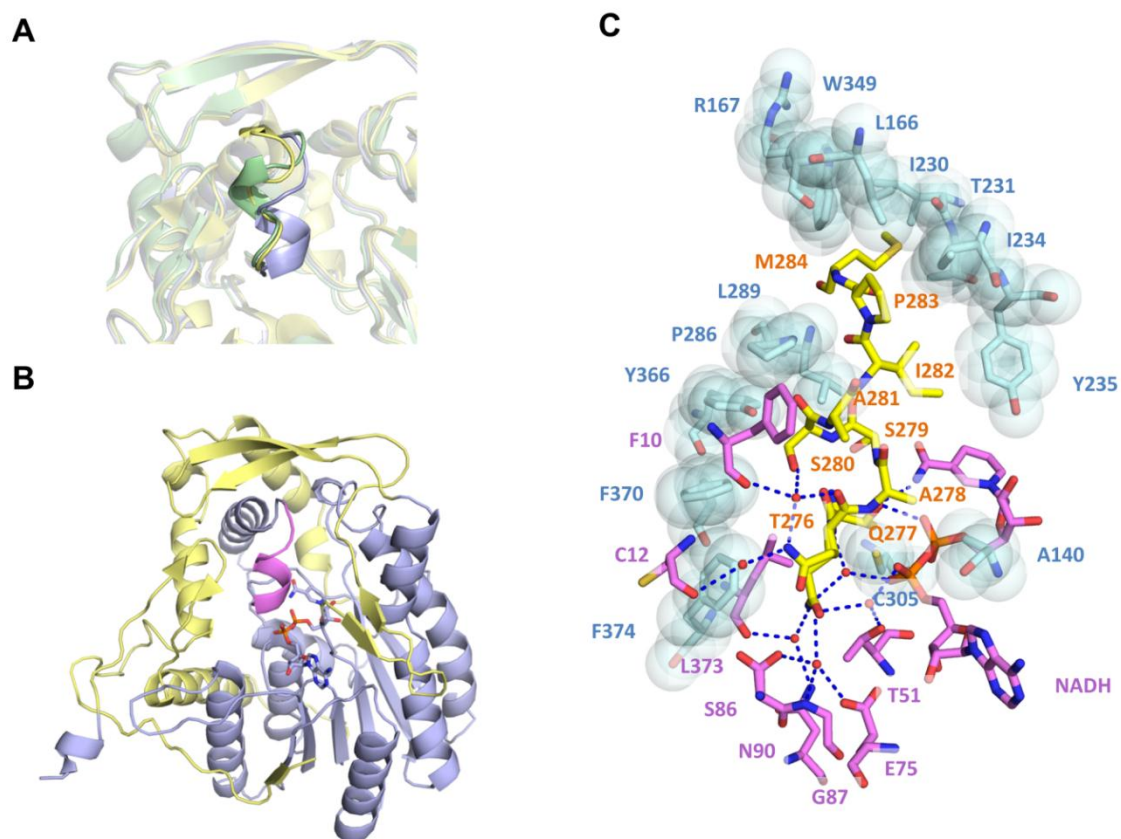


Figure 42: Stabilization of the substrate-binding loop in FabV

A) Superposition of apo BpFabV (green) and YpFabV in the binary (light blue) and ternary (yellow) complex with the substrate binding-loop highlighted. B) Ribbon diagram of the YpFabV binary complex in blue with the additional structural elements of FabV colored in yellow and the substrate-binding loop in violet. The cofactor is drawn in all-bond representation. C) The substrate-binding loop (yellow) stabilization by van der Waals interactions (cyan residues with transparent spheres) and hydrogen bonds (dashed lines and violet residues).

Importantly the center of the helix is stabilized by hydrogen bond interactions from the carbonyl oxygen of F10 to the carbonyl group of T276 and the hydroxyl group of S280, which is mediated by an ordered water molecule. The C-terminal half of the substrate-binding loop is entangled in van der Waals interactions (cyan in Figure 42C). The hydrophobically interacting residues are part of the following helix $\alpha 9$ (P286 and L289), of helix $\alpha 10$ (C305) and the loop carrying the catalytic residue Y235 (I230, T231, I234 and Y235). The other half of hydrophobically interacting amino acids is located on additional

structural elements of FabV. A140 interacts from $\beta 7$ and L166 and R167 from hairpin $\beta 9/\beta 10$. W349, Y366, F370 and F374 originate from the additional C-terminal α -helices $\alpha 12$ and $\alpha 14$. Binding of the cofactor does not seem to be essential for substrate-binding loop stabilization, since the loop is already helical in the apo BpFabV structure.

4.1.4 NADH binding

The second determining motif for subfamily assignment in the SDR superfamily is the glycine-rich cofactor binding motif of the Rossmann fold, more precisely on the loop between strand $\beta 1$ and helix $\alpha 1$ in FabI and the corresponding strand $\beta 3$ and helix $\alpha 2$ in FabV (cf. blue box in sequence alignment in Figure 39 and Supplemental Figure 58 and Figure 59). The motif was defined as GxxxxSxA (Kallberg et al., 2002). The alignments depicted in Figure 39 (BpFabI, BpFabV and YpFabV) and Supplemental Figure 58 (YpFabV and EcFabI_{tcl}) differ in this region. The alignment of YpFabV with EcFabI_{tcl} requires no gap whereas the alignment of BpFabI, BpFabV and YpFabV inserts a gap of 4 residues in this motif. Since the secondary structure elements align well in the sequence alignment in Figure 39, it seems that the loop connecting $\beta 3$ and $\alpha 2$ is shorter in FabV compared to FabI, but can provide similar interactions (interacting residues are marked yellow in the blue box in Figure 39). Therefore also this motif is not retained in FabV. If FabV, which is closely related to FabI, shall be assigned to the same subfamily of diverse SDR proteins, the motifs have to be revised. Otherwise FabV has to be grouped into a separate subfamily of “even more diverse” SDR proteins.

The cofactor NADH is not only bound by interactions with amino acids from the Rossmann fold. NADH is involved in a tight hydrogen bond network and further stabilized by hydrophobic contacts to surrounding residues (analyzed with the help of Ligplot+ (Laskowski and Swindells, 2011; Wallace et al., 1995)). An overview of all interactions of NADH in the YpFabV binary complex is depicted in Figure 43A with the residues interacting via hydrogen bonds depicted in violet and the hydrophobically interacting residues in cyan. The hydrogen bond network is illustrated in detail in Figure 43 B-D. The adenine ring of NADH (N6 and N1) is stabilized by hydrogen bonds to the side chain of D111 and the carbonyl oxygen of G110. A solvent water molecule mediates hydrogen bonds to the carbonyl group of R143 and the hydroxyl of S141. The hydroxyl groups of the

adenine ribose interact with the main chain nitrogen atom of F74 and the hydroxyl group and main chain nitrogen of S50. The pyrophosphate group is entangled in a hydrogen bond network involving two water molecules and one sodium ion (Figure 43C).

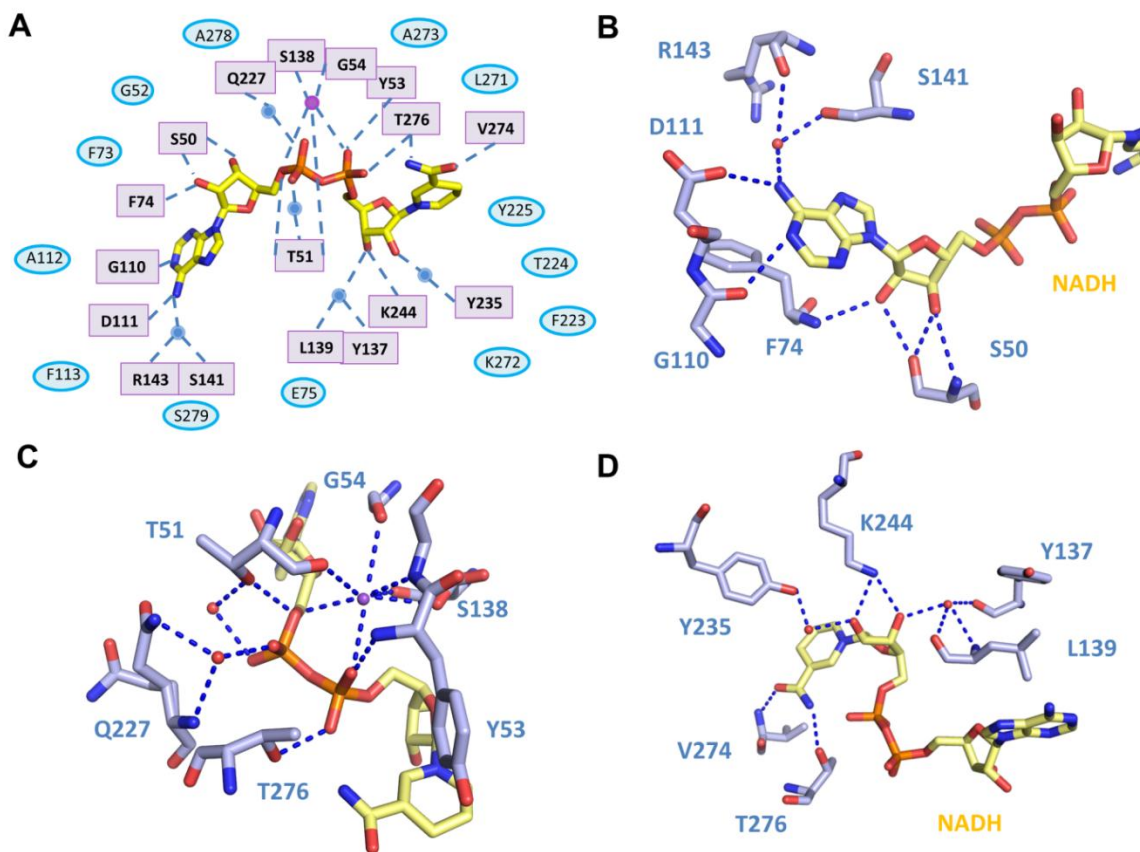


Figure 43: Cofactor binding of YpFabV

A) Schematic overview of the interactions of NADH (yellow) with YpFabV; residues providing van der Waals interactions are displayed in cyan and hydrogen bonds in violet. B)/C)/D) Detailed hydrogen bond interactions (dashed lines) of the adenine ring and the ribose (B), the pyrophosphate (C) and the nicotinamide ring and the neighboring ribose (D).

The sodium ion mediates interactions from both phosphate groups (OAZ and O5*) to the carbonyl and hydroxyl groups of S138, the carbonyl group of G54 and the carbonyl group of T51. T51 also interacts with its hydroxyl group directly to O5* and via a water bridge to OAB of the adenine phosphate. The oxygen OAC of this phosphate interacts with the backbone as well as with the side chain nitrogen of Q227 via a water molecule. The nicotinamide phosphate interacts via its oxygen OAZ with the backbone nitrogen of Y53 and via the OAY oxygen with the hydroxyl group of T276. The catalytic residues Y235 and K244 are involved in interactions with the nicotinamide ribose (Figure 43D). The cofactor

is stabilized by interactions of the side chain of K244 to both hydroxyl groups of the ribose and a water-mediated hydrogen bond of the Y235 hydroxyl to the 2' hydroxyl group. The second hydroxyl group is further stabilized by a water mediated interaction to the backbone of Y137 and L139. The amide group of the nicotinamide ring is interacting with the carbonyl to the backbone nitrogen of V274 and with the amino group to the hydroxyl of T276.

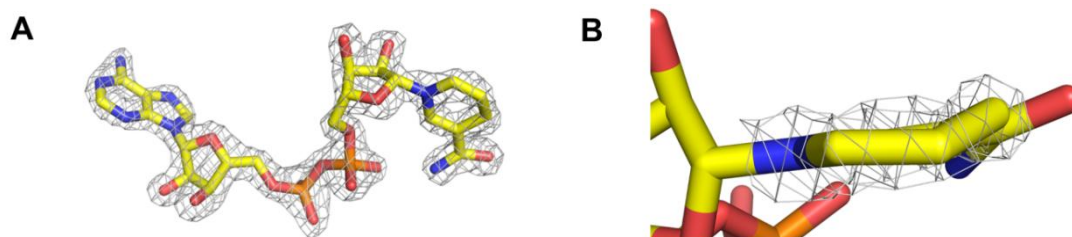


Figure 44: OMIT electron density map of NADH (YpFabV binary)

A) 2Fo-Fc - OMIT map (contour level 1σ) of the NADH molecule. B) Zoomed view of the OMIT map of the nicotinamide ring.

During model building the question arose, whether the NADH, applied in the co-crystallization trial, is still in the reduced form or if it might have been oxidized to NAD^+ . Most FabI structures had been co-crystallized with NAD^+ (and an inhibitor). Structurally NADH differs from NAD^+ only in a slight kink of the nicotinamide ring. The oxidized nicotinamide ring of NAD^+ is in a planar, aromatic conformation. From the experimental data with the best resolution of about 2 Å, it is difficult to judge if the ring is planar or slightly kinked (Figure 44). During refinement the conformation of NADH is influenced by the geometric restrains given in the library file of the molecule. However, even when the nicotinamide ring was defined to be planar, it deviated from planarity after a refinement cycle. Another indication that the structures contain NADH rather than NAD^+ is the fact that YpFabV never crystallized with NAD^+ but only in the presence of NADH. Moreover the inhibitors, which were co-crystallized with the T276S variant of YpFabV, preferred binding in the presence of NADH compared to NAD^+ . Since there was no indication that the cofactor is present in the crystal structure in the oxidized form, it was modeled as NADH.

4.1.1.1 Influence of the T276S variant on NADH binding

The T276S variant of YpFabV in the binary complex shows no changes in the protein structure or the cofactor position in comparison to the wild type protein. The structures can be aligned with an RMSD value of only 0.27 Å according to the SSM analysis (Krissinel and Henrick, 2004). Structural comparison of the binary wild type YpFabV complexes containing the hexahistidine-tag with the cleaved protein yielded a larger RMSD value of 0.55 Å. The amino acids threonine and serine only differ in one methyl group, which is missing in serine. Although it does not display major structural changes, the T276S variant behaves differently than the wild type protein in enzyme kinetics (Carla Neckles, unpublished data (Neckles, 2012)). The K_d values of the T276S variant for NADH and the substrate analog *trans*-2-dodecenoyl-CoA (ddCoA) were $4.2 \pm 0.05 \mu\text{M}$ and $32.9 \pm 0.4 \mu\text{M}$, respectively. The wild type K_d values for NADH and ddCoA were $13 \pm 0.8 \mu\text{M}$ and $13 \pm 0.7 \mu\text{M}$, respectively. These changes in affinity are also reflected in a modified mechanism. The wild type YpFabV, displaying comparable K_d values for substrate and cofactor, catalyzes the enoyl reduction in a random Bi Bi mechanism, where either the substrate or the cofactor could bind first. The T276S variant, with an about 10-fold higher affinity for the cofactor than for the substrate, catalyzes the reaction in an ordered Bi Bi mechanism with the cofactor binding first and leaving last (Carla Neckles, unpublished data (Neckles, 2012)). Interestingly, FabV from *B. mallei* (BmFabV) was reported to catalyze the reaction in an ordered Bi Bi mechanism (Lu and Tonge, 2010). A superposition of the residues interacting with NADH, does not indicate changes in the conformation which could lead to a loss/gain of interactions (Figure 45A). The residues T276 and S276 are retained in the same position and can both interact with the cofactor (Figure 45B). There is no substantial change in the distance between the interacting atoms. Since there is no influence on the conformation of the protein structure or the ligand position, another explanation might be differing interactions to solvent molecules, since many interactions of FabV to the cofactor are mediated by water molecules. The interaction-mediating solvent molecules described above are all retained in the T276S variant structure, however, there are two additional water molecule in the vicinity of S276 in the active site, which are not present in the wild type structure, since they are extruded by the additional methyl group of T276 (Figure 45C). One of these water molecules mediates an additional

interaction between the sulfhydryl group of C305 and the oxygen atoms OAY and OAZ of the nicotinamide phosphate group (Figure 45D). This additional interaction might not be the sole background of the higher NADH affinity of the T276S variant. The analysis of solvent molecules in protein structures is highly dependent on the resolution of the experimental data. The higher the resolution, the more solvent molecules become visible in the electron density. At a resolution of 2 Å most of the defined water molecules in the active site should be visible in the active site.

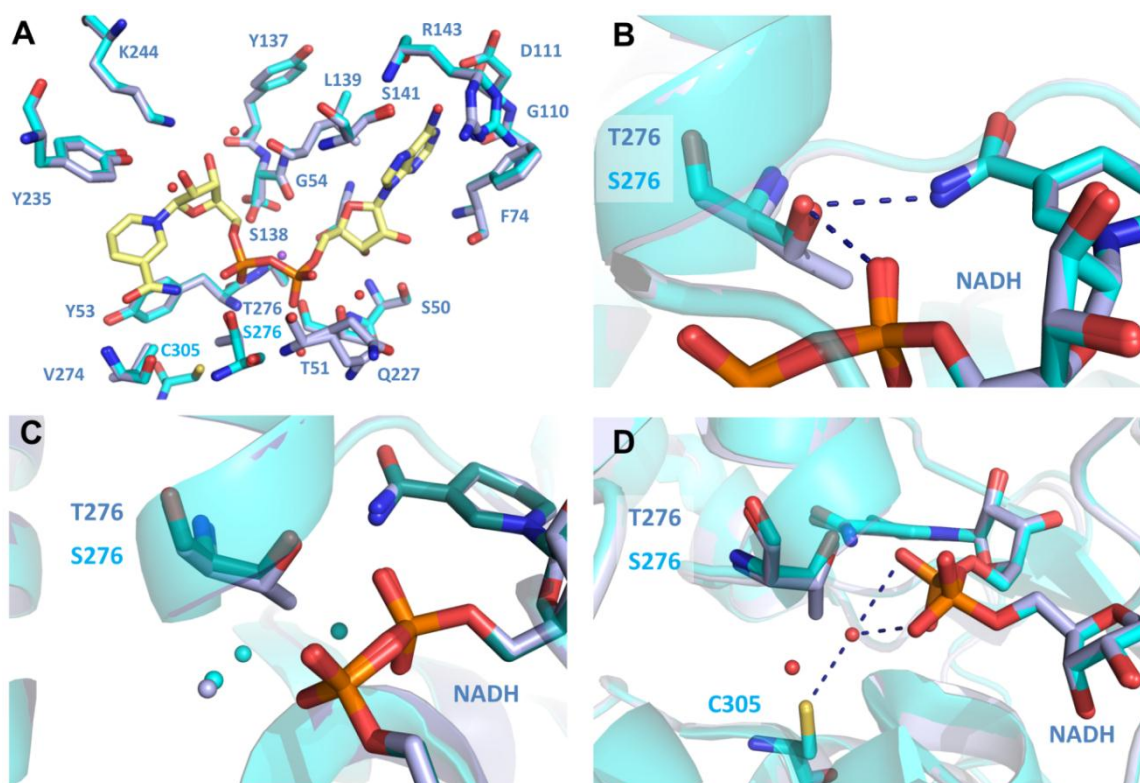


Figure 45: Impact of T276S variant on NADH binding

A) Superposition of NADH-interacting residues in the YpFabV binary complexes of the wild type (light blue) and the T276S variant (cyan) in all-bond representation. NADH is shown in yellow. B) Hydrogen bonds (dashed lines) of T276 and S276. C) Water molecules (colored according to the structure) in the vicinity to the T276 methyl group. D) Additional hydrogen bond interaction of the T276S variant.

At this point it can not be ruled out that additional water molecules which have not been observed in the crystal structure affect cofactor binding. The differing cofactor affinity of the variant also has an influence on inhibitor binding. The 2-pyridone inhibitor PT171 (corresponding to PT173, but without the amino group at the ortho position of the B-ring, cf. Table 20) showed an IC_{50} value of $6 \pm 1 \mu\text{M}$ for the variant but $> 50 \mu\text{M}$ for the wild

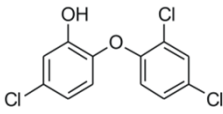
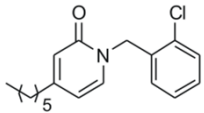
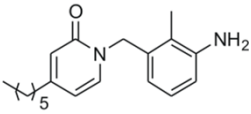
type. The 2-pyridone inhibitors might prefer binding to the variant because the affinity is increased in the presence of NADH versus NAD⁺ (Carla Neckles, unpublished data, (Neckles, 2012)). In contrast, the diphenyl ether inhibitors derived from triclosan usually bind in a ternary complex with NAD⁺. Apart from the increased NADH affinity of the variant, also changes in the set of bound solvent molecules in the active site might influence ligand affinities.

4.1.5 Inhibitor binding

The 2-pyridone inhibitors PT172 and PT173 inhibit the YpFabV variant with higher affinity compared to triclosan. Triclosan inhibits the variant with a K_i value of $71 \pm 4 \mu\text{M}$, whereas PT172 and PT173 exhibit K_i values of $2.1 \pm 0.4 \mu\text{M}$ and $1.5 \pm 0.3 \mu\text{M}$, respectively (cf. Table 20).

Table 20: Inhibitors of the T276S variant (Hirschbeck et al., 2012)

The cLogP was determined with ChemBioDraw Ultra 12.0

Inhibitor	Structure	Molecular weight (Da)	clogP	K_i (μM)
triclosan		289.54	5.53	71 ± 4
PT172		303.83	5.54	2.1 ± 0.4
PT173		298.20	4.00	1.5 ± 0.3

The elevated NADH affinity favors the binding of the 2-pyridone inhibitors, but on the other hand impairs the binding of the diphenyl ether inhibitor triclosan. For BmFabV a K_i value for triclosan of $0.4 \mu\text{M}$ was reported (Lu and Tonge, 2010) and for YpFabV IC_{50} values of $5 \pm 1 \mu\text{M}$ and $>50 \mu\text{M}$ have been determined for the wild type and the variant, respectively (Carla Neckles, unpublished data (Neckles, 2012)). Since the diphenyl ether inhibitors prefer binding in the presence of NAD⁺, the tight binding of NADH in the variant

may reduce its affinity. The 2-pyridone inhibitors contain a hexyl-chain at the meta position of the A-ring (the pyridone ring). Structure-activity relationship studies on diphenyl ether inhibitors in FabI revealed a favorable effect of an alkyl-chain on binding since it is mimicking the enoyl substrate in the active site (Lu and Tonge, 2008; Luckner et al., 2010). Unfortunately diphenyl ether inhibitors are susceptible to drug metabolism in phase II conjugation reactions. Triclosan was reported to be conjugated at the 2'-hydroxyl group to glucuronide and sulfate conjugates (DeSalva et al., 1989). Therefore inhibitors with a 2-pyridone scaffold were explored for binding in FabV, since it showed promising inhibitory results in FabI from *S. aureus*, *Toxoplasma gondii* and *B. anthracis* (Tipparaju et al., 2008; Tipparaju et al., 2010; Yum et al., 2007). Another favorable feature of the 2-pyridone scaffold is a reduction of the logP value compared to the diphenyl ether scaffold. One additional issue of the diphenyl ether inhibitors is their high hydrophobicity. It is not surprising that a hydrophobic molecule binds with high affinity to the substrate binding pocket of the enoyl-ACP reductases since the substrate itself is hydrophobic, but high hydrophobicity impairs the oral bioavailability of a potential drug candidate. PT172 and PT173 display clogP values of 5.54 and 4.00 (cf. Table 20), respectively; their diphenyl ether counterparts (with the same substituents) would have clogP values of 6.95 and 5.69, respectively.

The ternary complexes of the YpFabV variant showed no major structural changes in the overall structure compared to the binary complex. The structures can be aligned with an RMSD of 0.2 Å (SSM). Since binding of triclosan and other slow binding inhibitors to FabI leads to ordering of the substrate-binding loop, it is interesting to observe that the substrate binding loop moves out of the binding pocket upon inhibitor binding in FabV (Figure 46). The loop shifts about 3 Å out of the binding pocket and affects also the conformation of the interacting β hairpin $\beta 1/\beta 2$. This movement is necessary to accommodate the inhibitor in the active site.

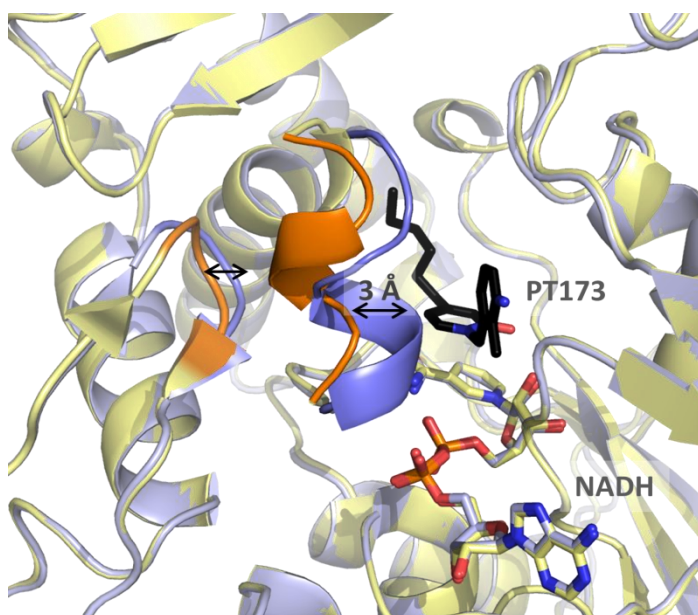


Figure 46: The substrate-binding loop shifts upon inhibitor binding

Superposition of the YpFabV T276S variant binary (light blue) and ternary (yellow) structure with highlighted substrate binding loops. PT173 (dark grey) and the NADH cofactors (yellow / light blue) are shown in all-bonds representation.

Interestingly, the apo BpFabV structure shares the open conformation of the substrate-binding loop with the ternary complex. The interaction to the cofactor seems to pull the helix deeper into the pocket. A closer view of the binding pocket of the ternary complexes shows that the two serine residues S276 and S279 interact with two water molecules in between the substrate-binding loop and the inhibitor (Figure 47A). Therefore the hydrophobic interaction between the helix and the inhibitor, as it is known from FabI and triclosan, cannot be formed. Notably the mutated residue S276 is involved in the interaction. The two water molecules replace the direct interactions of S276 to the cofactor at the amide and the phosphate group in the binary complex of the variant (cf. Figure 45B). The position of the cofactor itself is conserved in the binary and ternary complexes (cf. Figure 46). Since both T276 and S276 can form direct interactions to the cofactor, one might speculate that also T276 could form the hydrogen bond to the solvent water molecules in a ternary complex.

The binding mode of the 2-pyridone inhibitors in FabV is reminiscent to the binding of triclosan in FabI. It interacts with its keto group via two hydrogen bonds with the hydroxyl groups of Y235 and the nicotinamide ribose (Figure 47A). Furthermore the pyridone ring of the inhibitors forms a parallel displaced π - π stacking interaction with the nicotinamide ring of the cofactor. The superposition of both inhibitors shows that the pyridone ring (A-ring) assumes the same position in both structures, whereas the B-ring of PT172 is tilted

about 24° into the depth of the binding pocket (Figure 47B). The position of the hexyl chains is slightly flexible, which is also reflected in a rather diffuse electron density map of this part of the inhibitor. All interacting residues of PT172 and PT173 are depicted in Figure 47 C and D. PT173 interacts hydrophobically with A140, T221, Y225, A273 and M285. Due to the shifted B-ring, PT172 forms hydrophobic contacts additionally to M196. The hexyl chain of PT172 also interacts with H232, but since this part of the inhibitor was modeled into an ill-defined electron density in both inhibitors, this could also be be the case for PT173. With the amino group at the meta position of the B-ring PT173 forms hydrogen bonds to two solvent water molecules; one of them mediates a hydrogen bond interaction to the carbonyl group of S141 and the hydroxyl group of S155. The shift of the B-ring out of the pocket is probably due to this additional interaction, rather than steric hindrance.

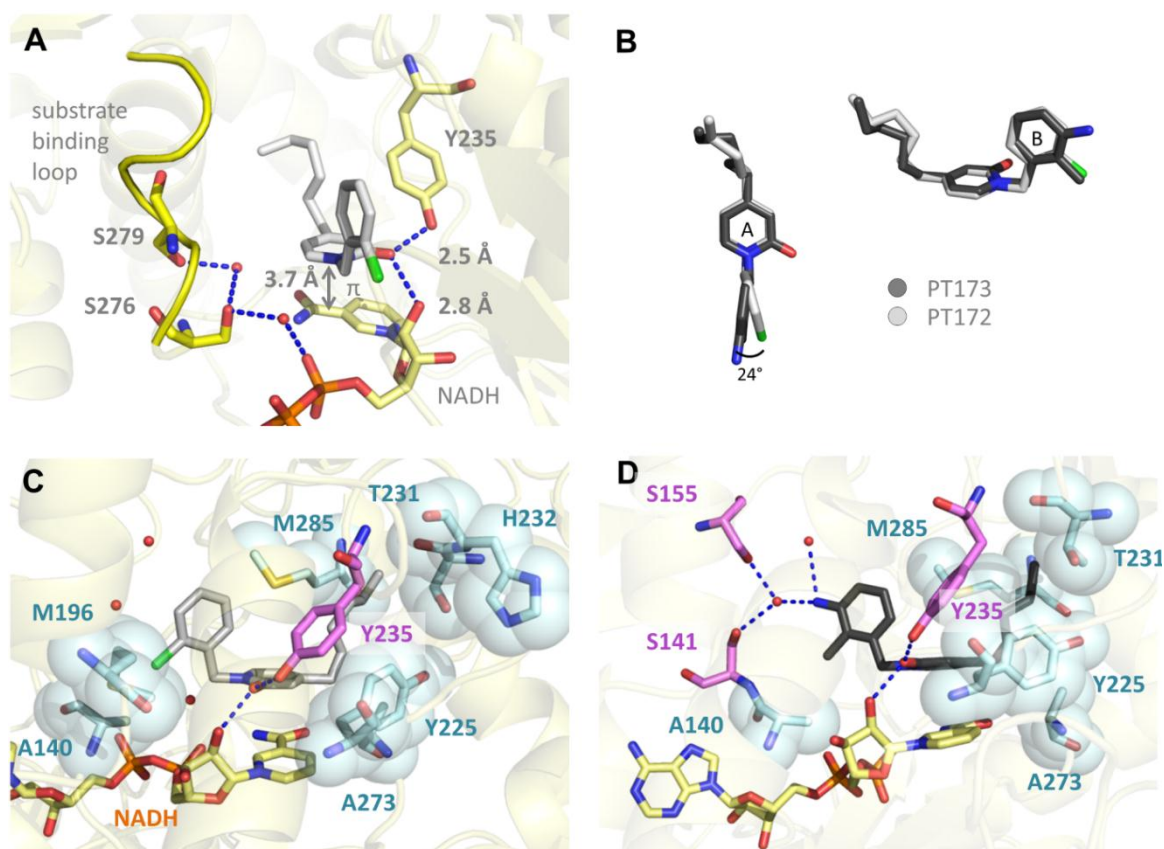


Figure 47: Inhibitor binding of PT172 and PT173 in YpFabV

A) PT172 (light grey) interacts through hydrogen bonds (dashed lines) with FabV and NADH and in a π -stacking interaction with NADH. The substrate binding loop is highlighted in yellow. B) Superposition of bound PT172 and PT173. C)/D) Residues interacting with PT172 (C) and PT173 (D) via hydrogen bonds (violet) and van der Waals contacts (cyan with transparent spheres).

The increased NADH affinity of the YpFabV variant might have facilitated obtaining a stable ternary complex for crystallization with respect to these rapid reversible inhibitors of FabV with rather low affinity. Although the 2-pyridone inhibitors, described in the ternary complexes do not bind with the same affinity to wild type YpFabV, the structural characterization of the ternary variant structure reveal a promising binding mode of the inhibitors and how the protein structure reacts upon inhibitor binding, which might help to design improved inhibitors for the FabV binding pocket.

4.1.6 Potential ACP interaction site

Despite the low sequence identity and the difference in size, the active site and the binding pocket of FabV is very similar to FabI. The binary complex of YpFabV is most similar to the triclosan-bound form of FabI (cf. Figure 38A), which is characterized by the closed, helical conformation of the substrate-binding loop. The usually flexible substrate-binding loop is thought to interact hydrophobically with the substrate thereby closing the pocket. In FabV this “closing mechanism” is already observed in the binary complex and the active site pocket is surrounded by additional structural elements such as the three β -hairpins ($\beta 1/\beta 2$, $\beta 7/\beta 8$ and $\beta 9/\beta 10$) and the helices $\alpha 11$, $\alpha 12$, $\alpha 13$ and $\alpha 14$. The question therefore arises how the substrate enters this very close active site.

In FabI two entry sites have been described, the “minor portal” and the wider “major portal” (Rozwarski et al., 1999). In an EcFabI-ACP complex structure the acyl-panthetein adduct was not visible in the electron density, but it could be modeled by molecular dynamic simulations and was proposed to enter the active site through the minor portal (Rafi et al., 2006). In the analysis of solvent channels in the binary YpFabV complex structure with MOLE and CAVER (Petrek et al., 2007; Petrek et al., 2006) both entry channels could be confirmed (Figure 48A). The minor portal however, is constrained by the tight substrate-binding loop conformation and the β hairpin $\beta 9/\beta 10$ and therefore very narrow. Another aspect of the substrate entry is a binding site for the acyl-carrier protein ACP. There is no defined interaction motif for ACP, which is reasonable since ACP interacts with a variety of different enzymes involved in fatty acid biosynthesis and phospholipid metabolism, however all interactions are characterized by low affinity binding (low μM range). The small, acidic protein was reported to interact via its acidic

residues on helix $\alpha 11$ with its interaction partners, i.e. to patches containing electropositive sites combined with hydrophobic areas. In the EcFabI-ACP complex structure ACP binds to basic residues in helix $\alpha 8$ of FabI, C-terminal to the substrate-binding loop (Chan and Vogel, 2010; Parris et al., 2000; Rafi et al., 2006; Zhang et al., 2003a; Zhang et al., 2003b).

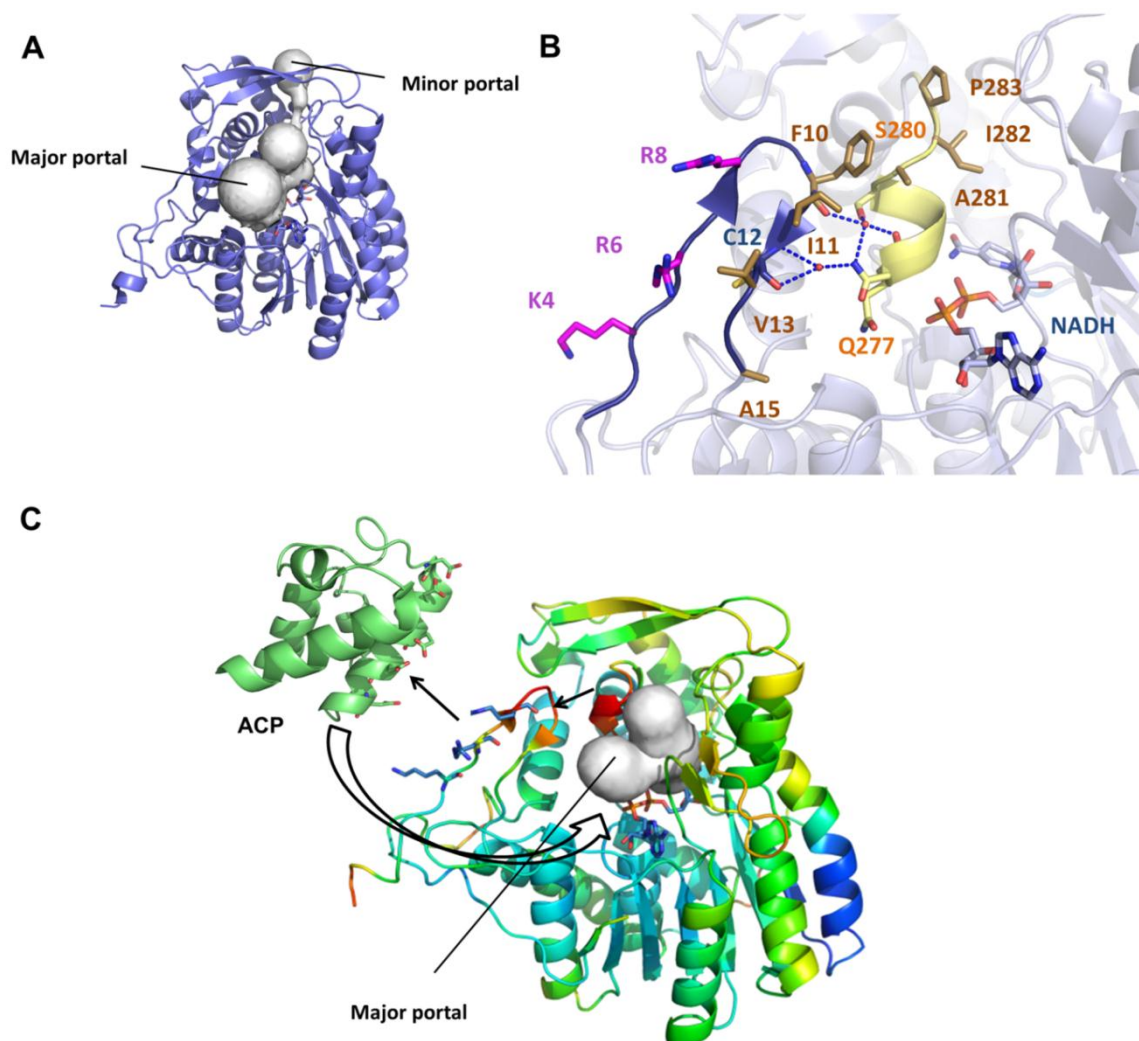


Figure 48: Hypothetical substrate-binding mechanism

A) Potential entry channels of the YpFabV binary complex (calculated with Caver) through the minor and major portals, shown as grey surfaces. B) Detailed view of the potential interaction site: basic residues are shown in magenta, hydrophobic residues in brown and the substrate-binding loop is highlighted in yellow. C) Hypothetical view towards substrate binding: The PT173-complex structure is colored according to its temperature factors (red=high, blue=low) with the basic residues K4, R6 and R8 in all-bond representation on strand $\beta 1$. The ACP could interact through its acidic residues with the basic residues of the N-terminal β -hairpin and thereby moving the connected substrate-binding loop (red) out of the pocket and opening the major portal for the substrate.

This helix is buried in FabV by the extended β hairpin $\beta 9/\beta 10$. Furthermore the basic residues, which are interacting with ACP in FabI are not conserved in FabV. Therefore a substrate entry through the minor portal seems implausible.

The second option is the entry through the major portal, which is the only side of the FabV binding pocket that is not covered by one of the additional structural element of this extended enoyl-ACP reductase isoform. In a complex structure of the *M. tuberculosis* isoform of FabI, InhA, with a C16 substrate analog, the N-acetyl cysteamine moiety, which would be physiologically coupled to ACP, points towards the major portal (Rozwarski et al., 1999). In vicinity to the major portal a potential ACP interaction site could be determined on the β -hairpin $\beta 1/\beta 2$ (Figure 48B). On the strand $\beta 1$ three prominent basic residues (K4, R6 and R8, depicted in violet), which are conserved among FabVs from different species (cf. Supplemental Figure 59, blue asterisks) could interact with the acidic ACP, while the enoyl substrate could enter the active site pocket via a patch of solvent-exposed hydrophobic residues (depicted in brown) on the strand $\beta 2$ and the upper part of the substrate-binding loop (depicted in yellow). The substrate-binding loop dynamics also support this hypothesis. In the ternary inhibitor structures the substrate-binding loop and the connected β -turn of hairpin $\beta 1/\beta 2$ are the only structural elements affected by inhibitor binding. Since the 2-pyridone inhibitors PT172 and PT173 with their hexyl chain could also be interpreted as substrate analogues, it seems probable that the same opening of these structures will occur upon substrate binding. Notably this opening movement broadens the major portal but not the minor portal. A potential binding mechanism is illustrated in Figure 48 C. According to this hypothesis ACP interacts with the basic residues on strand $\beta 1$, which might move towards the ACP upon binding. This outward movement is carried over to substrate binding, which broadens the major portal. The enoyl substrate can now enter the active site via the hydrophobic patch on strand $\beta 2$ through the opened major portal.

4.1.7 Potential FAD binding site

The authors of the paper characterizing the apo structure of the *X. oryzae* FabV (XoFabV) discussed a potential FAD binding site close to the C-terminus of FabV. The FAD binding motif FGFxxxxDY can be found among residues F373-Y383 in YpFabV and is conserved in various species (shown in the violet box in the sequence alignments in Figure 39 and Supplemental Figure 58 and Figure 59). Despite the binding motif the authors could not show FAD binding to XoFabV in isothermal titration calorimetry (ITC) or co-crystallization trials (Li et al., 2011). However, in the description of a FabV homolog in *Euglena gracilis*, a hint for a potential FAD interaction was noticed. In this protozoon the mitochondrial 2-trans-enoyl-CoA reductase with a protein sequence identity of 46% to YpFabV was reported to be a enoyl-CoA reductase involved in wax ester fermentation in mitochondria under anaerobic conditions (Hoffmeister et al., 2005). When the enzyme was purified natively from *E. gracilis*, it lost its activity if the purification buffers contained no FAD as additive. When the protein was recombinantly expressed in *E. coli*, the protein did not depend on FAD to retain activity. In the crystal structure of YpFabV the FAD motif is located lateral to the Rossmann fold, N-terminal to the last β -strand β 14 (Figure 49).

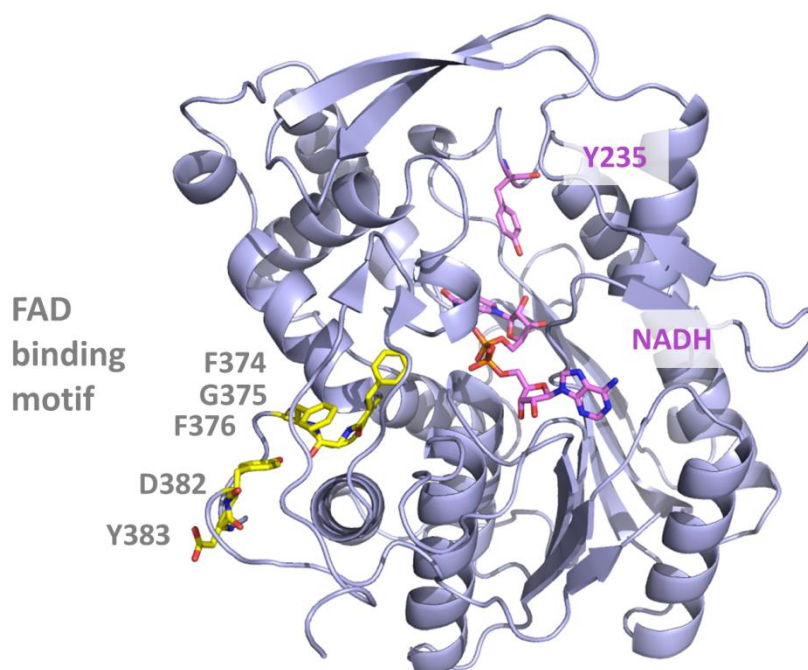


Figure 49: Potential FAD binding site

The YpFabV binary structure (blue) is shown with the catalytic Y235 and the cofactor in violet and the residues of the FAD binding motif in yellow in all-atoms representation.

The binding site is not in vicinity to the NADH or the catalytic center of FabV. This structural separation together with the result, that the recombinant mitochondrial 2-trans-enoyl-CoA reductase as well as the XoFabV exhibit the same activity with and without FAD lead to the conclusion that FAD has no functional role in the catalytic activity of FabV. For the FAS-II system in mycobacteria it was reported that the distinct enzymes of the elongation cycle interact with each other and that this complex formation is relevant for the function of the pathway (Cantaloube et al., 2011; Veyron-Churlet et al., 2004). If this is also true for the FAS-II system in other species, the FAD interaction might be involved in complex formation of FabV with other enzymes of the FAS-II pathway.

4.2 Functional considerations on FabV

The pronounced distinctions of FabV, compared to the SDR enoyl-ACP reductases FabI and FabL, especially the elongated active site motif, led to the question if FabV might have a distinct function or differing substrate specificity. Particularly in species possessing FabV along with FabI, FabV could adopt a specialized function. The increased size might indicate substrate specificity for longer enoyl substrates, as it is known from the FabI homolog InhA in *M. tuberculosis*. InhA has an elongated substrate binding loop generating an extended binding pocket, which is essential for the binding of substrates with a length of up to C56, which are utilized in mycolic acid synthesis (Dessen et al., 1995). The extended active site motif in FabV was suggestive of a different active site geometry, which might be an adaptation to a chemically different substrate such as unsaturated fatty acids. However, the structural data presented in this study reveal that the active site geometry of FabV matches with FabI and also the core of the binding pocket is structurally conserved. The additional structural elements could be attributed to the stabilization of the active site pocket of FabV and thereby facilitate its monomeric state. As the sole enoyl-ACP reductase in many species, such as *Y. pestis* or *V. cholerae*, it has to take over the function of FabI. Another indication that it assumes the same substrate specificity is the fact that *P. aeruginosa* FabV can compensate the inhibition of FabI (Zhu et al., 2010). On the other hand the mitochondrial 2-trans-enoyl-CoA reductase, a FabV homolog in the protozoon *Euglena gracilis*, was described to assume a different function

compared to FabV (Hoffmeister et al., 2005). The usage of Coenzyme A as carrier of the substrate instead of ACP indicated that this fatty acid biosynthesis pathway might be a reversal β -oxidation. The corresponding step of the β -oxidation is catalyzed by the acyl-CoA dehydrogenase/acyl-CoA oxidase in an oxidative and irreversible step. The reverse reaction therefore needs to be catalyzed by another enzyme. However, this change in function is associated with the active site motif Y(X₆)K, corresponding to FabI, not FabV. Therefore a specialization of FabV might be possible but there is no indication in the literature that it differs in function from FabI in the context of the FAS-II pathway.

The occurrence of four distinct enzymes, catalyzing the same step of the FAS-II elongation cycle might have originated in the environmental presence of FabI inhibitors, generating a selection pressure for organisms with alternative enzymes for this step. In fact several natural products, such as vinaxanthone from *Penicillium sp.* (Zheng et al., 2009), cephalochromin from an unspecified microbial origin (Zheng et al., 2007) or aquastatin A from *Sporothrix sp.* FN611 (Kwon et al., 2009), have been reported to inhibit FabI. One very interesting case is the FabV homolog BatG in *Pseudomonas fluorescens*, which shares 58% identity with YpFabV but exhibits the Y(X₆)K active site motif from FabI (Mattheus et al., 2010). *P. fluorescens* produces the FabI inhibitor kalimantacin/batumin. The enoyl-ACP reductase BatG is encoded in the batumin biosynthesis cluster. *P. fluorescens* gains a selection advantage over competing bacteria by inhibiting the FAS-II system via the antibacterial batumin; it protects itself from the harmful effect of batumin since it possesses BatG as a mechanism of self-resistance.

4.3 Structural characterization of BpFabI as potential drug target

B. pseudomallei possesses the enoyl-ACP reductase isoenzymes FabI and FabV. In order to characterize the structures of the complete set of enoyl-ACP reductases of this pathogen and explore the potential to generate inhibitors targeting both enzymes with sufficient affinity, crystal structures of BpFabI in the apo form and in the ternary complex with the cofactor NAD⁺ and a selection of five different inhibitors were solved.

4.3.1 Overall structure

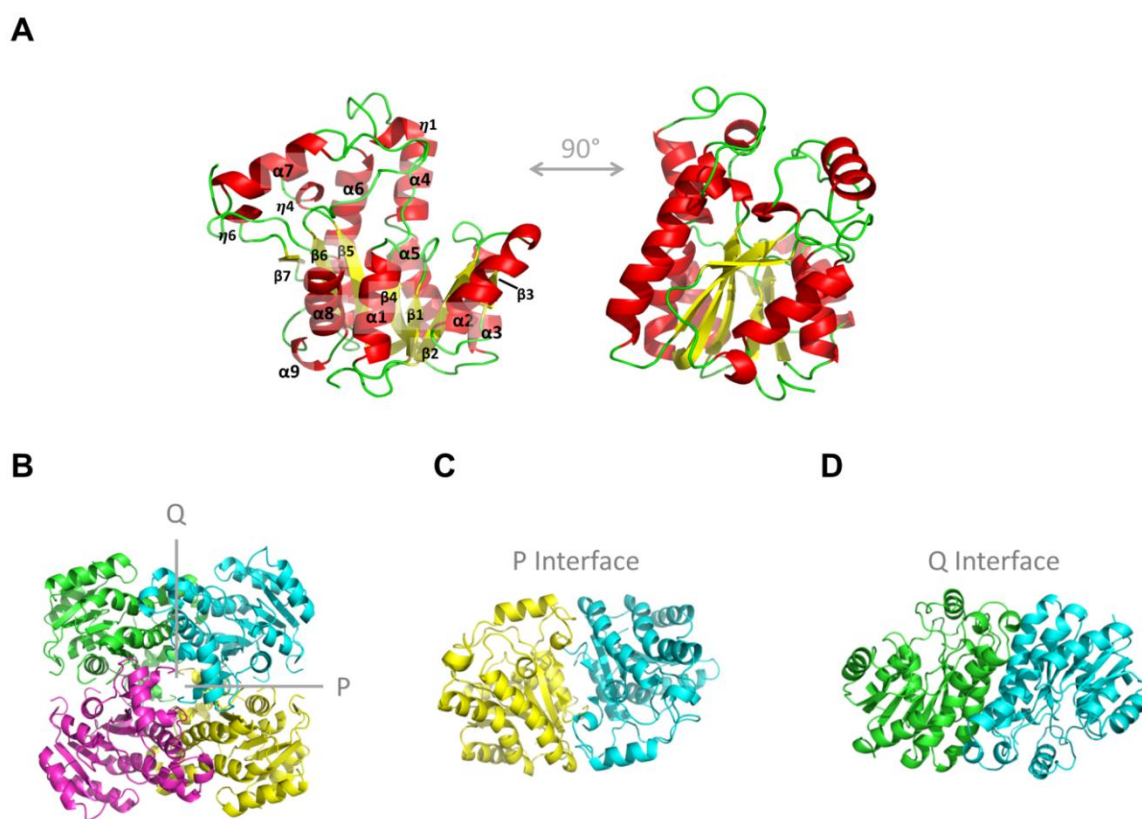


Figure 50: Overall structure of BpFabI

A) BpFabI apo monomer depicted in two orientations as ribbon diagram with α -helices in red ($\eta = 3_{10}$ helix), β -strands in yellow and loop regions in green. B) Tetrameric assembly of apo BpFabI, colored according to chain, with the P-Interface (C) and Q-interface indicated (D).

The apo structure of BpFabI shows the typical fold of FabI as a member of the diverse subfamily of SDR proteins (Figure 50A). The Rossmann fold provides stability to the

protein and builds up the NADH binding site. It is composed of a seven-stranded β -sheet with the typical strand order “3-2-1-4-5-6-7”. It is surrounded by three α -helices on each side. In the apo protein the helices α 1, α 2, α 3, α 4, α 5 and α 8 are forming an α -helical coating of the β -sheet. The ternary complexes contain an additional helix at the substrate-binding loop (α 7); therefore in the complex structures the last helix involved in the Rossmann fold is helix α 9. The Rossmann fold of FabI contains one β -strand and one α -helix less than FabV. Due to the three β -hairpin structures at the active site pocket of FabV the order of the sheet is extended to “14-5-4-3-6-11-12-13”. Remarkably the last β -strand β 14 of FabV returns to the beginning of the β -sheet. In contrast to FabV, the active site pocket in FabI is formed only by helical structures and loop regions from the C-terminal half of the polypeptide chain. β -strands are restricted to the Rossmann fold. The comparison of the newly solved apo BpFabI structure to the already deposited structure “3ek2” revealed minor changes in the overall structure. The alignment of both structures with the PDBeFOLD server in an SSM approach exhibited an RMSD value of 0.45 Å (Krissinel and Henrick, 2004). In both structures the N-terminal residue M1 was missing. At the C-terminus the last 5 and 7 residues were not represented in 3ek2 and BpFabI258, indicating that the C-terminus is not involved in interactions within the protein or through crystal contacts with other protein molecules and remains flexible. One difference between the structures is the substrate-binding loop. While this flexible loop ranging from K193 to A197 is not present in the 3ek2 structure, it is defined as loop in an open conformation in the apo BpFabI structure, since it is stabilized by a crystal contact (cf. Figure 35).

BpFabI exhibits the typical tetrameric oligomerization state of FabIs and SDR proteins in general. For FabI two characteristic interfaces have been described, the P and the Q interface (Figure 50B-D) (Baldock et al., 1998b). The interfaces of the apo BpFabI were analyzed with the PDBe PISA server (Protein Interfaces, Surfaces and Assemblies) (Krissinel and Henrick, 2007). The larger Q-interface contains 32 hydrogen bonds and 8 salt bridges. Table 21 contains the interactions from one molecule. Due to a two-fold axis of symmetry the interactions are mirrored in the second monomer. The Q-interface involves the helices α 4/ α 5 and α 6, which are connecting the Rossmann fold and the

active site pocket of FabI as “backbone” helices, and loop $\beta 3$ - $\alpha 3$. It buries a surface area of 1587.5 Å² and yields a gain of solvation free energy of $\Delta^i G = -22.3$ kcal/mol.

Table 21: Molecular interactions stabilizing Q-interface defined by PDBe PISA server

(all interactions mirrored in molecule 2)

Hydrogen bonds			Salt bridges		
Monomer 1	Dist. [Å]	Monomer 2	Monomer 1	Dist. [Å]	Monomer 2
ARG 110[NH1]	2.93	VAL 65[O]	ARG 110[NE]	2.94	ASP 68[OD1]
ARG 110[NH2]	2.89	VAL 65[O]	ARG 110[NH2]	2.83	ASP 68[OD1]
ARG 110[NE]	2.94	ASP 68[OD1]	ARG 110[NH1]	2.88	ASP 118[OD1]
ARG 110[NH2]	2.83	ASP 68[OD1]	ARG 110[NH1]	3.24	ASP 118[OD2]
SER 176[OG]	2.74	ASP 103[OD1]			
LYS 129[NZ]	2.91	LEU 105[O]			
LYS 129[NZ]	3.89	ASP 106[O]			
LYS 129[NZ]	2.91	LEU 108[O]			
ARG 110[NH1]	2.88	ASP 118[OD1]			
ARG 110[N]	3.20	TYR 122[OH]			
TYR 172[OH]	2.76	GLY 148[O]			
ARG 171[NH2]	3.03	ALA 149[O]			
ARG 171[NE]	3.08	GLU 150[O]			
TYR 172[OH]	3.46	ARG 151[O]			
ILE 153[N]	3.31	TYR 172[OH]			
LEU 105[N]	3.88	SER 176[OG]			

The smaller P-interface involves residues at the strand $\beta 7$, A179 at end of helix $\alpha 6$ and R218 on loop $\alpha 7$ - $\alpha 8$. The interface is stabilized by 12 hydrogen bonds and 4 salt bridges, again in a two-fold axis of symmetry (cf. Table 22). It covers a surface area of 1318.7 Å² and leads to a gain of solvation free energy of $\Delta^i G = -18.4$ kcal/mol.

Table 22: Molecular interactions stabilizing P-interface defined by PDBe PISA server

(all interactions mirrored in molecule 2)

Hydrogen bonds			Salt bridges		
Monomer 1	Dist. [Å]	Monomer 2	Monomer 1	Dist. [Å]	Monomer 2
ALA 179[N]	3.50	PRO 215[O]	HIS 246[ND1]	2.97	GLU 243[OE1]
ARG 218[NH2]	2.79	SER 238[O]	HIS 246[ND1]	3.40	GLU 243[OE2]
ASP 248[N]	3.29	GLY 239[O]			
SER 249[N]	2.94	GLY 239[O]			
HIS 246[ND1]	2.97	GLU 243[OE1]			
HIS 246[N]	2.95	GLU 243[OE2]			

4.3.2 Active site and NADH binding

Many crystal structures of FabI from *E. coli* or other pathogens are deposited in the PDB. Most of the structures are ternary complex structures with triclosan or another inhibitor. Only few FabI structures represent the apo form of the enzyme. In Figure 51 A the superposition of BpFabI with the two apo FabI structures of *S. aureus* (PDB ID 4alm), SaFabI (Schiebel et al., 2012) and Aquifex aeolicus (PDB ID 2p91), AaFabI, is illustrated.

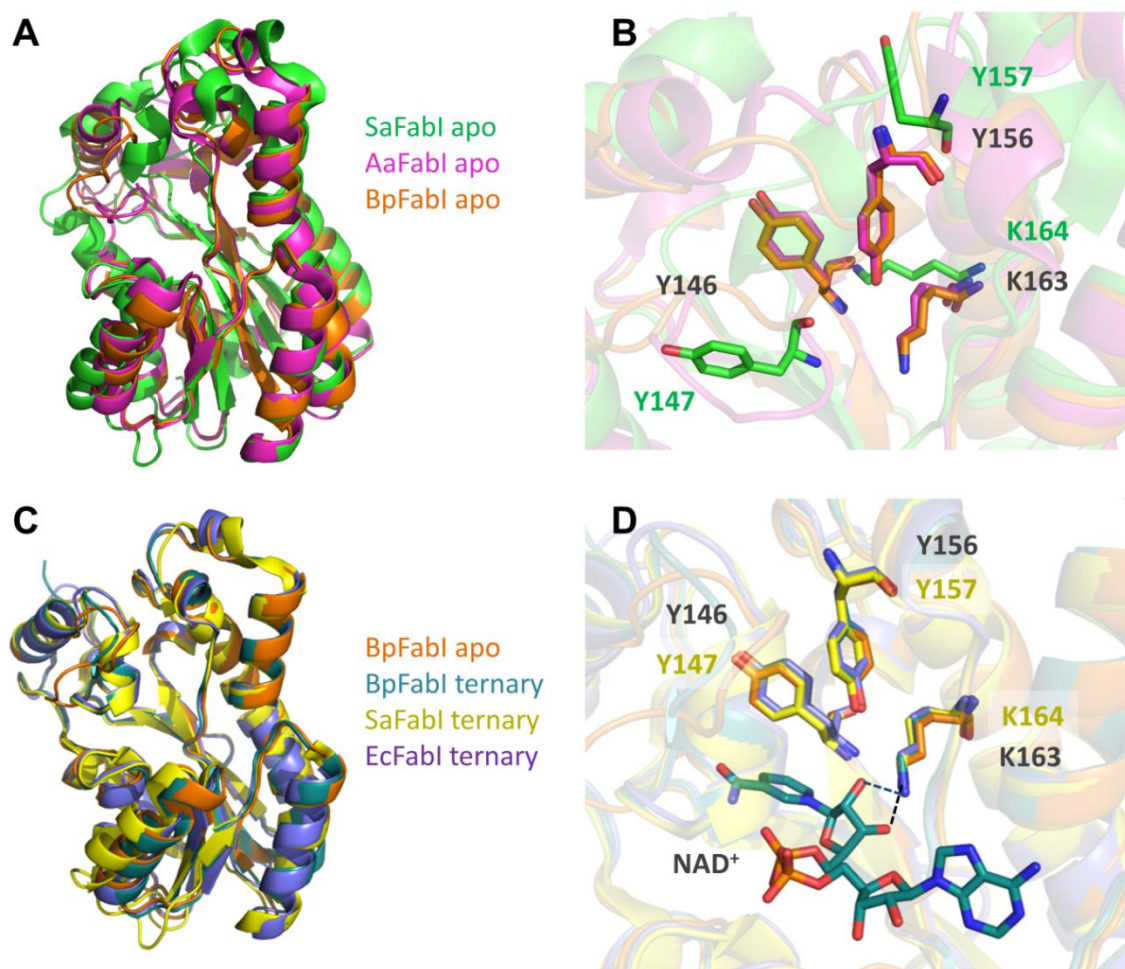


Figure 51: Active site of BpFabI

A)/B) Superposition of apo BpFabI (orange) with apo AaFabI (PDB ID 2p91; magenta) and apo SaFabI (PDB ID 4alm; green) in a ribbon diagram (A) and all-bonds representation of the active site residues (B).

C)/D) Superposition of apo BpFabI (orange) with the ternary (PT12) BpFabI complex (teal) and the ternary triclosan complexes of SaFabI (PDB ID 4all; yellow) and EcFabI (PDB ID 1c14; lilac) in a ribbon diagram (C) and all-bonds representation of the active site residues and NADH (D).

While the Rossmann fold is stable and similar in the three structures the active site pocket is less stringently ordered in the apo structures, especially in SaFabI, which exhibits different conformations in the four chains of the crystal structure (Schiebel et al., 2012). The differences in the substrate binding pockets are reflected in the high RMSD values of the structural alignment (SSM) to SaFabI and AaFabI of 1.30 Å and 0.96 Å, respectively. The active site motif of the diverse subfamily of SDR proteins in BpFabI is Y(x)₆K. The catalytic residues Y156 and K163 show the same conformation in the AaFabI and the BpFabI apo structure (Figure 51 B). This is also the case for the third characteristic residue in the FabI active site, Y146, which is thought to be involved in stabilization of the substrate. The active site residues of apo SaFabI (shifted by one residue in sequence: Y147, Y157 and K164) assume a different orientation due to the flexibility of SaFabI in the active site region. The superposition of apo BpFabI with ternary complexes of BpFabI (PT12), SaFabI (triclosan) and EcFabI (triclosan) the active site pocket reveal an increased similarity compared to the quite flexible apo-structures (Figure 51C). The ternary complex structure of BpFabI with PT12 was chosen for this comparison due to its higher resolution compared to the triclosan complex structure. Only the open substrate binding loop of the apo BpFabI exhibits a differing conformation. The RMSD value of the structural alignment (SSM) of the apo and ternary BpFabI structures is 0.54 Å. The alignment of the ternary BpFabI with the ternary triclosan complexes of EcFabI (1c14) (Qiu et al., 1999) and SaFabI (4all) (Schiebel et al., 2012) exhibited RMSD values of 0.67 Å and 1.07 Å, respectively. Even though the RMSD value of the superposition with the ternary SaFabI is quite high, the active site residues of all four structures are well aligned (Figure 51D). In the ternary structures K163 (K164 in SaFabI) interacts with the hydroxyl groups of the NADH cofactor and Y156 with the inhibitors (cf. 0). It seems that the active site residues in the apo structures are already in the right position for catalysis, when the binding pocket is not disordered as in SaFabI; in contrast to the catalytic residues in the apo structure of BpFabV, where Y235 has to be recruited into the active position by cofactor binding. However, this is not the case for all FabI structures. A binary structure (containing NAD⁺) of the FabI homolog InhA of *M. tuberculosis* (2aq8) (Oliveira et al., 2006) exhibits Y158 in a shifted orientation compared to the ternary complexes, thus a general rule cannot be derived.

The cofactor binding motif “GxxxxSxA” of the divergent superfamily of SDR proteins is present in BpFabI in the sequence GLLSNRSIA (starting with G13) (displayed in the blue box in Figure 39). The stretch is mainly involved in the binding of the pyro-phosphate group and the adenine-ribose of NAD⁺. As in FabV the cofactor in the ternary BpFabI complexes is bound through a tight hydrogen bond network involving several solvent water molecules and additional hydrophobic contacts. The binding site of BpFabI was analyzed in the PT12-complex structure (highest resolution) with the help of Ligplot+ (Laskowski and Swindells, 2011).

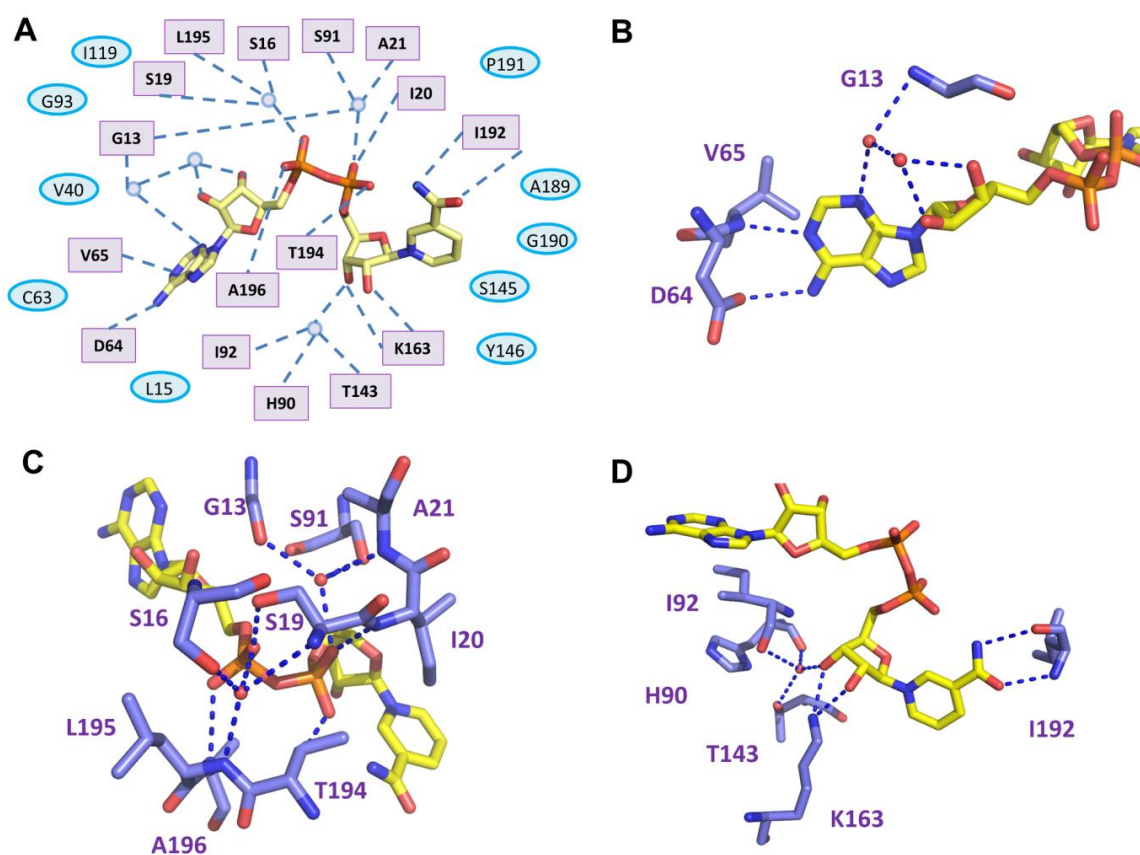


Figure 52: Cofactor binding of BpFabI

A) Schematic overview of the interactions of NADH (yellow) within BpFabI; residues providing van der Waals interactions are shown in cyan and hydrogen bonds in violet. B)/C)/D) Detailed hydrogen bond interactions (dashed lines) of the adenine ring and the ribose with the protein and solvent molecules (B).the pyrophosphate (C) and the nicotinamide ring as well as the ribose (D).

An overview of all interactions to the oxidized cofactor NAD⁺ is illustrated in Figure 52 A with the amino acids interacting via hydrogen bonds in violet and the residues involved in

hydrophobic interactions in cyan. The adenine ring (N6 and N1) forms hydrogen bonds to the side chain of D64 and the backbone nitrogen of V65. Two solvent water molecules are bridging the hydrogen bonds from the backbone nitrogen of G13 to both adenine-ribose hydroxyl groups and N3 in the adenine ring (Figure 52B). The phosphate next to the nicotinamide ring is bound with its oxygen OAZ via a water bridge to the carbonyl oxygen of G13, the hydroxyl group of S91 and the backbone nitrogen of A21. A second hydrogen bond from this atom is formed with the main chain nitrogen of I20. The hydroxyl group of T194 (hidden in the background in Figure 52C) interacts with the oxygen OAY of the same phosphate moiety. The second phosphate, next to the adenine ring, forms a hydrogen bond with its oxygen OAB to the backbone nitrogen of A196 and interacts through its oxygen OAC via a water bridge with the hydroxyl groups of S16 and S19 and the backbone nitrogen of L195 (Figure 52C). At the other end of the cofactor the amide group forms hydrogen bonds to the backbone nitrogen and carbonyl moiety of I192. The nicotinamide ribose binds with both hydroxyl groups to the catalytic residue K163. Furthermore, residues H90, I92 and T143 interact through their carbonyl groups and the hydroxyl group (T143) via a water bridge with a hydroxyl moiety (oxygen OBF) of the nicotine-ribose (Figure 52D).

In general the active site pocket and the catalytic residues as well as the cofactor binding site are quite conserved among FabIs from different species and also in BpFabI no major variation of the isoenzyme could be observed. Therefore BpFabI is a suitable target for a series of triclosan-derived inhibitors developed for FabI enzymes of different pathogens (Lu et al., 2009; Lu and Tonge, 2008, 2010; Luckner et al., 2010; Schiebel et al., 2012)

4.3.3 Inhibitor binding and substrate-binding loop dynamics

To explore the binding pocket of BpFabI for drug design, the enzyme was co-crystallized in ternary complexes with the oxidized cofactor NAD⁺ and a selection of 5 different triclosan-based inhibitors with various substituents at different positions of the A- and B-ring of the inhibitors. Furthermore apart from the well-established diphenyl ether scaffold (triclosan, PT02, PT12, and PT144) a 4-pyridone inhibitor was included in the study. The slow onset inhibitors triclosan, PT02 and PT404 inhibit BpFabV with low-nanomolar affinities and a high residence time (tR) in the enzyme (unpublished data, Weixuan Yu and Carla Neckles; and (Liu et al., 2011)), whereas the rapid reversible inhibitors PT12 and the 4-pyridone inhibitor PT155 exhibit an approximately 100-fold decreased affinity (cf. Table 23).

Table 23: Inhibitors of BpFabI (unpublished data, Weixuan Yu and Carla Neckles (Neckles, 2012); and (Liu et al., 2011))

cLogP determined with ChemBioDraw Ultra 12.0, tR = residence time, N/A = not measurable, ND = not determined.

Inhibitor	Structure	Molecular weight (Da)	cLogP	Ki (nM)	Slow onset?	tR (min)
triclosan		289.54	5.53	1.57±0.13	yes	83
PT02		228.29	4.88	1.30±0.01	yes	ND
PT12		315.36	6.21	361.47±58.31	no	N/A
PT404		311.69	5.02	0.837±0.2	yes	ND
PT155		314.42	3.26	IC ₅₀ 0.14 ± 0.02 μM [BpFabI] = 30 nM	no	N/A

The overall structure of the ternary complexes is very similar apart from the substrate-binding loop (Figure 53A). According to the hypothesis, that the slow binding behavior of

FabI inhibitors originates from the recruitment of the otherwise flexible substrate-binding loop, the loop should exhibit the closed, helical conformation for the slow onset inhibitors triclosan, PT02 and PT404. The hydrophobic residues A196 and A197 form hydrophobic contacts to the B-ring of the inhibitor, shown for triclosan in Figure 53B. This interaction was also observed in the presence of the rapid reversible inhibitor PT12, which should, according to the hypothesis, be bound in a binding pocket with an open substrate-binding loop, as shown for the ternary structure with PT155 (Figure 53A and Figure 54). This is the first time that the closed substrate-binding loop is observed in a FabI complex structure with a rapid reversible inhibitor.

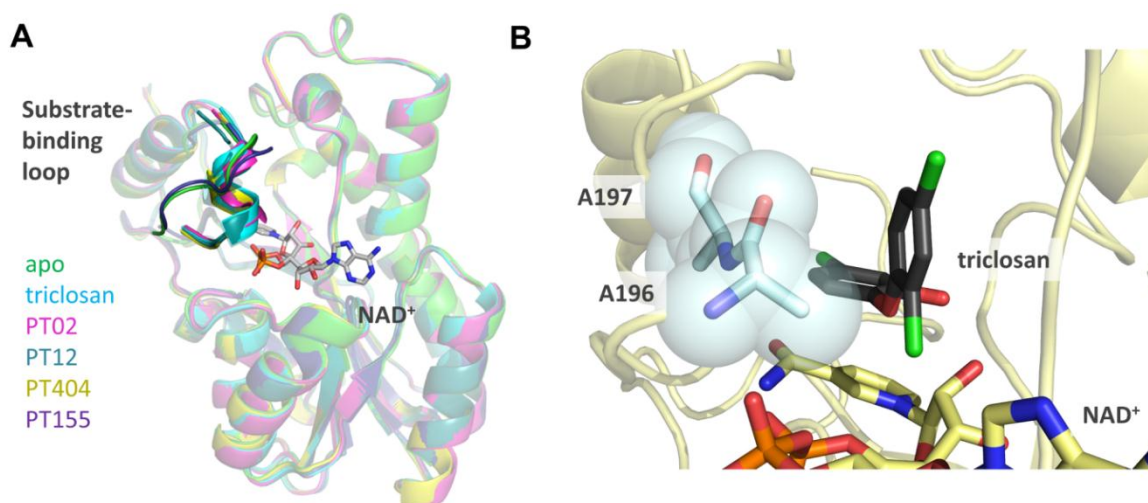


Figure 53: Substrate binding loop in ternary BpFabI complexes

A) Superposition of apo BpFabI and the ternary complexes with the substrate-binding loop and NAD⁺ (grey) highlighted in all-bonds representation. B) Hydrophobic interactions of A196 and A197 (cyan) to the B ring of triclosan (black); NAD⁺ is shown in yellow.

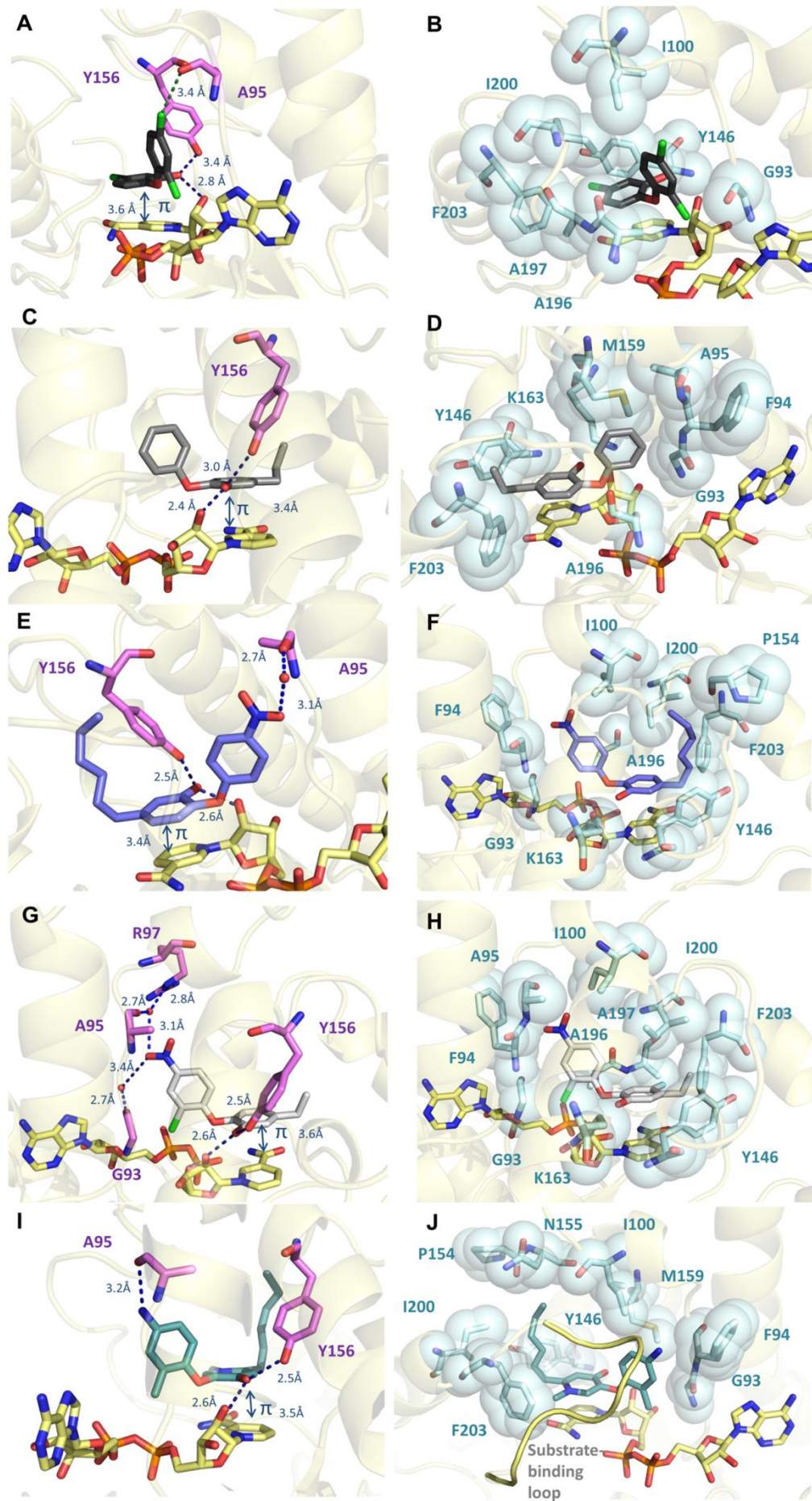
The interactions of the inhibitors with BpFabI in the ternary complexes are illustrated in detail in Figure 54 with residues forming hydrogen and halogen bonds in violet and amino acids involved in hydrophobic interactions depicted in cyan. Triclosan interacts in its known binding mode. The hydroxyl group of the A-ring forms hydrogen bonds to the hydroxyl group of the catalytic residue Y156 and the hydroxyl group of the nicotinamide-ribose (Figure 54A). The chloride substituent at the para position of the B ring forms a halogen bond to the carbonyl group of A95. The A-ring interacts in a parallel displaced π - π

stacking with the nicotinamide ring of NAD^+ . The π -stacking interaction is a central feature of all inhibitors, described in this study. Triclosan interacts through hydrophobic contacts with G93, I100, the active site residue Y146 and A196, A197, I200 and F203 on the substrate-binding (Figure 54B). PT02 contains no substituents at the B ring but a hydroxyl group and a propyl chain in the meta position at the A-ring. The hydroxyl group interacts with the hydroxyl groups of Y156 and the ribose (Figure 54C). Due to the missing substituents, the B-ring is more deeply located in the pocket (cf. Figure 55 A) and interacts therefore additionally with F94, A95, M159 and K163 in the depth of the pocket but loses some of the hydrophobic interactions at the opposite side including I100, A197 and I200 (Figure 54D). Although the interaction to A196 and I200 on the substrate-binding loop is lost, PT02 is a slow onset inhibitor. PT12 possesses a hexyl chain at the meta position of the A-ring and a nitro group at the para position of the B-ring. The nitro group is bridged via a water molecule to the carbonyl oxygen of A95 (Figure 54E). With the hexyl chain PT12 recruits additional hydrophobic interactions to P154 in the cavity, which is thought to accommodate the growing acyl chain of the substrate. Due to the bulky nitro group, the B-ring cannot enter the pocket as deep as PT02 and interacts hydrophobically with F94, A95 and I100 and I200 (Figure 54F). The interactions of PT12 to BpFabI do not essentially differ from a slow onset inhibitor such as PT02 or triclosan.

So far, there is no hint in the structure why PT12 causes a closure of the substrate-binding loop even though it is a rapid reversal inhibitor. One potential explanation might be a contribution to the stabilization of the helical, closed form of the loop by crystal contacts, which could be shown to stabilize the loop already in the apo form of BpFabI (cf. Figure 35).

Figure 54: Inhibitor binding in BpFabI (see following page)

Binding of (A/B) triclosan, (C/D) PT02, (E/F) PT12, (G/H) PT404 and (I/J) PT155 to BpFabI: Residues interacting via hydrogen bonds (blue dashed lines) and halogen bonds (green dashed line, in A) (A/C/E/G/I) are shown in violet and via van der Waals contacts in cyan with transparent spheres (B/D/F/H/J).



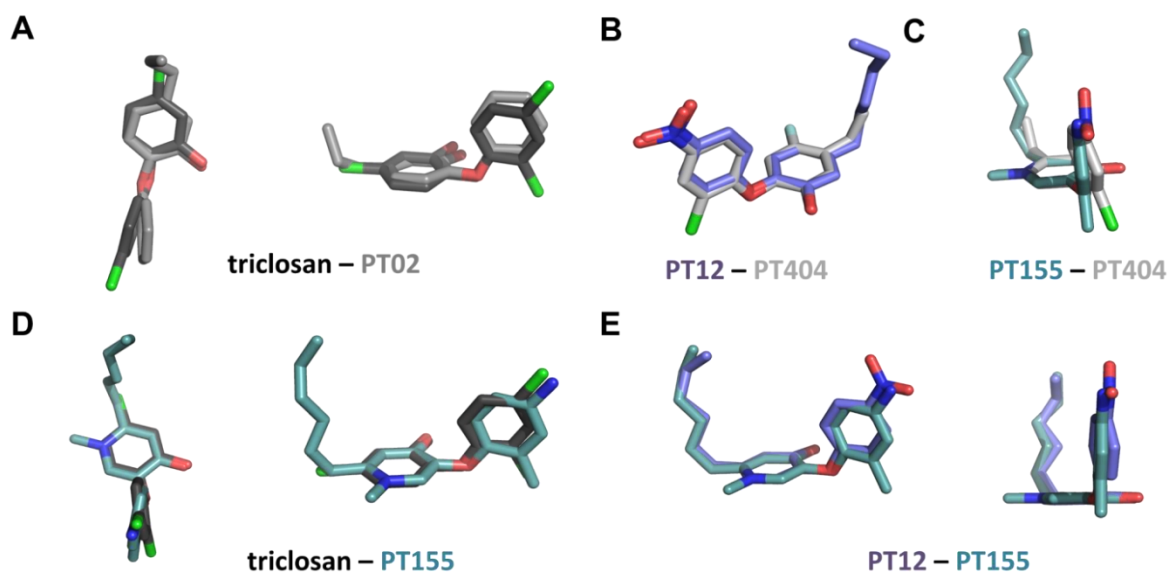


Figure 55: Comparison of inhibitor conformation

Superposition of inhibitors bound in ternary BpFbl complexes.

The slow onset inhibitor PT404 also possesses the nitro group at the B-ring but with an additional chloride at the ortho position. The A-ring exhibits a fluorine substituent at the para position and the alkyl chain is shorter (C2). Remarkably in the model of the PT404 ternary structure the nitro group shows interactions through hydrogen bonds bridged by water molecules with G93, A95 as well as delusively with R97, and not only to A95 as observed in the PT12 structure (Figure 54G). The superposition of the bound inhibitors (Figure 55B) shows no shift of the B-ring or the nitro group, which could explain the differing interactions. Both hydrogen bond mediating water molecules can be found in the two structures. The superposition of residues G93, A95 and R97 of the two ternary complexes reveals a difference in the interacting side chain of R97 (Figure 56). There is no clear electron density for this residue in both structures, indicating that it is flexible. A strong interaction would keep the side chain fixed in one conformation. This interaction is therefore not evident in both structures. The interaction of PT12 to the second water molecule, which would provide the interaction to G93, is with 4.0 Å too far apart for a regular hydrogen bond (maximum 3.6 Å). Already the contact of PT404 to the bridging water molecule with a distance of 3.4 Å is quite weak. Thus the only convincing hydrogen bond interaction of the nitro group in both inhibitors is the contact to A95.

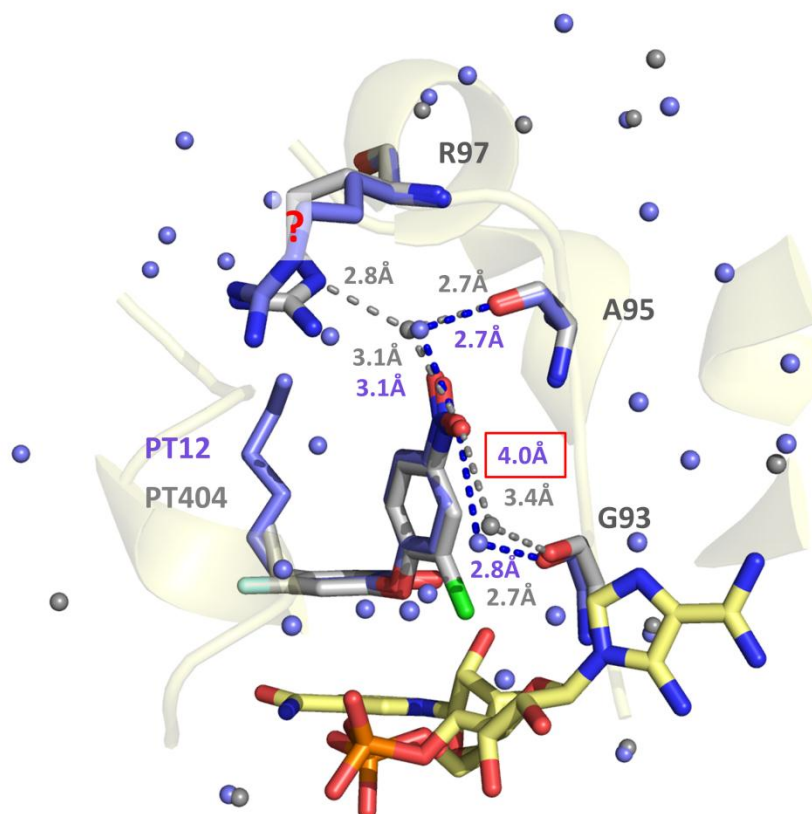


Figure 56: Interactions of the p-nitro moieties of PT12 and PT404 with their surrounding environment

The interactions of the nitro group of PT12 (lilac) and PT404 (light grey) with their surrounding residues are shown in all-bonds representation. Water molecules and hydrogen bonds (dashed lines) of the ternary complexes are colored according to the color of the inhibitor. The distance highlighted in the red box exceeds the usual length of a hydrogen bond and was therefore not considered as an interaction.

The 4-pyridone inhibitor PT155 contains an amino moiety at the para position of the B-ring and a methyl moiety at the ortho position of ring B and the para position of ring A, attached to the pyridone nitrogen. Additionally it contains a hexyl group at the meta position of the A ring, as in PT12. Apart from the hydrogen bonds of the keto group of the pyridone ring to the hydroxyl groups of Y156 and the nicotinamide-ribose, it forms a direct hydrogen bond with its amino group to the carbonyl oxygen of A95 (Figure 54I). With the hexyl chain and the ring substituents, PT155 attracts hydrophobic interactions from the depth of the pocket (G93, A94, I100, Y146, P154, N155, M159, I200 and F203) but does not recruit the interactions with the center of the substrate-binding loop (missing: A196 and A197) (Figure 54J). The substrate-binding loop is in an open conformation as in the apo structure, which is in agreement with the slow onset

hypothesis since PT155 was shown to be a rapid reversible inhibitor (Table 23). Superpositions with the inhibitors PT404, triclosan and PT12 show that the position of the A-ring is conserved but the B-ring is slightly bent out of the pocket at the bulky methyl substituent (Figure 55 C, D and E). Interestingly the rapid reversible inhibitors contain a hexyl chain at the meta position of the A-ring whereas the slow onset inhibitors have shorter substituents at this position. Previously it could be shown for BpFabI that the optimal alkyl chain length at this position is a C2 chain (Liu et al., 2011). The fact that the binding of the rapid reversible inhibitor PT12 led to the closure of the substrate-binding loop, whereas the 4-pyridone inhibitor PT155 bound in an open pocket in the crystal structure, might indicate that PT12 is “closer” to be a slow onset inhibitor. The crystal contact at the substrate binding loop might lower the number of interactions required to stabilize the substrate-binding loop in the closed helical form, since it supports the stabilized conformation. The inhibitor PT404 exhibited the best inhibition among the selection of inhibitors used in this study in *in vitro* experiments which is in good agreement with our structural analysis since it forms the highest number of hydrogen bond interactions and hydrophobic contacts in the crystal structures. The ethyl group is an optimal alkyl adduct and the fluorine substituent nicely fills a small cavity between A197 and F203. Furthermore the chlorine residue at the ortho position of ring B constrains the flexibility of the rings to each other, reducing the loss of entropy upon binding. A variety of additional inhibitors (diphenyl ethers, 2- and 4-pyridones) are available for future structural characterization. These structures may be necessary to address open questions which arose from the initially solved structures, such as the closure of the substrate-binding loop upon binding of the rapid reversible inhibitor PT12 or the differing formation of hydrogen bonds of the para-nitro groups of the B ring.

4.4 Future perspective: Inhibitors targeting FabI and FabV

The conserved active site pocket of the described FabV structures compared to FabI provides the potential to develop inhibitors that are active against both isoenzymes. Although FabV could only be co-crystallized with two 2-pyridone inhibitors (PT172 and PT173), the binding mode of these compounds corresponds to the binding of the diphenyl ether inhibitors in FabI, and therefore it is probable that also the diphenyl ethers and 4-pyridone inhibitors bind in a comparable conformation. Furthermore, the opened binding pocket of the ternary FabV complex structures can be used for modeling or docking approaches to develop new higher affinity inhibitors to the active site pocket of FabV.

In some cases also inhibitors targeting the unrelated isoenzymes FabI and FabK could be developed. Kitagawa et al. combined a 4-pyridone inhibitor, targeting FabI and a phenylimidazole inhibitor, targeting FabK to one molecule gaining a dual inhibitor, which could be shown to have potent antibacterial activity against *S. pneumonia* (FabI +FabK) (Kitagawa et al., 2007). An even more encouraging example is an aminopyridine inhibitor from GSK (GlaxoSmithKline), a precursor of the clinical candidate AFN-1252 (cf. Figure 7), which was reported to inhibit FabI and FabK and exhibited potent antibacterial activity against *S. pneumonia* and *S. aureus* without possessing an additional moiety for the inhibition of the flavo-protein FabK (Payne et al., 2002). If it is possible to target the non-related FabK with the same compound as FabI, it should be feasible to adapt the triclosan-based inhibitors to the structurally similar active site pocket of FabV.

The inhibition of the target enzyme is not the only factor which has to be taken into account during antibacterial drug development. Oral bioavailability of the agent and the penetration of the bacterial cell wall, especially in case of Gram-negative pathogens, are crucial factors. Christopher Lipinski described key properties of drugs which are affecting the pharmacokinetics (absorption, distribution, metabolism and excretion) of the agent in the human body (Lipinski et al., 2001). The "Lipinski rule of 5" state that a compound should not possess more than 5 hydrogen bond donors and 10 acceptors, the molecular weight of the compound should not exceed 500 Da and the partition coefficient logP (octanol/water) should not be higher than 5, to be an orally bioavailable drug. Antibacterial drugs, however, could be shown to be an exception of the rule of five in

various properties (cf. Table 24) (O’Shea and Moser, 2008). The authors compared physicochemical properties of drugs in general with antibacterials active against Gram-positives only and antibacterials active against Gram-negatives. Interestingly, antibacterial drugs are larger, especially the compounds that are solely active against Gram-positives have an average molecular weight of 813 Da compared to 338 Da in general drugs.

Table 24: Comparison of averaged physicochemical properties of general drugs and antibacterials with different spectrum (data from (O’Shea and Moser, 2008))

Compound property	General drugs (without antibacterials)	Antibacterials with only Gram-positive activity	Antibacterials with Gram-negative activity
MW (Da)	338	813	414
clogP	2.7	2.1	-0.1
clogD _{7.4}	1.6	-0.2	-2.8
PSA (polar surface area) (Å ²)	70	243	165
H-donor	1.6	7.1	5.1
H-acceptor	4.9	16.3	9.4

The size of antibacterials against Gram negatives is also elevated to 414 Da in average. With the size consequently also the number of hydrogen bond donors and acceptors is increased. Another difference is the reduced hydrophobicity of antibacterial drugs. The authors were also taking the clogD_{7.4} into account, the octanol/water partition coefficient at physiological pH, which is on average lower by a value of 2 than the clogP. For agents active against Gram-negatives the average clogP and clogD_{7.4} were -0.1 and -2.8, respectively, the compounds are thus very polar compared to general drugs. A reason for the difference in properties is the origin of antibacterial drugs. Most antibacterials are large and complex natural products, whereas the general drugs were often discovered from chemical small molecule libraries designed for easy synthetic chemistry. The usage of chemical libraries instead of natural product libraries in screenings for antibacterials probably contributed to the lack of new antibacterials in the last decades. However, not

only the spectrum but also the target location of the antibacterial drug is decisive for its properties. Most of the drugs against Gram-negatives act outside the inner membrane, i.e. in the periplasmic space. Agents with cytoplasmic targets (as the FAS-II enzymes) have to traverse the inner membrane and therefore have to exhibit some lipophilicity. Analysis of the agents active against cytoplasmic targets in Gram-negatives (6 chemical classes) revealed molecular masses ranging from 337 to 586 Da, and logP values of -0.5 to 3.0 (Silver, 2011). Remarkably only 2 (tetracycline and chloramphenicol) of the 6 classes which are passively diffusing into the Gram-negative cytoplasm (in *E. coli*) are natural products, the remaining classes are synthetics.

Concerning the triclosan-based inhibitors in this study, the greatest problem to meet these conditions is the high hydrophobicity of the compounds. The clogP value of the diphenyl ether inhibitors is around 5. A switch to the pyridone scaffold, which is also less susceptible to drug metabolism in phase II conjugation reactions, would lead to the reduction of the logP values of the inhibitors. The 4-pyridone inhibitor PT155 exhibits a clogP of only 3.26 (cf. Table 23). A possibility to further reduce the hydrophobicity might be to introduce additional nitrogen atoms into the ring system or attach polar substituents. The long alkyl chain could be shortened to 2-3 carbon atoms, since a longer chain length does not improve the affinities in BpFabI (Liu et al., 2011) or YpFabV (Carla Neckles, unpublished data (Neckles, 2012)). An oxygen atom (ether) could be introduced into the alkyl-chain as it can be observed in the clinical trial candidate CG400549 (cf. Figure 7). The 4-pyridone scaffold is of particular interest in the approach to generate inhibitors against both isoenzymes, FabI and FabV, since the 4-pyridine agents PT156 and PT157 exhibited promising IC₅₀ values of <1μM for BpFabI, BpFabV and YpFabV (Carla Neckles, unpublished data (Neckles, 2012), compounds synthesized by Dr. Pan Pan).

The structural data presented in this thesis as well as the kinetic data of our collaborators Carla Neckles, Nina Liu and Weixuan Yu (Prof. Peter Tonge's laboratory, Stony Brook University, NY), hold a lot of promise that an effective inhibitor against FabV or maybe also against both isoenzymes, FabI and FabV can be derived from the previously developed triclosan-based inhibitors.

5. References

- Achtman, M., Zurth, K., Morelli, G., Torrea, G., Guiyoule, A., and Carniel, E. (1999). *Yersinia pestis*, the cause of plague, is a recently emerged clone of *Yersinia pseudotuberculosis*. *Proc Natl Acad Sci U S A* *96*, 14043-14048.
- Adams, P.D., Afonine, P.V., Bunkoczi, G., Chen, V.B., Davis, I.W., Echols, N., Headd, J.J., Hung, L.W., Kapral, G.J., Grosse-Kunstleve, R.W., *et al.* (2010). PHENIX: a comprehensive Python-based system for macromolecular structure solution. *Acta Crystallogr D Biol Crystallogr* *66*, 213-221.
- Alexandre Yersin, B.W. (2010). Etymologia: yersinia. *Emerg Infect Dis* *16*, 496.
- Athan, E., Allworth, A.M., Engler, C., Bastian, I., and Cheng, A.C. (2005). Melioidosis in tsunami survivors. *Emerg Infect Dis* *11*, 1638-1639.
- Balaban, N.Q., Merrin, J., Chait, R., Kowalik, L., and Leibler, S. (2004). Bacterial persistence as a phenotypic switch. *Science* *305*, 1622-1625.
- Baldock, C., de Boer, G.J., Rafferty, J.B., Stuitje, A.R., and Rice, D.W. (1998a). Mechanism of action of diazaborines. *Biochemical pharmacology* *55*, 1541-1549.
- Baldock, C., Rafferty, J.B., Sedelnikova, S.E., Baker, P.J., Stuitje, A.R., Slabas, A.R., Hawkes, T.R., and Rice, D.W. (1996). A mechanism of drug action revealed by structural studies of enoyl reductase. *Science* *274*, 2107-2110.
- Baldock, C., Rafferty, J.B., Stuitje, A.R., Slabas, A.R., and Rice, D.W. (1998b). The X-ray structure of *Escherichia coli* enoyl reductase with bound NAD⁺ at 2.1 Å resolution. *Journal of Molecular Biology* *284*, 1529-1546.
- Banerjee, A., Dubnau, E., Quemard, A., Balasubramanian, V., Um, K.S., Wilson, T., Collins, D., de Lisle, G., and Jacobs, W.R., Jr. (1994). *inhA*, a gene encoding a target for isoniazid and ethionamide in *Mycobacterium tuberculosis*. *Science* *263*, 227-230.
- Bassetti, M., Ginocchio, F., Mikulska, M., Taramasso, L., and Giacobbe, D.R. (2011). Will new antimicrobials overcome resistance among Gram-negatives? Expert review of anti-infective therapy *9*, 909-922.
- Battye, T.G., Kontogiannis, L., Johnson, O., Powell, H.R., and Leslie, A.G. (2011). iMOSFLM: a new graphical interface for diffraction-image processing with MOSFLM. *Acta Crystallogr D Biol Crystallogr* *67*, 271-281.
- Bertani, G. (1951). Studies on lysogenesis. I. The mode of phage liberation by lysogenic *Escherichia coli*. *J Bacteriol* *62*, 293-300.
- Blair, J.M., and Piddock, L.J. (2009). Structure, function and inhibition of RND efflux pumps in Gram-negative bacteria: an update. *Curr Opin Microbiol* *12*, 512-519.
- Blow, D. (2003). *Outline of Crystallography for Biologists*. New York, Oxford University Press.
- Boe, L., Danielsen, M., Knudsen, S., Petersen, J.B., Maymann, J., and Jensen, P.R. (2000). The frequency of mutators in populations of *Escherichia coli*. *Mutation research* *448*, 47-55.
- Bos, K.I., Schuenemann, V.J., Golding, G.B., Burbano, H.A., Waglechner, N., Coombes, B.K., McPhee, J.B., DeWitte, S.N., Meyer, M., Schmedes, S., *et al.* (2011). A draft genome of *Yersinia pestis* from victims of the Black Death. *Nature* *478*, 506-510.
- Boucher, H.W., Talbot, G.H., Bradley, J.S., Edwards, J.E., Gilbert, D., Rice, L.B., Scheld, M., Spellberg, B., and Bartlett, J. (2009). Bad bugs, no drugs: no ESCAPE! An update from the Infectious Diseases Society of America. *Clin Infect Dis* *48*, 1-12.
- Buehner, M., Ford, G.C., Moras, D., Olsen, K.W., and Rossmann, M.G. (1973). D-glyceraldehyde-3-phosphate dehydrogenase: three-dimensional structure and evolutionary significance. *Proc Natl Acad Sci U S A* *70*, 3052-3054.
- Butler, T. (2009). Plague into the 21st century. *Clin Infect Dis* *49*, 736-742.

References

- Cantaloube, S., Veyron-Churlet, R., Haddache, N., Daffe, M., and Zerbib, D. (2011). The Mycobacterium tuberculosis FAS-II dehydratases and methyltransferases define the specificity of the mycolic acid elongation complexes. *PLoS one* *6*, e29564.
- CCP4 (1994). CCP4 (Collaborative Computational Project, Number 4) The CCP4 suite: programs for protein crystallography. *Acta Crystallogr D Biol Crystallogr* *50*, 760-763.
- Chan, D.I., and Vogel, H.J. (2010). Current understanding of fatty acid biosynthesis and the acyl carrier protein. *Biochem J* *430*, 1-19.
- Chayen, N.E. (2004). Turning protein crystallisation from an art into a science. *Current opinion in structural biology* *14*, 577-583.
- Chen, I., and Dubnau, D. (2004). DNA uptake during bacterial transformation. *Nat Rev Microbiol* *2*, 241-249.
- Chen, V.B., Arendall, W.B., 3rd, Headd, J.J., Keedy, D.A., Immormino, R.M., Kapral, G.J., Murray, L.W., Richardson, J.S., and Richardson, D.C. (2010). MolProbity: all-atom structure validation for macromolecular crystallography. *Acta Crystallogr D Biol Crystallogr* *66*, 12-21.
- Cheng, A.C. (2010). Melioidosis: advances in diagnosis and treatment. *Current opinion in infectious diseases* *23*, 554-559.
- Cheng, A.C., and Currie, B.J. (2005). Melioidosis: epidemiology, pathophysiology, and management. *Clin Microbiol Rev* *18*, 383-416.
- Cheng, A.C., Stephens, D.P., Anstey, N.M., and Currie, B.J. (2004). Adjunctive granulocyte colony-stimulating factor for treatment of septic shock due to melioidosis. *Clin Infect Dis* *38*, 32-37.
- Chopra, I., O'Neill, A.J., and Miller, K. (2003). The role of mutators in the emergence of antibiotic-resistant bacteria. *Drug resistance updates : reviews and commentaries in antimicrobial and anticancer chemotherapy* *6*, 137-145.
- Clark, D.P., DeMendoza, D., Polacco, M.L., and Cronan, J.E., Jr. (1983). Beta-hydroxydecanoyl thio ester dehydrase does not catalyze a rate-limiting step in Escherichia coli unsaturated fatty acid synthesis. *Biochemistry* *22*, 5897-5902.
- Currie, B.J., and Jacups, S.P. (2003). Intensity of rainfall and severity of melioidosis, Australia. *Emerg Infect Dis* *9*, 1538-1542.
- Debono, M., Barnhart, M., Carrell, C.B., Hoffmann, J.A., Occolowitz, J.L., Abbott, B.J., Fukuda, D.S., Hamill, R.L., Biemann, K., and Herlihy, W.C. (1987). A21978C, a complex of new acidic peptide antibiotics: isolation, chemistry, and mass spectral structure elucidation. *J Antibiot (Tokyo)* *40*, 761-777.
- DeSalva, S.J., Kong, B.M., and Lin, Y.J. (1989). Triclosan: a safety profile. *American journal of dentistry* *2 Spec No*, 185-196.
- Dessen, A., Quemard, A., Blanchard, J.S., Jacobs, W.R., Jr., and Sacchettini, J.C. (1995). Crystal structure and function of the isoniazid target of Mycobacterium tuberculosis. *Science* *267*, 1638-1641.
- Duncan, C.J., and Scott, S. (2005). What caused the Black Death? *Postgraduate medical journal* *81*, 315-320.
- Egan, A.F., and Russell, R.R. (1973). Conditional mutations affecting the cell envelope of Escherichia coli K-12. *Genetical research* *21*, 139-152.
- Emsley, P., and Cowtan, K. (2004). Coot: model-building tools for molecular graphics. *Acta Crystallogr D Biol Crystallogr* *60*, 2126-2132.
- Escaich, S., L. Prouvensier, M. Saccomani, L. Durant, A. Denis, C. Soulama, F. Faivre, Y. Bonvin, V. Gerusz, and M. Oxoby (2008). MUT37307 FabI inhibitor: in vitro and in vivo antibacterial activity against S. aureus. 48th Intersci Conf Antimicrob Agents Chemother, Washington, DC American Society for Microbiology, Washington, DC *Abstr F1-333*.
- Evans, P. (2006). Scaling and assessment of data quality. *Acta Crystallogr D Biol Crystallogr* *62*, 72-82.
- Fan, F., Yan, K., Wallis, N.G., Reed, S., Moore, T.D., Rittenhouse, S.F., DeWolf, W.E., Jr., Huang, J., McDevitt, D., Miller, W.H., *et al.* (2002). Defining and combating the mechanisms of triclosan resistance in clinical isolates of Staphylococcus aureus. *Antimicrob Agents Chemother* *46*, 3343-3347.

References

- Gal, D., Mayo, M., Spencer, E., Cheng, A.C., and Currie, B.J. (2005). Short report: application of a polymerase chain reaction to detect *Burkholderia pseudomallei* in clinical specimens from patients with suspected melioidosis. *The American journal of tropical medicine and hygiene* *73*, 1162-1164.
- Galimand, M., Carniel, E., and Courvalin, P. (2006). Resistance of *Yersinia pestis* to antimicrobial agents. *Antimicrob Agents Chemother* *50*, 3233-3236.
- Ghosh, D., Sawicki, M., Pletnev, V., Erman, M., Ohno, S., Nakajin, S., and Duax, W.L. (2001). Porcine carbonyl reductase. structural basis for a functional monomer in short chain dehydrogenases/reductases. *J Biol Chem* *276*, 18457-18463.
- Giske, C.G., Monnet, D.L., Cars, O., and Carmeli, Y. (2008). Clinical and economic impact of common multidrug-resistant gram-negative bacilli. *Antimicrob Agents Chemother* *52*, 813-821.
- Gouet, P., Robert, X., and Courcelle, E. (2003). ESPript/ENDscript: Extracting and rendering sequence and 3D information from atomic structures of proteins. *Nucleic Acids Res* *31*, 3320-3323.
- Guiyoule, A., Gerbaud, G., Buchrieser, C., Galimand, M., Rahalison, L., Chanteau, S., Courvalin, P., and Carniel, E. (2001). Transferable plasmid-mediated resistance to streptomycin in a clinical isolate of *Yersinia pestis*. *Emerg Infect Dis* *7*, 43-48.
- Guiyoule, A., Rasoamanana, B., Buchrieser, C., Michel, P., Chanteau, S., and Carniel, E. (1997). Recent emergence of new variants of *Yersinia pestis* in Madagascar. *J Clin Microbiol* *35*, 2826-2833.
- Heath, R.J., and Rock, C.O. (1995). Enoyl-acyl carrier protein reductase (*fabI*) plays a determinant role in completing cycles of fatty acid elongation in *Escherichia coli*. *J Biol Chem* *270*, 26538-26542.
- Heath, R.J., and Rock, C.O. (2000). A triclosan-resistant bacterial enzyme. *Nature* *406*, 145-146.
- Heath, R.J., and Rock, C.O. (2002). The Claisen condensation in biology. *Natural product reports* *19*, 581-596.
- Heath, R.J., and Rock, C.O. (2004). Fatty acid biosynthesis as a target for novel antibacterials. *Curr Opin Investig Drugs* *5*, 146-153.
- Heath, R.J., Su, N., Murphy, C.K., and Rock, C.O. (2000). The enoyl-[acyl-carrier-protein] reductases *FabI* and *FabL* from *Bacillus subtilis*. *J Biol Chem* *275*, 40128-40133.
- Heath, R.J., Yu, Y.T., Shapiro, M.A., Olson, E., and Rock, C.O. (1998). Broad spectrum antimicrobial biocides target the *FabI* component of fatty acid synthesis. *J Biol Chem* *273*, 30316-30320.
- Hentzer, M., Eberl, L., Nielsen, J., and Givskov, M. (2003). Quorum sensing : a novel target for the treatment of biofilm infections. *BioDrugs : clinical immunotherapeutics, biopharmaceuticals and gene therapy* *17*, 241-250.
- Hirschbeck, M.W., Kuper, J., Lu, H., Liu, N., Neckles, C., Shah, S., Wagner, S., Sotriffer, C.A., Tonge, P.J., and Kisker, C. (2012). Structure of the *Yersinia pestis* *FabV* enoyl-ACP reductase and its interaction with two 2-pyridone inhibitors. *Structure* *20*, 89-100.
- Hoffmeister, M., Piotrowski, M., Nowitzki, U., and Martin, W. (2005). Mitochondrial trans-2-enoyl-CoA reductase of wax ester fermentation from *Euglena gracilis* defines a new family of enzymes involved in lipid synthesis. *J Biol Chem* *280*, 4329-4338.
- Holm, L., and Park, J. (2000). DaliLite workbench for protein structure comparison. *Bioinformatics* *16*, 566-567.
- Jenni, S., Leibundgut, M., Boehringer, D., Frick, C., Mikolasek, B., and Ban, N. (2007). Structure of fungal fatty acid synthase and implications for iterative substrate shuttling. *Science* *316*, 254-261.
- Kabsch, W. (2010). Xds. *Acta Crystallogr D Biol Crystallogr* *66*, 125-132.
- Kabsch, W., and Sander, C. (1983). Dictionary of protein secondary structure: pattern recognition of hydrogen-bonded and geometrical features. *Biopolymers* *22*, 2577-2637.
- Kallberg, Y., Oppermann, U., Jornvall, H., and Persson, B. (2002). Short-chain dehydrogenases/reductases (SDRs). *Eur J Biochem* *269*, 4409-4417.

References

- Karlowsky, J.A., Kaplan, N., Hafkin, B., Hoban, D.J., and Zhanel, G.G. (2009). AFN-1252, a FabI inhibitor, demonstrates a *Staphylococcus*-specific spectrum of activity. *Antimicrob Agents Chemother* 53, 3544-3548.
- Kavanagh, K.L., Jornvall, H., Persson, B., and Oppermann, U. (2008). Medium- and short-chain dehydrogenase/reductase gene and protein families : the SDR superfamily: functional and structural diversity within a family of metabolic and regulatory enzymes. *Cell Mol Life Sci* 65, 3895-3906.
- Kim, K.H., Ha, B.H., Kim, S.J., Hong, S.K., Hwang, K.Y., and Kim, E.E. (2011). Crystal Structures of Enoyl-ACP Reductases I (FabI) and III (FabL) from *B. subtilis*. *J Mol Biol* 406, 403-415.
- Kitagawa, H., Ozawa, T., Takahata, S., Iida, M., Saito, J., and Yamada, M. (2007). Phenylimidazole derivatives of 4-pyridone as dual inhibitors of bacterial enoyl-acyl carrier protein reductases FabI and FabK. *J Med Chem* 50, 4710-4720.
- Kool, J.L. (2005). Risk of person-to-person transmission of pneumonic plague. *Clin Infect Dis* 40, 1166-1172.
- Krissinel, E., and Henrick, K. (2004). Secondary-structure matching (SSM), a new tool for fast protein structure alignment in three dimensions. *Acta Crystallogr D Biol Crystallogr* 60, 2256-2268.
- Krissinel, E., and Henrick, K. (2007). Inference of macromolecular assemblies from crystalline state. *J Mol Biol* 372, 774-797.
- Kuo, M.R., Morbidoni, H.R., Alland, D., Sneddon, S.F., Gourlie, B.B., Staveski, M.M., Leonard, M., Gregory, J.S., Janjigian, A.D., Yee, C., *et al.* (2003). Targeting tuberculosis and malaria through inhibition of Enoyl reductase: compound activity and structural data. *J Biol Chem* 278, 20851-20859.
- Kwon, Y.J., Fang, Y., Xu, G.H., and Kim, W.G. (2009). Aquastatin A, a new inhibitor of enoyl-acyl carrier protein reductase from *Sporothrix* sp. FN611. *Biological & pharmaceutical bulletin* 32, 2061-2064.
- Laemmli, U.K. (1970). Cleavage of structural proteins during the assembly of the head of bacteriophage T4. *Nature* 227, 680-685.
- Langer, G., Cohen, S.X., Lamzin, V.S., and Perrakis, A. (2008). Automated macromolecular model building for X-ray crystallography using ARP/wARP version 7. *Nat Protoc* 3, 1171-1179.
- Laskowski, R.A., and Swindells, M.B. (2011). LigPlot+: multiple ligand-protein interaction diagrams for drug discovery. *J Chem Inf Model* 51, 2778-2786.
- Leitenberg, M. (2001). Biological weapons in the twentieth century: a review and analysis. *Critical reviews in microbiology* 27, 267-320.
- Lewis, K. (2005). Persister cells and the riddle of biofilm survival. *Biochemistry Biokhimiia* 70, 267-274.
- Li, H., Zhang, X., Bi, L., He, J., and Jiang, T. (2011). Determination of the crystal structure and active residues of FabV, the enoyl-ACP reductase from *Xanthomonas oryzae*. *PloS one* 6, e26743.
- Limmathurotsakul, D., and Peacock, S.J. (2011). Melioidosis: a clinical overview. *Br Med Bull* 99, 125-139.
- Lipinski, C.A., Lombardo, F., Dominy, B.W., and Feeney, P.J. (2001). Experimental and computational approaches to estimate solubility and permeability in drug discovery and development settings. *Advanced drug delivery reviews* 46, 3-26.
- Liu, N., Cummings, J.E., England, K., Slayden, R.A., and Tonge, P.J. (2011). Mechanism and inhibition of the FabI enoyl-ACP reductase from *Burkholderia pseudomallei*. *J Antimicrob Chemother* 66, 564-573.
- Lowell, J.L., Wagner, D.M., Atshabar, B., Antolin, M.F., Vogler, A.J., Keim, P., Chu, M.C., and Gage, K.L. (2005). Identifying sources of human exposure to plague. *J Clin Microbiol* 43, 650-656.
- Lu, H., England, K., am Ende, C., Truglio, J.J., Luckner, S., Reddy, B.G., Marlenee, N.L., Knudson, S.E., Knudson, D.L., Bowen, R.A., *et al.* (2009). Slow-onset inhibition of the FabI enoyl reductase from *francisella tularensis*: residence time and in vivo activity. *ACS Chem Biol* 4, 221-231.
- Lu, H., and Tonge, P.J. (2008). Inhibitors of FabI, an enzyme drug target in the bacterial fatty acid biosynthesis pathway. *Acc Chem Res* 41, 11-20.
- Lu, H., and Tonge, P.J. (2010). Mechanism and inhibition of the FabV enoyl-ACP reductase from *Burkholderia mallei*. *Biochemistry* 49, 1281-1289.

References

- Luckner, S.R., Liu, N., am Ende, C.W., Tonge, P.J., and Kisker, C. (2010). A slow, tight binding inhibitor of InhA, the enoyl-acyl carrier protein reductase from *Mycobacterium tuberculosis*. *J Biol Chem* **285**, 14330-14337.
- Luckner, S.R., Machutta, C.A., Tonge, P.J., and Kisker, C. (2009). Crystal structures of *Mycobacterium tuberculosis* KasA show mode of action within cell wall biosynthesis and its inhibition by thiolactomycin. *Structure* **17**, 1004-1013.
- Machutta, C.A., Bommineni, G.R., Luckner, S.R., Kapilashrami, K., Ruzsicska, B., Simmerling, C., Kisker, C., and Tonge, P.J. (2010). Slow onset inhibition of bacterial beta-ketoacyl-acyl carrier protein synthases by thiolactomycin. *J Biol Chem* **285**, 6161-6169.
- Maharjan, B., Chantratita, N., Vesaratchavest, M., Cheng, A., Wuthiekanun, V., Chierakul, W., Chaowagul, W., Day, N.P., and Peacock, S.J. (2005). Recurrent melioidosis in patients in northeast Thailand is frequently due to reinfection rather than relapse. *J Clin Microbiol* **43**, 6032-6034.
- Marrakchi, H., Choi, K.H., and Rock, C.O. (2002a). A new mechanism for anaerobic unsaturated fatty acid formation in *Streptococcus pneumoniae*. *J Biol Chem* **277**, 44809-44816.
- Marrakchi, H., Laneelle, G., and Quemard, A. (2000). InhA, a target of the antituberculous drug isoniazid, is involved in a mycobacterial fatty acid elongation system, FAS-II. *Microbiology* **146 (Pt 2)**, 289-296.
- Marrakchi, H., Zhang, Y.M., and Rock, C.O. (2002b). Mechanistic diversity and regulation of Type II fatty acid synthesis. *Biochemical Society transactions* **30**, 1050-1055.
- Massengo-Tiasse, R.P., and Cronan, J.E. (2008). *Vibrio cholerae* FabV defines a new class of enoyl-acyl carrier protein reductase. *J Biol Chem* **283**, 1308-1316.
- Mattheus, W., Masschelein, J., Gao, L.J., Herdewijn, P., Landuyt, B., Volckaert, G., and Lavigne, R. (2010). The kalimantacin/batumin biosynthesis operon encodes a self-resistance isoform of the FabI bacterial target. *Chem Biol* **17**, 1067-1071.
- Matthews, B.W. (1968). Solvent content of protein crystals. *J Mol Biol* **33**, 491-497.
- McCoy, A.J., Grosse-Kunstleve, R.W., Adams, P.D., Winn, M.D., Storoni, L.C., and Read, R.J. (2007). Phaser crystallographic software. *J Appl Crystallogr* **40**, 658-674.
- Meyer, A.L. (2005). Prospects and challenges of developing new agents for tough Gram-negatives. *Curr Opin Pharmacol* **5**, 490-494.
- Morris, R.J., Perrakis, A., and Lamzin, V.S. (2003). ARP/wARP and automatic interpretation of protein electron density maps. *Methods in enzymology* **374**, 229-244.
- Murshudov, G.N., Vagin, A.A., and Dodson, E.J. (1997). Refinement of macromolecular structures by the maximum-likelihood method. *Acta Crystallogr D Biol Crystallogr* **53**, 240-255.
- Neckles, C.S., S.; Pan, P.; Bommineni, G. R.; Hirschbeck, M.W.; Yu, W.; Liu, N.; Kisker, C.; Tonge, P. J. (2012). Mechanism, Inhibition and Comparison of *Yersinia pestis* Enoyl-ACP Reductase, FabV, to *Burkholderia pseudomallei* Enoyl-ACP Reductases, FabI and FabV. manuscript in preparation.
- Novak, R., and Shlaes, D.M. (2010). The pleuromutilin antibiotics: a new class for human use. *Curr Opin Investig Drugs* **11**, 182-191.
- O'Shea, R., and Moser, H.E. (2008). Physicochemical Properties of Antibacterial Compounds: Implications for Drug Discovery. *Journal of Medicinal Chemistry* **51**, 2871-2878.
- Oliveira, J.S., Pereira, J.H., Canduri, F., Rodrigues, N.C., de Souza, O.N., de Azevedo, W.F., Jr., Basso, L.A., and Santos, D.S. (2006). Crystallographic and pre-steady-state kinetics studies on binding of NADH to wild-type and isoniazid-resistant enoyl-ACP(CoA) reductase enzymes from *Mycobacterium tuberculosis*. *J Mol Biol* **359**, 646-666.
- Oppermann, U., Filling, C., Hult, M., Shafqat, N., Wu, X., Lindh, M., Shafqat, J., Nordling, E., Kallberg, Y., Persson, B., *et al.* (2003). Short-chain dehydrogenases/reductases (SDR): the 2002 update. *Chem Biol Interact* **143-144**, 247-253.
- Painter, J., and Merritt, E.A. (2006). Optimal description of a protein structure in terms of multiple groups undergoing TLS motion. *Acta Crystallogr D Biol Crystallogr* **62**, 439-450.

References

- Pannu, N.S., Murshudov, G.N., Dodson, E.J., and Read, R.J. (1998). Incorporation of prior phase information strengthens maximum-likelihood structure refinement. *Acta Crystallogr D Biol Crystallogr* *54*, 1285-1294.
- Pantoliano, M.W., Petrella, E.C., Kwasnoski, J.D., Lobanov, V.S., Myslik, J., Graf, E., Carver, T., Asel, E., Springer, B.A., Lane, P., *et al.* (2001). High-density miniaturized thermal shift assays as a general strategy for drug discovery. *J Biomol Screen* *6*, 429-440.
- Parikh, S.L., Xiao, G., and Tonge, P.J. (2000). Inhibition of InhA, the enoyl reductase from *Mycobacterium tuberculosis*, by triclosan and isoniazid. *Biochemistry* *39*, 7645-7650.
- Park, H.S., Yoon, Y.M., Jung, S.J., Kim, C.M., Kim, J.M., and Kwak, J.H. (2007). Antistaphylococcal activities of CG400549, a new bacterial enoyl-acyl carrier protein reductase (FabI) inhibitor. *J Antimicrob Chemother* *60*, 568-574.
- Parris, K.D., Lin, L., Tam, A., Mathew, R., Hixon, J., Stahl, M., Fritz, C.C., Seehra, J., and Somers, W.S. (2000). Crystal structures of substrate binding to *Bacillus subtilis* holo-(acyl carrier protein) synthase reveal a novel trimeric arrangement of molecules resulting in three active sites. *Structure* *8*, 883-895.
- Patterson, A.L. (1934). A Fourier Series Method for the Determination of the Components of Interatomic Distances in Crystals. *Physical Review* *46*, 372-376.
- Patterson, A.L. (1935). A direct method for the determination of the components of inter-atomic distances in crystals. *Zeitschrift fuer Krystallographie* *90*, 517-554.
- Payne, D.J., Miller, W.H., Berry, V., Brosky, J., Burgess, W.J., Chen, E., DeWolf Jr, W.E., Jr., Fosberry, A.P., Greenwood, R., Head, M.S., *et al.* (2002). Discovery of a novel and potent class of FabI-directed antibacterial agents. *Antimicrob Agents Chemother* *46*, 3118-3124.
- Payne, D.J., Warren, P.V., Holmes, D.J., Ji, Y., and Lonsdale, J.T. (2001). Bacterial fatty-acid biosynthesis: a genomics-driven target for antibacterial drug discovery. *Drug Discov Today* *6*, 537-544.
- Peacock, S.J. (2006). Melioidosis. *Current opinion in infectious diseases* *19*, 421-428.
- Perry, R.D., and Fetherston, J.D. (1997). *Yersinia pestis*--etiologic agent of plague. *Clin Microbiol Rev* *10*, 35-66.
- Perutz, M.F. (1956). Isomorphous replacement and phase determination in non-centrosymmetric space groups. *Acta Cryst* *9*, 867-873.
- Peterson, L.R. (2009). Bad bugs, no drugs: no ESCAPE revisited. *Clin Infect Dis* *49*, 992-993.
- Petrek, M., Kosinova, P., Koca, J., and Otyepka, M. (2007). MOLE: a Voronoi diagram-based explorer of molecular channels, pores, and tunnels. *Structure* *15*, 1357-1363.
- Petrek, M., Otyepka, M., Banas, P., Kosinova, P., Koca, J., and Damborsky, J. (2006). CAVER: a new tool to explore routes from protein clefts, pockets and cavities. *BMC Bioinformatics* *7*, 316.
- Qiu, X., Janson, C.A., Court, R.I., Smyth, M.G., Payne, D.J., and Abdel-Meguid, S.S. (1999). Molecular basis for triclosan activity involves a flipping loop in the active site. *Protein Sci* *8*, 2529-2532.
- Quemard, A., Sacchettini, J.C., Dessen, A., Vilcheze, C., Bittman, R., Jacobs, W.R., Jr., and Blanchard, J.S. (1995). Enzymatic characterization of the target for isoniazid in *Mycobacterium tuberculosis*. *Biochemistry* *34*, 8235-8241.
- Rafferty, J.B., Simon, J.W., Baldock, C., Artymiuk, P.J., Baker, P.J., Stuitje, A.R., Slabas, A.R., and Rice, D.W. (1995). Common themes in redox chemistry emerge from the X-ray structure of oilseed rape (*Brassica napus*) enoyl acyl carrier protein reductase. *Structure* *3*, 927-938.
- Rafi, S., Novichenok, P., Kolappan, S., Zhang, X., Stratton, C.F., Rawat, R., Kisker, C., Simmerling, C., and Tonge, P.J. (2006). Structure of acyl carrier protein bound to FabI, the FASII enoyl reductase from *Escherichia coli*. *J Biol Chem* *281*, 39285-39293.
- Ramachandran, G.N., Ramakrishnan, C., and Sasisekharan, V. (1963). Stereochemistry of polypeptide chain configurations. *J Mol Biol* *7*, 95-99.
- Richard, J.L., and Grimes, D.E. (2008). Bioterrorism: class A agents and their potential presentations in immunocompromised patients. *Clin J Oncol Nurs* *12*, 295-302.

References

- Rozwarski, D.A., Vilcheze, C., Sugantino, M., Bittman, R., and Sacchettini, J.C. (1999). Crystal structure of the *Mycobacterium tuberculosis* enoyl-ACP reductase, InhA, in complex with NAD⁺ and a C16 fatty acyl substrate. *J Biol Chem* *274*, 15582-15589.
- Rupp, B. (2010). *Biomolecular crystallography : principles, practice, and application to structural biology* (New York: Garland Science).
- Schiebel, J., Chang, A., Lu, H., Baxter, M.V., Tonge, P.J., and Kisker, C. (2012). Staphylococcus aureus FabI: inhibition, substrate recognition, and potential implications for in vivo essentiality. *Structure* *20*, 802-813.
- Schrodinger, LLC (2010). *The PyMOL Molecular Graphics System, Version 1.3r1*.
- Schuttelkopf, A.W., and van Aalten, D.M. (2004). PRODRG: a tool for high-throughput crystallography of protein-ligand complexes. *Acta Crystallogr D Biol Crystallogr* *60*, 1355-1363.
- Schweizer, H.P. (1998). Intrinsic resistance to inhibitors of fatty acid biosynthesis in *Pseudomonas aeruginosa* is due to efflux: application of a novel technique for generation of unmarked chromosomal mutations for the study of efflux systems. *Antimicrob Agents Chemother* *42*, 394-398.
- Sheldrick, G.M. (2008). A short history of SHELX. *Acta crystallographica Section A, Foundations of crystallography* *64*, 112-122.
- Silver, L.L. (2011). Challenges of antibacterial discovery. *Clin Microbiol Rev* *24*, 71-109.
- Smart, J.K. (1997). History of chemical and biological warfare: an American perspective. In: Sidell, FR, Takafuji, ET, Franz, DR (Eds), *Medical Aspects of Chemical and Biological Warfare*, Borden Institute, Walter Reed Army Medical Center, Washington DC.
- Smith, S. (1994). The animal fatty acid synthase: one gene, one polypeptide, seven enzymes. *FASEB journal : official publication of the Federation of American Societies for Experimental Biology* *8*, 1248-1259.
- Spellberg, B., Gidos, R., Gilbert, D., Bradley, J., Boucher, H.W., Scheld, W.M., Bartlett, J.G., and Edwards, J., Jr. (2008). The epidemic of antibiotic-resistant infections: a call to action for the medical community from the Infectious Diseases Society of America. *Clin Infect Dis* *46*, 155-164.
- Stewart, M.J., Parikh, S., Xiao, G., Tonge, P.J., and Kisker, C. (1999). Structural basis and mechanism of enoyl reductase inhibition by triclosan. *J Mol Biol* *290*, 859-865.
- Szinicz, L. (2005). History of chemical and biological warfare agents. *Toxicology* *214*, 167-181.
- Taylor, G.L. (2010). Introduction to phasing. *Acta Crystallogr D Biol Crystallogr* *66*, 325-338.
- Thompson, J.D., Higgins, D.G., and Gibson, T.J. (1994). CLUSTAL W: improving the sensitivity of progressive multiple sequence alignment through sequence weighting, position-specific gap penalties and weight matrix choice. *Nucleic Acids Res* *22*, 4673-4680.
- Tipparaju, S.K., Joyasawal, S., Forrester, S., Mulhearn, D.C., Pegan, S., Johnson, M.E., Mesecar, A.D., and Kozikowski, A.P. (2008). Design and synthesis of 2-pyridones as novel inhibitors of the *Bacillus anthracis* enoyl-ACP reductase. *Bioorg Med Chem Lett* *18*, 3565-3569.
- Tipparaju, S.K., Muench, S.P., Mui, E.J., Ruzheinikov, S.N., Lu, J.Z., Hutson, S.L., Kirisits, M.J., Prigge, S.T., Roberts, C.W., Henriquez, F.L., *et al.* (2010). Identification and development of novel inhibitors of *Toxoplasma gondii* enoyl reductase. *J Med Chem* *53*, 6287-6300.
- Titball, R.W., and Leary, S.E. (1998). Plague. *Br Med Bull* *54*, 625-633.
- Tsay, J.T., Rock, C.O., and Jackowski, S. (1992). Overproduction of beta-ketoacyl-acyl carrier protein synthase I imparts thiolactomycin resistance to *Escherichia coli* K-12. *J Bacteriol* *174*, 508-513.
- Velankar, S., Alhroub, Y., Best, C., Caboche, S., Conroy, M.J., Dana, J.M., Fernandez Montecelo, M.A., van Ginkel, G., Golovin, A., Gore, S.P., *et al.* (2012). PDBe: Protein Data Bank in Europe. *Nucleic Acids Res* *40*, D445-452.
- Veyron-Churlet, R., Guerrini, O., Mourey, L., Daffe, M., and Zerbib, D. (2004). Protein-protein interactions within the Fatty Acid Synthase-II system of *Mycobacterium tuberculosis* are essential for mycobacterial viability. *Molecular microbiology* *54*, 1161-1172.

References

- Vonrhein, C., Blanc, E., Roversi, P., and Bricogne, G. (2007). Automated structure solution with autoSHARP. *Methods Mol Biol* 364, 215-230.
- Wallace, A.C., Laskowski, R.A., and Thornton, J.M. (1995). LIGPLOT: a program to generate schematic diagrams of protein-ligand interactions. *Protein Eng* 8, 127-134.
- Ward, W.H., Holdgate, G.A., Rowsell, S., McLean, E.G., Pauptit, R.A., Clayton, E., Nichols, W.W., Colls, J.G., Minshull, C.A., Jude, D.A., *et al.* (1999). Kinetic and structural characteristics of the inhibition of enoyl (acyl carrier protein) reductase by triclosan. *Biochemistry* 38, 12514-12525.
- WHO (2004). Human plague in 2002 and 2003. *Wkly Epidemiol Rec* 79, 301-306.
- Wiersinga, W.J., van der Poll, T., White, N.J., Day, N.P., and Peacock, S.J. (2006). Melioidosis: insights into the pathogenicity of *Burkholderia pseudomallei*. *Nat Rev Microbiol* 4, 272-282.
- Williamson, E.D. (2009). Plague. *Vaccine* 27 *Suppl* 4, D56-60.
- Wright, H.T., and Reynolds, K.A. (2007). Antibacterial targets in fatty acid biosynthesis. *Current Opinion in Microbiology* 10, 447-453.
- Xu, H., Sullivan, T.J., Sekiguchi, J., Kirikae, T., Ojima, I., Stratton, C.F., Mao, W., Rock, F.L., Alley, M.R., Johnson, F., *et al.* (2008). Mechanism and inhibition of saFabI, the enoyl reductase from *Staphylococcus aureus*. *Biochemistry* 47, 4228-4236.
- Yum, J.H., Kim, C.K., Yong, D., Lee, K., Chong, Y., Kim, C.M., Kim, J.M., Ro, S., and Cho, J.M. (2007). In vitro activities of CG400549, a novel FabI inhibitor, against recently isolated clinical staphylococcal strains in Korea. *Antimicrob Agents Chemother* 51, 2591-2593.
- Zhang, Y., and Cronan, J.E., Jr. (1998). Transcriptional analysis of essential genes of the *Escherichia coli* fatty acid biosynthesis gene cluster by functional replacement with the analogous *Salmonella typhimurium* gene cluster. *J Bacteriol* 180, 3295-3303.
- Zhang, Y.M., Marrakchi, H., White, S.W., and Rock, C.O. (2003a). The application of computational methods to explore the diversity and structure of bacterial fatty acid synthase. *J Lipid Res* 44, 1-10.
- Zhang, Y.M., Wu, B., Zheng, J., and Rock, C.O. (2003b). Key residues responsible for acyl carrier protein and beta-ketoacyl-acyl carrier protein reductase (FabG) interaction. *J Biol Chem* 278, 52935-52943.
- Zheng, C.J., Sohn, M.J., and Kim, W.G. (2009). Vinaxanthone, a new FabI inhibitor from *Penicillium* sp. *J Antimicrob Chemother* 63, 949-953.
- Zheng, C.J., Sohn, M.J., Lee, S., Hong, Y.S., Kwak, J.H., and Kim, W.G. (2007). Cephalochromin, a FabI-directed antibacterial of microbial origin. *Biochem Biophys Res Commun* 362, 1107-1112.
- Zhu, L., Lin, J., Ma, J., Cronan, J.E., and Wang, H. (2010). Triclosan resistance of *Pseudomonas aeruginosa* PAO1 is due to FabV, a triclosan-resistant enoyl-acyl carrier protein reductase. *Antimicrob Agents Chemother* 54, 689-698.

6. Appendix

6.1 Supplemental Figures

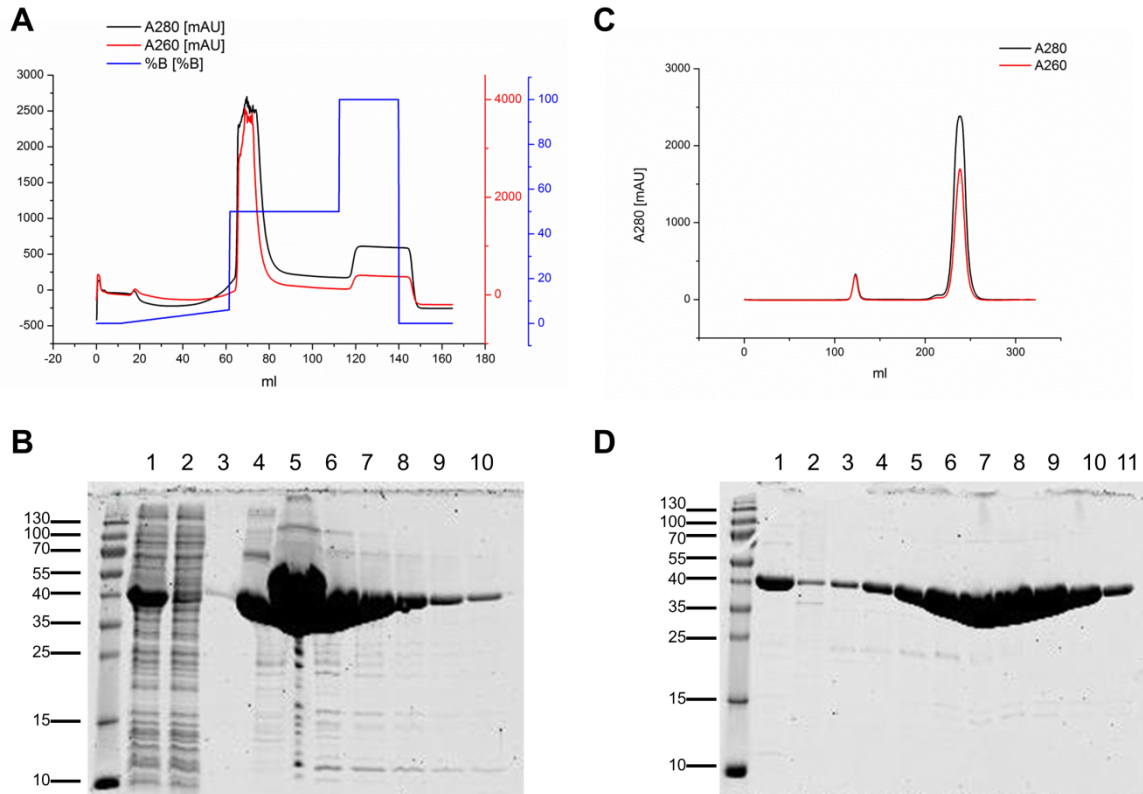


Figure 57: Purification of BpFabV

A) Chromatogram of a Histrap purification with a step gradient, absorption at 280 nm (black) and 260 nm (red), % Elution buffer (blue). B) SDS-PAGE of Histrap purification: (1) Load, (2) Flowthrough, (3) wash out unbound sample, (4-10) elution. C) Chromatogram of size exclusion chromatography, absorption at 280 nm (black) and 260 nm (red). B) SDS PAGE of size exclusion chromatography: (1) aggregate peak (at approx.120 ml) (2-11) main peak.

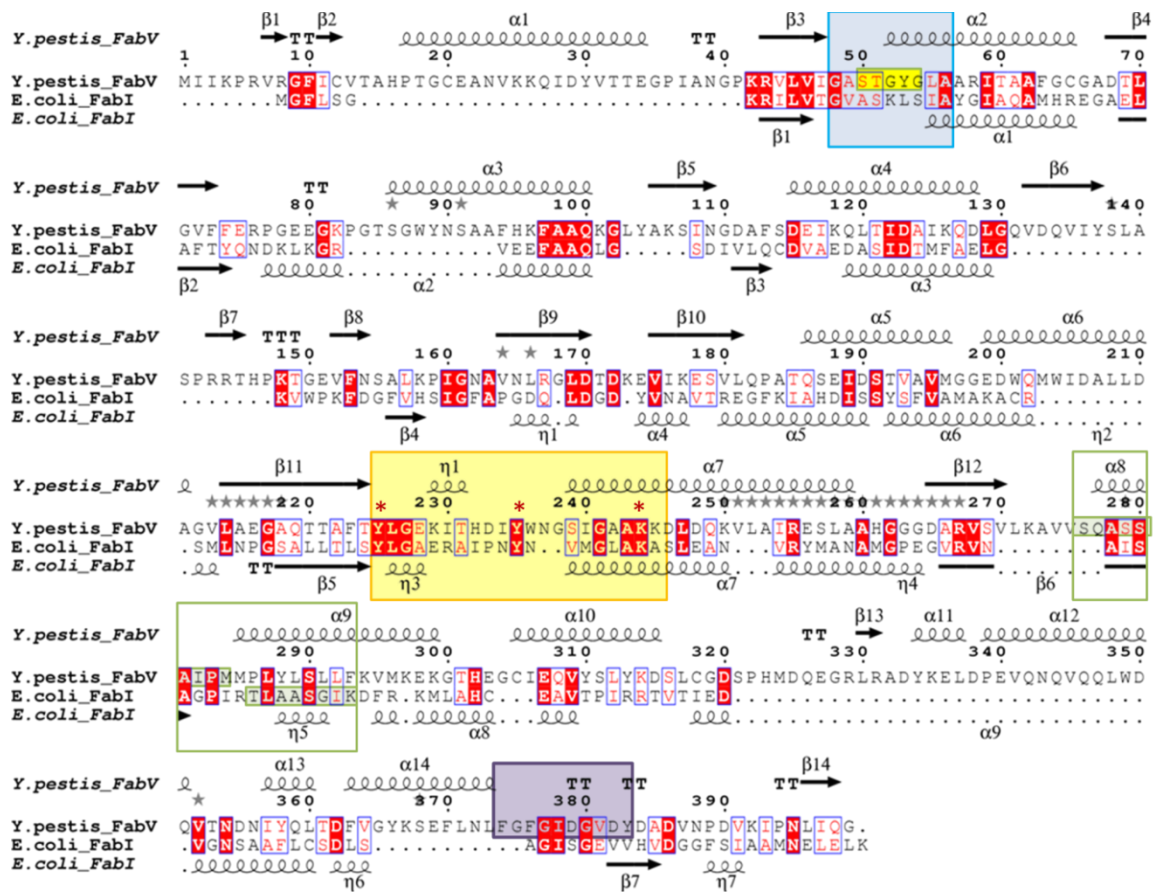


Figure 58: Sequence alignment of YpFabV and EcFabI

Sequence alignment (ClustalW, (Thompson et al., 1994)) of YpFabV and EcFabI with the cofactor binding motif shown in a blue box and with the described interaction partners of the cofactor highlighted in yellow. The active site region is highlighted in a yellow box with the catalytic residues marked by red asterisks. The substrate-binding loop is marked with a green box and the potential FAD binding site of FabV in a lilac box. Secondary structure elements are indicated by arrows and spirals for β-strands and α-helices, respectively and shown above (*YpFabV* binary) and below (*EcFabI_{tc}*) the sequence. 3₁₀helices are labeled with η and β-turns with TT. The conserved residues are highlighted in the blue boxes with the most conserved residues colored in white with a red background.

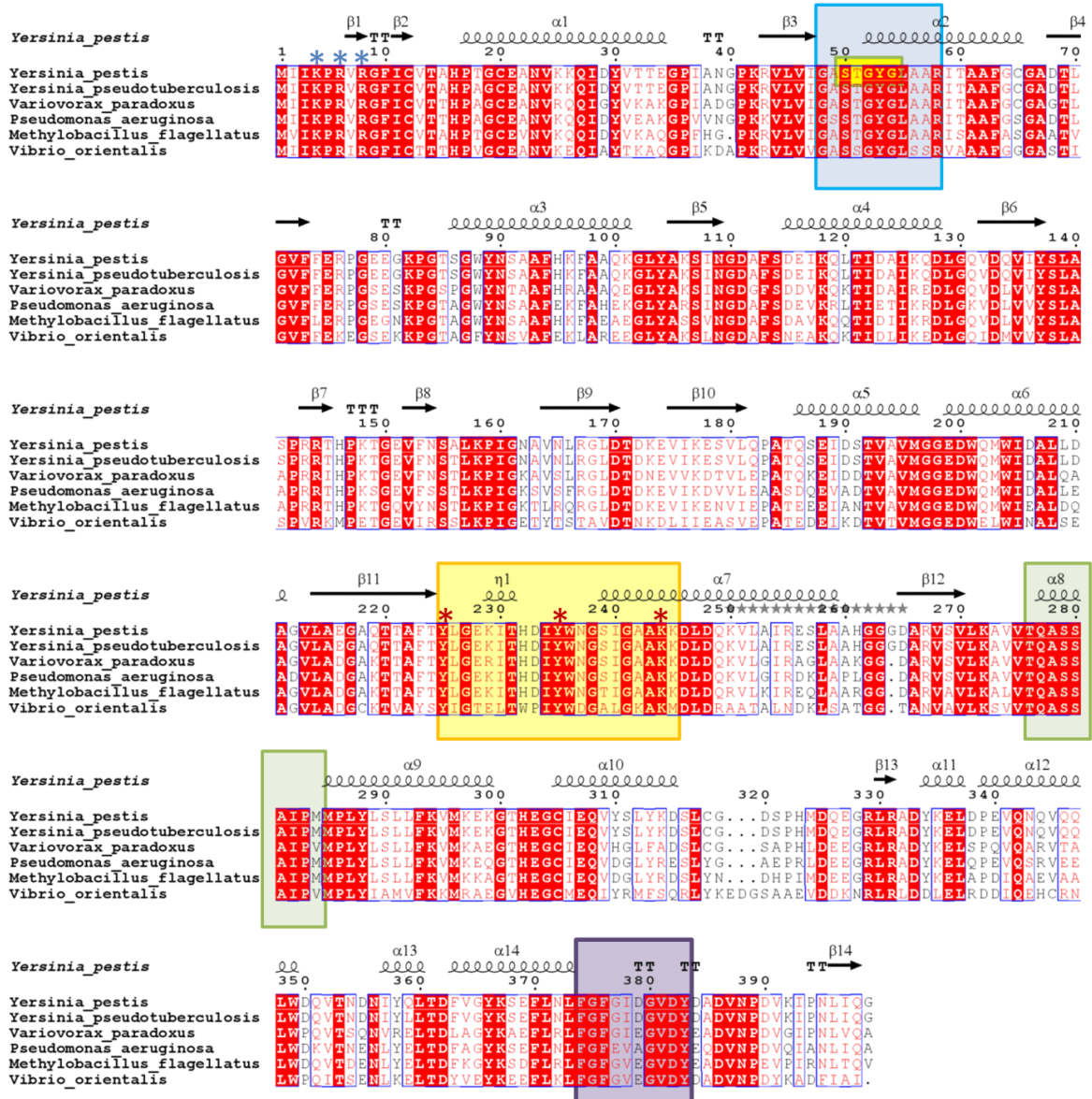


Figure 59: Sequence alignment of FabV proteins from different species

Sequence alignment (ClustalW, (Thompson et al., 1994)) of FabV from different species with the cofactor binding motif shown in a blue box and with the described interaction partners of the cofactor highlighted in yellow. The active site region is highlighted in a yellow box with the catalytic residues marked by red asterisks. The substrate-binding loop is marked with a green box and the potential FAD binding site of FabV in a lilac box. The conserved basic residues (potential ACP interaction) are marked with blue asterisks. Secondary structure elements are indicated by arrows and spirals for β -strands and α -helices, respectively and shown above (*YpFabV* binary) the sequence. 3_1 helices are labeled with η and β -turns with TT. The conserved residues are highlighted in blue boxes with the most conserved residues colored in white with a red background.

6.2 Abbreviations

Table 25: Abbreviations

AA	Acrylamide
AA/ BAA	Acrylamid/bisacrylamide
AccABCD	Acetyl-CoA Carboxylase
ACP	Acyl-carrier protein
Amp	Ampicillin
APS	Ammonium peroxydisulfate
ATP	Adenosine-5'-triphosphate
BAA	Bisacrylamide
BESSY	Berliner Elektronen-Speicherring Gesellschaft für Synchrotronstrahlung
CCD	Charge-coupled device
CoA	Coenzyme A
Coot	Crystallographic Object-Oriented Toolkit
CV	Column volume
Da	Dalton
DMSO	Dimethyl sulfoxide (DMSO)
DNA	Deoxyribonucleic acid
DSSP	Define Secondary Structure of Proteins
DTT	Dithiothreitol (DTT)
EDTA	Ethylenediaminetetraacetic acid
ESRF	European Synchrotron Radiation Facility
FabA	β -hydroxydecanoyl-ACP dehydratase/isomerase
FabB	β -ketoacyl-ACP synthase II
FabD	Malonyl-CoA-ACP transacetylase
FabF	β -ketoacyl-ACP synthase I
FabG	β -ketoacyl-ACP reductase
FabH	β -ketoacyl-ACP synthase III
FabI	Enoyl-ACP reductase I
FabK	Enoyl-ACP reductase II
FabL	Enoyl-ACP reductase III
FabM	<i>Trans</i> -2- <i>cis</i> -3-enoyl-ACP isomerase
FabV	Enoyl-ACP reductase IV
FabZ	β -hydroxyacyl-ACP dehydratase
FAS	Fatty acid biosynthesis
FPLC	Fast Protein Liquid Chromatography
IC50	half maximal inhibitory concentration
IMAC	Immobilized Metal Affinity Chromatography
IPTG	Isopropyl- β -thiogalactoside
IPTG	Isopropyl β -D-1-thiogalactopyranoside
K_i	inhibition constant
LB	Luria broth
MDR	Multi-drug resistant
MES	2-(N-morpholino)ethanesulfonic acid
MR	Molecular Replacement

MWCO	Molecular weight cut off
NADH	Nicotinamide adenine dinucleotide
NCS	Noncrystallographic symmetry
NTA	Nitrilotriacetic acid
OD	Optical density
PAGE	Polyacrylamide gel electrophoresis
PDB	Protein Data Bank
PEG	Polyethyleneglycol
PEG	Polyethylene glycol
RMSD	Root mean square deviation
SDR	Short chain Dehydrogenase/Reductase
SDS	Sodium dodecyl sulfate
SDS-PAGE	sodium dodecyl sulfate polyacrylamide gel electrophoresis
SEC	Size exclusion chromatography
SIRAS	Single isomorphous replacement with anomalous scattering
SSM	Secondary Structure Matching
TED	Triscarboxymethylethylenediamine
TEMED	Tetramethylethylenediamine
TEMED	Tetramethylethylenediamine
TLS	Translation, Libration, Screw motion
TCL	Triclosan
Tris	Tris(hydroxymethyl)aminomethane
XDR	extensively drug resistant
XDS	X-ray Detector Software

Amino acids

Table 26: Abbreviations of amino acids

Alanine	A
Arginine	R
Asparagine	N
Asparatic acid	D
Cysteine	C
Glutamic acid	E
Glutamine	Q
Glycine	G
Histidine	H
Isoleucine	I
Leucine	L
Lysine	K
Methionine	M
Phenylalanine	F
Proline	P
Serine	S
Threonine	T
Tryptophan	W
Tyrosine	Y
Valine	V

6.3 List of Figures, Tables and Equations

Figures

Figure 1: Systemic antibacterials approved by the US Food and Drug Administration, modified from (Spellberg et al., 2008)	3
Figure 2: Cell wall of Gram-positive (A) and Gram-negative (B) bacteria.....	5
Figure 3: Spectra and target locations of antibacterials, modified after (Silver, 2011).....	6
Figure 4: Endemic distribution of Melioidosis, modified after (Cheng and Currie, 2005).....	8
Figure 5: Black death, 16th century woodcut	10
Figure 6: Scheme of the FAS-II elongation cycle.....	13
Figure 7: FabI Inhibitors.....	17
Figure 8: Inhibition of phospholipid synthesis of <i>P. aeruginosa</i> PAO1 wild type and mutants by triclosan (Zhu et al., 2010).....	20
Figure 9: Size-exclusion chromatography.....	33
Figure 10: Crystallization by vapor diffusion	36
Figure 11: Harker construction for the SIR approach.....	44
Figure 12: Harker construction for the SIRAS approach.....	45
Figure 13: FabV Expression.....	49
Figure 14: Thermofluor analysis of BmFabV.....	50
Figure 15: Purification of YpFabV T276S	51
Figure 16: Purification of wild-type YpFabV	52
Figure 17: Thrombin cleavage	54
Figure 18: T276S YpFabV crystals from different crystallization screens	56
Figure 19: Diffraction pattern and crystal (corner) of YpFabV	57
Figure 20: YpFabV structure (teal) as ribbon diagram with bound iodines (purple).	58
Figure 21: Ramachandran plots for the YpFabV T276S variant (A) and wild-type (B) structures.....	61
Figure 22: Artificial dimer interface in YpFabV T276S structure	62
Figure 23: Crystallization conditions of binary cofactor complexes of cleaved YpFabV	63
Figure 24: Co-crystallization (A-C) with 2-pyridone inhibitors PT172 (D) and PT173 (E).....	64
Figure 25: Alternate conformations in the cleaved YpFabV structures.....	67
Figure 26: Evaluation of inhibitor fitting	68
Figure 27: Crystallization conditions of apo BpFabV	69
Figure 28: MES molecule in the active site of BpFabV2	72
Figure 29: Ramachandran plot for (A) BpFabV1 and (B) BpFabV2	73
Figure 30: Loop distortion in BpFabV1 by crystal contact	74
Figure 31: SDS-PAGE of cell lysate from the expression test of BpFabI in pLysS <i>E.coli</i> cells at 25 °C.....	75
Figure 32: Thermofluor analysis on BpFabI	76
Figure 33: Purification of BpFabI	77

Figure 34: Crystallization condition of BpFabI in its apo form (A) and in the ternary complexes with the cofactor NAD⁺ and the inhibitor triclosan (TCL) (B), PT02 (C), PT404 (D), PT12 (E) or PT155 (F). 79

Figure 35: Stabilization of the substrate-binding loop by crystal contacts 82

Figure 36: Validation of ligand fitting. 85

Figure 37: Structure of YpFabV..... 86

Figure 38: Structural comparison of YpFabV (binary complex containing NADH) with EcFabI (ternary complex containing NAD⁺ and triclosan) 88

Figure 39: Sequence alignment of BpFabI, BpFabV and YpFabV..... 89

Figure 40: Active site of FabV 90

Figure 41: Active site residues in FabV apo structures..... 92

Figure 42: Stabilization of the substrate-binding loop in FabV 93

Figure 43: Cofactor binding of YpFabV 95

Figure 44: OMIT electron density map of NADH (YpFabV binary)..... 96

Figure 45: Impact of T276S variant on NADH binding 98

Figure 46: The substrate-binding loop shifts upon inhibitor binding 101

Figure 47: Inhibitor binding of PT172 and PT173 in YpFabV 102

Figure 48: Hypothetical substrate-binding mechanism..... 104

Figure 49: Potential FAD binding site 106

Figure 50: Overall structure of BpFabI 109

Figure 51: Active site of BpFabI 112

Figure 52: Cofactor binding of BpFabI 114

Figure 53: Substrate binding loop in ternary BpFabI complexes..... 117

Figure 54: Inhibitor binding in BpFabI (see following page)..... 118

Figure 55: Comparison of inhibitor conformation..... 120

Figure 56: Interactions of the p-nitro moieties of PT12 and PT404 with their surrounding environment ... 121

Figure 57: Purification of BpFabV 134

Figure 58: Sequence alignment of YpFabV and EcFabI..... 135

Figure 59: Sequence alignment of FabV proteins from different species 136

Tables

Table 1: Bioweapons: pathogens and diseases 7

Table 2: Known enoyl-ACP reductases of important pathogens..... 15

Table 3: Inhibitors..... 22

Table 4: Expression Vectors..... 23

Table 5: *Escherichia coli* strains 23

Table 6: Enzymes, Kits and Miscellaneous Reagents..... 23

Table 7: Crystallization screens 24

Appendix

Table 8: Technical equipment	24
Table 9: Consumable supplies	26
Table 10: Software.....	26
Table 11: Different Ni-affinity chromatography procedures.....	32
Table 12: Buffers for the affinity chromatography.....	32
Table 13: Gel Filtration Buffers.....	34
Table 14: SDS PAGE - gel recipe and solutions	35
Table 15: Thermofluor	36
Table 16: Data collection and refinement statistics of YpFabV structures (incl. hexahistidine tag)	59
Table 17: Data collection and refinement statistics for the cleaved YpFabV structures.....	65
Table 18: Data collection and refinement statistics of the BpFabV structures	71
Table 19: Data collection and refinement statistics of the BpFabI apo structure and ternary inhibitor complexes.....	81
Table 20: Inhibitors of the T276S variant (Hirschbeck et al., 2012)	99
Table 21: Molecular interactions stabilizing Q-interface defined by PDBe PISA server	111
Table 22: Molecular interactions stabilizing P-interface defined by PDBe PISA server.....	111
Table 23: Inhibitors of BpFabI (unpublished data, Weixuan Yu and Carla Neckles (Neckles, 2012); and (Liu et al., 2011)).....	116
Table 24: Comparison of averaged physiochemical properties of general drugs and antibacterials with different spectrum (data from (O'Shea and Moser, 2008))	124
Table 20: Abbreviations.....	137
Table 21: Abbreviations of amino acids	138
Table 22: Thermofluor screen	146
Table 23: Salt Screen I	146
Table 24: PEG pH 6.5 Screen	148

Equations

Equation 1: Bragg's law	39
Equation 2: Linear merging R-value	41
Equation 3: Precision-indicating merging R-value.....	41
Equation 4: Inverse Fourier transform	41
Equation 5: Relation of structure factor and amplitudes.....	42
Equation 6: Calculation of structure factors.....	42
Equation 7: Patterson function P_{uvw}	42
Equation 8: Matthew's coefficient	43
Equation 9: Isomorphous difference	44
Equation 10: R-value	46

6.4 DNA and amino acid sequences of protein constructs

The vector part of the constructs is shown in blue and the mutation in the T276S variant of YpFabV is marked in yellow and red.

YpFabV wild type

DNA sequence:

ATGGGCAGCAGCCATCATCATCATCACAGCAGCGGCCTGGTGCCGCGCGGCAGCCATATGCTCGAGA
TGATTATAAAACCACGTGTACGCGGCTTTATCTGTGTGACAGCTCATCCGACGGGCTGTGAAGCCAACGTC
AAGAAGCAGATCGACTACGTCAACAACAGAAGGCCCAATCGCTAATGGTCTAAAAGAGTATTAGTGATTG
GTGCGTCAACTGGATACGGGTTAGCAGCCCGGATCACAGCAGCATTGGTTGTGGCGCCGATACGCTGGG
CGTTTTCTTTGAACGCCCCGGTGAAGAAGGCAAACCCGGAACCTCCGGTTGGTACAATAGCGCGGCTTTCC
ACAAATTTGCGGCACAGAAAGGCTTGTACGCAAAAAGCATCAACGGCGATGCGTTCTCTGATGAGATCAA
ACAACACTGACTATCGATGCTATCAAGCAAGATCTGGGTCAAGTTGATCAGGTTATCTATAGCCTTGCTTCACC
ACGACGCACCCATCCGAAAACGGGCGAAGTGTTTAACTCGGCACTGAAACCTATCGGTAATGCTGTTAATT
TGCGTGGTCTGGACACCGATAAAGAAGTTATCAAGGAATCGGTCTTGCAACCGGCAACACAAAGCGAGAT
CGACAGTACAGTGGCCGTCATGGGTGGCGAAGACTGGCAGATGTGGATTGACGCTCTGTTGGACGCTGGC
GTACTGGCCGAAGGGGCACAAACGACAGCATTACCTATCTAGGCGAAAAAATTACTCACGATATTTACTG
GAACGGTTCATTGGCGCAGCCAAAAAAGATCTGGACCAGAAGGTGCTGGCTATCCGCGAGAGCCTGGCG
GCTCACGGCGGTGGCGATGCTCGCGTATCCGTATTAAGCAGTCGTGACCCAAGCCAGCTCTGCCATTCC
AATGATGCCTCTGTATTTATCATTGCTATTTAAAGTGATGAAAGAGAAAGGCACTCACGAAGGCTGCATCG
AGCAGGTCTATCCCTGTATAAAGACAGCCTGTGCGGCGATTACCCGCATATGGACCAAGAAGGTCGTCTG
CGGGCTGATTACAAAGAATTGGATCCTGAAGTCCAAAATCAGGTTGAGCAGTTGTGGGATCAGGTTACCAA
CGACAACATTTATCAGCTAACTGATTCGTTGGTTATAAATCAGAGTTCCTAAATCTGTTCCGTTTTCGGTATT
GACGGTGTGGATTATGATGCAGACGTTAACCTGATGTAAAAATCCCTAACTTGATTACAGGGTTAA

Amino acid sequence:

MGSSHHHHHSSGLVPRGSHMLEMIIKPRVRGFCVTAHPTGCEANVKKQIDYVTTTEGPIANGPKRVLVIGAST
GYGLAARITAAFSGADTLGVFFERPGEEGKPGTSGWYNSAAFHKFAAQKGLYAKSINGDAFSDIQLTIDAIAK
QDLGQVDQVIYSLASPRRTHPKTGEVFNSALKPIGNAVNLRGLDTEKVIKESVLQPATQSEIDSTVAVMGGED
WQMWIDALLDAGVLAEGAQTTAFTYLGEKITHDIYWNGSIGAAKKDLQKVLAIRESLAAHGGGDARVSVLKA
VVTQASSAIPMMPLYLSLLFKVMKEKGTHEGCIEQVYSLYKDSLCDSPHMDQEGRLRADYKELDPEVQNQVQ
QLWDQVTNDNIYQLTDFVGYKSEFLNLFVGFIDGVDYDADVNPDKIPNLIQG

YpFabV T265S

DNA sequence:

ATGGGCAGCAGCCATCATCATCATCACAGCAGCGGCCTGGTGCCGCGCGGCAGCCATATGCTCGAGA
TGATTATAAAACCACGTGTACGCGGCTTTATCTGTGTGACAGCTCATCCGACGGGCTGTGAAGCCAACGTC
AAGAAGCAGATCGACTACGTCAACAACAGAAGGCCCAATCGCTAATGGTCTAAAAGAGTATTAGTGATTG
GTGCGTCAACTGGATACGGGTTAGCAGCCCGGATCACAGCAGCATTGGTTGTGGCGCCGATACGCTGGG
CGTTTTCTTTGAACGCCCCGGTGAAGAAGGCAAACCCGGAACCTCCGGTTGGTACAATAGCGCGGCTTTCC
ACAAATTTGCGGCACAGAAAGGCTTGTACGCAAAAAGCATCAACGGCGATGCGTTCTCTGATGAGATCAA
ACAACACTGACTATCGATGCTATCAAGCAAGATCTGGGTCAAGTTGATCAGGTTATCTATAGCCTTGCTTCACC
ACGACGCACCCATCCGAAAACGGGCGAAGTGTTTAACTCGGCACTGAAACCTATCGGTAATGCTGTTAATT
TGCGTGGTCTGGACACCGATAAAGAAGTTATCAAGGAATCGGTCTTGCAACCGGCAACACAAAGCGAGAT
CGACAGTACAGTGGCCGTCATGGGTGGCGAAGACTGGCAGATGTGGATTGACGCTCTGTTGGACGCTGGC

GTACTGGCCGAAGGGGCACAAACGACAGCATTACCTATCTAGGCGAAAAAATTACTCACGATATTTACTG
GAACGGTTCCATTGGCGCAGCCAAAAAAGATCTGGACCAGAAGGTGCTGGCTATCCGCGAGAGCCTGGCG
GCTCACGGCGGTGGCGATGCTCGCGTATCCGTATTAAGCAGTCGTG **T**CCCAAGCCAGCTCTGCCATTCC
AATGATGCCTCTGTATTTATCATTGCTATTTAAAGTGATGAAAGAGAAAGGCACTCACGAAGGCTGCATCG
AGCAGGTCTATCCCTGTATAAAGACAGCCTGTGCGGCGATTACCCGCATATGGACCAAGAAGGTCGTCTG
CGGGCTGATTACAAAGAATTGGATCCTGAAGTCCAAAATCAGGTTTACGAGTTGTGGGATCAGGTTACCAA
CGACAACATTTATCAGCTAACTGATTCGTTGGTTATAAATCAGAGTTCCTAAATCTGTTCCGGTTCCGGTATT
GACGGTGTGGATTATGATGCAGACGTTAACCTGATGTAAAAATCCCTAACTTGATTACAGGGTTAA

Amino acid sequence:

MGSSHHHHHHSSGLVPRGSHMLEMIIKPRVRGFICVTAHPTGCEANVKKQIDYVTTEGPIANGPKRVLVIGAST
GYGLAARITAAFVCGADTLGVFFERPGEEGKPGTSGWYNSAAFHKFAAQKGLYAKSINGDAFSEIKQLTIDAIAK
QDLGQVDQVIYSLASPRRTHPKTGEVFNALKPIGNAVNLRGLDLDKEVIKESVLQPATQSEIDSTVAVMGGED
WQMWIDALLDAGVLAEGAQTFTAFTYLGEKITHDIYWNWSIGAAKKDLQKVLAIRESLAAHGGGDARVSVLKA
VV **S**QASSAIPMMPLYLSLLFKVMKEKGTHEGCIQVYSLYKDSLKGDSPHMDQEGRLRADYKELDPEVQNQVQ
QLWDQVTNDNIYQLTDFVGYKSEFLNLFVGFIDGVDYDADVNPDKIPNLIQG

BpFabV

DNA sequence:

ATGGGCAGCAGCCATCATCATCATCACAGCAGCGGCCTGGTGCCGCGCGGCAGCCATATGCTCGAGA
TGATCATCAAACCGCGCGTACGCGGCTTCATCTGCGTCAACCACCCACCCCGCCGGCTGCGCGGGCAGCGTT
CGCGAGCAGATCGGTACGTCGCCC GCCGCGGCCGATCGAGCGCGGCCCGAAGAAGGTGCTCGTGATC
GGCGCGTCGACGGGCTACGGGCTCGCCGCGCGCATCGCCGCCGTTCCGGCGCGGGCGCGGCGACGCTC
GGGGTGTCTTCGAGCGCGCGCCGGCGGACGCGAAGCCCGGCACGCGCCGGTGGTACAACAGCGCGGCG
TTCCACGACGAAGCGGCCGCGCGGGCCTCCAGGCGACGAGCGTCAACGGCGACGCGTTCTCCGACGAGA
TCAAGCACAAGACGATCGATGCGATCCGGCGCGATCTCGGCAGGTGGACCTTGTCGTCTACAGCGTCGC
CGCGCCGCGCAGGACGCATCCGAAAACGGGCGTCACGCATCAGTCGACGTTGAAGCCGATCGGCCACGCG
GTGCGGCTGCGCGGCATCGATACGGACAACGAGGCGATCAAGGAAACGCTGCTGCAGCCGGCCACGCCC
GACGAGATCGCGGACACGGTCGCCGTGATGGGCGGCGAGGACTGGCGCATGTGGATCGACGCGCTCGAT
GCGGGCGGAGTGCTTGCCGACGGCGCGAAGACGACCGGTTACGTATCTGGGCGAGCAGGTCACGCAC
GACATCTACTGGAACGGCTCGATCGGCGAAGCGAAGAAGGATCTCGACCGCACCGTGCTCGCGCTGCGCG
GCAAGCTCGCCGCGCGGGCGGCGACGCGCGCTCTCGGTGCTGAAGGCGGTCGTCACGCAGGCGAGCT
CCGCGATCCCGATGATGCCGCTCTACCTGTGCTGCTCTTCAAGGTGATGAAGGCGCGGCGCACGCATGAA
GGCTGCATCGAGCAGGTCGACGGCCTGTTGCGCGACAGCCTGTACGGCGCGAGCCGACGTCGACGCGG
AAGGCCGGCTGCGCGGACCGCCTCGAGCTCGATCCGGCCGTGACGGCGCGCTGCTCGAGCTGTGGG
ACCAGGTGACGAGCAATCTGTATACGCTCACCGATTCGCCGGCTACAAGGCCGAATTCCTGCGCCTG
TTCGGCTTCGGGATCGACGGCGTCGATTACGATGCGCCTGTGAGCCGAACGTACGGATTCCGAATCTGAT
CGAATGA

Amino acid sequence:

MGSSHHHHHHSSGLVPRGSHMIIKPRVRGFICVTTHPAGCAASVREQIAYVARRGPIERGPKKVLVIGASTGYG
LAARIAAAFVGAATLGVFFERAPADAKPGTAGWYNSAAFHDEAAARGLQATSVNGDAFSEIKHKTIDAIRR
DLGQVDLVVYSVAAPRTHPKTGVTHTQSTLKPIGHAVRLRGIDTDNEAIKETLLQPATPDEIADTVAVMGGED
WRMWIDALDAAGVLADGAKTTAFTYLGEQVTHDIYWNWSIGEAKKDLDRTVLALRGKLAARGGDARVSVLKA
VVTQASSAIPMMPLYLSLLFKVMKARGTHEGCIQVDGLLRDSLYGAQPHVDAEGRRLRADRLELDPVQARVL
ELWDQVTDNLYTLTDFAGYKAEFLRLFVGFIDGVDYDAPVEPNVRIPNLIE

PaFabV

DNA sequence:

ATGGGCAGCAGCCATCATCATCATCACAGCAGCGGCCCTGGTGCCGCGCGGCAGCCATATGCTCGAGA
TGATCATCAAACCGCGCGTGCCTGCTTTCATCTGCGTCACTACCCATCCGGCAGGCTGCGAGGCCAACGTC
AAGCAACAGATCGACTACGTCGAGGCCAAGGGCCCCGTCGTC AACGGACCGAAGAAGGTCCTGGTCATCG
GTTCCCTCCACCGGCTATGGCCTGGCTGCCCGCATACCGCCGCTTCGGTTCGGGCGCCGATAACCTCGGG
GTGTTCTTCGAGCGTCCGGGCAGCGAGAGCAAGCCGGGCACCGCCGGCTGGTACAACCTCGGCGGCCTTCG
AGAAGTTCGCCCACGAGAAAGGCCTGTATGCCCGCAGCATCAATGGCGACGCTTCTCCGACGAGGTGAA
GCGGCTGACCATCGAGACCATCAAGCGCGATCTCGGCAAGGTCGACCTGGTGGTCTACAGCCTGGCCGCG
CCGCGCCGTACCCATCCGAAGAGCGGCGAAGTGTTCTCCTCGACCCTCAAGCCGATCGGCAAGTCCGGTCA
GCTTCCGTGGCCTGGACACCGACAAGGAAGTGATCAAGGACGTGGTCTGGAGGCGCCAGCGACCAGG
AGGTCGCCGATAACGTTGCGGTGATGGGCGGCGAGGACTGGCAGATGTGGATCGACGCGCTGCTGGAGG
CCGACGTGCTGGCCGACGGCGCGAAGACCACCGCTTACCTACCTGGGCGAGAAGATCACCCACGACAT
CTACTGGAACGGTTCATCGGCGCAGCCAAGAAGGATCTCGACCAGAAGGTCCTCGGTATCCGCGACAAG
CTCGCCCCGCTGGGCGGCGACGCGCGCTCTCGGTGCTCAAGGCGGTGGTGACCCAGGCCAGCTCGGCG
ATCCCGATGATGCCGCTGTACCTGTCGCTGCTGTTCAAGGTGATGAAGGAGCAGGGTACCCACGAAGGTT
GCATCGAGCAGGTCGACGGCCTGTACCGGGAGAGCCTGTACGGCGCCGAGCCGCGCCTCGACGAGGAAG
GCCGCTGCGTGCCGACTACAAGGAAGTGCAGCCGGAAGTGCAGTCCCGTGTGAGGAGCTGTGGGACA
AGGTAACCAACGAGAACCTTTACGAATTGACCGACTTCGCCGGCTACAAGAGCGAGTTCCTCAACCTGTTT
GGTTTCGAGGTCGCTGGGGTCGACTACGAGCAGGACGTCAACCCGGACGTGCAGATCGCCAACCTGATCC
AGGCCTGA

Amino acid sequence:

MGSSHHHHHSSGLVPRGSHMIKPRVRGFCVTTHPAGCEANVKQIDYVEAKGPVVNGPKKVLVIGSSTGY
GLAARITAAFSGADTLGVFFERPGSESKPGTAGWYNSAAFEKFAHEKGLYARSINGDAFSDEVKRLTIETIKRDL
GKVDLVVYSLAAPRRTHPKSGEVFSSTLKPIGKSVSFRGLDTEKVIKDVVLEAASDQEVADTVAVMGGEDWQ
MWIDALLEADVLDGAKTTAFTYLGEKITHDIYWNGSIGAAKKDLQKVLGIRDKLAPLGGDARVSVLKAVVTQ
ASSAIPMMPLYLSLLFKVMKEQGTHEGCIQVDGLYRESLYGAEPRLDEEGRRLRADYKELQPEVQSRVEELWDK
VTNENLYELTDFAGYKSEFLNLFGEVAGVDYEQDVNPDVQIANLIQA

BpFabi

DNA sequence:

ATGGGCTTTCTGACGGTAAACGTATTCTGCTGACGGCCTCTTGTCGAACCGTTCGATCGCTTACGGCATC
GCCAAGGCGTGCAAGCGCGAAGGCGCCGAGCTGGCGTTCACCTACGTGCGCGATCGCTTCAAGGATCGCA
TCACCGAGTTCGCGGCCGAGTTCGGCAGCGAACTCGTGTTCCCGTGCATGTCGCCGACGATGCGCAGAT
CGATGCGCTCTTCGCGTCGCTGAAGACGCACTGGGATTCGCTCGACGGCCTCGTCCACTCGATCGGCTTCG
CGCCGCGCGAGGCGATCGCGGGCGACTTCCTCGACGGCCTCACGCGCGAGA AACTTCCGCATCGCGCACGA
CATCTCCGCATACAGCTTCCCCGCGCTCGCGAAGGCGGCGCTGCCGATGCTGTGCGGACGATGCGTCGCTGC
TCACGCTGTGATCTCGGCGCGGAGCGGGCGATCCCGAACTACAACACGATGGGCCTCGCGAAGGCGGC
GCTCGAGGCGAGCGTGCGCTATCTCGCGGTGTCGCTCGGCGCGAAGGGCGTGCGCGTGAACGCGATCTC
GGCGGGCCCCGATCAAGACGCTCGCGGCAAGCGGCATCAAGAGCTTCGGCAAGATCCTCGATTTGTCGAG
AGCAACTCGCCGCTCAAGCGCAACGTGACGATCGAGCAGGTCGGCAACGCGGGCGCGTTCCTGCTGTCGG
ACCTCGCGAGCGGCGTACGGCCGAAGTCATGCACGTCGACTCGGGCTTCAACGCGGTGGTGGGCGGGA
TGGCCGGCCTCGAGGAATAA **AAGCTTGCGGCCGCACTCGAGCACCACCACCACCACCTGA**

Amino acid sequence:

MGFLDGKRILLGLLSNRSIAYGIAKACKREGAELAFYVGDREFKDRITFAAEFGSELVFPDVAADDAQIDALFASLKTHWDS
LDGLVHSIGFAPREAIAGDFLDGLTRENFRIDHISAYSPALAKAALPMLSDDASLLTSLYGAERAIIPNYNTMGLAKAALEA
SVRYLAVSLGAKGVRVNAISAGPIKTLAASGIKSFGLDFVESNSPLKRNVTIEQVGNAGAFLLSDLASGVTA EVMHVD SGF
NAVVGGMAGLEE **KLAAALEHHHHHH**

6.5 Thermofluor Screen

Table 27: Thermofluor screen

A1	100mM	citrate pH 4.5	E1	100mM	Cacodylate pH 6.0
A2	100mM	Bis-Tris pH 7.0	E2	100mM	Bis-Tris propane pH 7
A3	100mM	Imidazole pH6.5	E3	100mM	MOPS pH 7.0
A4	100mM	Hepes pH 8.0	E4	100mM	BICINE pH 9.0
A5	100mM	Tris pH 8.5	E5	100mM	Glycylglycine pH 8.5
A6		Reference	E6		Reference
B1	100mM	acetate pH 4.6	F1	100mM	Cacodylate pH 6.5
B2	100mM	ADA pH 6.5	F2	100mM	PIPES pH 6.5
B3	100mM	Imidazole pH 8.0	F3	100mM	MOPS pH 7.5
B4	100mM	HEPES pH8.5	F4	100mM	Tris pH 7.0
B5	100mM	Tris pH 9	F5	100mM	CHES pH 9.0
B6		Reference	F6		Water
C1	100mM	MES pH 5.5	G1	100mM	Bis-Tris pH 5.5
C2	100mM	ADA pH 7.0	G2	100mM	PIPES pH 7.0
C3	100mM	Na/K PO4 pH 6.8	G3	100mM	HEPES pH 7.0
C4	100mM	BICINE pH 8.0	G4	100mM	Tris pH 7.5
C5	100mM	TAPS pH 8.0	G5	100mM	CHES pH 9.5
C6		Reference	G6		Water
D1	100mM	MES pH 6.5	H1	100mM	Bis-Tris pH 6.5
D2	100mM	Bis-Tris propane pH 6	H2	100mM	PIPES pH 7.5
D3	100mM	Na/K-PO4 pH 7.55	H3	100mM	HEPES pH 7.5
D4	100mM	BICINE pH 8.5	H4	100mM	Tris pH 8.0
D5	100mM	TAPS pH 9.0	H5	100mM	CAPS pH 9.8
D6		Reference	H6		Water

6.6 Crystallization screens

Table 28: Salt Screen I

A1	2,2	M	Sodium formate	0,1	M	Imidazole pH 8.0
A2	2,5	M	Sodium formate	0,1	M	Imidazole pH 8.0
A3	2,8	M	Sodium formate	0,1	M	Imidazole pH 8.0
A4	3	M	Sodium formate	0,1	M	Imidazole pH 8.0
A5	3,3	M	Sodium formate	0,1	M	Imidazole pH 8.0
A6	2,2	M	Sodium formate	0,1	M	Sodium acetate pH 4.6
A7	2,5	M	Sodium formate	0,1	M	Sodium acetate pH 4.6
A8	2,8	M	Sodium formate	0,1	M	Sodium acetate pH 4.6
A9	3	M	Sodium formate	0,1	M	Sodium acetate pH 4.6
A10	3,3	M	Sodium formate	0,1	M	Sodium acetate pH 4.6
A11	2,2	M	Potassium formate	0,1	M	Imidazole pH 8.0
A12	2,5	M	Potassium formate	0,1	M	Imidazole pH 8.0
B1	2,8	M	Potassium formate	0,1	M	Imidazole pH 8.0
B2	3	M	Potassium formate	0,1	M	Imidazole pH 8.0
B3	3,15	M	Potassium formate	0,1	M	Imidazole pH 8.0

Appendix

B4	2,2	M	Potassium formate	0,1	M	Sodium acetate pH 4.6
B5	2,5	M	Potassium formate	0,1	M	Sodium acetate pH 4.6
B6	2,8	M	Potassium formate	0,1	M	Sodium acetate pH 4.6
B7	3	M	Potassium formate	0,1	M	Sodium acetate pH 4.6
B8	3,15	M	Potassium formate	0,1	M	Sodium acetate pH 4.6
B9	3	M	Sodium formate	0,1	M	Glycyl-glycine pH 8.5
B10	3	M	Potassium formate	0,1	M	Glycyl-glycine pH 8.5
B11	3	M	Sodium formate	0,1	M	Citric acid pH 4.0
B12	3	M	Potassium formate	0,1	M	Citric acid pH 4.0
C1	2	M	Ammonium sulfate	0,1	M	TRIS pH 8.5
C2	1,8	M	Ammonium sulfate	0,1	M	TRIS pH 8.5
C3	1,6	M	Ammonium sulfate	0,1	M	TRIS pH 8.5
C4	2,2	M	Ammonium sulfate	0,1	M	TRIS pH 8.5
C5	2,5	M	Ammonium sulfate	0,1	M	TRIS pH 8.5
C6	3	M	Ammonium sulfate	0,1	M	TRIS pH 8.5
C7	2	M	Ammonium sulfate	0,1	M	Imidazole pH 8.0
C8	2	M	Ammonium sulfate	0,1	M	Sodium acetate pH 4.6
C9	2	M	Ammonium sulfate	0,1	M	BICINE pH 9.0
C10	2	M	Ammonium sulfate	0,1	M	Glycyl-glycine pH 8.5
C11	2	M	Sodium nitrate	0,1	M	Sodium acetate pH 4.6
C12	1,8	M	Sodium nitrate	0,1	M	Sodium acetate pH 4.6
D1	1,6	M	Sodium nitrate	0,1	M	Sodium acetate pH 4.6
D2	2,2	M	Sodium nitrate	0,1	M	Sodium acetate pH 4.6
D3	2,5	M	Sodium nitrate	0,1	M	Sodium acetate pH 4.6
D4	3	M	Sodium nitrate	0,1	M	Sodium acetate pH 4.6
D5	2	M	Sodium nitrate	0,1	M	Imidazole pH 8.0
D6	2	M	Sodium nitrate	0,1	M	TRIS pH 8.5
D7	2	M	Sodium nitrate	0,1	M	BICINE pH 9.0
D8	2	M	Sodium nitrate	0,1	M	Glycyl-glycine pH 8.5
D9	1	M	Sodium malonate	0,1	M	Sodium acetate pH 4.6
D10	1,2	M	Sodium malonate	0,1	M	Sodium acetate pH 4.6
D11	1,5	M	Sodium malonate	0,1	M	Sodium acetate pH 4.6
D12	1,7	M	Sodium malonate	0,1	M	Sodium acetate pH 4.6
E1	1,4	M	Sodium malonate	0,1	M	Imidazole pH 8.0
E2	1,4	M	Sodium malonate	0,1	M	Sodium citrate pH 5.6
E3	1,4	M	Sodium malonate	0,1	M	TRIS pH 8.5
E4	1	M	Sodium malonate pH 6.0	0,1	M	Sodium citrate pH 5.6
E5	1,2	M	Sodium malonate pH 6.0	0,1	M	Sodium citrate pH 5.6
E6	1,5	M	Sodium malonate pH 6.0	0,1	M	Sodium citrate pH 5.6
E7	1,7	M	Sodium malonate pH 6.0	0,1	M	Sodium citrate pH 5.6
E8	1,4	M	Sodium malonate pH 6.0	0,1	M	Imidazole pH 8.0
E9	1,4	M	Sodium malonate pH 6.0	0,1	M	TRIS pH 8.5
E10	1	M	Na/K tartrate			
E11	1,3	M	Na/K tartrate			
E12	1,5	M	Na/K tartrate			
F1	1,7	M	Na/K tartrate			
F2	2	M	Na/K tartrate			
F3	1	M	Na/K tartrate	0,1	M	TRIS pH 8.5
F4	1,3	M	Na/K tartrate	0,1	M	TRIS pH 8.5
F5	1,5	M	Na/K tartrate	0,1	M	TRIS pH 8.5
F6	1,7	M	Na/K tartrate	0,1	M	TRIS pH 8.5
F7	1	M	Ammonium nitrate	0,1	M	TRIS pH 8.5
F8	2	M	Ammonium nitrate	0,1	M	TRIS pH 8.5

Appendix

F9	2,5	M	Ammonium nitrate	0,1	M	TRIS pH 8.5
F10	4	M	Ammonium nitrate	0,1	M	TRIS pH 8.5
F11	2,5	M	Ammonium nitrate	0,1	M	Sodium acetate pH 4.6
F12	1	M	Potassium fluoride			
G1	1	M	Potassium iodide	0,1	M	TRIS pH 8.5
G2	1,2	M	Potassium iodide	0,1	M	TRIS pH 8.5
G3	1,5	M	Potassium iodide	0,1	M	TRIS pH 8.5
G4	1	M	Potassium phosphate dibasic	0,1	M	Sodium acetate pH 4.6
G5	1,5	M	Potassium phosphate dibasic	0,1	M	Sodium acetate pH 4.6
G6	2	M	Potassium phosphate dibasic	0,1	M	Sodium acetate pH 4.6
G7	2,5	M	Potassium phosphate dibasic	0,1	M	Sodium acetate pH 4.6
G8	3	M	Potassium phosphate dibasic	0,1	M	Sodium acetate pH 4.6
G9	1	M	Potassium phosphate dibasic	0,1	M	TRIS pH 8.5
G10	1,5	M	Potassium phosphate dibasic	0,1	M	TRIS pH 8.5
G11	2	M	Potassium phosphate dibasic	0,1	M	TRIS pH 8.5
G12	2,5	M	Potassium phosphate dibasic	0,1	M	TRIS pH 8.5
H1	3	M	Potassium phosphate dibasic	0,1	M	TRIS pH 8.5
H2	1	M	Sodium tartrate	0,1	M	Imidazole pH 8.0
H3	1,2	M	Sodium tartrate	0,1	M	Imidazole pH 8.0
H4	1,5	M	Sodium tartrate	0,1	M	Imidazole pH 8.0
H5	1,8	M	Sodium tartrate	0,1	M	Imidazole pH 8.0
H6	2	M	Sodium tartrate			
H7	0,5	M	Sodium thiocyanate			
H8	0,7	M	Sodium thiocyanate			
H9	1	M	Sodium thiocyanate			
H10	0,7	M	Sodium thiocyanate	0,1	M	Sodium acetate pH 4.6
H11	0,8	M	Sodium thiocyanate	0,1	M	Sodium acetate pH 4.6
H12	0,9	M	Sodium thiocyanate	0,1	M	Sodium acetate pH 4.6

Table 29: PEG pH 6.5 Screen

A1	0,1	M	MES pH 6.5	23	%	PEG 2000 MME
A2	0,1	M	MES pH 6.5	28	%	PEG 2000 MME
A3	0,1	M	MES pH 6.5	33	%	PEG 2000 MME
A4	0,1	M	MES pH 6.5	20	%	PEG 3000
A5	0,1	M	MES pH 6.5	25	%	PEG 3000
A6	0,1	M	MES pH 6.5	30	%	PEG 3000
A7	0,1	M	MES pH 6.5	20	%	PEG 4000
A8	0,1	M	MES pH 6.5	25	%	PEG 4000
A9	0,1	M	MES pH 6.5	30	%	PEG 4000
A10	0,1	M	MES pH 6.5	20	%	PEG 6000
A11	0,1	M	MES pH 6.5	25	%	PEG 6000
A12	0,1	M	MES pH 6.5	30	%	PEG 6000
B1	0,1	M	MES pH 6.5	20	%	PEG 200
B2	0,1	M	MES pH 6.5	24	%	PEG 200
B3	0,1	M	MES pH 6.5	28	%	PEG 200
B4	0,1	M	MES pH 6.5	30	%	PEG 200
B5	0,1	M	MES pH 6.5	20	%	PEG 350 MME
B6	0,1	M	MES pH 6.5	25	%	PEG 350 MME
B7	0,1	M	MES pH 6.5	30	%	PEG 350 MME
B8	0,1	M	MES pH 6.5	20	%	PEG 400
B9	0,1	M	MES pH 6.5	25	%	PEG 400

Appendix

B10	0,1	M	MES pH 6.5	30	%	PEG 400	
B11	0,1	M	MES pH 6.5	20	%	PEG 550 MME	
B12	0,1	M	MES pH 6.5	25	%	PEG 550 MME	
C1	0,1	M	MES pH 6.5	30	%	PEG 550 MME	
C2	0,1	M	MES pH 6.5	20	%	PEG 1000	
C3	0,1	M	MES pH 6.5	25	%	PEG 1000	
C4	0,1	M	MES pH 6.5	30	%	PEG 1000	
C5	0,1	M	MES pH 6.5	20	%	PEG 1500	
C6	0,1	M	MES pH 6.5	25	%	PEG 1500	
C7	0,1	M	MES pH 6.5	30	%	PEG 1500	
C8	0,1	M	MES pH 6.5	20	%	PEG 5000 MME	
C9	0,1	M	MES pH 6.5	25	%	PEG 5000 MME	
C10	0,1	M	MES pH 6.5	30	%	PEG 5000 MME	
C11	0,1	M	MES pH 6.5	23	%	PEG 2000 MME	0,05 M Calcium chloride
C12	0,1	M	MES pH 6.5	28	%	PEG 2000 MME	0,05 M Calcium chloride
D1	0,1	M	MES pH 6.5	33	%	PEG 2000 MME	0,05 M Calcium chloride
D2	0,1	M	MES pH 6.5	20	%	PEG 3000	0,05 M Calcium chloride
D3	0,1	M	MES pH 6.5	25	%	PEG 3000	0,05 M Calcium chloride
D4	0,1	M	MES pH 6.5	30	%	PEG 3000	0,05 M Calcium chloride
D5	0,1	M	MES pH 6.5	20	%	PEG 550 MME	0,05 M Calcium chloride
D6	0,1	M	MES pH 6.5	25	%	PEG 550 MME	0,05 M Calcium chloride
D7	0,1	M	MES pH 6.5	30	%	PEG 550 MME	0,05 M Calcium chloride
D8	0,1	M	MES pH 6.4	28	%	PEG 2000 MME	
D9	0,1	M	MES pH 6.4	33	%	PEG 2000 MME	
D10	0,1	M	MES pH 6.4	25	%	PEG 3000	
D11	0,1	M	MES pH 6.4	30	%	PEG 3000	
D12	0,1	M	MES pH 6.4	25	%	PEG 550 MME	0,05 M Calcium chloride
E1	0,1	M	MES pH 6.4	30	%	PEG 550 MME	0,05 M Calcium chloride
E2	0,1	M	MES pH 6.3	28	%	PEG 2000 MME	
E3	0,1	M	MES pH 6.3	33	%	PEG 2000 MME	
E4	0,1	M	MES pH 6.3	25	%	PEG 3000	
E5	0,1	M	MES pH 6.3	30	%	PEG 3000	
E6	0,1	M	MES pH 6.3	25	%	PEG 550 MME	0,05 M Calcium chloride
E7	0,1	M	MES pH 6.3	30	%	PEG 550 MME	0,05 M Calcium chloride
E8	0,1	M	MES pH 6.6	28	%	PEG 2000 MME	
E9	0,1	M	MES pH 6.6	33	%	PEG 2000 MME	
E10	0,1	M	MES pH 6.6	25	%	PEG 3000	
E11	0,1	M	MES pH 6.6	30	%	PEG 3000	
E12	0,1	M	MES pH 6.6	25	%	PEG 550 MME	0,05 M Calcium chloride
F1	0,1	M	MES pH 6.6	30	%	PEG 550 MME	0,05 M Calcium chloride
F2	0,1	M	MES pH 6.7	30	%	PEG 2000 MME	0,04 M Calcium chloride
F3	0,1	M	MES pH 6.7	30	%	PEG 3000	0,04 M Calcium chloride
F4	0,1	M	MES pH 6.7	30	%	PEG 550 MME	0,04 M Calcium chloride
F5	0,1	M	MES pH 6.7	30	%	PEG 2000 MME	0,03 M Calcium chloride
F6	0,1	M	MES pH 6.7	30	%	PEG 3000	0,03 M Calcium chloride
F7	0,1	M	MES pH 6.7	30	%	PEG 550 MME	0,03 M Calcium chloride
F8	0,1	M	MES pH 6.5	30	%	PEG 2000 MME	0,02 M Calcium chloride
F9	0,1	M	MES pH 6.5	30	%	PEG 3000	0,02 M Calcium chloride
F10	0,1	M	MES pH 6.5	30	%	PEG 550 MME	0,02 M Calcium chloride
F11	0,1	M	MES pH 6.5	30	%	PEG 2000 MME	0,01 M Calcium chloride
F12	0,1	M	MES pH 6.5	30	%	PEG 3000	0,01 M Calcium chloride
G1	0,1	M	MES pH 6.5	30	%	PEG 550 MME	0,01 M Calcium chloride
G2	0,1	M	MES pH 6.5	30	%	PEG 2000 MME	0,06 M Calcium chloride

Appendix

G3	0,1	M	MES pH 6.5	30	%	PEG 3000	0,06	M	Calcium chloride
G4	0,1	M	MES pH 6.5	30	%	PEG 550 MME	0,06	M	Calcium chloride
G5	0,1	M	MES pH 6.5	25	%	PEG 4000	0,05	M	Calcium chloride
G6	0,1	M	MES pH 6.5	30	%	PEG 4000	0,05	M	Calcium chloride
G7	0,1	M	MES pH 6.5	25	%	PEG 6000	0,05	M	Calcium chloride
G8	0,1	M	MES pH 6.5	30	%	PEG 6000	0,05	M	Calcium chloride
G9	0,1	M	MES pH 6.5	20	%	PEG 200	0,05	M	Calcium chloride
G10	0,1	M	MES pH 6.5	24	%	PEG 200	0,05	M	Calcium chloride
G11	0,1	M	MES pH 6.5	20	%	PEG 350 MME	0,05	M	Calcium chloride
G12	0,1	M	MES pH 6.5	25	%	PEG 350 MME	0,05	M	Calcium chloride
H1	0,1	M	MES pH 6.5	20	%	PEG 400	0,05	M	Calcium chloride
H2	0,1	M	MES pH 6.5	25	%	PEG 400	0,05	M	Calcium chloride
H3	0,1	M	MES pH 6.5	25	%	PEG 1000	0,05	M	Calcium chloride
H4	0,1	M	MES pH 6.5	30	%	PEG 1000	0,05	M	Calcium chloride
H5	0,1	M	MES pH 6.5	25	%	PEG 1500	0,05	M	Calcium chloride
H6	0,1	M	MES pH 6.5	30	%	PEG 1500	0,05	M	Calcium chloride
H7	0,1	M	MES pH 6.5	20	%	PEG 5000 MME	0,05	M	Calcium chloride
H8	0,1	M	MES pH 6.5	25	%	PEG 5000 MME	0,05	M	Calcium chloride
H9	0,1	M	MES pH 6.5	30	%	PEG 5000 MME	0,05	M	Calcium chloride
H10	0,1	M	MES pH 6.5	30	%	PEG 2000 MME	0,05	M	magnesium chloride low
H11	0,1	M	MES pH 6.5	30	%	PEG 3000	0,05	M	magnesium chloride low
H12	0,1	M	MES pH 6.5	30	%	PEG 550 MME	0,05	M	magnesium chloride low

Acknowledgements

In the first place I would like to thank Professor Caroline Kisker for the guidance and her trustful supervision during my work on the PhD thesis. A special thanks to Professor Peter Tonge and Professor Christoph Sotriffer for the close collaboration on the project and helpful discussions and their good advice during the committee meetings.

I share the credit of my work with many people, who contributed to the project. Dr. Jochen Kuper helped with the experimental phasing of the first FabV structure; he and Professor Hermann Schindelin helped and taught me a lot in the field of X-ray crystallography. Dr. Sylvia Luckner introduced me to protein crystallography. I would like to thank the colleagues from the SFB 630, especially my lab mates Christin Schäfer, Johannes Schiebel and Uwe Dietzel, for their input and discussion. I am thankful to Professor Christoph Sotriffer's group for providing me some insight into their exciting docking experiments, especially to Steffen Wagner for the patient help with the software. I am particularly grateful for the fruitful collaborations with our collaborators in Professor Peter Tonge's laboratory in Stony Brook, namely Howard Lu, Nina Liu, Carla Neckles and Weixuan Yu. I want to thank the members of the Kisker and Schindelin groups for the good working environment in and outside the lab.

In the end I would like to thank my family and friends, especially my parents, for all the support and understanding throughout the last years.

Affidavit

(eidesstattliche Erklärung)

I hereby declare that my thesis entitled

“Structure-based drug design on the enoyl-ACP reductases of *Yersinia pestis* and *Burkholderia pseudomallei*”

is the result of my own work. I did not receive any help or support from commercial consultants. All sources and/or materials applied are listed and specified in the thesis.

Furthermore, I verify that this thesis, has not yet been submitted as part of another examination process neither in identical nor in similar form.

Würzburg.....

date

signature

List of publications

Hirschbeck, M.W., Kuper, J., Lu, H., Liu, N., Neckles, C., Shah, S., Wagner, S., Sotriffer, C.A., Tonge, P.J., and Kisker, C. (2012). Structure of the *Yersinia pestis* FabV enoyl-ACP reductase and its interaction with two 2-pyridone inhibitors. *Structure* 20, 89-100.

Neckles, C.S., S.; Pan, P.; Bommineni, G. R.; **Hirschbeck, M.W.**; Yu, W.; Liu, N.; Kisker, C.; Tonge, P. J. (2012). Mechanism, Inhibition and Comparison of *Yersinia pestis* Enoyl-ACP Reductase, FabV, to *Burkholderia pseudomallei* Enoyl-ACP Reductases, FabI and FabV. manuscript in preparation.